PB88-178587

Influence of Coal Mineral Matter on the Effectiveness of Dry Sorbent Injection for SO2 Control

Energy and Environmental Research Corp.
Irvine, CA

Prepared for

Environmental Protection Agency
Research Triangle Park, NC

Aug 87

U.S. Department of Commerce
National Technical Information Service
NTIS

PB88-178587

EPA/600/7-87/020
August 1987

INFLUENCE OF COAL MINERAL MATTER ON THE EFFECTIVENESS OF DRY SORBENT INJECTION FOR SO_2 CONTROL

Prepared by:

D. M. Slaughter
W. J. Thomson
T. W. Peterson
S. L. Chen
W. R. Seeker
D. W. Pershing

Energy and Environmental Research Corporation
18 Mason
Irvine, CA 92718-2798

EPA Contract No. 68-02-3987

EPA Project Officer
David A. Kirchgessner
Air and Energy Engineering Research Laboratory
Research Triangle Park, NC 27711

AIR AND ENERGY ENGINEERING RESEARCH LABORATORY
OFFICE OF RESEARCH AND DEVELOPMENT
U.S. ENVIRONMENTAL PROTECTION AGENCY
RESEARCH TRIANGLE PARK, NC 27711

REPRODUCED BY
U.S. DEPARTMENT OF COMMERCE
NATIONAL TECHNICAL
INFORMATION SERVICE
SPRINGFIELD, VA. 22161

TECHNICAL REPORT DATA
(Please read Instructions on the reverse before completing)

1. REPORT NO. EPA/600/7-87/020	2.	3. RECIPIENT'S ACCESSION NO. PB88 - 178587/AS
4. TITLE AND SUBTITLE Influence of Coal Mineral Matter on the Effectiveness of Dry Sorbent Injection for SO_2 Control		5. REPORT DATE August 1987
		6. PERFORMING ORGANIZATION CODE
7. AUTHOR(S) D. M. Slaughter, W. J. Thomson, T. W. Peterson, S. L. Chen, W. R. Seeker, and D. W. Pershing		8. PERFORMING ORGANIZATION REPORT NO.
9. PERFORMING ORGANIZATION NAME AND ADDRESS Energy and Environmental Research Corporation 18 Mason Irvine, California 92718-2798		10. PROGRAM ELEMENT NO.
		11. CONTRACT/GRANT NO. 68-02-3987
12. SPONSORING AGENCY NAME AND ADDRESS **EPA, Office of Research and Development** **Air and Energy Engineering Research Laboratory** **Research Triangle Park, NC 27711**		13. TYPE OF REPORT AND PERIOD COVERED
		14. SPONSORING AGENCY CODE **EPA/600/13**

15. SUPPLEMENTARY NOTES AEERL project officer is David A. Kirchgessner, Mail Drop 4, 919/541-4021.

16. ABSTRACT The report describes the use of laboratory-, bench-, and pilot-scale facilities to examine the impact of mineral matter on calcium-based sorbent reactivity toward SO2. Two areas of concern were investigated: (1) deleterious effects of coal ash, and (2) beneficial (promoter) effects of additive and ash minerals. The mechanisms of sorbent/mineral interactions were also studied using a variety of sophisticated techniques, including scanning electron microscopy, energy dispersive spectroscopy, x-ray spectroscopy, x-ray microprobing, and dynamic x-ray diffractometry. Coal ash deactivation was shown to occur through the formation of calcium silicates which reduces calcium availability and promotes sintering of the sorbent. However, this mechanism was found important only when the ash and sorbent were intimately contacted prior to firing. Alkali metals and chromium-series transition elements were found to promote sorbent reactivity. The basic mechanisms involved the increase of mass transfer within sorbent particles by altering the pore structure, as well as increased solid product layer diffusion (increased ion mobility). The alkali metals were also found to react directly with SO2.

17. KEY WORDS AND DOCUMENT ANALYSIS

a. DESCRIPTORS		b. IDENTIFIERS/OPEN ENDED TERMS	c. COSATI Field/Group	
Pollution	Coal	Pollution Control	13B	21D
Sulfur Dioxide	Alkali Metals	Stationary Sources	07B	
Sorbents	Chromium	Coal Ash	11G	
Reactivity			07D	
Calcium				
Minerals			08G	

18. DISTRIBUTION STATEMENT **Release to Public**	19. SECURITY CLASS *(This Report)* **Unclassified**	21. NO. OF PAGES 271
	20. SECURITY CLASS *(This page)* **Unclassified**	22. PRICE

EPA Form 2220-1 (9-73)

NOTICE

This document has been reviewed in accordance with U.S. Environmental Protection Agency policy and approved for publication. Mention of trade names or commercial products does not constitute endorsement or recommendation for use.

ABSTRACT

Laboratory -, bench -, and pilot-scale facilities were used to examine the impact of mineral matter on calcium-based sorbent reactivity toward SO_2. Two areas of concern were investigated: 1) deleterious effects of coal ash, 2) beneficial (promotor) effects of additive and ash minerals. The mechanisms of sorbent-mineral interactions were also studied using a variety of sophisticated techniques. These include scanning electron microscopy, energy dispersive spectroscopy, X-ray spectroscopy, X-ray microprobing, and dynamic X-ray diffractometry.

Coal ash deactivation was shown to occur through the formation of calcium silicates which reduces calcium availability and promotes sintering of the sorbent. However, this mechanism was found important only when the ash and sorbent were intimately contacted prior to firing.

Alkali metals and chromium-series transition elements were found to promote sorbent reactivity. The basic mechanisms involved the increase of mass transfer within sorbent particles by altering the pore structure, as well as increased solid product layer diffusion (increased ion mobility). The alkali metals were also found to react directly with SO_2.

TABLE OF CONTENTS

Section Page

E.0 EXECUTIVE SUMMARY E-1

PART I. INTRODUCTION 1-1

1.0 PROGRAM DEFINITION AND APPROACH 1-1

1.1 Technical Background 1-1
1.1.1 Calcium-Based Sorbents (Without Additives) . . . 1-1
1.1.2 Calcium-Based Sorbents with Additives 1-4
1.2 Program Objectives and Approach 1-4
1.2.1 Program Objectives 1-4
1.2.2 Program Approach 1-5
1.3 Report Organization 1-6

PART II. EQUIPMENT AND MATHEMATICAL SYSTEMS 2-1

2.0 EXPERIMENTAL FACILITIES 2-1

2.1 Boiler Simulator Furnace 2-1
2.1.1 Furnace System 2-1
2.1.2 Measurement Systems 2-3
2.2 Control Temperature Tower 2-7
2.3 Dynamic X-ray Diffractometer 2-11
2.3.1 Equipment Description 2-11
2.3.2 Experimental Procedure 2-17

3.0 MATHEMATICAL MODELS 3-1

3.1 The Equilibrium NASA Computer Code 3-1
3.2 The MAEROS Computer Code 3-2

4.0 SOLID CHARACTERIZATION (FUELS, SORBENTS, PROMOTERS) 4-1

4.1 Fuels 4-1
4.2 Calcium-Based Sorbents 4-1
4.3 Sorbent-Additive Mixtures 4-5
4.3.1 Premixed Powders 4-5
4.3.2 Evaporative Deposition 4-6
4.3.3 Pressure Hydration 4-15

TABLE OF CONTENTS (Continued)

Section Page

4.3.4 Vaporized Promoters--The Rotary Kiln 4-18

PART III. INTERACTION MECHANISMS 5-1

5.0 COAL ASH/SORBENT 5-1

5.1 Fate of Mineral Matter 5-1
5.2 Ash/Sorbent Interaction and Reaction 5-1
5.3 LIMB Simulation Tests 5-6
5.4 Conclusions 5-10

6.0 PROMOTION OF CALCIUM-BASED SORBENTS 6-1

6.1 Formulation of Hypotheses 6-1
6.1.1 Contact Mechanism 6-1
6.1.2 Sulfation Enhancement Mechanism 6-2
6.2 Promoters Investigated 6-4
6.2.1 Chromium 6-7
6.2.2 Alkali Metals 6-25
6.2.3 Iron 6-37
6.3 Conclusions 6-42

7.0 PROMOTER/COAL ASH 7-1

7.1 Promoter/Ash Interaction 7-1
7.1.1 Sodium/Ash Interaction 7-3
7.1.2 Chromium/Ash Interaction 7-15
7.2 Sodium Condensation on Ash and Sorbent Particles . . . 7-25
7.2.1 Coal Type 7-30
7.2.2 Ash Distributions 7-30
7.2.3 Sorbents 7-31
7.2.4 Additive Characteristics 7-31
7.2.5 The Simulations 7-35
7.3 Conclusions 7-54

TABLE OF CONTENTS (Continued)

Section		Page
PART IV.	PROCESS EVALUATION	8-1
8.0	SULFATION RATES FOR DOPED SORBENTS	8-1
8.1 Reaction Kinetics for Vicron Sulfation	8-1
8.1.1 Effect of Calcination	8-2
8.1.2 Effect of Surface Area	8-2
8.1.3 The Effect of SO_2 Concentration	8-5
8.1.4 The Effect of Temperature	8-7
8.1.5 Sintering	8-7
8.2 Reaction Kinetics for Doped Sorbents	8-12
8.2.1 Effect of Dopant and Sorbent Type	8-12
8.2.2 Effect of Temperature	8-15
8.3 Conclusions	8-16
9.0	PARAMETRIC STUDY ON PREMIXED POWDERS AND SPECIAL DOPED SORBENTS	9-1
9.1 Premixed Powders (A Parametric Study)	9-1
9.1.1 Comparison of Combustion Facilities	9-1
9.1.2 Sodium Chemical Form and Size	9-4
9.1.3 Injection Temperature and Location	9-7
9.1.4 Sorbent Type	9-7
9.2 Special Sorbents	9-11
9.2.1 Sodium Deposited Carbonates	9-11
9.2.2 Promoted Calcines	9-15
9.2.3 Promoted Hydrates	9-20
9.3 Conclusions	9-23
PART V.	CLOSURE	10-1
10.0	CONCLUSIONS	10-1
10.1 Interaction Mechanisms	10-1
10.2 Processs Evaluation	10-2
11.0	REFERENCES	11-1

TABLE OF CONTENTS (Concluded)

Section Page

PART VI. APPENDICES A-1

A Quality Assurance A-1

B Development of the DXRD Technique B-1

LIST OF FIGURES

Figure		Page
2-1	Boiler Simulator Furnace (BSF)	2-2
2-2	Distributed mixing burner schematic, BSF (tertiary air ports not shown)	2-4
2-3	Continuous monitoring sampling system	2-5
2-4	SO_2 continuous monitoring system	2-6
2-5	Thermal profile of the Boiler Simulator Furnace	2-8
2-6	Cross-sectional views of the control temperature tower . . .	2-9
2-7	Premixed burner	2-10
2-8	CTT thermal profiles	2-12
2-9	DXRD apparatus	2-13
2-10	Siemens D50V diffractometer	2-14
2-11	Sample holder	2-16
3-1	Interaction mechanisms	3-3
3-2	Time and temperature dependence in a pulverized coal fired boiler	3-4
4-1	High resolution photographs of Vicron, precalcine Vicron, Longview hydrate and EER pressure hydrate (Micrograph No. 03902, 04002, 04101 and 44501, respectively)	4-4
4-2	Photographs of premixed sorbents (Micrograph No. 03900--no dopant; 10006--Na; 04300--Cr; 04200--Fe)	4-7
4-3	Apparatus for generation of precalcined sorbents	4-9
4-4	Sedigraph analysis for calcined Vicron	4-10
4-5	Pore distribution of precalcined Vicron (compared to raw Vicron)	4-12
4-6	Varian setup for depositions (Cr, Na, and Fe)	4-13
4-7	Photographs of precalcine sorbents (Micrograph No. 17301--no dopant; 17600-Na; 17500-Cr; 17400-Fe)	4-14

LIST OF FIGURES (Continued)

Figure Page

4-8 Pressure hydrator setup 4-16

4-9 Photographs of pressure hydrates with insoluble promoters (Micrograph No. 87803 and 87900--no dopant; 35001 and 49901--Fe). 4-19

4-10 Photographs of pressure hydrates with soluble promoters (Micrographs No. 87802--no dopant; 49900--Na, 58701--Cr; 49300-Fe) 4-21

4-11 Rotary kiln schematic 4-23

4-12 Charging system 4-24

5-1 Fate of mineral matter during coal combustion 5-2

5-2 Influence of contacting mineral ash with Vicron on sulfur capture 5-4

5-3 SEM photograph of fired Vicron with ash 5-5

5-4 Characteristic time for coagulation of particles in turbulent flow in furnaces. (Air at 1773K, $\varepsilon = 100\ m^2/sec^3$) as function of particle size and number density 5-7

5-5 Effect of fuel type on capture with Vicron and Longview . . . 5-9

6-1 Estimation of diffusion coefficients for different diffusion mechanisms 6-5

6-2 Performance of SO_2/SO_3 catalysts as a function of temperature 6-6

6-3 The extent of Cr_2O_3 vaporization as a function of stoichiometric ratio and temperature 6-8

6-4 Equilibrium chromium species predicted by thermodynamic calculations 6-9

6-5 Comparison of sulfur capture between fired Vicron with and without Cr_2O_3 present at two different temperatures 6-11

6-6 Influence of Cr_2O_3 (bulk) concentration on sulfur capture . . 6-12

6-7 Scanning electron micrographs of fired Vicron (21229, 21237) and Vicron with Cr_2O_3 (1000, 1001) 6-13

LIST OF FIGURES (Continued)

Figure — Page

6-8 Phase diagram for CaO-Cr_2O_3 mixtures 6-15

*6-9 EDS analysis of chromium promoted Vicron (shown in Figure 6-7, No. 01000); chromium intensity map 6-16

*6-10 EDS analysis of chromium promoted Vicron (shown in Figure 6-7, No. 01000); sulfur intensity map 6-18

*6-11 EDS analysis of chromium promoted Vicron (shown in Figure 6-7, No. 01001); chromium intensity map 6-19

6-12 Line-scan of Ca, Cr, and S from a microprobe of a sulfated Vicron (with Cr_2O_3) sample 6-20

6-13 Influence of kinetic rate on sulfation and ultimate capture on a chromium promoted calcine 6-23

6-14 Morphology of sulfated chromium promoted calcine (Micrographs No. 10703--0% Cr; No. 33310, 33305, and 33306--Ca/Cr 16) 6-24

*6-15 EDS analysis of sulfated chromium promoted calcine (shown in Figure 6-14, No. 33305); sulfur intensity map 6-26

6-16 Summary of sulfur capture with alkali metals 6-27

6-17 The extent of sodium vaporized 6-28

6-18 Equilibrium sodium species predicted by thermodynamic calculations 6-29

6-19 Comparison in sulfur capture between fired Vicron with and without $NaHCO_3$ present at two different temperatures 6-31

6-20 Influence of Na_2CO_3 (bulk) concentration on sulfur capture 6-32

6-21 Influence of sodium (surface) concentration on surface morphology of a fired Vicron (Micrograph No. 20404--0% Na; No. 10001--6% Na; 20001--12% Na; and No. 20712--12% Na atomic) 6-34

6-22 Influence of kinetic rate on sulfation and ultimate capture on a sodium promoted calcine 6-35

6-23 Morphology of sulfated sodium promoted calcine (Micrographs No. 10720--0% Na; No. 99916; 99918 and 99915--Ca/Na = 25 atomic ratio) 6-36

LIST OF FIGURES (Continued)

Figure Page

6-24 Sulfur capture between fired Vicron with and without Fe_2O_3 present at two different temperatures 6-38

6-25 Sulfur capture between pressure hydrate with and without Fe present for two fuels 6-39

6-26 Influence of kinetic rate on sulfation and ultimate capture wion an iron promoted calcine 6-40

6-27 Morphology of sulfated iron promoted calcine (Micrographs No. 10700--0% Fe; No. 33412, 33421, and 33413--Ca/Fe = 16 atomic ratio) 6-41

*6-28 EDS analysis of sulfated iron promoted calcine (shown in Figure 6-27, No. 33413); sulfur intensity map 6-43

7-1 Enhancement comparison between coal and gas 7-2

7-2 The effect of coal mineral matter on $NaHCO_3$ enhancement . . . 7-4

7-3 The effect of coal ash on $NaHCO_3$ 7-5

7-4 $NaHCO_3$ capture with coal and gas 7-6

7-5 SEM photograph of sulfated Vicron/sodium fired with coal . . 7-8

*7-6 Spectrograph from EDS analysis of Na promoted Vicron fired with coal (see Figure 7-5) 7-9

*7-7 Elemental distribution maps from EDS analysis of Na promoted Vicron fired with coal (see Figure 7-5) 7-10

*7-8 Sodium intensity map from EDS analysis of Na promoted Vicron fired with coal (see Figure 7-5) 7-11

*7-9 Calcium intensity map EDS analysis of Na promoted Vicron fired with coal (see Figure 7-5) 7-12

*7-10 Sulfur intensity map from EDS analysis of Na promoted Vicron fired with coal (see Figure 7-5) 7-13

*7-11 Silicon intensity map from EDS analysis of Na promoted Vicron fired with coal (see Figure 7-5) 7-14

7-12 Capture Correlation 7-16

7-13 The effect of coal mineral matter on Cr_2O_3 7-17

LIST OF FIGURES (Continued)

Figure Page

7-14 The effect of coal ash on Cr_2O_3 enhancement 7-18

7-15 Influence of coal cleaning 7-20

7-16 SEM photograph of sulfated Vicron/chromium fired with coal 7-22

*7-17 Spectrograph from EDS analysis of Cr promoted Vicron fired with coal (see Figure 7-16) 7-23

*7-18 Elemental distribution maps from EDS analysis of Cr promoted Vicron fired with coal (see Figure 7-16) 7-24

*7-19 Chromium intensity map from EDS analysis of Cr promoted Vicron fired with coal (see Figure 7-16) 7-26

*7-20 Calcium intensity map from EDS analysis of Cr promoted Vicron fired with coal (see Figure 7-16) 7-27

*7-21 Sulfur intensity map from EDS analysis of Cr promoted Vicron fired with coal (see Figure 7-16) 7-28

*7-22 Silicon intensity map from EDS analysis of Cr promoted Vicron fired with coal (see Figure 7-16) 7-29

7-23 Simulation EER01 7-40

7-24 Simulation EER01a 7-41

7-25 Simulation EER01b 7-42

7-26 Simulation EER02 7-43

7-27 Simulation EER02a 7-44

7-28 Simulation EER02b 7-45

7-29 Simulation EER03 7-46

7-30 Simulation EER03a 7-47

7-31 Simulation EER03b 7-48

7-32 Simulation EER04 7-49

7-33 Simulation EER04a 7-50

7-34 Simulation EER04b 7-51

LIST OF FIGURES (Continued)

Figure Page

7-35 Simulation EER05a 7-52

7-36 Simulation EER05b 7-53

8-1 Vicron calcination rates (T = 923 K) 8-3

8-2 Vicron sulfation as a function of SO_2 concentration (6% O_2, remainder N_2, 923 K) 8-6

8-3 Vicron sulfation as a function of temperature (simulation gas) 8-8

8-4 Vicron sintering as a function of temperature 8-9

8-5 Sulfation of evaporatively doped limestone (simulation gas, T = 923 K) 8-13

8-6 Sulfation of doped pressure hydrate limestone (simulation gas, T = 923 K) 8-14

8-7 Sulfation of sodium doped pressure hydrate sample as a function of temperature (simulation gas) 8-17

8-8 Sulfation of chromium doped pressure hydrate sample as a function of temperature (simulation gas) 8-18

8-9 Sulfation comparisons for pressure hydrate samples at 1083 K (simulation gas) 8-19

9-1 BSF vs. CTT comparison for gas 9-2

9-2 BSF vs. CTT comparison for coal 9-3

9-3 Capture enhancement with Na-based additives 9-5

9-4 Influence of additive particle size 9-6

9-5 Injection locations (e.g., temperature) of sodium and Vicron on sulfur capture 9-8

9-6 Sulfur capture of sodium bicarbonate premixed with a variety of calcium-based sorbents 9-10

9-7 Kiln fired carbonate (micrograph No. 43900, and 44303--no Na; No. 45602, and 44904--Na) 9-12

9-8 Sulfur capture with sodium promoted carbonates 9-14

LIST OF FIGURES (Concluded)

Figure Page

9-9 Kiln fired calcine at 1033 K (Micrograph No. 44900, 44901, 44902, and 44083) 9-16

9-10 Sulfur capture with sodium promoted calcines 9-17

9-11 Kiln fired calcine at 1310 K (micrograph No. 47104 and 47103--no Na; No. 47002 and 47001--Na 9-19

9-12 Sulfur capture with sodium promoted pressure hydrates . . . 9-21

9-13 Sulfur capture with promoted pressure hydrates 9-22

9-14 SEM photographs of sulfated Cr_2O_3 doped pressure hydrate . . 9-24

*9-15 EDS analysis of sulfated Cr_2O_3 doped pressure hydrate; sulfur intensity map (micrograph No. 50054) 9-25

(*) Energy dispersion spectroscopy (EDS) played a major role in the study reflected by this report. Unfortunately, only black-and-white copies of the spectrographs are provided in this report. Copies in full color are available for inspection only at EPA's Air and Energy Engineering Research Laboratory, Research Triangle Park, NC 27711.

LIST OF TABLES

Table Page

4-1 Fuel Properties 4-2

4-2 Sorbent Properties 4-3

4-3 Pressure Hydrate Physical and Chemical Properties 4-20

4-4 Characteristics of Kiln-Produced Sorbents 4-26

5-1 Fuel Composition 5-8

5-2 S/Na Ratio Comparison 5-11

6-1 Possible Sulfation Reactions 6-3

7-1 Fuel Analysis 7-21

7-2 Coal Characterization 7-32

7-3 Sorbent Characterization 7-33

7-4 Additive Characterization 7-34

7-5 Simulations Performed 7-37

7-6 Critical Condensation Temperatures 7-38

8-1 BET Measurements on Selected Samples 8-4

9-1 Characteristics of Kiln-Produced Sorbents 9-13

EXECUTIVE SUMMARY

This report summarizes the results of the research program conducted by the Energy and Environmental Research Corporation (EER) for the U.S. Environmental Protection Agency to examine in detail the interactions between calcium based sorbents and chemical species which could either enhance or detract from the sorbents ability to capture SO_2 in pulverized coal flames. Previous, limited experimental studies at EER had indicated that sorbent performance would be influenced by various inorganic compounds, particularly those occurring in coal mineral matter.

Program Objectives

The overall program objectives were to:

- determine the influence of mineral ash constituents on the sulfur capture performance of calcium based sorbents,
- define the chemical compounds which can enhance the ability of the calcium based sorbents to capture SO_2 and identify the mechanism(s) of promotion,
- establish the influence of mineral ash on the effectiveness of sorbent promoters, and
- optimize the process for addition of the promoter materials to the sorbents.

Program Scope

A combined experimental and theoretical approach was used in this study. Programs examined the physical and chemical changes of a wide variety of sorbents with carefully selected chemical additives under different composition environments and over the range of time temperature histories. Experimental testing was conducted in furnace facilities ranging from laboratory to small pilot scale with both natural gas and coal as the primary fuel. Thermal histories ranging from near isothermal to highly quenched conditions were considered. Fundamental mechanistic information on the interactions between the promoters and calcium based sorbents were obtained from a dynamic X-ray diffractometer (DXRD) and from extensive investigation of solid samples extracted from the combustion furnaces. Chemical and elemental analysis techniques included electron microscopy (scanning and transmission), energy dispersion spectroscopy and x-ray diffractrometry. DXRD was used to trace the formation of chemical species and the destruction of solid, promoted and unpromoted, calcium compounds as a function of time and temperature. Microscopy and spectroscopy techniques were used to characterize the physical morphology and elemental spatial distribution of the promoter, calcium sorbent, and chemical constituents of the mineral ash. X-ray analysis was used to quantify chemical species present. Equilibrium calculations based on free energy minimization were used to characterize the probable gas and solid phase species. The MAEROS computer program was used to involve the multicomponent population balance equations governing the coagulation, fragmentation, condensation, and nucleation of the ash and promoter aerosols system.

Coal/Sorbent Interactions

Under certain, limited conditions coal mineral matter can influence the effectiveness of calcitic sorbents. If the mineral matter and sorbent are in direct, intimate contact (particularly by simultaneous pulverization) prior to injection and if they are injected through the burner into the temperature regions of a boiler, sorbent performance may be reduced. The controlling mechanism appears to involve the formation of low melting eutectics: the calcium reacts chemically with various alumina and silica components of the ash and becomes unavailable for subsequent sulfation. Because of this interaction (and because of the deleterious effects of the flame zone on the sorbent itself) burner injection can not be recommended. If, however, the sorbent is injected separately from the pulverized coal (either with the secondary air or downstream) then essentially no sorbent deactivation due to mineral matter occurs. Modelling calculations indicate that particle-

particle collision frequencies are simply not adequate to deactivate a significant number of the sorbent particles. Figure 1 shows data obtained in the 293 kW boiler simulator furnace (BSF) with both limestone (i.e., Vicron) and hydrated (i.e., Longview) sorbents injected with the fuel and downstream. A wide range of normal and cleaned coals were tested in this sequence and the results compare favorably with the data taken firing natural gas. No evidence of ash deactivation was observed with any coal. Therefore, the performance of the current LIMB concept (separate downstream sorbent injection) should not be significantly degraded by mineral ash effects.

Promoter/Sorbent Interactions

A major series of promoter screening tests indicated that chromium series transition elements and alkali metals can effectively increase the ability of calcium based sorbents to capture SO_2. Figure 2 summarizes data obtained in the bench scale Control Temperature Tower (CTT) furnace with limestone and indicates that all of the alkali metals significantly enhance the measured SO_2 capture. The primary enhancement mechanism is not chemical catalysis of the SO_2 to SO_3 reaction step; rather, these materials react chemically with the CaO to produce local, physical changes in the sorbent which enhance sorbent capture. In particular, both the chromium series elements and the alkali metals appear to induce particle fragmentation, creation of large cracks, and pore enlargement, all of which serve to increase the accessibility of the interior calcium and decrease the rate of site loss by pore mouth plugging. In addition, the promoters often produce low melting eutectics with the CaO and this liquid phase may enhance the local transport of the SO_2 to the unreacted CaO. In addition to affecting the sorbent morphology, the alkali metal promoters also directly react with SO_2 to produce sulfate products; they effectively function as sorbents themselves. The chromium compounds do not exhibit this behavior.

Coal/Promoter Interactions

Unfortunately, the effectiveness of promoted sorbents for SO_2 control may be significantly less in actual, coal fired systems than in SO_2 doped,

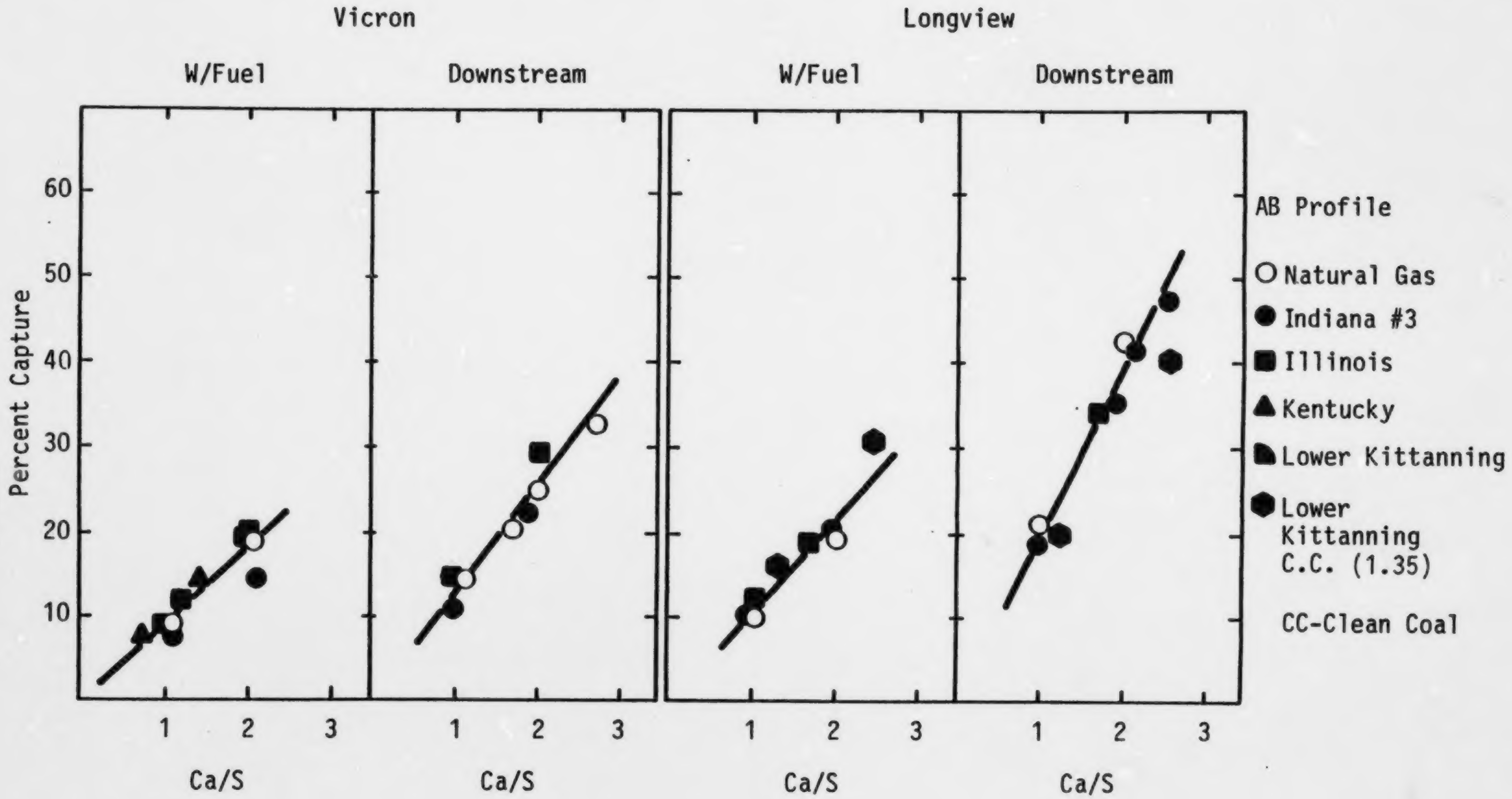

Figure 1. Effect of fuel type on capture with Vicron and Longview.

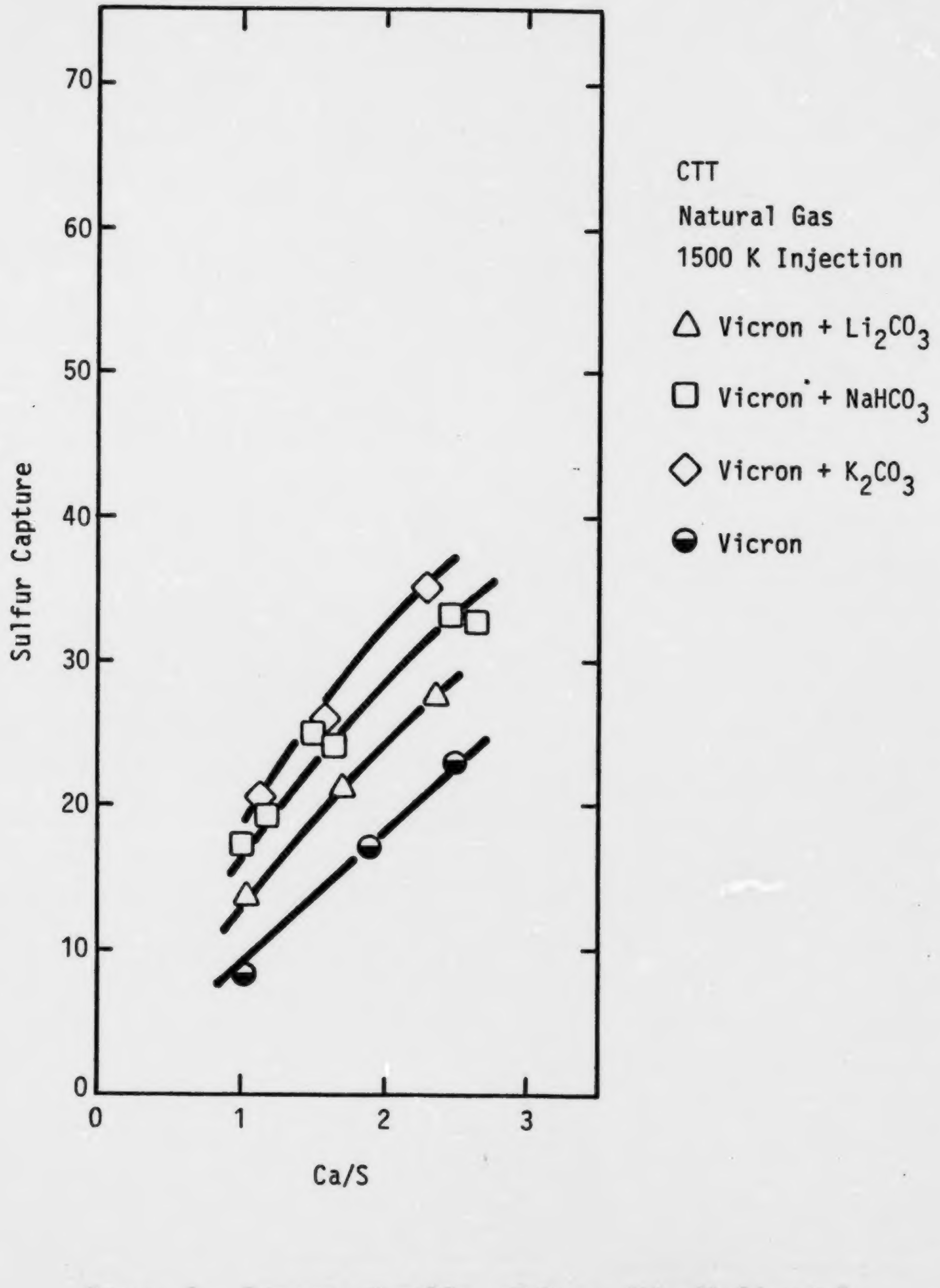

Figure 2. Summary of sulfur capture with alkali metals.

natural gas tests due to the presence of coal mineral matter, in particular the submicron ash aerosol. Figure 3 summarizes a wide series of tests conducted to evaluate the influence of coal mineral matter constituents on the promotion of limestone and hydrated sorbents by both $NaHCO_3$ and Cr_2O_3. These data indicate that under all conditions tested both the sodium and the chromium produced significant increases in sorbent utilization in the ash free experiments (natural gas firing). However, with all of the sodium promotion cases and with the chromium cases where the sorbent was added within the burner zone, the promotion effect was greatly reduced with coal firing. Only when the sorbent was added downstream and the promoter was Cr_2O_3, was the beneficial effect retained in the presence of coal firing. With sodium promotion external contact between the promoted sorbent and the coal is not required; separate injection still leads to deactivation. EDS analysis confirmed the presence of sodium on the mineral ash as well as the sorbent, suggesting the controlling mechanism is vaporization and uniform sodium condensation. Condensation modeling calculations indicated that more than 90 percent of the added sodium could condense on the submicron ash aerosol if the sorbent particles are large and the internal surface area is not readily available. X-ray diffractograms indicated that the condensed sodium reacted with the refractory oxides in the coal ash to form sodium silicates, thereby effectively reducing the sodium available for direct reaction with SO_2. Thus, the effectiveness of sodium promotion is reduced in coal fired systems simply because the promoter itself condenses on the submicron ash aerosol and the amount available for enhancement of the calcium sorbent is greatly reduced. The coal ash has less influence on chromium promotion because chromium is a far less volatile promoter. EDS analysis indicated that the chromium was primarily associated with the calcium; little chromium was found with the ash, particularly in the downstream injection cases.

Application Considerations

Parametric process studies indicated that the chemical form of the sodium promoter is not significant. Particle size can influence promotion; large particles may not be completely vaporized and dispersed in the

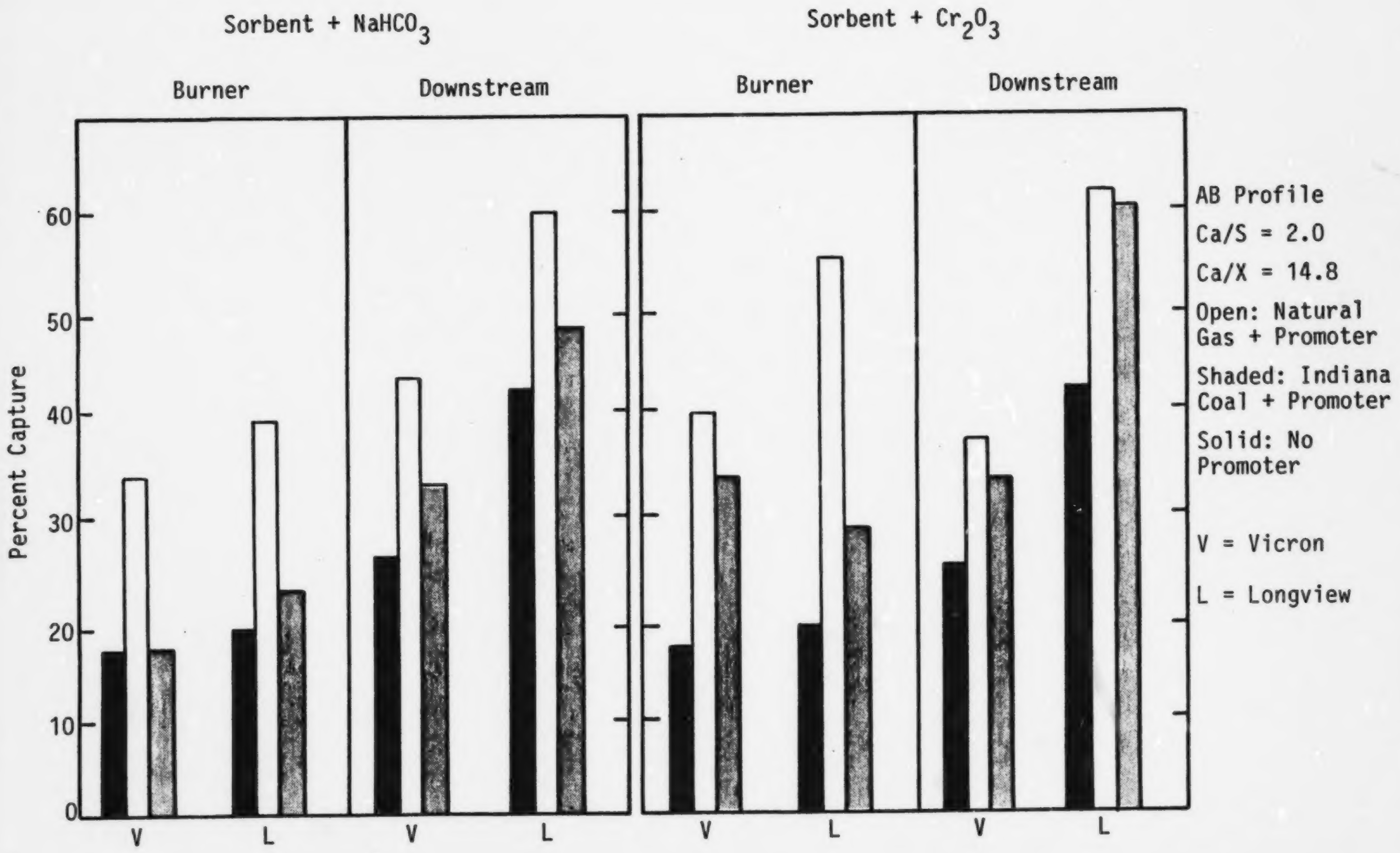

Figure 3. Enhancement comparison between coal and gas.

residence time available. Because of the vapor phase transport of the alkali metals, they need not be injected with the sorbent particles to provide effective promotion (in the absence of an ash aerosol).

Various, externally generated promoted sorbents were produced and evaluated in an attempt to avoid the deleterious effects of the ash aerosol. However, even hydration in the presence of sodium did not overcome this problem; at normal LIMB injection temperatures the sodium still tends to vaporize initially and a large fraction ultimately condenses on the submicron aerosol. Conversely, chromium promotion can be optimized to produce extremely high capture levels, although chromium promoted sorbents are almost certainly environmentally unacceptable. Figure 4 illustrates data obtained with a chromium promoted pressure hydrated calcitic sorbent and indicates that capture levels in excess of 70 percent were achieved at a Ca/S ratio of 2.0. Unfortunately, to date it has not been possible to identify an environmentally acceptable promoter capable of inducing the morphological changes produced by chromium with a sufficiently low volatility to avoid vaporization and subsequent scavenging by the ash aerosol.

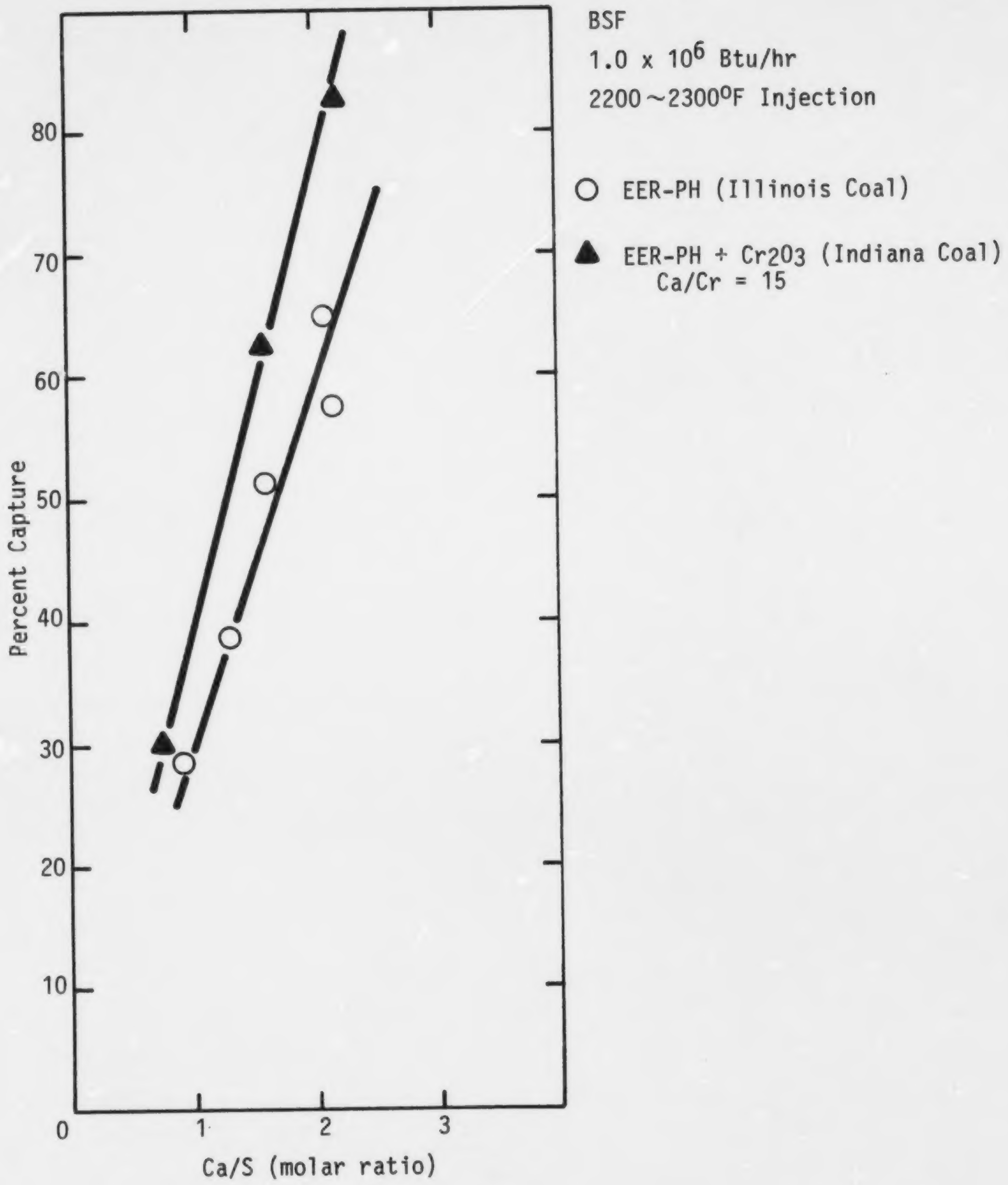

Figure 4. Chromium promoted, calcitic pressure hydrate.

PART I. INTRODUCTION

1.0 PROGRAM DEFINITION AND APPROACH

The addition of dry calcium-based sorbents in coal-fired boilers provides an alternative means for SO_2 emissions control. The process envisions the use of calcium-based sorbents to achieve intermediate levels of SO_2 removal (50-60 percent). The process is especially attractive as a retrofit for existing boilers because of the potentially low capital cost (and space requirements) relative to other control technologies.

1.1 Technical Background

Acceptable levels of SO_2 removal were not achieved at an early demonstration of dry limestone injection technology (1,2) even with a large stoichiometric excess of limestone. Since that time, a large body of research has been conducted to define the limestone-SO_2 process and determine its application in full-scale pulverized coal utility boilers.

1.1.1 Calcium-Based Sorbents (Without Additives)

The overall sulfation process includes a coupled reaction scheme; the calcium carbonates (or hydrates) decompose to the calcium oxide which can then react with oxygen and SO_2 to produce a solid $CaSO_4$. Under oxidizing conditions the overall reaction leading to sulfur capture by lime particles is

$$CaCO_3\ [Ca(OH)_2] = CaO + CO_2\ [H_2O] \qquad (1.1)$$

$$CaO + 1/2\ O_2 + SO_2 = CaSO_4 \qquad (1.2)$$

The physical characteristics of the calcined sorbents (i.e., particle size, pore volume, and surface area produced from reaction 1.1) influence the ultimate sulfur capture (3-6). Particle diameter and pore size distribution are believed to control the accessibility of the calcium; while surface area indicates the crystallites potential for reaction with SO_2 (or other competing reactions). Carbonates calcine relatively quickly (less than 250 ms) at typical combustion conditions. They begin with low initial surface areas (less than 5 m^2/g); surface area increases rapidly and then decreases as calcination proceeds. Particle fragmentation can be significant and the extent of fragmentation increases with increasing calcination temperature. As the carbonates calcine and sinter, the number of large and medium size pores increases with increasing temperature and time; in contrast the number of micropores increases initially and then dramatically declines with both increasing temperature and time.

The hydrated sorbents typically have a smaller mean particle size and a higher initial porosity and surface area as a result of the preprocessing steps: kiln calcination and hydration. The surface area of the calcitic hydrates is relatively insensitive to both residence time and temperature during calcination. The pressure slaked dolomitic hydrates exhibit an early peak in surface area and a strong sensitivity to calcination temperature. In general, the hydrated sorbents calcine significantly faster and contain a more porous structure than the corresponding carbonate analogs.

The sulfation reaction (reaction 1.2) has been studied in fundamental experiments and addressed theoretically. The heterogeneous nature of the reaction and the fact that the product $CaSO_4$, is a solid complicates the process. The steps leading to reaction include:

- Diffusion of gaseous reactant to the particle's surface
- Diffusion through pores to the particle's interior
- Diffusion through the product layer
- Reaction at the product-reactant interface

Previous experimental studies provide some insight regarding the steps that are rate controlling and the intrinsic oxygen and SO_2 concentration dependence of the reaction. However, the situation is complicated because an experimental evaluation of the intrinsic kinetics must exclude the consideration of diffusional effects. In general, the diffusion of SO_2 to the particle offers little or no resistance to reaction (7). Conclusions regarding the relative importance of pore and product layer diffusion are difficult to find; all experiments to date have been unsuccessful in decoupling the effects of pore and product-layer diffusion. Time-resolved sulfation data indicate that initial sulfation is very rapid and occurs on a time scale of 100-200 ms. Subsequently sulfation slows dramatically, either because the heterogeneous reaction kinetics and product layer diffusion coefficients are sufficiently fast to produce pore mouth closure or because the product layer diffusion is slow and large product layers effectively cover the available surface.

The intrinsic kinetics of the SO_2-lime reaction have been reported as being zero (8), 1/2 (9,10), and 1st (11) order in SO_2 and weakly dependent on oxygen concentration. Activation energies for the SO_2-lime reaction have been estimated to be between 8-130 kcal/gmol; the high values were from the early stages of the reaction and the lower values from the latter stages. It appears likely that the pore diffusion, product layer diffusion, and chemisorption of SO_2, are each linear processes with respect to SO_2 concentration. However, depending on which step is rate controlling, these series resistances may not produce an overall linear system. In addition, if pore plugging is controlling (12) the overall sulfation process, the dependence on SO_2 concentration may vary with the in situ pore size distribution of the calcined sorbent. Hence, increasing the gas phase sulfur concentration could increase the local reaction rate and result in more extensive pore (and site) blockage. Premature pore blockage could reduce the number of easily accessible calcium sites which in turn would reduce the overall sulfation rate. Therefore, it is possible that with different sorbent materials the overall reaction order could appear positive, negative, or zero depending on the pore structure which developed during the calcination process.

In summary, there is agreement that diffusion to the particle surface is not rate limiting except for larger particles. The importance of pore and product-layer diffusion appears to be a function of diameter, conversion time, and temperature. The intrinsic oxygen dependence appears to be weak and the SO_2 dependence is not well understood.

1.1.2 Calcium-Based Sorbents with Additives

Recent studies examining the influence of minerals (and coal-ash) of sulfur capture with calcium-based sorbents indicated that minerals were able able to both promote and deactivate the calcium sorbents. Initially Cr_2O_3 was found to dramatically improve the sulfur capture of limestone (13). Chromium combined with calcium-based sorbents (Ca/Cr atomic ratio = 15) increased sulfur capture by 150-300 percent at conditions simulating a coal-fired boiler. Subsequently, alkali metal compounds (lithium, sodium, potassium, etc.) were found to produce similar results (13,14). While small amounts of alkali metals (e.g., Ca/Na atomic ratio = 15) enhanced sulfur capture with calcium oxide, they were also found to react with SO_2 to form alkali metal sulfates. Some refractory oxides and clays typically found in coals were proved to reduce the effectiveness of the calcium-based sorbents both with and without promoters present (15).

1.2 Program Objectives and Approach

Calcium utilizations have been improved by 10 to 20 percent (relative to early limestone results) by the physical alteration of the sorbent before and during injection (e.g., present hydration methods). By using promoters in conjunction with these advanced sorbents calcium utilization in excess of 35 percent have been achieved under simulated boiler conditions. However, previous studies have not attempted to optimize promoted sorbents or identify the critical mechanisms.

1.2.1 Program Objectives

The work described herein examined in greater detail mineral interactions with calcium-based sorbents to determine the possible uses and restrictions of the promoter/sorbent technology. The mechanism of promoter action on the calcium-based sorbents was uncertain; therefore, the program also focused on both overall promoter effects and mechanism characterization. The program objectives were to:

- Determine the influence of mineral ash on sulfur capture performance of calcium-based sorbents.

- Determine the method by which promoters enhance the ability of calcium-based sorbents to capture gas-phase sulfur.

- Determine the influence of mineral ash on promoter effectiveness and availability to react with calcium-based sorbents.

- Optimize the processes for addition of the promoter to the calcium-based sorbent and for injection of the promoter/sorbent into the coal-fired boiler.

1.2.2 Program Approach

The program examined the physical and chemical changes of a wide variety of sorbents with additives under different chemical environments and over a range of time-temperature histories. Testing was conducted in experimental facilities ranging from laboratory to pilot scale. Two combustion furnaces, the Control Temperature Tower (CTT) and the Boiler Simulator Furnace (BSF), were used. Both facilities are down-fired and can be fired with either natural gas or coal. The CTT can operate under near-isothermal conditions as well as provide a range of temperature profiles. The BSF is able to directly simulate time and temperature profiles of pulverized coal fired boilers.

Fundamental information to elucidate the interaction between promoters and calcium-based sorbents was obtained from a dynamic X-ray diffractometer (DXRD) and extensive investigation of extracted solids (from DXRD, CTT, and BSF). Chemical and elemental analyses included electron microscopy (scanning and transmission), energy dispersive spectroscopy and X-ray diffractometry. The DXRD was used to trace the formation of chemical species and the destruction of solid, promoted (and unpromoted) calcium compounds as a function of temperature and time. Prepared samples were placed on a heated strip and surrounded by a simulated combustion gas (2000 ppm SO_2, 6% O_2, 8% CO_2 in N_2). Microscopy and spectroscopy techniques were used to characterize the physical morphology and elemental spacial distribution of the promoter, calcium sorbent and the chemical constituents of the mineral ash. The chemical species present were determined with an X-ray diffractometer.

1.3 Report Organization

This document provides the details of research on the effectiveness of promoted calcium-based sorbents. To effectively transmit the technical results with interpretation, the report was divided into six major parts:

I. Introduction

II. Equipment and Mathematical Systems

III. Interaction Mechanisms

IV. Process Evaluation

V. Closure

VI. Appendices

Equipment and Mathematical Systems (Sections 2-4) provide the detailed description of the experimental facilities, analytical techniques, mathematical models, fuels, and manufactured calcium-based sorbents used in this research. The mechanisms of sorbent promotion and deactivation are discussed in Part III, Interaction Mechanisms (Sections 5-7). Part IV, Process Evaluation (Sections 8 and 9), examines possible processes that may be successful in adapting the technology to pulverized coal fired boilers. Conclusions and recommendations are included in Part V, Closure (Section 10). Part VI (Appendices A and B) provides additional information to support the technical reliability of the generated data as well as results not included in the previous parts.

PART II. EQUIPMENT AND MATHEMATICAL SYSTEMS

2.0 EXPERIMENTAL FACILITIES

In understanding the mechanism for increased sulfur capture and potential applications of calcium-based sorbents with promoters, three experimental facilities were used. Two were combustion furnaces which were capable of burning both natural gas and coal. The third was a specially designed diffractometer equipped with an environmental chamber. The objective of this chapter is to provide a description of the equipment used in this program.

2.1 Boiler Simulator Furnace

The EER Boiler Simulator Furnace (BSF) has been the flagship furnace for the study of limestone injection processes under the most realistic conditions possible at the pilot scale. The BSF was designed and constructed with EPA funds specifically to evaluate the process parameters associated with LIMB technology.

2.1.1 Furnace System

The furnace system was designed to produce variable combustion conditions in order to simulate a wide variety of coal firing schemes, including wall firing, tangential firing, turbo, arch, tower, steamer, and cyclone. There was no attempt to simulate directly the hardware of each of these types of firing systems. In particular, the unit was designed to simulate the time/temperature/stoichiometry histories of typical full scale utility boilers. A schematic of the 293 kW BSF is shown in Figure 2-1. The facility consists of two main sections: a refractory-lined vertical radiant tower and a horizontal convective section containing air-cooled heat exchangers. The radiant tower has an ID of 55 cm and an OD of 98 cm and consisted of eight modular sections with multiple access ports. The BSF can be used to simulate a wide range of time/temperature profiles by positioning

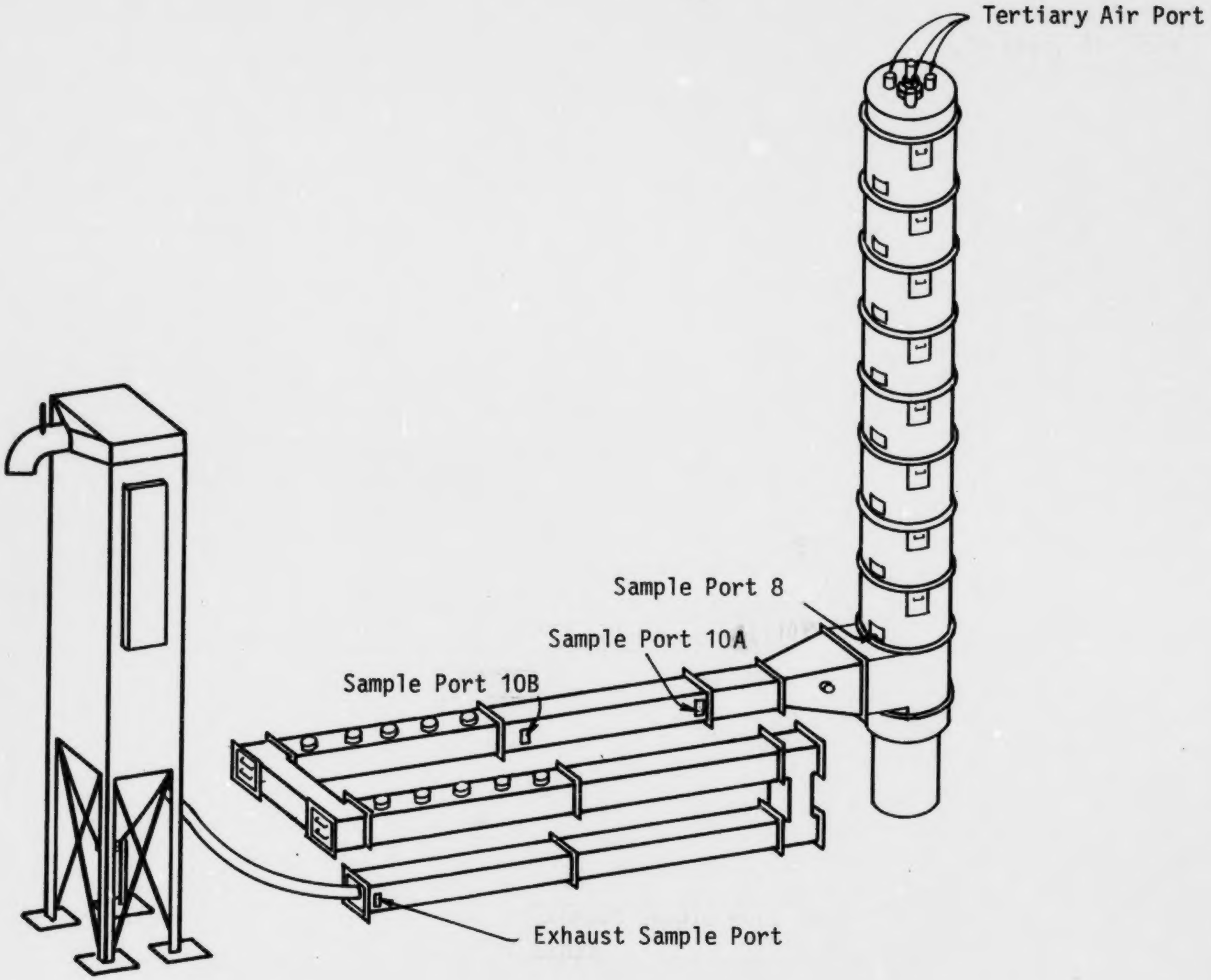
Tertiary Air Port
Sample Port 8
Sample Port 10A
Sample Port 10B
Exhaust Sample Port

Figure 2-1. Boiler Simulator Furnace (BSF).

water-cooled panels or rods appropriately in the furnace. The horizontal convective section contains air-cooled tube bundles that simulate the superheaters, economizers, and air heaters in a boiler.

The furnace is equipped with a versatile Distributed Mixing Burner (DMB) as shown in Figure 2-2. Two secondary air streams supply the burner and the air swirl can be controlled by modifying the swirl and axial air flow rates. The burner has four external staging air ports supplied with separately metered tertiary air. The burner is designed to fire coal or natural gas.

The sorbent may be added to the system in several ways: pulverized with the coal, added with the coal in the primary air, added with the tertiary air, or added directly into the furnace with a small amount of transport gas (either air or nitrogen). A small twin-screw volumetric feeder feeds the sorbent and metered gas to the injection location.

Detailed documentation on the BSF facility can be found in an earlier report (16).

2.1.2 Measurement Systems

Measurements that were performed during the course of this program included gaseous species concentrations, solid composition and physical characteristics, and gas temperatures.

Exhaust gas samples were taken with a stainless-steel, water-jacket probe and analyzed using standard continuous instrumentation for O_2, CO, and CO_2. The schematic of the sampling system is shown in Figure 2-3. SO_2 samples were pulled through the phase discrimination portion of the probe which separated any sorbent particles from the gas stream. The SO_2 samples were then carried via a heated sample line to a permeation dryer and on to a DuPont nondispersive ultraviolet SO_2 analyzer. Figure 2-4 shows the schematic of the SO_2 sampling system.

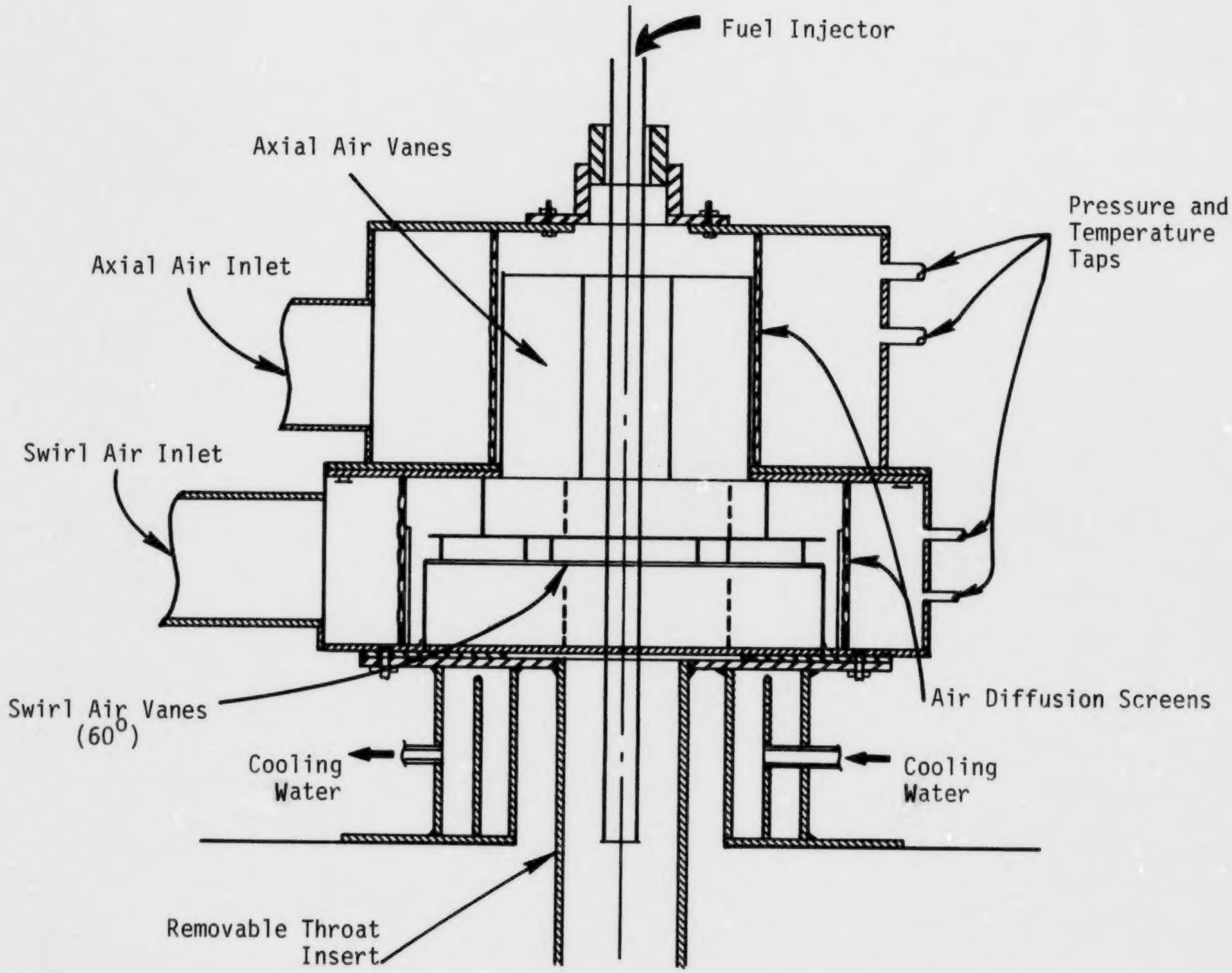
Fuel Injector
Axial Air Vanes
Axial Air Inlet
Pressure and Temperature Taps
Swirl Air Inlet
Swirl Air Vanes (60°)
Air Diffusion Screens
Cooling Water
Cooling Water
Removable Throat Insert

Figure 2-2. Distributed mixing burner schematic, BSF (tertiary air ports not shown).

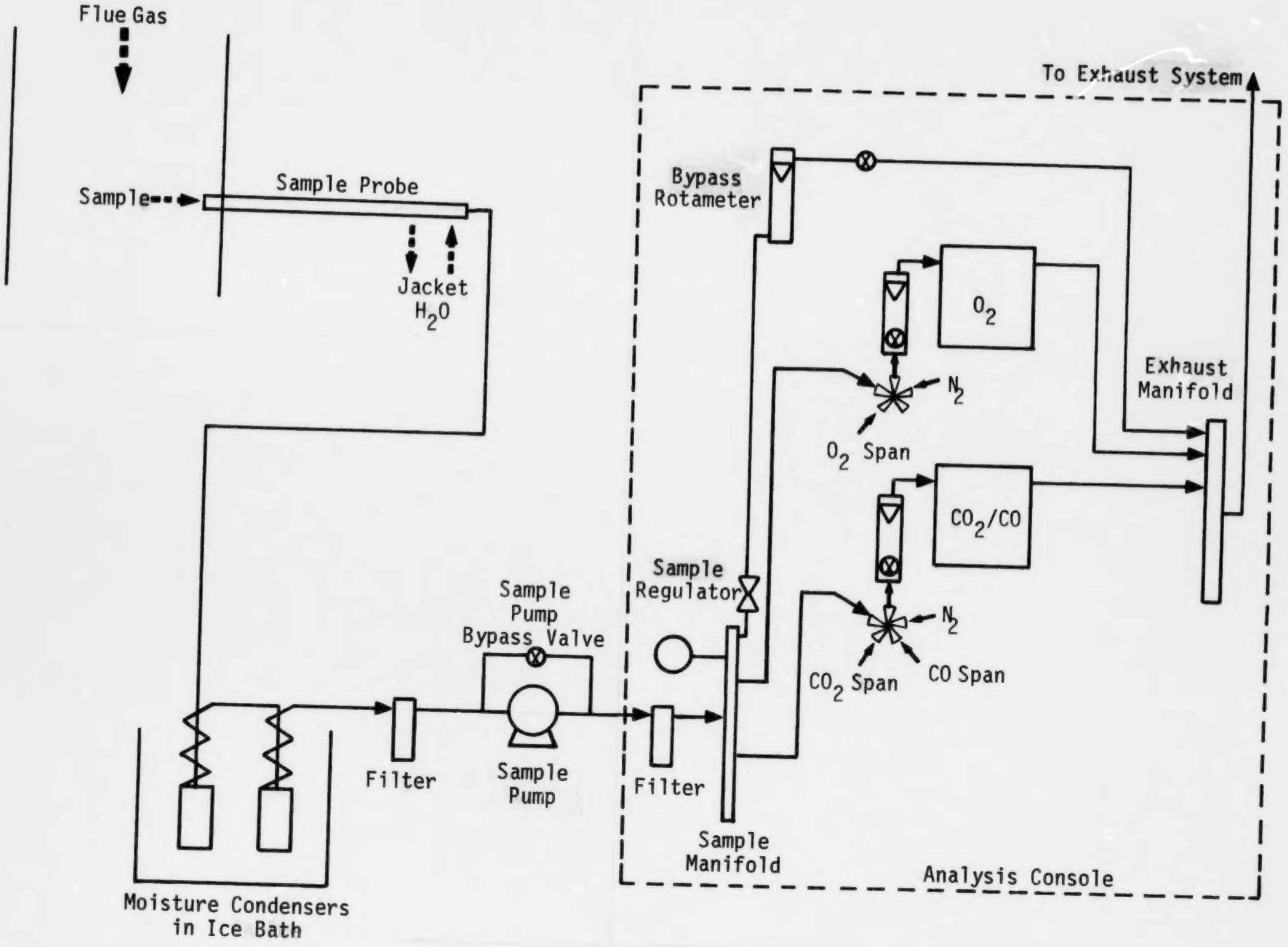
Flue Gas
Sample
Sample Probe
Jacket H_2O
Moisture Condensers in Ice Bath
Filter
Sample Pump Bypass Valve
Sample Pump
Filter
Sample Regulator
Sample Manifold
Bypass Rotameter
O_2
N_2
O_2 Span
CO_2/CO
N_2
CO_2 Span
CO Span
Exhaust Manifold
To Exhaust System
Analysis Console

Figure 2-3. Continuous monitoring sampling system.

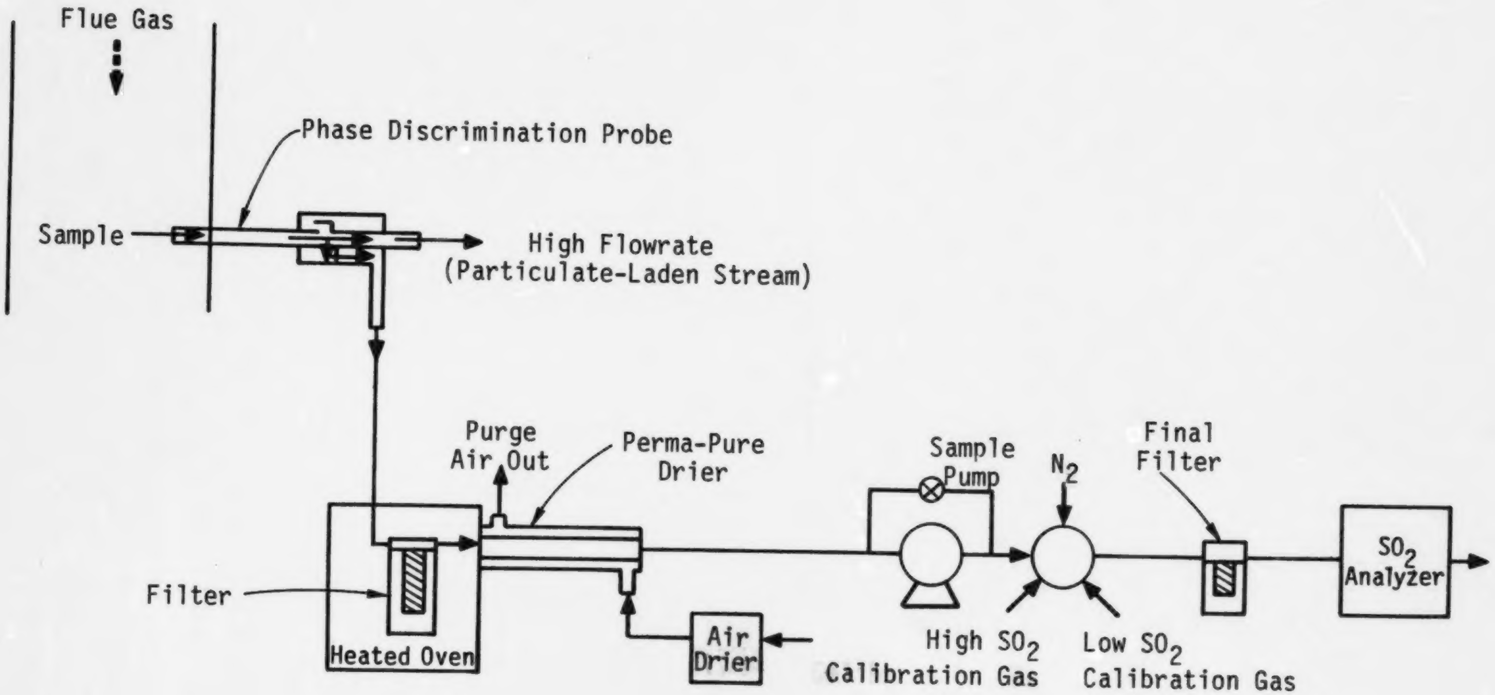
Flue Gas
Phase Discrimination Probe
Sample
High Flowrate
(Particulate-Laden Stream)
Purge
Air Out
Perma-Pure
Drier
Sample
Pump
N_2
Final
Filter
SO_2
Analyzer
Filter
Heated Oven
Air
Drier
High SO_2
Calibration Gas
Low SO_2
Calibration Gas

Figure 2-4. SO_2 continuous monitoring system.

Solid sorbent samples for physical and chemical characterization were collected with a stainless-steel, controlled temperature probe followed immediately by a high-temperature filter. At the conclusion of sampling, N_2 was used to reduce the sample filter temperature to ambient. The samples were carefully extracted and stored in sealed containers. Analyses of the samples included surface area by BET, surface morphology by SEM, and surface elemental concentration by dispersed X-ray spectroscopy.

Gas temperatures were characterized with a suction pyrometer. Figure 2-5 shows the thermal profile of the BSF.

2.2 Control Temperature Tower

The Control Temperature Tower (CTT) is another facility used in this program. The 18 kW CTT was designed and constructed as a reactor for studying high-temperature chemical processes that are temperature sensitive and require multiple zone analysis. Figure 2-6 shows an overall diagram of the CTT (Details provided in 17). The reactor entry (top section) includes a 45.7 cm long quarl that diverges from 5.1 cm to 20.3 cm. The long quarl stabilizes the flame and establishes a one-dimensional flow pattern. There are numerous ports along the axis of the reactor for inserting supplementary equipment, such as zone separation chokes, fuel and air injectors, and cooling coils.

The CTT can manipulate the time/temperature profile (as shown in Figure 2-9) by firing one or both of the backfired heating sections (second and fourth sections from the top). The backfired sections employ natural gas burners which fire in the direction opposite to the main combustion gas. The backfired effluent passes through channels in the refractory walls surrounding the main combustion zone (see the radial cross-sectional view in Figure 2-6). Backfiring in this manner minimized the temperature decay of the combustion products in the main combustion zone. The temperature profile could be further altered by inserting cooling coils in the main combustion chamber.

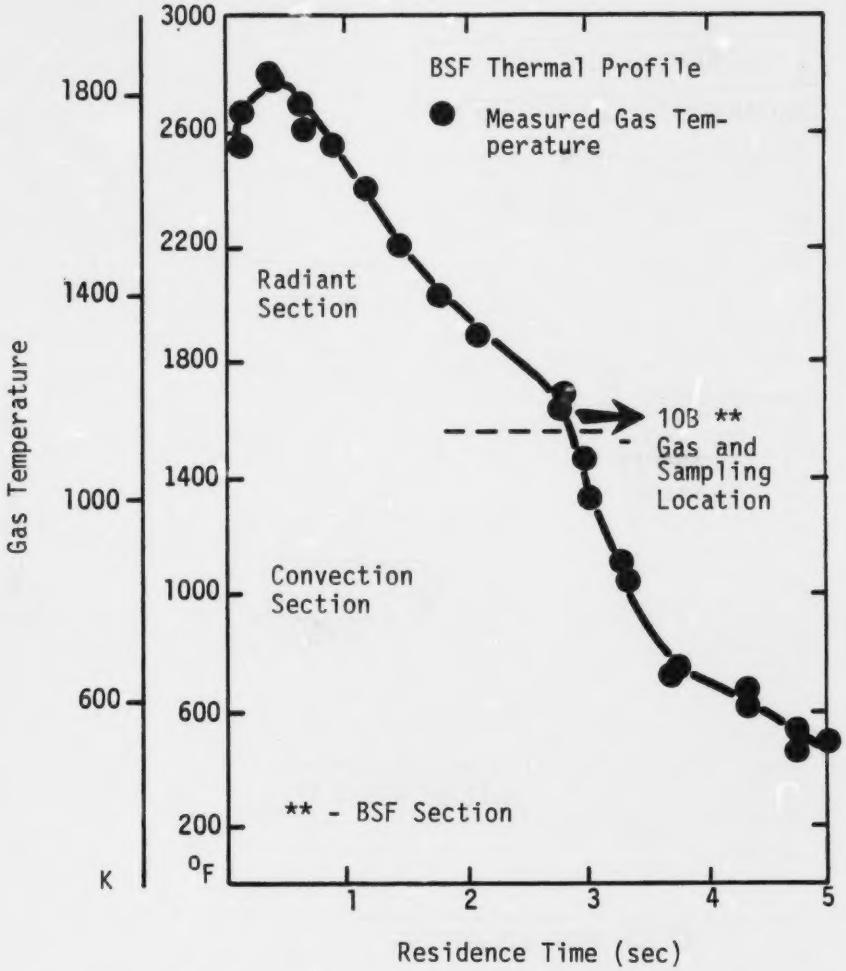

Figure 2-5. Thermal profile of the Boiler Simulator Furnace.

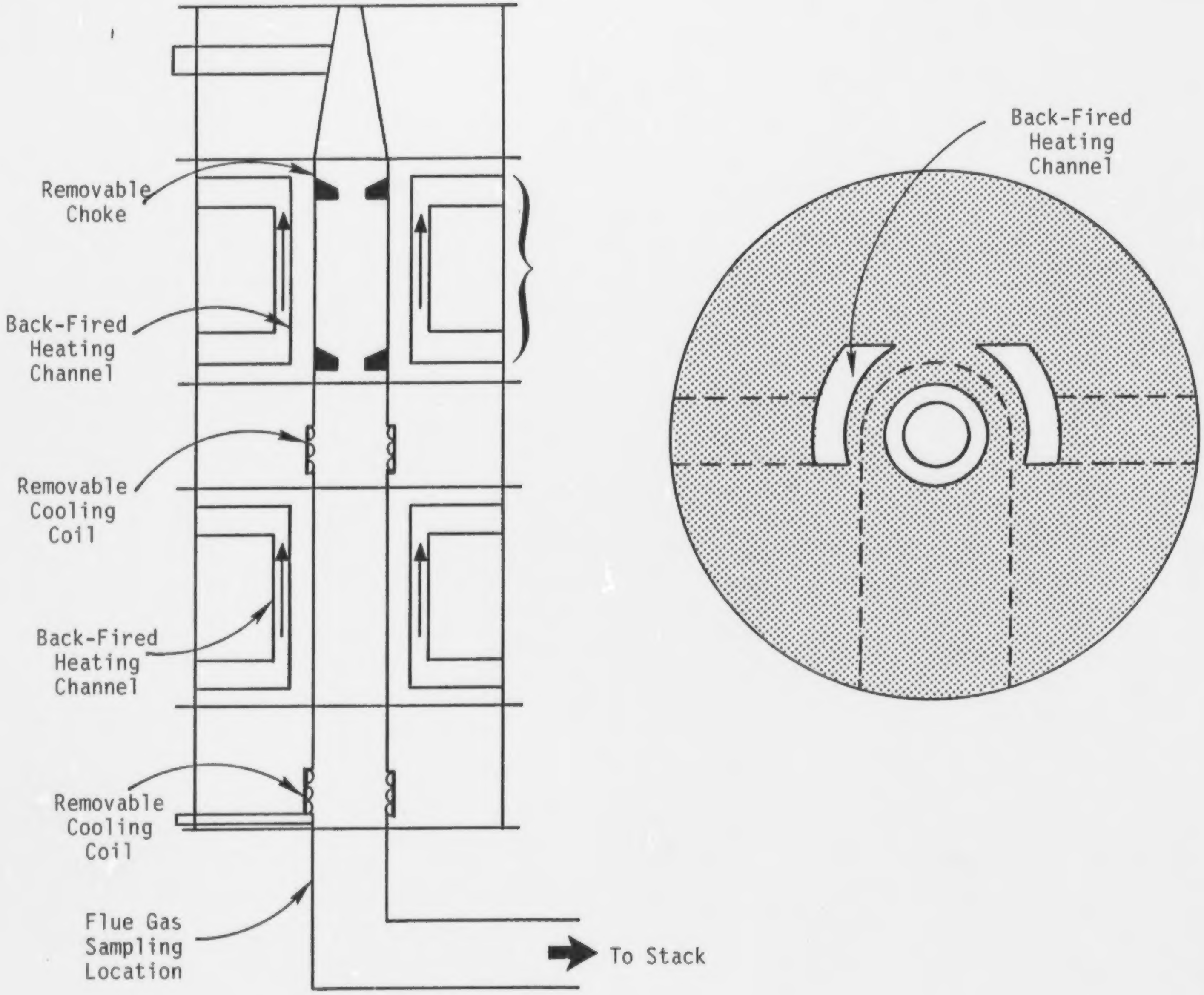
Removable Choke
Back-Fired Heating Channel
Removable Cooling Coil
Back-Fired Heating Channel
Removable Cooling Coil
Flue Gas Sampling Location
To Stack
Back-Fired Heating Channel

Figure 2-6. Cross-sectional views of the control temperature tower.

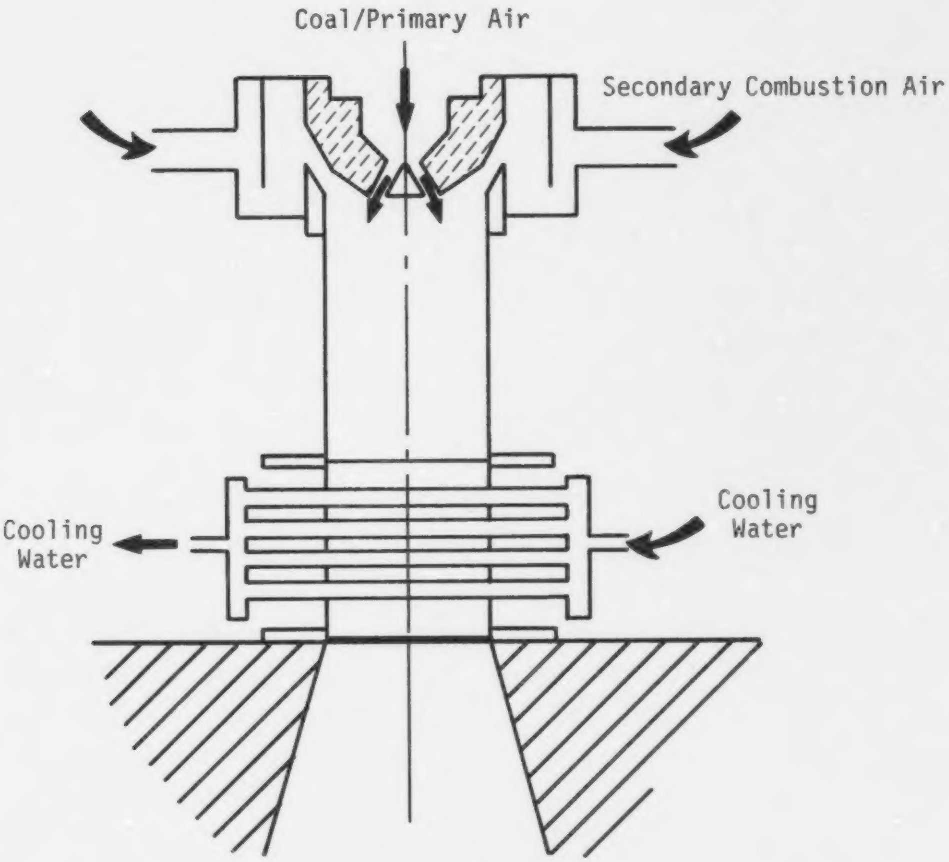
Coal/Primary Air
Secondary Combustion Air
Cooling Water
Cooling Water

Figure 2-7. Premixed burner.

The cross-sectional layout of the premixed burner used on the CTT is shown in Figure 2-7. Six 0.32 cm holes inject the primary air and fuel (natural gas or coal) radially outward into a mixing chamber. The preheated secondary air is injected radially inward into the mixing chamber where the air and fuel mix uniformly. The premixed burner produces essentially a one-dimensional, plug-flow flame with no backmixing. The cooling matrix located at the exit of the burner prevented the fuel/air mixture from preigniting in the mixing chamber.

The gas and solid extraction and measurement procedures for the CTT were the same as for the BSF (see Section 2.2). The majority of the sorbents tested in the CTT were injected downstream with a radial injection positioned at the centerline of the furnace. Either natural gas or coal was used as the fuel and the upper backfired channels were fired up while the lower ones were turned off (see Figure 2-6). Figure 2-8 shows the time/temperature histories between the sorbent injection point and the gas sampling location for both fuels.

2.3 Dynamic X-ray Diffractometer (DXRD)

The DXRD technique combines the capabilities of a modern, computer-controlled powder diffractometer with a temperature/gas composition controlled hot stage to dynamically follow the changes in solid species concentrations as chemical reactions occur.

2.3.1 Equipment Description

Figure 2-9 shows a schematic of the diffractometer and the associated accessories for operating in the DXRD mode. The DACO microprocessor is essential to DXRD, as it controls goniometer movement and transfers the goniometer position, scintillation counter output, and time to the PDP 11/23+ for storage. The sample is contained in a high-temperature cell and its temperature is controlled with a Micristar programmable controller.

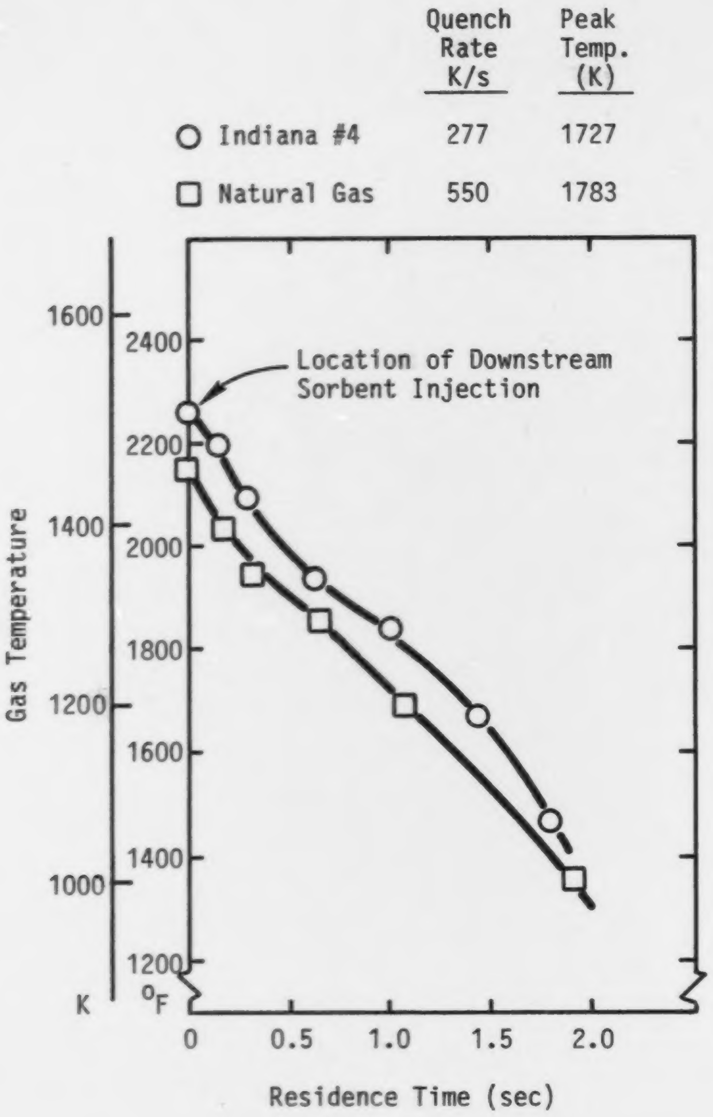

Figure 2-8. CTT thermal profiles.

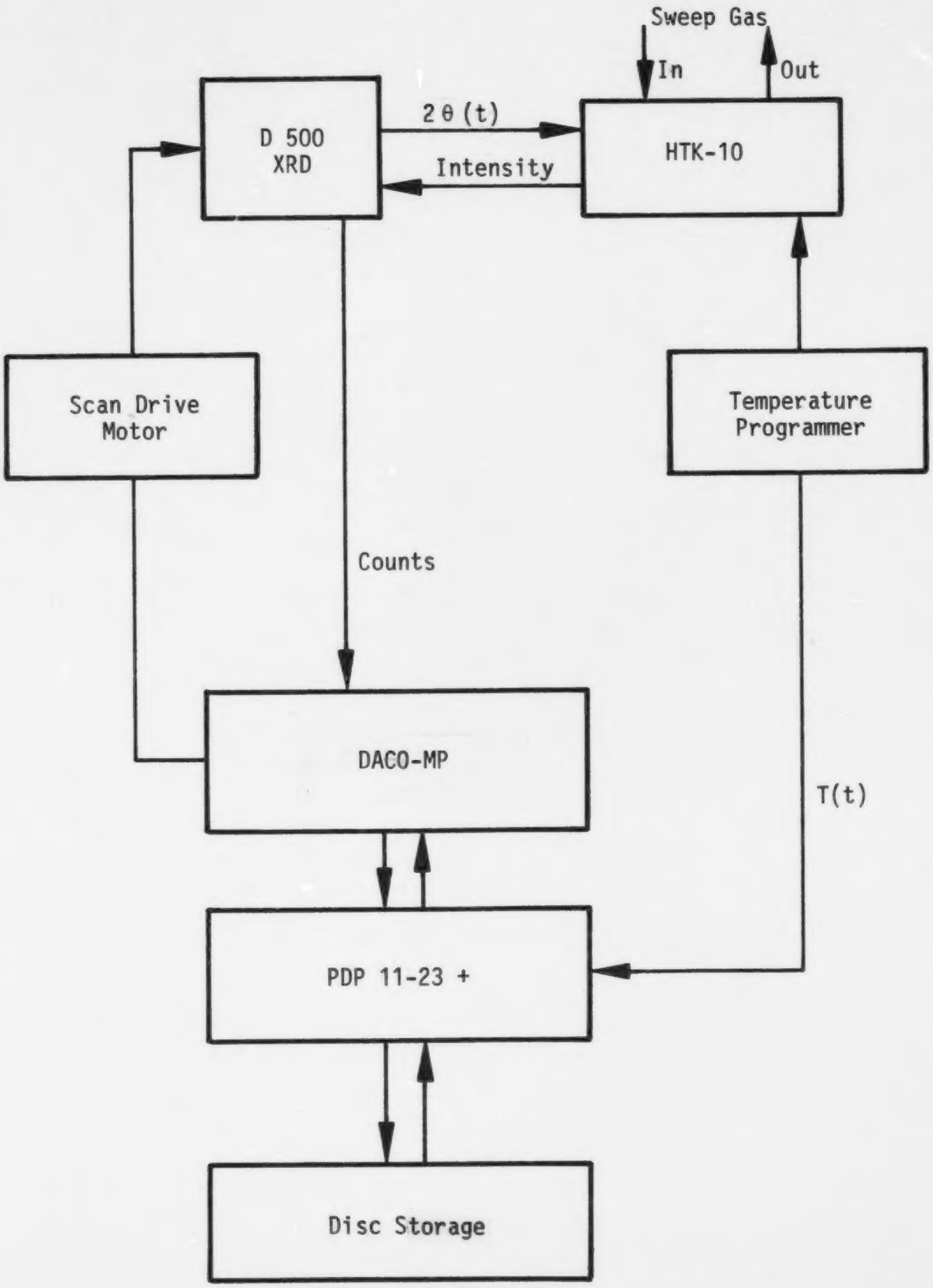
Sweep Gas
In
Out
D 500
XRD
2θ(t)
Intensity
HTK-10
Scan Drive
Motor
Temperature
Programmer
Counts
DACO-MP
T(t)
PDP 11-23 +
Disc Storage

Figure 2-9. DXRD apparatus.

A Siemens D500 diffractometer (as shown in Figure 2-10 with and without environmental chamber installed) performs the powder X-ray diffraction for DXRD. This model uses a flat sample bed and allows the sample and scintillation counter to rotate in such a way as to keep the angle at which the diffracted X-rays are measured equal to the angle of the incident X-rays. This provides the optimum focusing geometry. Two independent step motors drive the sample and scintillation counter, but during normal operation their movement is coupled to maintain good focusing geometry. A Kristalloflex 810 X-ray generator sends the high voltage and current to a Cu X-ray tube to produce Cu K-α X-rays (λ = 1.5405). The X-ray generator was set to 40 kV and 30 milliamps for all of the experiments reported here. As the X-rays leave the X-ray tube, they pass through an aperture diaphragm holder that contains two 1^{o} aperture. The diffracted beam passes through the final aperture, through a monochromator and into the NaI scintillation counter.

A DACO-MP computer, also a Siemens product, controls the goniometer and directs the handling of digital data. Goniometer movement is programmable. Twenty independent peak scans may be programmed to execute without operator intervention, and up to 1600 scans may be programmed with minimal operator intervention. Twenty to sixty scans are sufficient for typical DXRD applications. A delay time of any duration may also be included before any scan to slow data collection in the case of a slow reaction. Without delay times, the typical delay between adjacent scans is about 10 seconds. In this time, the goniometer is slewed to the next position and counting of the next peak is begun.

Scan data (time, angle and intensity) are passed from the DACO-MP to an RL02 disk on a DEC PDP 11/23+ computer. An algorithm developed by Siemens integrates peak intensities. Alternately, data may be retrieved to be subjected to other integration methods. At the end of a run, the time, integrated intensities and peak positions are combined with physical data to calculate the mole fractions of each phase at each scan time.

The sample enclosure is an Anton-PAAR, HTK-10 high-temperature chamber. The sample holder, which also serves as the heating element, is a platinum

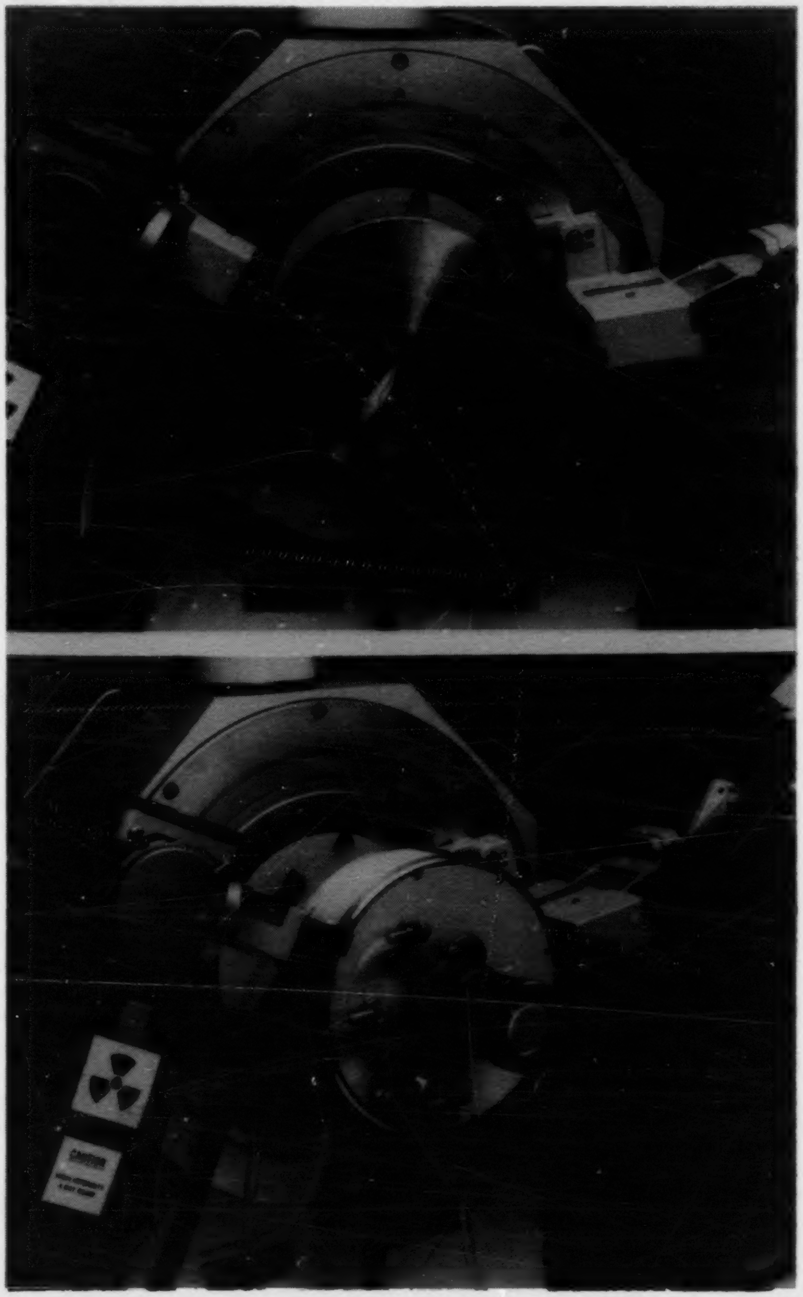

Figure 2-10. Siemens D50V diffractometer.

strip that measures 10.16 cm long, 0.95 cm wide and 0.1016 cm thick and is shown in Figure 2-11. It is controlled by a Micristar Model 828D programmable temperature controller. The controller draws 12 volts and a maximum current near 160 amps. The actual voltage drop across the heating strip is on the order of 0.5 volts. The heating strip can be heated from room temperature to 1273 K in 30 seconds in 35 kPa N_2 flowing at 1.0 liter per minute, and is enclosed in a one liter flow-through gas chamber to allow control of gas composition. Since the chamber is designed to operate below ambient pressure, a pump placed downstream of the chamber induces gas flow. X-rays penetrate this chamber through an aluminum-coated mylar foil. Cooling water is continuously pumped through this chamber and is diverted to the ends of the heating strip as the controller dictates; the maximum cooling rate is 10 K per second.

2.3.2 Experimental Procedure

Early in the developmental stage of DXRD, it was found that sample movement (as the goniometer moved) caused significant problems. This was overcome by using a relatively thick sample bed (1.2 mm was typical) contained within a platinum frame (1.27 cm by 0.95 cm) which was cemented to the heating strip. Unfortunately, this caused a large temperature difference between the top and bottom of the sample. Type-S thermocouples of .20 mm diameter wire were placed both at the center of the underside of the heating strip and in the sample bed, as near the top of the sample as possible while keeping the thermocouple covered. This revealed that the bottom of the strip was typically 60 to 80 K hotter than the upper thermocouple when the bottom thermocouple read 873 K. Fortunately, the temperature gradient through the sample did not detract from the uniformity of temperature in the measured sample. Because of attenuation, only a very thin skin at the top of the sample was visible to X-rays. In the case of $CaCO_3$, for instance, 90 percent of the diffracted X-rays were diffracted from the upper 100 units of the sample bed. Consequently, temperature control and data logging were all done from the upper thermocouple. As will be discussed below, a new method for the difference between the thermocouple reading and the true surface temperature.

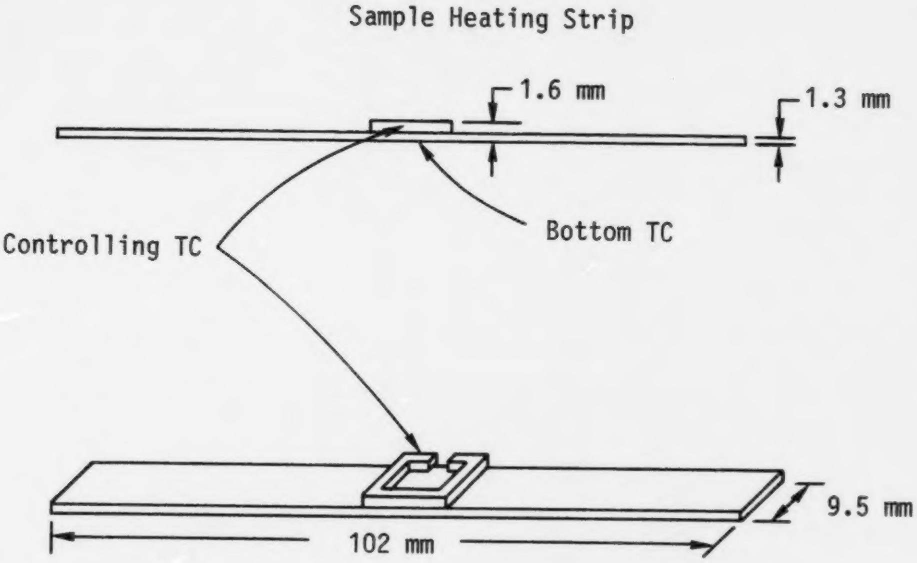
Sample Heating Strip
1.6 mm
1.3 mm
Controlling TC
Bottom TC
9.5 mm
102 mm

(Actual Size)

TC - Thermocouple

Figure 2-11. Sample holder.

Since much of the work involved comparison of different samples, it was important to establish a standardized procedure for each experiment. This consisted of the following:

1. The sample was heated to 1023 K in flowing N_2 over a period of 1 minute. The sample was then calcined in flowing N_2 at 1023 K for 1 hour.

2. A preliminary XRD scan located the CaO peak and identified any other species which might be present.

3. The simulation gas was fed to the reactor at about 0.8 l/min and the DXRD data were collected. Most samples were run for total times of 40-60 minutes.

4. At the end of the DXRD run, another XRD scan was taken to determine if unexpected species had been formed.

As stated earlier, the comparison runs were conducted in a simulation gas (2000 ppm SO_2, 8 percent CO_2, 6 percent O_2, balance N_2) which was purchased "to order" from Linde. In addition, in some runs, temperatures were varied from 923 K to 1083 K. Temperatures as well as SO_2 concentrations were also varied (500-15,000 ppm) in the kinetic studies of Vicron sulfation and a few additional experiments were conducted to determine the effect of CO_2 concentration.

3.0 MATHEMATICAL MODELS

Preliminary thermodynamic, and particle collision (and subsequent growth) calculations were done with the assistance of two computer programs, NASA Equilibrium and MAEROS codes, respectively. This section provides a brief summary of the codes.

3.1 The Equilibrium NASA Computer Code

The "NASA" code developed by Gordon and McBride (18) is a theoretical program that can determine complex chemical equilibrium compositions based on the thermodynamic properties of a chemical system. It can easily be applied to reactions occurring in chemical processing equipment (e.g., furnaces, boilers, nozzles, shock tubes).

The NASA Program can be used to calculate equilibrium compositions from two assigned thermodynamic states in a system, namely:

1. Temperature-pressure
2. Enthalpy-pressure
3. Entropy-pressure
4. Temperature-volume
5. Internal energy-volume
6. Entropy-volume

The program handles condensed phases, mole fractions of trace species, and ionized species. It can also calculate the enthalpies of certain reactants. The only inputs needed for this capability are the reactants and two thermodynamic states. The information can be printed out in conventional charts such as the Mollier Diagram.

3.2 The MAEROS Computer Code

The formation and evolution of ash aerosol from mineral constituents found in pulverized coal depends on a number of physical and chemical processes. In turn, the relative importance of these individual processes depends in large part on the thermodynamic properties of the materials in question, as well as on the environmental conditions which the aerosol sees during the coal combustion process. These mechanisms are many, and can be represented schematically by Figure 3-1. In this figure are shown the many pathways that ash constituents can follow in evolving from an individual constituent in the coal particle to a size-distribution and composition-distribution in the ash aerosol. In Figure 3-2 is a qualitative representation of the temperature profile experienced in a pulverized coal fired boiler, as well as approximate descriptions of the combustor position as a function of residence time. Also shown are the sequential processes of devolatilization and char burnout that each individual coal particle undergoes.

Above these various time-lines is a schematic of the multiple processes affecting the ash formation, shown in the approximate temporal position when that process would occur. Early in the char burnout process, the more volatile species in the ash (such as the alkali components) would vaporize, at least partially, to form gas-phase species. Larger ash inclusions could coalesce in varying degrees as the char continues to burn out, and char fragmentation would then give rise to a distribution of ash particles in the larger sizes (probably greater than 2 μm).

As the combustion gases reach peak temperatures and begin to cool, those species that partially or completely vaporized earlier in the burnout phase will begin to saturate. This saturation takes place due to their decreasing equilibrium vapor pressure brought on by a drop in temperature. Obviously, those species with lower equilibrium vapor pressure will reach their saturation level sooner than those species with higher equilibrium vapor pressures. If there is sufficient surface area in the particle phase on which to condense out these vapors, condensation will be the preferred route. If, on

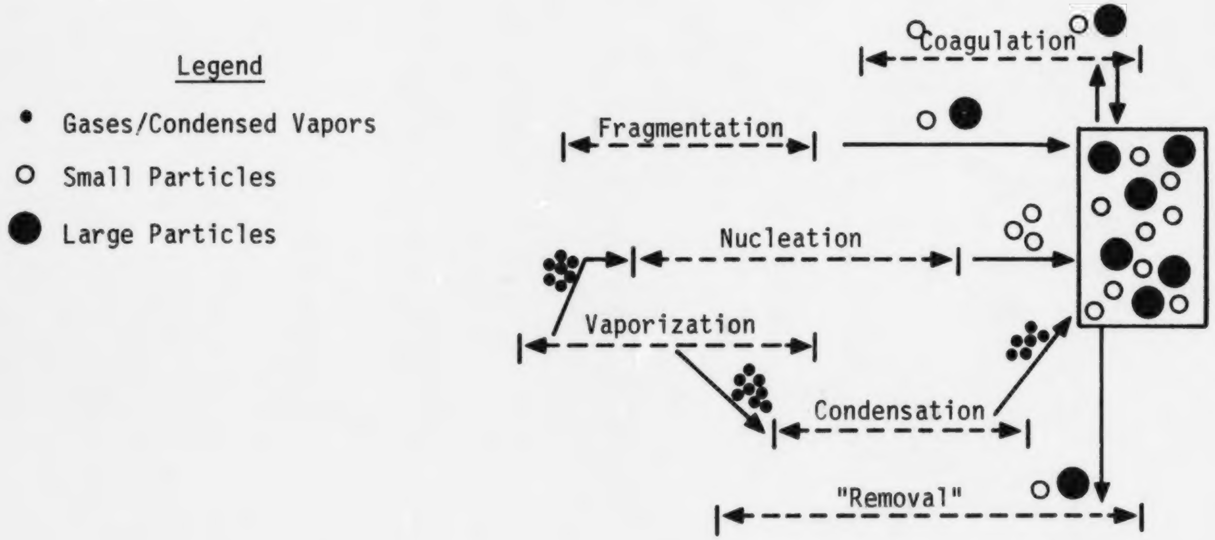
Legend
• Gases/Condensed Vapors
○ Small Particles
● Large Particles
Coagulation
Fragmentation
Nucleation
Vaporization
Condensation
"Removal"

Figure 3-1. Interaction mechanisms.

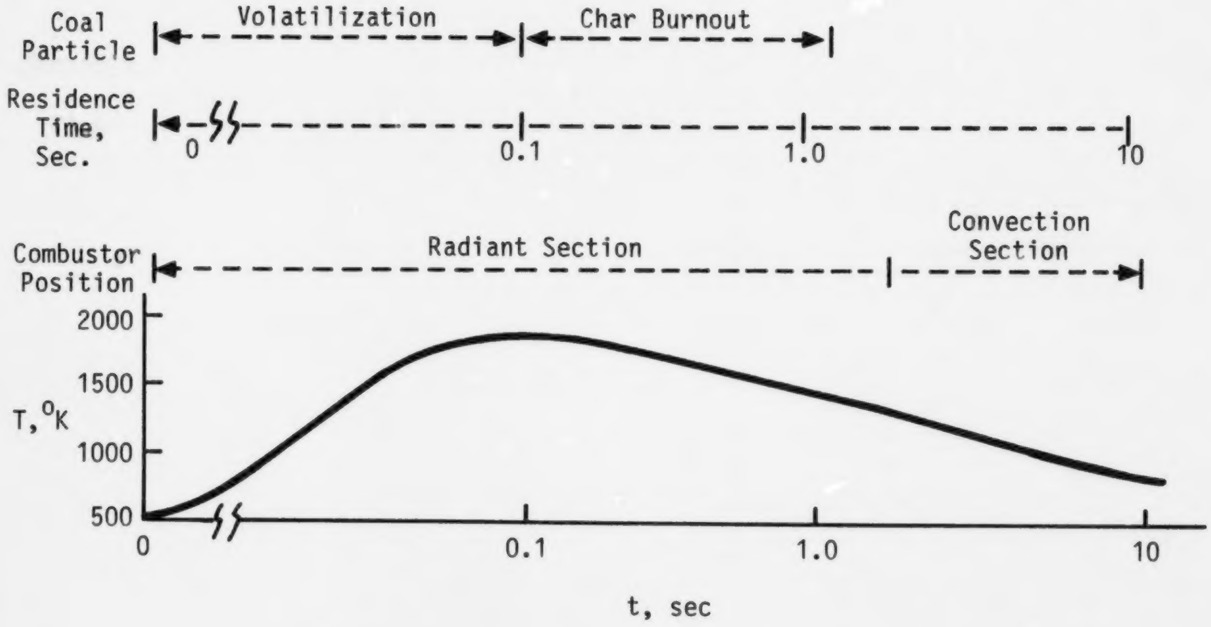

Figure 3-2. Time and temperature dependence in a pulverized coal fired boiler.

the other hand, the particulate phase is void of significant surface area eligible for condensation, new particles will be formed by nucleation. It is likely, therefore, that nucleation will be important early in the submicron ash formation process, when the least volatile species reach saturation. These nucleated particles can then themselves act as sites for future condensation, thereby causing condensation to be the preferred method of gas-to-particle conversion.

The resultant size distribution at this point in the process would be characterized by two modes. Fragmentation would produce larger particles (mass median diameters in the 2 to 10 μm range), whereas nucleation followed by condensation would produce smaller, submicron particles. Simultaneous to these processes, all particles are eligible to coagulate with other particles, thereby increasing the mean size of the coagulated particles. Since coagulation is a quadratic process (as will be seen below, in the discussion of the governing equations), it will be much more important for particle sizes with high number concentrations, namely the fresh nucleated submicron particles. Coagulation is a much less important mechanism for the larger particles, although it usually cannot be completely neglected.

In studying the disposition of additives in a combustion environment already containing ash particles and sorbent particles, there is already considerable surface area available for condensation. Not only is there the surface area associated with the submicron ash aerosol and the coarse mode aerosol, there is also the surface area associated with the sorbent. Strictly, one must now talk about the aerosol dynamics occurring among a four-component system: the submicron ash, the coarse mode ash, the sorbent particles and the additive eligible for particle formation.

The governing population balance equation for such a four-component system is a bit unwieldy to be presented here. The one-component version of that equation is given by:

$$\frac{n}{t} = \frac{1}{2}\int_0^v \beta(u,v-u)n(u,t)n(v-u,t)du - \int_0^\infty (u,v)n(v,t)n(u,t)du +$$

$$\int_0^\infty \phi(u)\omega(u,v)n(u,t)du - \phi(v)n(v,t) - \frac{\partial}{\partial v}(I(v)n(v,t)) + S(v,t) - R(v,t)$$

where

$n(v,t)\,dv$ = aerosol number density in a volume size range $(v,v+dv)$

$R(v,t)$ = aerosol removal rate

$S(v,t)$ = aerosol source rate

$\beta(u,v)$ = coagulation kernel between particles of volume u & v

$\phi(v)$ = fragmentation rate for particles of volume v

$\omega(u,v)dv$ = fragmentation distribution function, i.e., number of particles generated in a size range $(v,v+dv)$ upon breakage of a single particle of size u

$I(v)$ = condensation/evaporation rate for a single particle

The above equation describes the evolution of a distribution of aerosol particles influenced by coagulation, fragmentation, condensation, nucleation and other sources, and sinks such as deposition. The first two terms on the right-hand side of the equation represent changes in the distribution due to coagulation. As can be seen, coagulation depends quadratically on the aerosol number density $n(v,t)$. Hence, those particles at higher concentrations will undergo coagulation much more rapidly than particles at lower concentrations. Practically, this means that the smaller particles, present in much higher number concentrations than the larger particles, will be strongly influenced by coagulation. The third and fourth terms in the equation represent spectrum changes due to fragmentation, which, as can be seen, depends linearly on the concentration of the fragmenting particles. Size changes due to condensation and evaporation of material to and from the aerosol particle are represented by the next term in which I(v) denotes the rate at which material arrives or leaves the particle surface. Finally, S(v,t) and R(v,t) represent sources and sinks of aerosol particles, again as a function of particle size. These mechanisms can represent nucleation, source streams, deposition, exit streams, etc.

A numerical model is available (the MAEROS code, 19) which solves the multicomponent form of the equation above, provided the appropriate forms for the mechanisms are supplied. In order to study the disposition of additives in the presence of submicron ash, coarse mode ash, and sorbent, the following mechanisms and parameters must be input:

- The mechanism of coagulation (assumed to follow the Smoluchowski model).
- The mechanism of condensation (assumed to obey standard diffusion equations, with non-continuum corrections where necessary).
- The saturation vapor pressure of the species of interest.
- The initial size distributions of the ash and sorbent.
- The time-temperature profile of the combustion gases.

It is assumed that, at the time the additive begins to convert from the gas to the particle phase, fragmentation of ash is unimportant. This is a reasonable assumption since additive condensation or nucleation will almost certainly occur after char burnout is complete. It is also assumed that there are no major sinks of aerosol and additive (such as deposition to the walls, slagging, fouling, etc.). While these mechanisms are obviously active to some degree, it is doubtful that they are of such importance as to control the size distribution of the ash or the condensed additive.

In Section 7, a series of simulations are described that help to explain the effect of ash particles in the sorbent/additive system. These simulations were performed using the MAEROS model mentioned above, focusing particularly on the mechanisms of condensation and coagulation in a four-component system.

4.0 SOLID CHARACTERIZATION (FUELS, SORBENTS, PROMOTERS)

The characteristics of the fuels, calcium-based sorbents, and promoters used in this study are summarized in this section.

4.1 Fuels

Eight different fuels were used in the program. Of these, one was natural gas and the remaining seven were coals of varying composition. Three of the seven coals were cleaned coals containing low ash and sulfur. Table 4-1 lists the properties of the coals used. Note that ash content of the coals ranges from 5 to 42 percent and that sulfur levels range from 0.9 to 6 percent, both on a dry basis. For all the fuels, SiO_2 dominated the ash composition followed by Al_2O_3. Other ash constituents were present in lesser amounts. The fuels tested were specifically chosen to determine what effect, if any, ash quantity had on promoted and unpromoted sorbents.

4.2 Calcium-Based Sorbents

The sorbents used in this study include a high calcitic Vicron 45-3 limestone, Longview atmospheric hydrate, and an EER-produced pressure hydrate. Table 4-2 summarizes the properties of these calcium-based sorbents. In Figure 4-1 high resolution photographs of Vicron 45-3, precalcine Vicron (SA = 25 m^2/g), Longview hydrate, and EER pressure hydrates are presented in micrographs No. 03902, 04002, 04101, and 44501, respectively. These photographs provide a comparison of the particle size and surface morphology of the different sorbents. In general, Vicron 45-3 and its precalcine are larger than the hydrates. The hydrates contain larger pores (i.e., cracks and channels) than the relatively closed pore structure of the Vicron sorbents. The EER pressure hydrate contains, in general, smaller particles than the atmospheric hydrate, while there appears no significant difference in particle size between Vicron and its precalcine.

TABLE 4-1. FUEL PROPERTIES

Analysis (Wt %)	Nat. Gas	Indiana	Illinois	Lower Kittanning	Kentucky No. 11	Lower Kittanning (Sg. 1.35)
Proximate (as rec'd)						
H_2O	-	5.07	15.77	11.23	28.09	12.29
Volatile Matter	100.0	30.24	35.44	15.27	19.37	17.45
Fixed Carbon	-	55.35	40.39	51.44	24.13	65.16
Ash	-	9.34	8.38	22.05	30.51	5.10
Ultimate						
H_2O	-	5.07	15.79	11.23	28.09	12.25
C	72.15	72.16	70.71	65.93	42.94	84.71
H	23.04	4.71	4.86	3.59	3.03	4.45
N	1.94	1.32	1.12	1.17	0.88	1.69
S	-	1.06	3.94	1.40	4.32	0.77
Cl	-	-	0.12	0.05	-	0.10
O	0.59	10.87	9.30	3.07	6.39	2.53
Ash	0	9.88	9.95	24.84	42.43	5.81
HHV (kW/kg)	14.67	8.10	9.12	7.44	5.01	9.57
Ash						
SiO_2		58.63	46.74	56.29	50.39	48.29
Al_2O_3		23.56	16.56	26.84	18.16	29.95
Fe_2O_3		10.26	18.33	8.38	12.99	12.58
CaO		0.95	6.21	0.65	5.02	2.03
MgO		0.36	0.85	0.67	1.14	0.56
K_2O		1.49	2.12	2.54	3.42	1.46
Na_2O		0.22	1.55	0.27	0.49	0.28
TiO_2		0.99	0.85	0.94	1.35	1.85
P_2O_5		0.47	0.18	0.16	1.65	0.29

TABLE 4-2. SORBENT PROPERTIES

Sorbent	Vicron 45-3	Longview Hydrate	EER Pressure Hydrate
Physical Properties			
B.E.T. SA (m^2g)	2.0	16.1	6.8
Density (g/cm^3)	2.7	2.3	2.3
Median Particle Size (mm)	9.8	3.9	2.1
Chemical Properties (wt %)			
Ca	39.2	48.8	51.6
Mg	0.33	1.21	0.57
Na	0.007	0.01	0.01
Si	0.09	0.30	0.18
Al	0.02	0.15	0.19
F_e	0.06	0.14	0.24
C	11.90	0.43	1.06
H	0.08	2.48	2.35
N	0.0	0.0	0.0
S	0.01	0.02	0.02
K	0.01	0.03	0.03

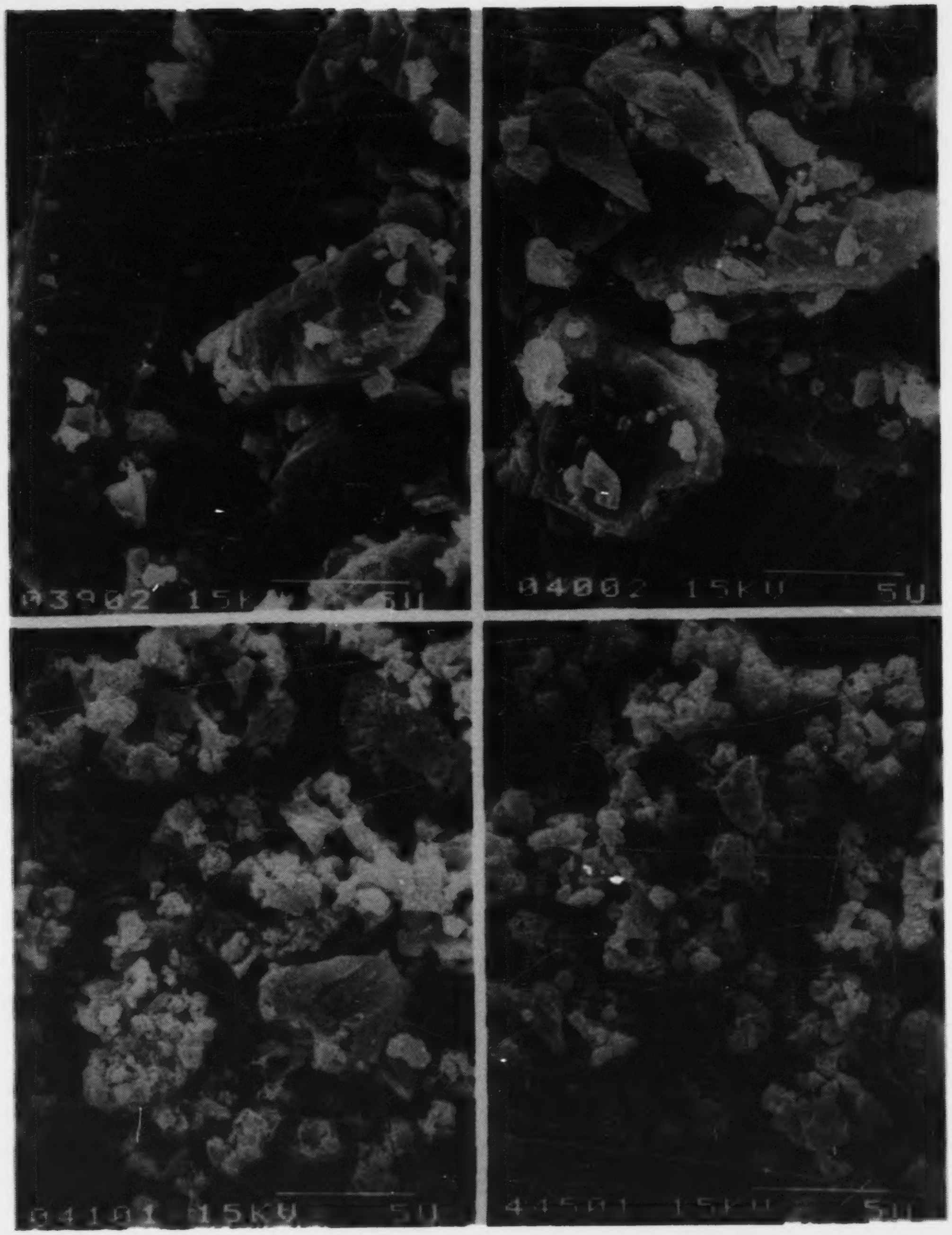
03902 15KV 5U
04002 15KV 5U
04101 15KV 5U
44501 15KV 5U

Figure 4-1. High resolution photographs of Vicron, precalcine Vicron, Longview hydrate, and EER pressure hydrate (Micrograph No. 03902; 04002, 04101, and 44501, respectively).

4.3 Sorbent-Additive Mixtures

It is apparent that the addition of promoters to calcium-based sorbents increased the sorbents' ability to capture sulfur. To provide both mechanistic and process understanding, special calcium-based sorbents with promoters were manufactured and tested in the experimental furnaces (BSF and CTT) and in the DXRD. This section provides detailed description of the equipment and procedure that was used to place the dopant on the calcium-based sorbent. There were four methods used to manufacture sorbents with additives:

a) Premixed Powders

b) Evaporative Deposition

c) Pressure Hydration

d) Vaporized Deposition--Rotary Kiln

In general, the manufactured sorbents were physically and chemically characterized by SEM, EDS, BET surface area, mercury intrusion porosimetry, and X-ray diffraction (when appropriate).

4.3.1 Premixed Powders

Premixed calcium-based sorbents with additives were tested due to low cost and ease of preparation. (The dopant was not attached as with the other three methods except by possible electrostatic forces.) The promoters were added in a variety of chemical-based sorbents to produce a solid-solid mixture. The initial particle size combined with the relative volatility of the dopant dictates the extent of distribution of the promoter on the calcium sorbent. The smaller the promoter particle relative to calcium sorbent (assuming a non-volatile dopant, e.g., Cr_2O_3, Fe_2O_3) the better the promoter will distribute on available calcium particles. If the dopant particle is greater than the sorbent, a small number of sorbent particles may encapsulate the promoter reducing the dopant's ability to interact with the remaining sorbent particles. Of course, if the promoter is relatively volatile (e.g.,

$NaHCO_3$) under the thermal conditions of injection then particle size is not as important.

Preparation Procedure for Premixed Powders

To produce a uniform mixture the combined additive and sorbent was mixed in a mechanical "cement" mixer. A predetermined molar ratio of calcium to additive was mixed in a container until a uniform powder resulted. The mixture was characterized by SEM/EDS techniques.

Characteristics of Premixed Powders

Mixtures of dopant and Vicron have been analyzed to provide relative particle sizes. Figure 4-2 shows micrographs of the promoter compared to the Vicron 45-3 (Vicron without an additive is shown in micrograph No. 03900). The particle size of the sodium bicarbonate was much larger than the Vicron as shown in photograph No. 10006. (The large particle in the center is $NaHCO_3$.) In contrast, the Cr_2O_3 particles are at least two orders of magnitude smaller than the mean size of Vicron (i.e., 11 μm); the small particles located in the center and top of a Vicron particle shown in micrograph No. 04300 are Cr_2O_3. (Note the scale at the bottom of the photograph.) Photograph No. 04200 shows Fe_2O_3 (lower-left) and Vicron particles. The mean size of the Fe_2O_3 particles is slightly larger (i.e., 30 μm) than the 11 μm determined for Vicron 45-3. From the microscopic inspection of the mixtures the chromium dopant clearly indicated the best dispersion.

4.3.2 Evaporative Deposition

The technique was simply to deposit the promoter on the surface of the calcine without the dopant reacting into the crystalline CaO, thus preventing changes in the initial physical and chemical characteristics of the calcium sorbent. This way it was possible to record chemical and physical changes of the doped sorbent when placed under a combustion environment. The quantity of material produced from this technique was on the order of several grams,

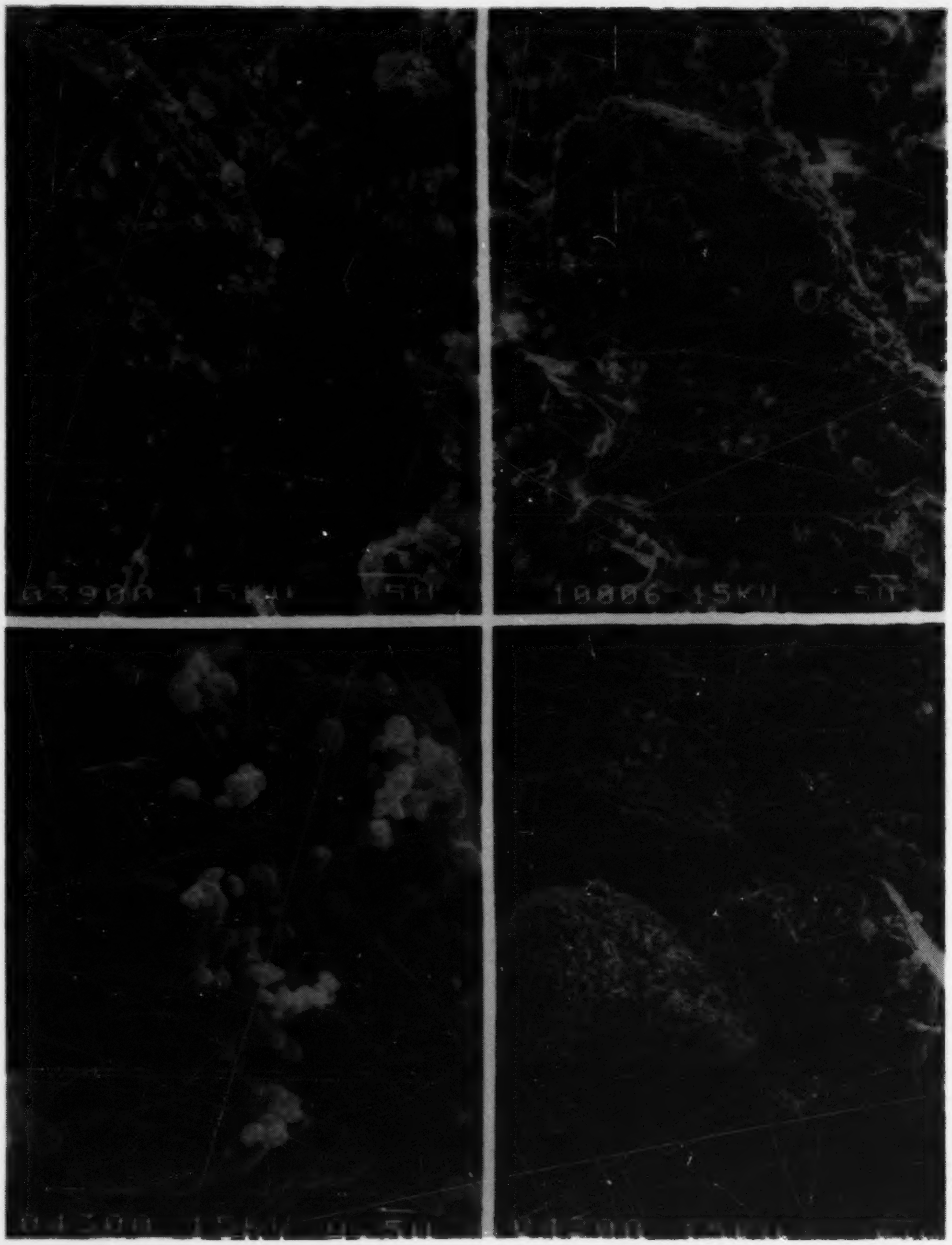
03900 15KV 5U
10006 15KV 5U

Figure 4-2. Photographs of premixed sorbents (Micrograph No. 03900--no dopant; 10006--Na, 04300--Cr. 04200--Fe).

therefore the manufactured sorbent was used only in diffractometer experiments.

Calciner Description

Manufacturing the doped Vicron precalcine was done by calcining Vicron to obtain a relatively high surface area material then depositing the dopant on the calcine. In order to generate high surface-area precalcined materials for testing in the DXRD, the apparatus in Figure 4-3 was used. (A complete description can be found in Ref. 20). The apparatus consists of a 20-cm diameter stainless-steel can placed in an electrically heated box furnace. The can was fitted with a heavy lid which has a single hole for thermocouple access and to allow purge gas and CO_2 to escape. Limestone was supported in a thin bed on a 400 mesh stainless steel screen. Beneath the screen was a spiral made from 6.4 mm stainless steel tubing. The spiral had small holes drilled on the underside and acts as a flow distributor for the purge gas which enters through a long coil of stainless steel tubing located inside the box furnace. It was found that, even when operating with fine limestone having a mass mean size of 11 microns, the particles did not elutriate out of the bed; hence no screen above the limestone bed was necessary.

Preparation of Evaporated Calcines

Operation of the precalcination apparatus consisted of passing nitrogen through the bed of powdered limestone at high temperature. The mass of limestone and flow of nitrogen were balanced to provide the shortest calcination time at the lowest possible temperature. Typical operating conditions were 973 K, 60 g limestone, 0.55 l/s N_2. CO_2 resulting from calcination is swept away from the limestone by the nitrogen, thereby lowering the local CO_2 concentration and accelerating the calcination rate. The calcine produced has similar mass mean particle size and "observable" surface morphology as the parent carbonate. (Results from sedigraph analysis are provided in Figure 4-4; Figure 4-1, micrograph No. 03902 and 04002 show Vicron and its calcine, respectively.) A significant difference between the two stones is the large number of micropores found in the calcine. This

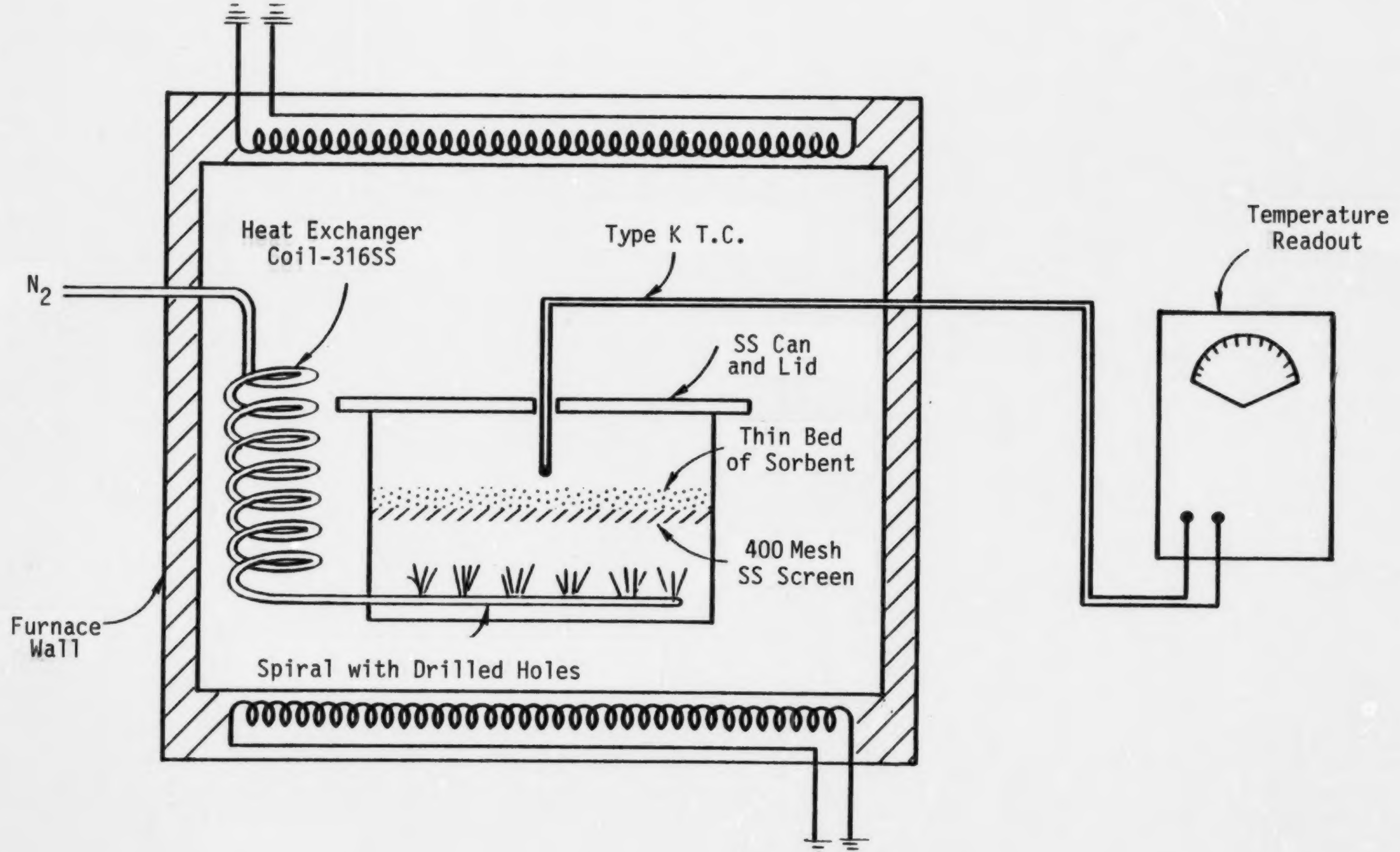
Heat Exchanger
Coil-316SS
Type K T.C.
Temperature
Readout
N_2
SS Can
and Lid
Thin Bed
of Sorbent
400 Mesh
SS Screen
Furnace
Wall
Spiral with Drilled Holes

Figure 4-3. Apparatus for generation of precalcined sorbents.

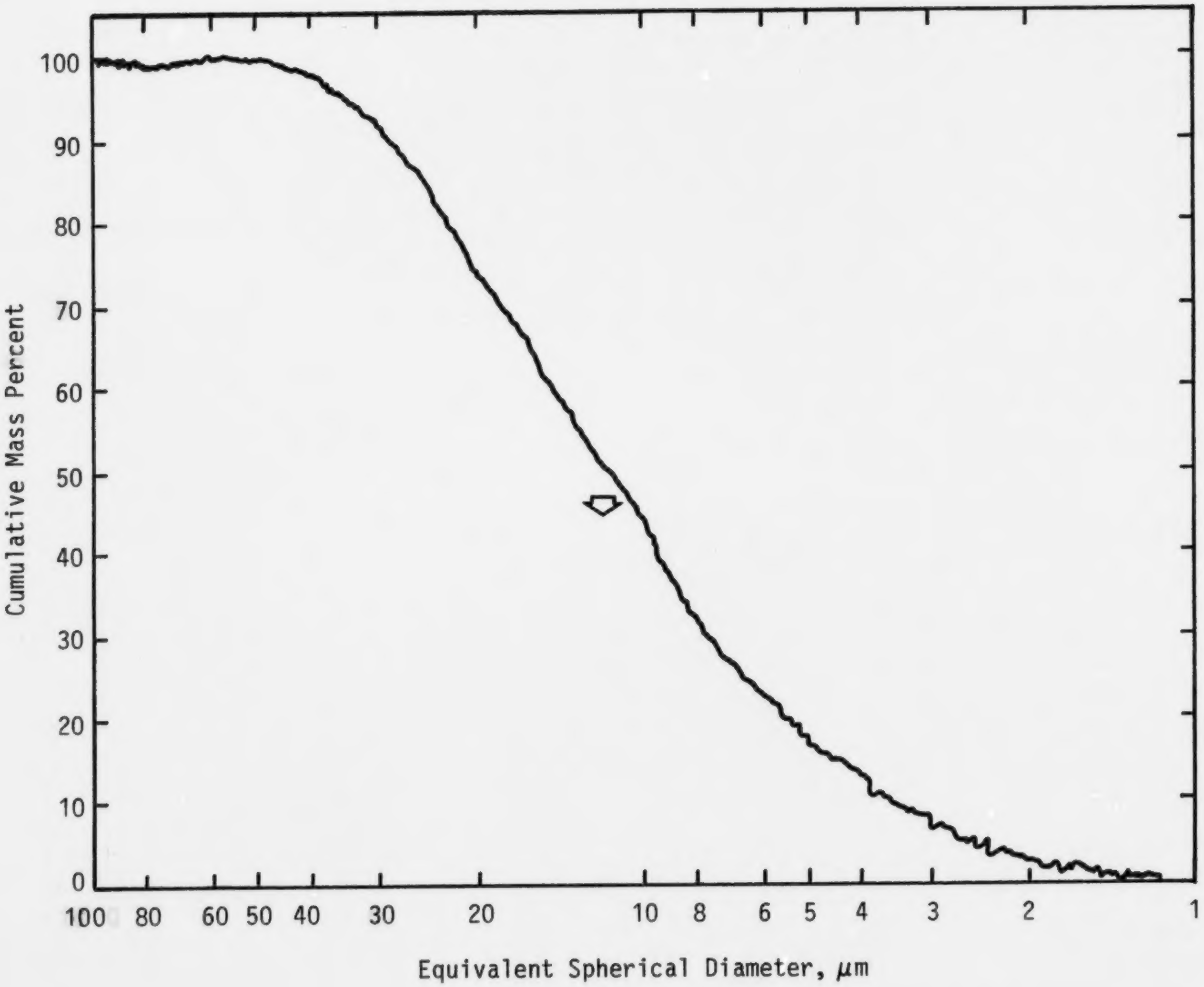

Figure 4-4. Sedigraph analysis for calcined Vicron.

finding is substantiated by both BET surface area and mercury intrusion measurements. Results shown in Figure 4-5.

The dopant was placed on the calcine with an evaporator. Evaporative deposition technique which involved sending an electrical current through an additive in an evacuated chamber. The heat generated by the electrical resistance evaporated the additive onto a sorbent placed in the center of the chamber. A Varian VE-10 evaporator was used; Figure 4-6 shows the basic set-up.

A thin layer of precalcined Vicron 45-3 (CaO) was placed onto a stainless steel screen. The 400 mesh screen was placed on a rotating stage in the chamber. Because the Varian was equipped with two pairs of electrodes, two circuits were constructed, allowing for two charges of additive to be supplied in the chamber. Tungsten coil wire boats complete each circuit, as Figure 4-6 shows. In generation the boats were first filled with additive, and the chamber evacuated. The current was then increased or maintained until all of the additive had evaporated, at which point the precalcine with additive was removed, bottled, and stored under vacuum until tested in the dynamic diffractometer.

Characteristics of Doped Calcines

As noted above, the evaporation technique was to simply deposit the promoter on the surface of the calcine without reacting into the crystalline CaO, thus not altering the initial physical and chemical characteristics of the precalcine sorbent. SEM and EDS analyses were performed to characterize the influence and the relative amount of the deposited promoter. High-resolution photographs shown in Figure 4-7 indicate that the evaporation of the promoter had little effect on the overall morphology of the precalcine (compared to the sorbent without a dopant, micrograph No. 17301), regardless of the additives used. The particles with promoters shown in micrographs No. 17600 (Na deposit), 17500, (Cr deposit) and 17400 (Fe deposit) did not appear different in particle size or pore structure (which would not have been the case if the additive reacted into the CaO matrix). In addition, X-ray

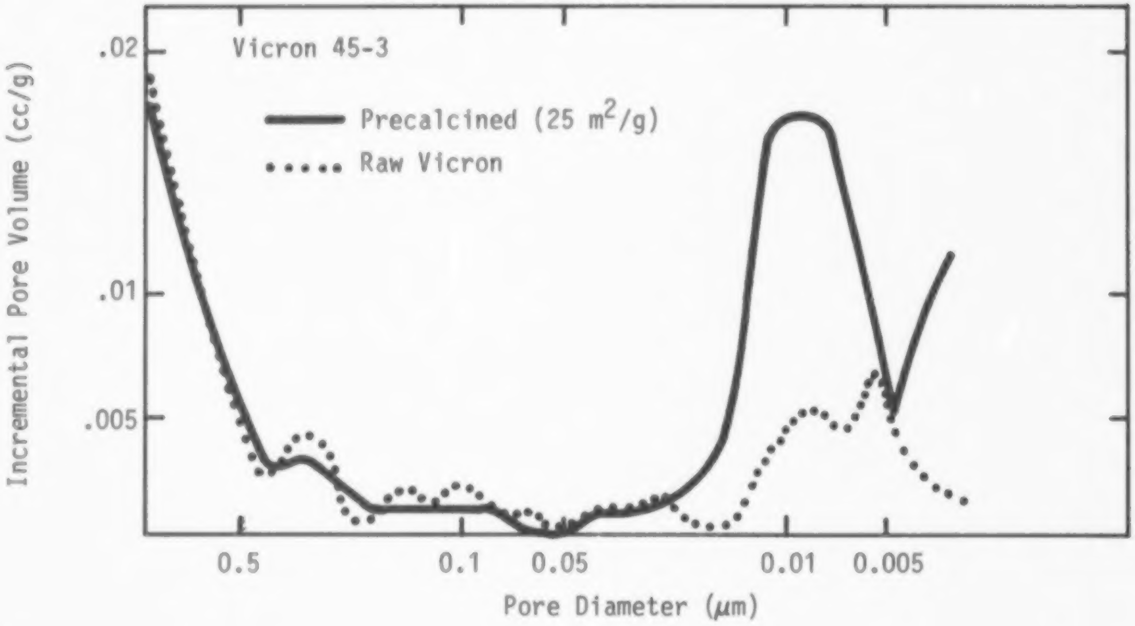

Figure 4-5. Pore distribution of precalcined Vicron compared to raw Vicron).

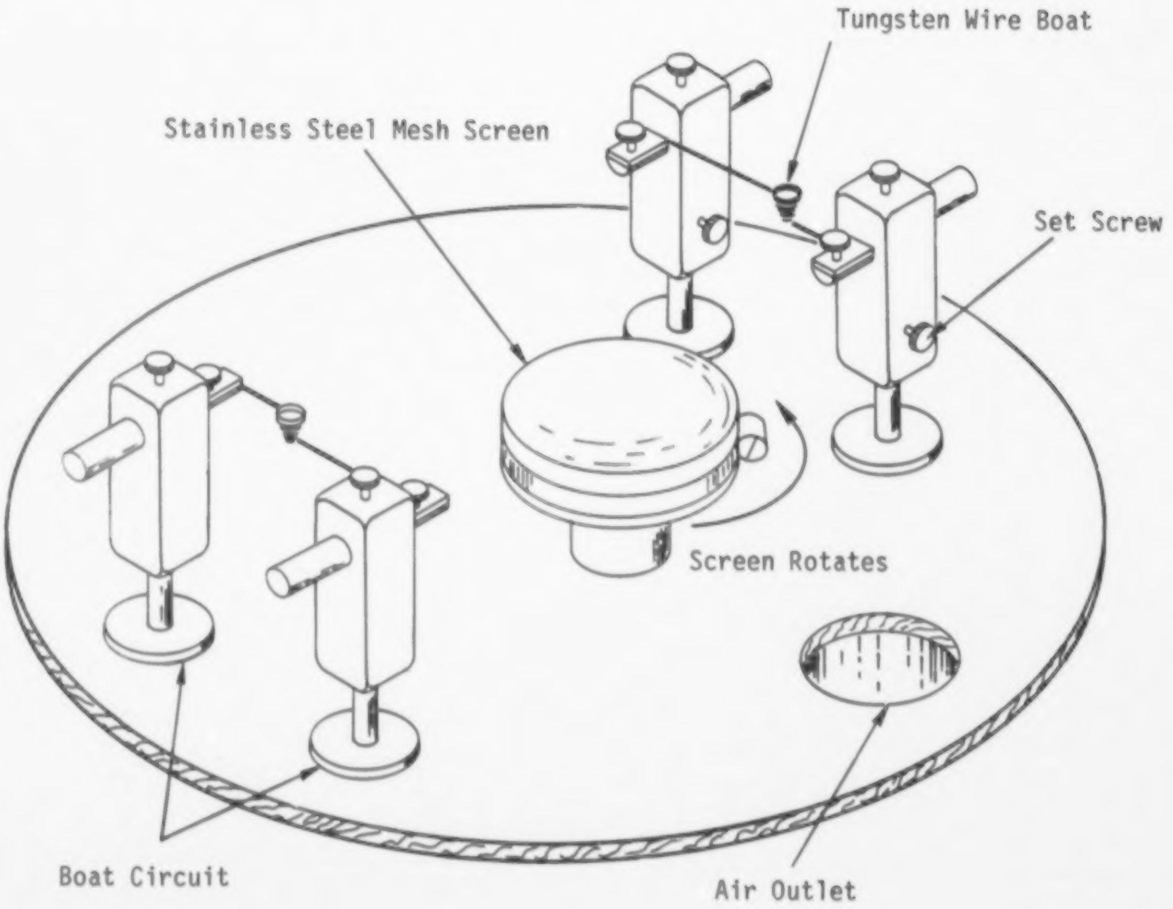
Tungsten Wire Boat
Stainless Steel Mesh Screen
Set Screw
Screen Rotates
Boat Circuit
Air Outlet

Figure 4-6. Varian setup for depositions (Cr, Na and Fe).

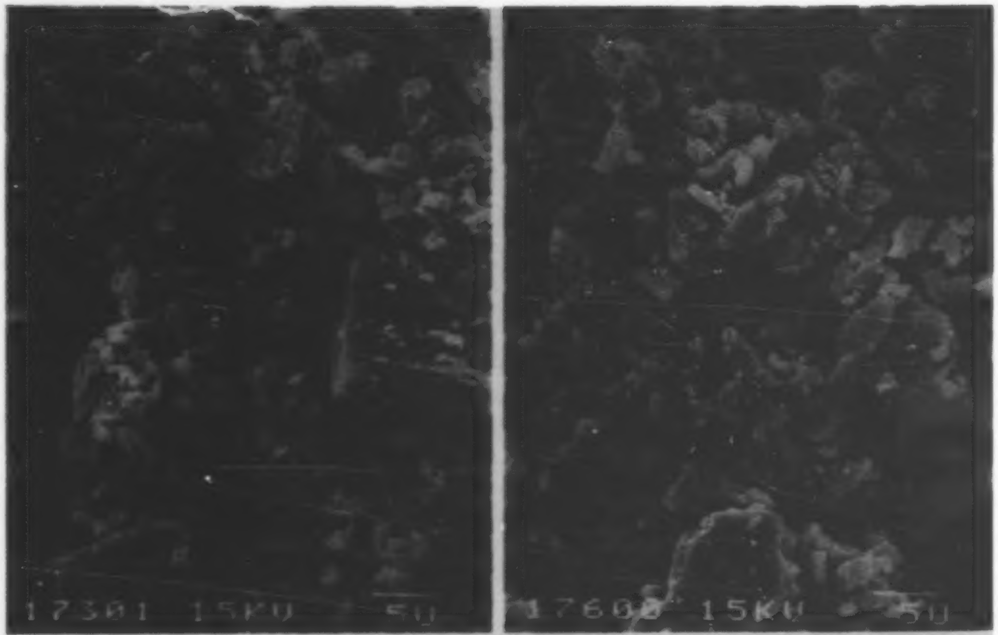
17301 15KV 5U
17600 15KV 5U
17500 15KV 5U
17400 15KV 5U

Figure 4-7. Photographs of precalcine sorbents (Micrograph No. 17301--no dopant; 17600--Na; 17500--Cr; 17400--Fe).

diffraction analysis of the sorbent with chromium failed to show the presence of $CaCrO_4$ indicating no significant reaction with the calcium. (Based on EDS analysis, the Ca/Cr, Ca/Fe, Ca/Na atomic rates were approximately 16, 16, and 25, respectively.)

4.3.3 Pressure Hydration

Pressure hydration involves performing the water-CaO reaction in a sealed vessel under an elevated pressure and temperature. The water is mixed in at a stoichiometric ratio of 1.3-1.4 to ensure a complete reaction. As the heat and pressure increases, the excess water becomes steam. At about 150 psi, the hydrate is released into a porous collecting chamber at atmospheric pressure, which effectively "explodes" the particles and allows the excess steam to escape into the ambient air. The result is a fairly dry product with a fine particle size. Promoter addition to the hydration water was performed to determine if significant promotion effects were possible during the hydration process, the additive was contacted (with possible reaction) to the calcium-based sorbent.

Hydrator Description

The EER hydrator (21), as illustrated in Figure 4-8, was used to produce doped pressure hydrates. The reactor was sized to minimize the surface area to volume ratio for the vessel (26 cm in diameter by 60 cm long) and designed for a working pressure of 150 psig and a 9 kg per batch capacity. A 4-inch charge hatch was located on the top and center of the hydrator. The reactor ends were designed to accommodate the mixing shaft, pressure gauge, thermocouple ports, and discharge orifice.

When hydrating, pressure developed as soon as water was mixed with lime. Water was introduced into the reactor by a pressurized tank via fingers that extend from the mixing shaft. This configuration dispersed the water effectively in the reaction chamber. The system pressure was controlled with a valve and pressure regulator. The control valve automatically decompressed the reactor whenever pressure exceeded the set pressure limit. In case of a

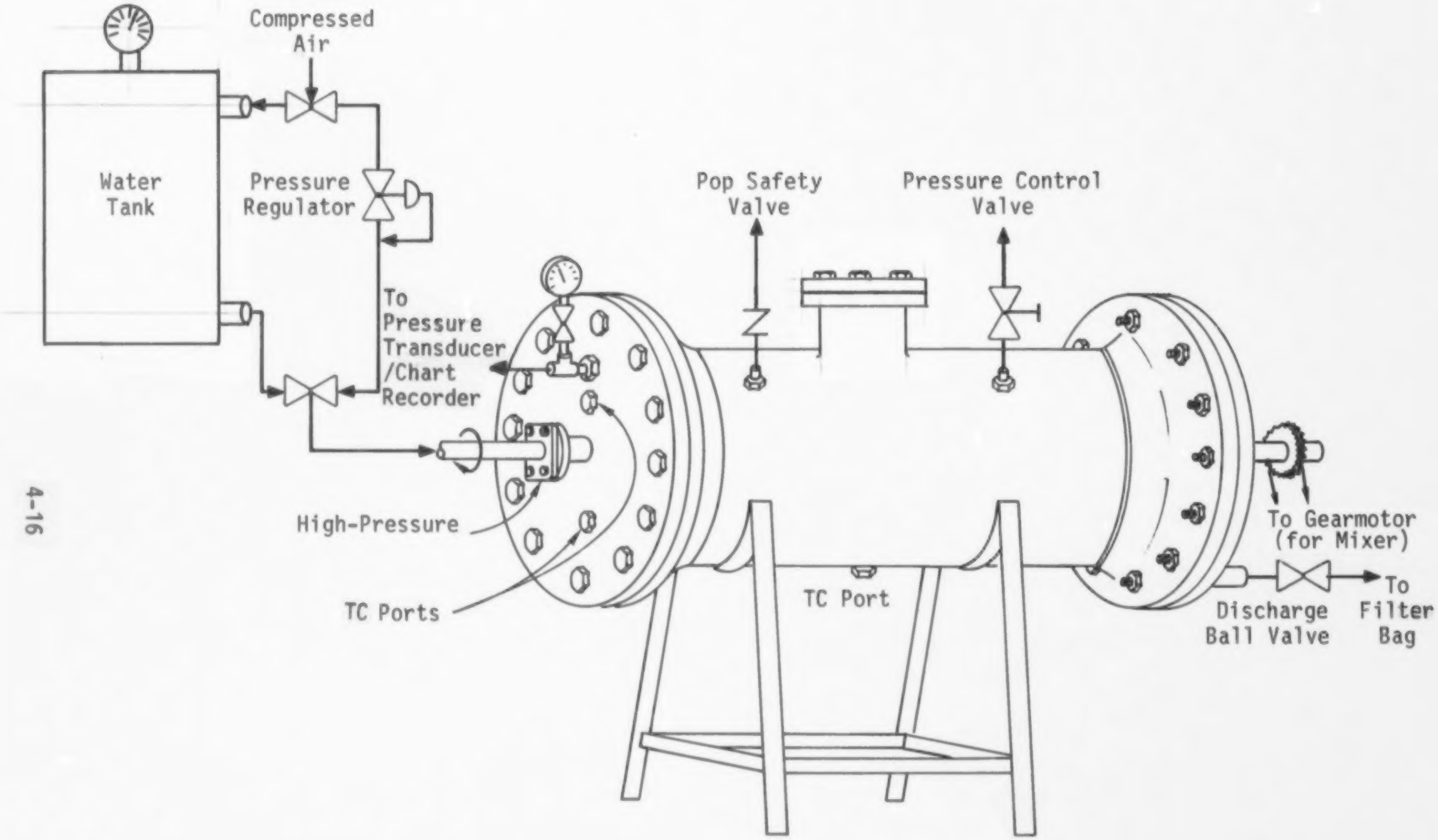
Water Tank
Compressed Air
Pressure Regulator
To Pressure Transducer /Chart Recorder
Pop Safety Valve
Pressure Control Valve
High-Pressure
TC Ports
TC Port
To Gearmotor (for Mixer)
Discharge Ball Valve
To Filter Bag

Figure 4-8. Pressure hydrator setup.

large pressure drop, compressed air was supplied to the vessel. Four temperature controlled 11 cm belts supplied heat, if necessary, to provide thermal stability and control of the hydration process.

The product was discharged from the reactor via a ball valve located at the bottom of the hydration vessel. The amount that the ball valve was opened controls the discharge flow rate. A manometer displayed the pressure drop across the valve, therefore enabled discharge flow rates to be calculated. The product was collected in a cotton cloth filter bag which permitted steam to escape leaving a relatively dry calcium sorbent.

Preparation Procedure for Doped Hydrates

The procedures for generating doped hydrates are essentially the same as those detailed by Overmoe (21) for straight pressure hydrates. Initially the reactor was preheated. When the space gas temperature has reached 344 K, the reactor was loaded with quicklime. The charge hatch was opened, 6.8 kg of quicklime were added, the hatch was sealed, and the mixing shaft turned on at a low rpm to establish a uniform temperature in the reactor. The desired amount of water and aqueous additive solution were first mixed together then added to the holding tank.

After the space gas temperature reached 366 K, the water tank was pressurized to 1034 KN/m^2 (gauge) with nitrogen, and the mixing shaft was set at 30 RPM. The reactor inlet valve was then opened to allow a surge of water to enter the reactor. In general, the time during water addition was approximately 10 minutes. After water was added, another 10 minutes of reaction time was allowed before discharge began. The outlet valve was then opened and reactor pressure dropped to 690 KN/m^2/(gauge). The valve was then adjusted such that the effluent flowrate was equal to the nitrogen flowrate so that an isobaric discharge was maintained. Discharge continued until solids were no longer present or hydrator temperature dropped below 366 K. The hydrate was placed in a plastic bag, sealed, labeled, and stored in airtight buckets.

Characteristics of Doped Pressure Hydrates

The promoters used in the pressure hydration process included chromium, sodium, and iron. Table 4-3 summarizes the measured chemical and physical properties of the generated pressure hydrates. In general, all the doped hydrates were larger than the straight pressure hydrate. The addition of solid promoter, i.e., Fe_2O_3, to CaO had very little effect on morphology of the resultant pressure hydrate as shown in Figure 4-9 (e.g., micrograph No. 35001 for the iron promoted hydrate, and micrograph No. 87803 for the straight pressure hydrate).

In the case of premixing water soluble additives (i.e., CrO_3, $Fe(NO_3)_3$, and NaOH) with the hydration water, there were observable and measured (see Table 4-3) physical differences between the hydrates. High resolution photographs of these sorbents are provided in Figure 4-10. The sodium hydrate took on a very smooth and glassy appearance (shown in micrograph No. 49900), with the particle size on the same order of magnitude as the pressure hydrate without sodium. The hydrate doped with CrO_3 (micrograph No. 58701) yielded fairly rough particles with isolated areas of surface smoothing, X-ray diffraction results indicated chromium reacted with the CaO to form $CaCrO_4$. In contrast, the iron dopant did not show any diffraction patterns of Ca/iron compounds; the iron was deposited on the surface in the form of $Fe(NO_3)_3$. There was not a significant difference in morphology between the baseline pressure hydrate and the iron-doped sorbent (micrograph No. 49300 and 87802, respectively).

4.3.4 Vaporized Promoters--The Rotary Kiln

This method allows the sodium to react and promote with calcium sorbent (see Section 6) before injection into the boiler. Potentially more sodium will be able to react with the calcium sorbent without reaction with the mineral ash (see Section 7). A rotary kiln was used to generate the sodium promoted sorbents.

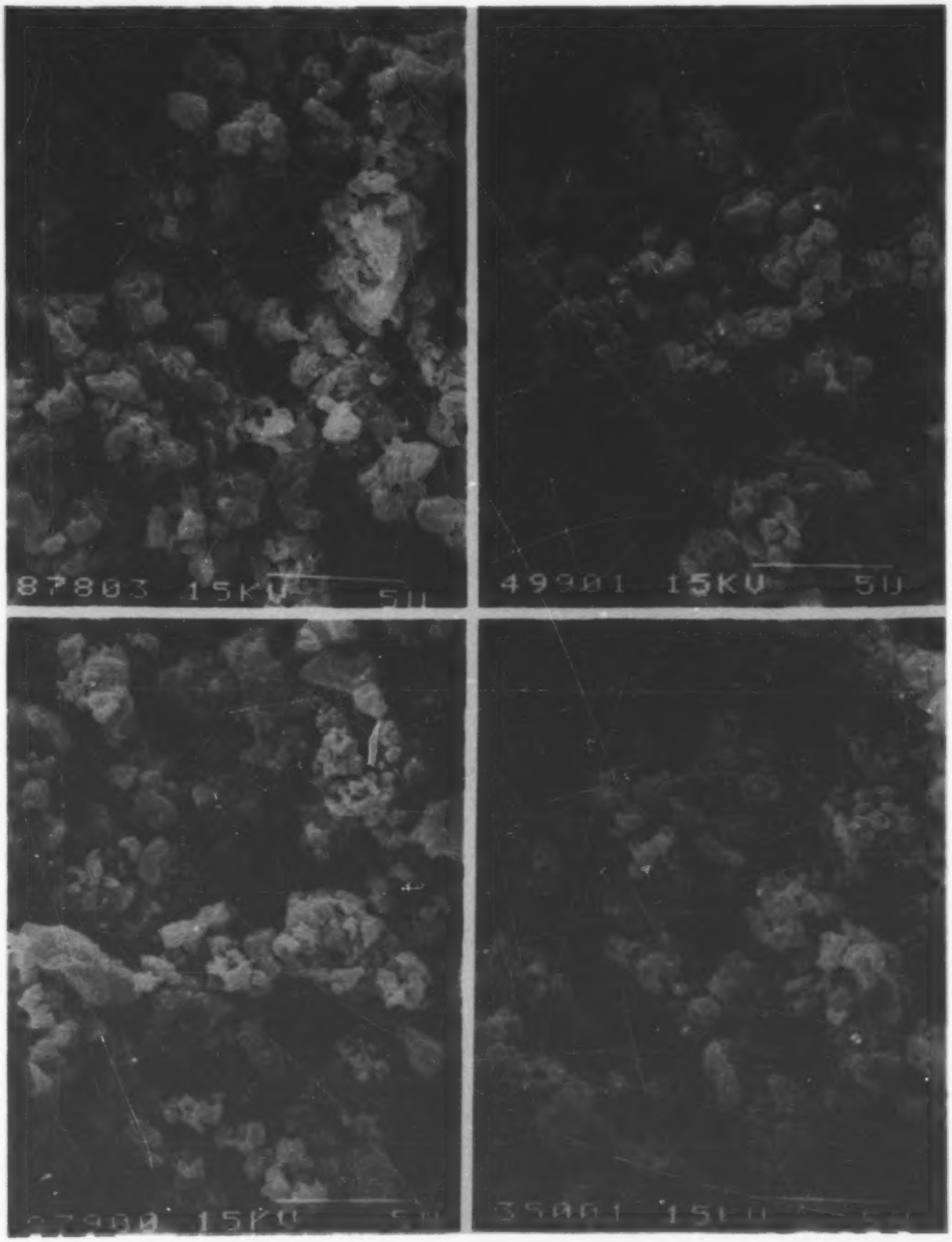
87803 15KV 5U
49001 15KV 5U
87900 15KV 5U
35001 15KV

Figure 4-9. Photographs of pressure hydrates with insoluble promoters Micrograph No. 87803 and 87900--no dopant; 35001 and 49001-Fe).

TABLE 4-3. PRESSURE HYDRATE PHYSICAL AND CHEMICAL PROPERTIES

Sorbent	Pressure Hydrate				
Promoter	(Cr_2O_3(ag)	NaOH(ag)	(Baseline)	$Fe(NO_3)_3$(ag)	Fe_2O_3(s)
BET Surface Area (m^2/g)		2.43	8.5	5.62	8.50
Density (g/cm^3)		2.24	2.16	2.25	-
Median Particle Size (μm)		5.8	2.5	3.5	-
Chemical Composition (wt %)					
Ca	38.6	46.7	52.5	41.6	49.3
Mg			0.57		
Na		2.17	0.01		
Si			0.18		
Al			0.19		
Fe			0.24	3.11	
C	1.21	3.13	4.54	2.70	0.26
H	2.49	2.44	2.58	2.22	2.35
N	0.05	0.07	0.08	1.81	0.00
S	0.01	0.04	0.06	0.01	0.01
Others	Ca/Cr 5.6	Ca/Na 12.3	K = 0.3 P = 0.01	Ca/Fe 18.6	

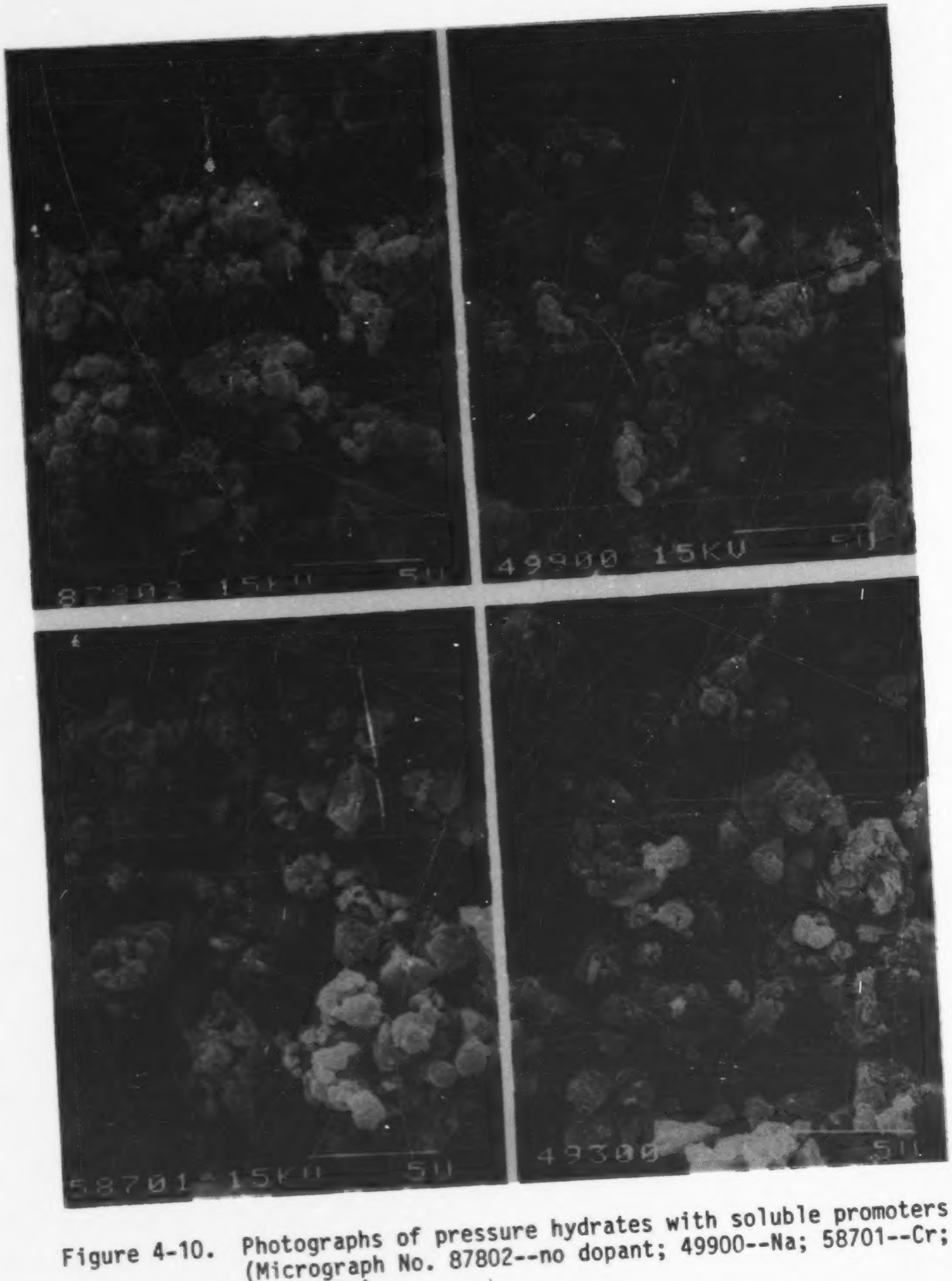
87802 15KV 5U
49900 15KV 5U
58701 15KV 5U
49300 5U

Figure 4-10. Photographs of pressure hydrates with soluble promoters (Micrograph No. 87802--no dopant; 49900--Na; 58701--Cr; 49300--Fe).

Rotary Kiln

A schematic diagram of EER's rotary kiln is shown in Figure 4-11. The facility consists of a horizontal barrel which rotates at 0.1 to 5 rpm, an elbow section, and a vertical control temperature section. A gas burner, with a load capability of 146 kW was installed at the front end of the barrel section and adjusted to give the desired flame configuration over the bed. $NaHCO_3$ fed from a screw auger feeder was injected with the burner air. A secondary or after-burner was located in the upper region of the elbow section for the purpose of burning any uncombusted gases that escaped the main combustion zone. This burner was also fired with natural gas at a nominal rate of 22 kW.

The vertical portion of the kiln contained two backfire chambers that supplied heat through a refractory wall to the main furnace duct. The backfired sections were completely isolated from the main duct and were exhausted through the two side stacks shown in the figure. The main exhaust was pulled from the kiln with an ID fan and then directed to a baghouse to collect any solids entrained in the flue.

Figure 4-12 illustrates the charging system that was used to introduce the Vicron 45-3 into the kiln bed. During normal operation the refractory gate was closed. When the furnace conditions were stable, the loading chamber door was opened and the charge placed in the bucket. The loading chamber was then closed and the refractory gate was opened. The bucket was then pushed into the kiln as desired and rotated 180^o to empty the contents onto the bed. The bucket was then pulled out and the gate closed. This procedure was usually carried out in about 15-20 seconds.

Generation Procedure

Before sorbent generation the kiln was cleaned to avoid any contamination. The kiln was sealed and the main burners lit (the after-burners were not fired). During heatup and steady-state operation, thermocouples located within the refractory walls were monitored. Gas temperatures were measured

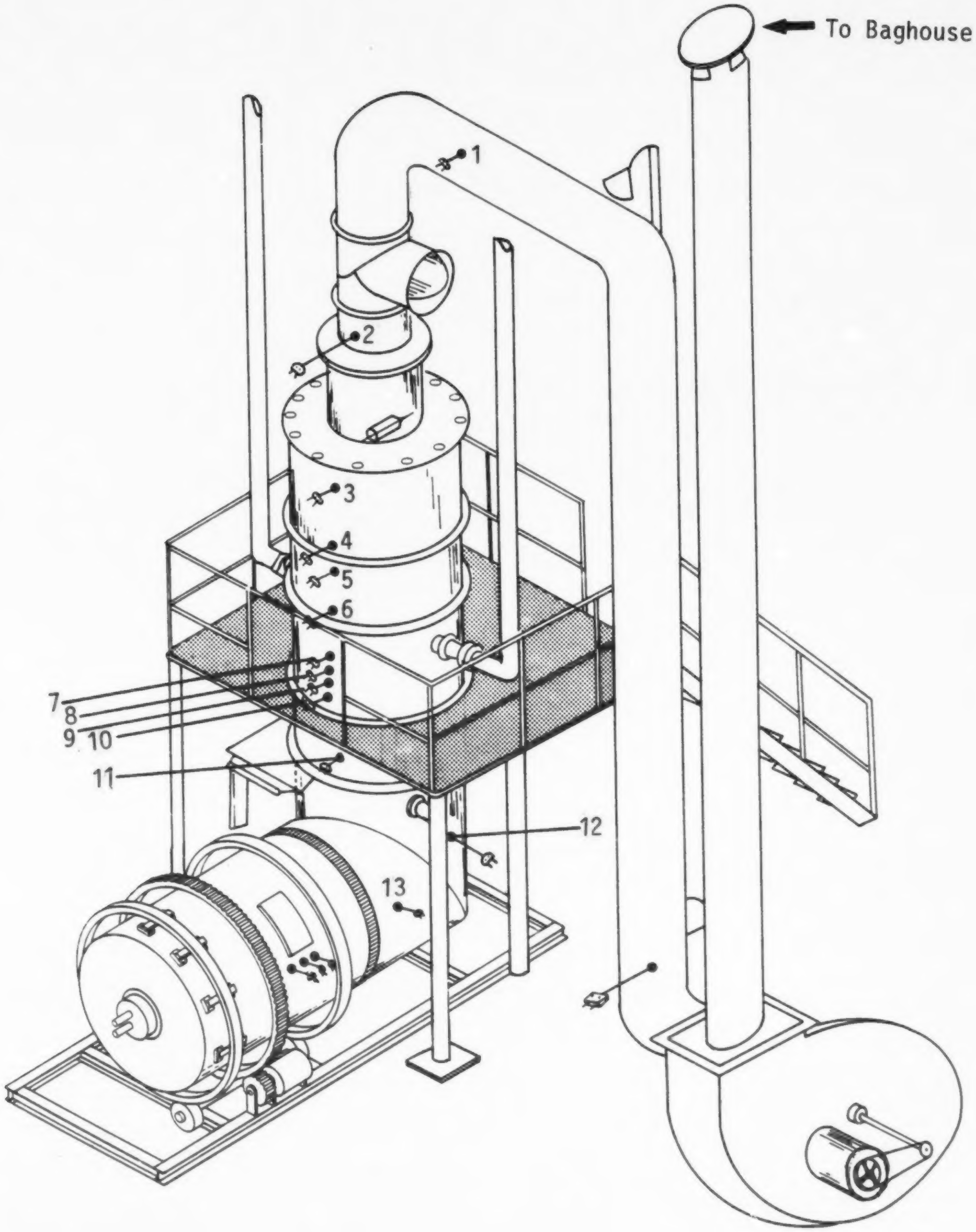
To Baghouse
1
2
3
4
5
6
7
8
9
10
11
12
13

Figure 4-11. Rotary kiln schematic.

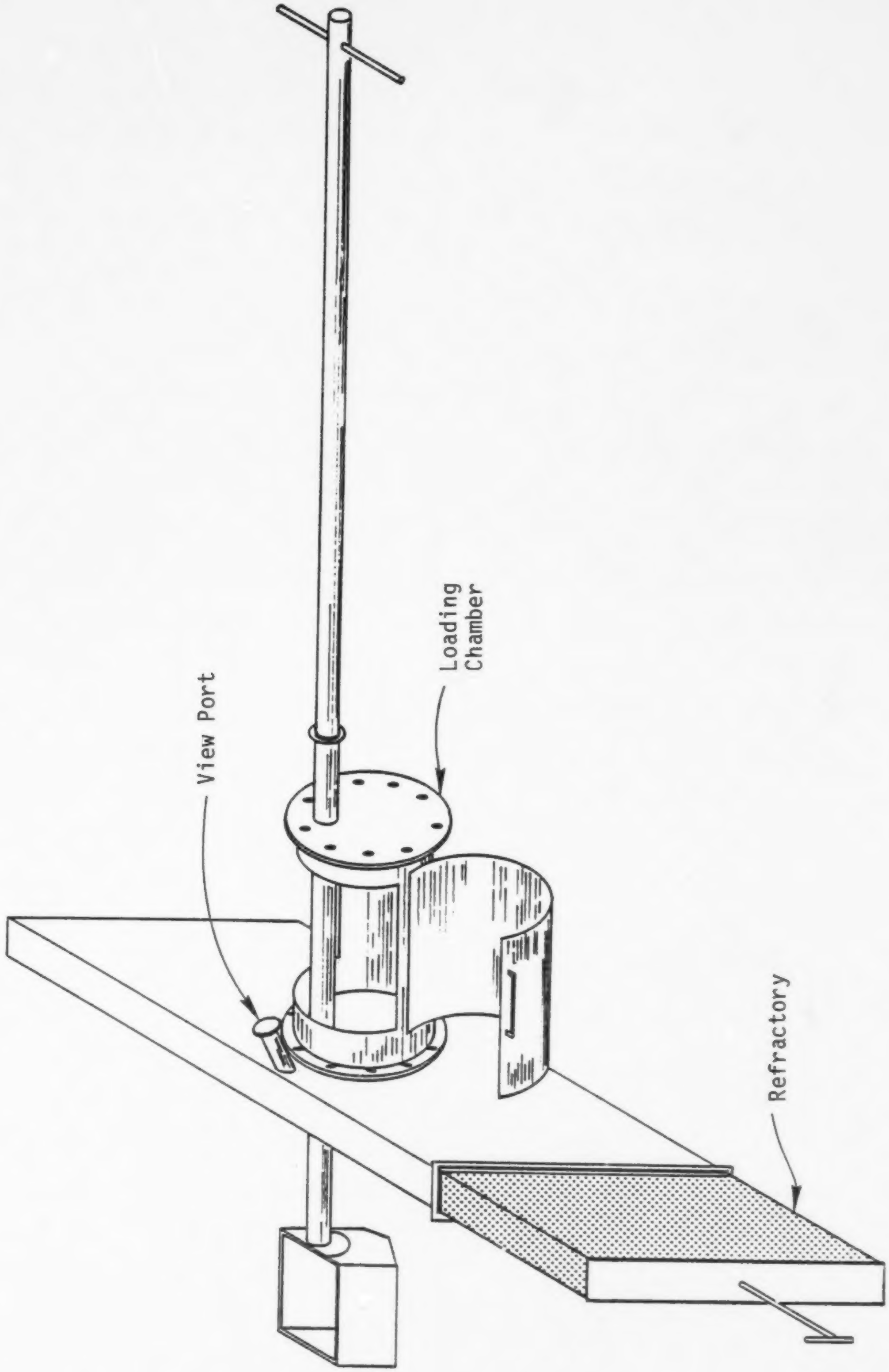
View Port
Loading Chamber
Refractory

Figure 4-12. Charging system.

with a suction pyrometer. At the desired steady-state conditions, Vicron was added. Temperatures and solid samples were extracted every fifteen minutes to effectively monitor the impact of the combustion environment on the calcium sorbent. Sodium bicarbonate was fed by a vibrating screw auger feeder and injected through the main kiln burner.

Sorbent Characteristics

Several thermal conditions were used to generate a variety of calcium-based sorbents (with and without sodium). In all cases, Vicron 45-3 was the initial limestone used. Table 4-4 summarizes the kiln conditions under which the sorbents were manufactured. Included in this table are results of selected chemical and physical measurements that characterize these manufactured sorbents. The explanation of the selected kiln conditions and the description of sorbent morphology will be provided in detail in Section 9 with the sulfation results.

TABLE 4-4. CHARACTERISTICS OF KILN-PRODUCED SORBENTS

Conditions	Surface Area (m^2/g)	Weight Percent					Calculated Percent $CaCO_3$	Ca/Na (Atomic Ratio)
		Ca	C	H	N	Na		
Raw Vicron	0.76	39.38	11.98	0.01	0.00	-	101.5	-
533 K, No Na	0.82	37.76	11.79	0.04	0.00	-	104.2	-
533 K, W/Na	0.74	37.66	11.46	0.05	0.00	0.810	101.6	26.7
1060 K, No Na	0.72	39.84	9.80	0.01	0.00	-	82.1	-
1055 K, W/Na	0.58	38.87	10.29	0.07	0.00	1.00	88.4	22.3
1322 K, No Na	-	66.4	0.50	0.09	0.00	-	2.5	-
1322 K, W/Na	1.22	63.7	0.16	0.02	0.00	0.63	0.8	58
1161 K, W/Na	1.25	65.2	0.17	0.00	0.00	0.45	0.9	83

PART III. INTERACTION MECHANISMS

5.0 COAL ASH/SORBENT

Mineral matter is converted to ash during the combustion of coal. The point at which it becomes ash is arbitrary, but there is evidence (15) that indicates certain minerals present in coal can deactivate sorbents. This section presents the experimental results which were obtained to elucidate the effects of coal ash on overall SO_2 capture efficiencies with calcium-based sorbents.

5.1 Fate of Mineral Matter

The fate of mineral matter during the combustion process is complicated as shown in Figure 5-1. Approximately 1 percent of the mineral matter contained in a typical coal vaporizes during the combustion process. With low-ranked coals the vaporized ash is composed primarily of magnesium oxides (probably due to the vaporization of organically bound Mg) and, in the case of high-sodium coals, sodium oxides. With bituminous coals the vaporized ash tends to be primarily composed of silicon and iron suboxides. Ultimately these vaporized materials nucleate, condense and coagulate to form a fraction of the ash (particle size < 1 micron) which is significant in terms of particle number density although relatively minor in terms of total mass. Large molten particles (1-100 micron) may be produced from agglomeration of coagulated ash particles or from the sintered extraneous ash.

5.2 Ash/Sorbent Interaction and Reaction

The influence of mineral ash on the effectiveness of calcium-based sorbents for sulfur capture was determined experimentally for three situations:

- Injection of premixed Vicron and mineral ash
- Separate injection of Vicron and ash

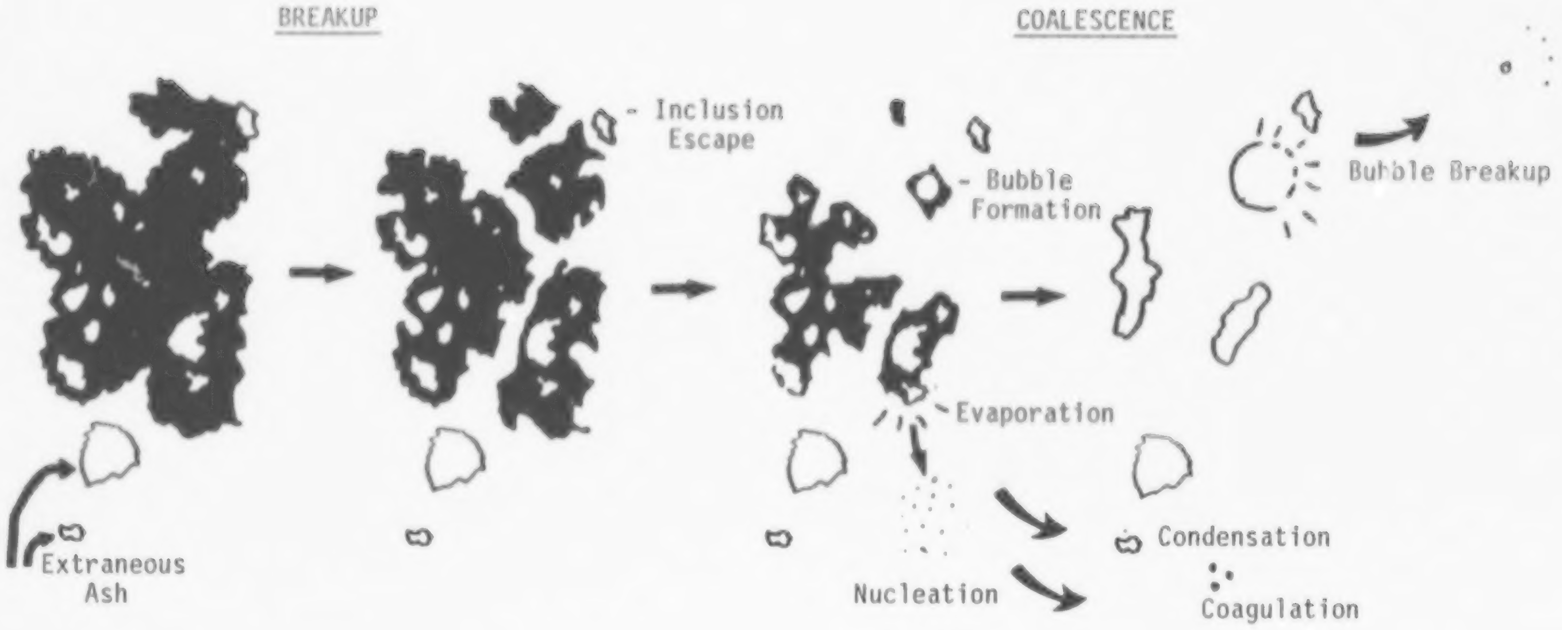
BREAKUP
COALESCENCE
Inclusion Escape
Bubble Formation
Bubble Breakup
Evaporation
Extraneous Ash
Nucleation
Condensation
Coagulation

Figure 5-1. Fate of mineral matter during coal combustion.

- Injection of Vicron 45-3 alone

The sorbents were injected near the burner in the BSF fired with natural gas. (For these tests the quench rate of 333 K/S in the sulfation zone was used.)

Results comparing the effect of the ash placed in initial contact with the sorbent to the effect of sorbent injection alone showed a severe reduction in sulfur capture for the combined ash injection as shown in Figure 5-2. Characterization of the extracted solids (from port 10b) by chemical analysis and surface morphology using X-ray diffraction and scanning electron microscopy (SEM), respectively, indicated that the calcium chemically combined with the ash to form a variety of crystalline phases including calcium silicates, calcium-alumino-silicates, and calcium aluminates. In general, results from high-resolution photographs (provided in Figure 5-3) of the fired Vicron and the mineral ash along with energy dispersive spectrographs suggest that both the calcium and components of the mineral ash may also be present in non-crystalline solid phases. (The smoothed appearance of the particles suggest a liquid phase was formed sometime during the process.) Combining the sorbent with the ash prior to injection clearly reduced the number of easily accessible CaO sites available to react with gas-phase sulfur.

When sorbent particles are present in close proximity to the mineral ash, the volatile components may actually condense on the sorbent. Deactivation is then assumed to occur by a multi-step process. First, the particles collide (if they are not already in direct contact). The particles continue to adhere to each other because the surface of at least one of the particles is "sticky." This stickiness may be due to sodium and magnesium salts which vaporize and then condense on the sorbent particles. Alternatively it may be due to solid phase reactions which occur at the point of contact between the two particles. Low melting point eutectics are probably formed. Finally, there is more extensive chemical reaction and more complete fusion of the stuck particles. If the particle sizes are relatively similar they may tend to form agglomerates. If the particle sizes are vastly different, the particles may appear as a large particle with small fragments

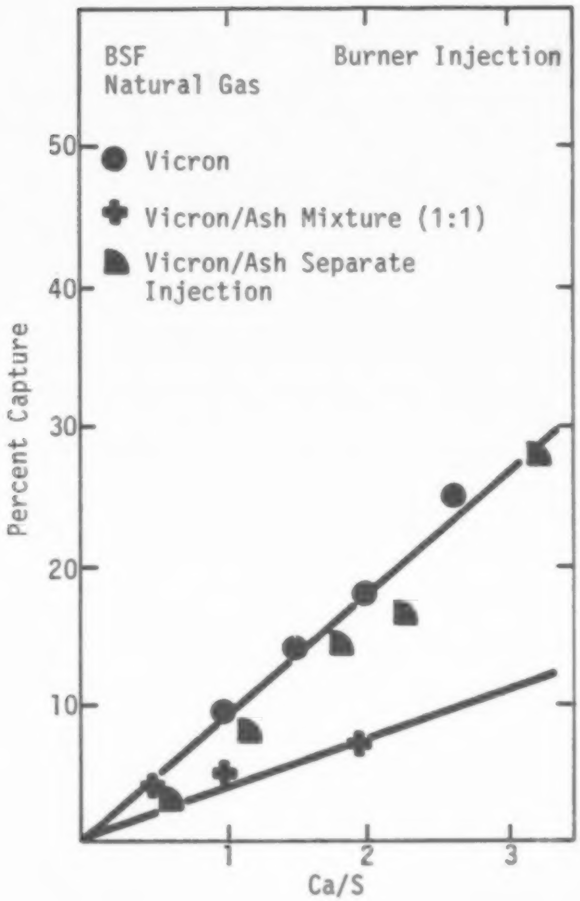

Figure 5-2. Influence of contacting mineral ash with Vicron on sulfur capture.

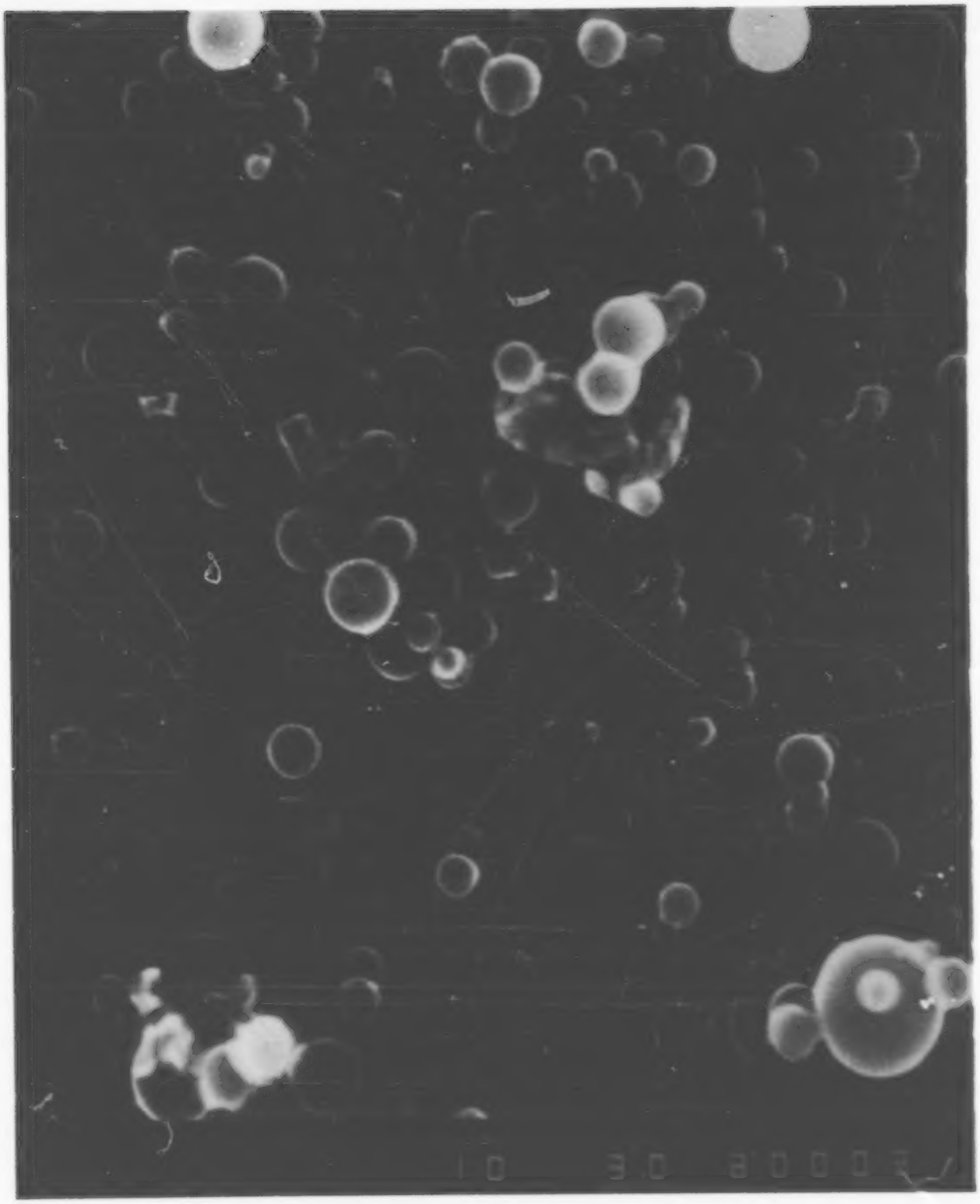

Figure 5-3. SEM photograph of fired Vicron with ash.

adhering to its surface. In either case it is likely that the mineral matter and sorbent compositions both influence the propensity for this interaction to occur.

Sulfur capture results for separate injection of Vicron 45-3 and mineral ash in the BSF is also shown in Figure 5-2. It is clear the sulfur capture for separate injection of the sorbent and mineral ash is at the same level as determined for injection of Vicron (alone) under similar combustion conditions. This result suggests the extent of interaction is strongly controlled by particle collisions rather than by sorbent interactions with the ash vapor (and to a limited extent the submicron ash aerosol). Collision theory supports these experimental results. Simple particle collision calculations show that the number of ash-sorbent collisions in 3 seconds (estimated time in boiler) is small. Characteristic times for coagulation (and Brownian interaction) of particles in turbulent flow have been tabulated for air at 1773 K with a turbulent energy dissipation rate of 100 m^2/s^3 as a function of particle size and particle number density. The calculated results are given in Figure 5-4. The particle density of a typical sorbent-ash mixture in a coal-fired system with LIMB would be on the order of a 2×10^4 particles / cm^3. Assuming the diameter of the ash and sorbent particles is 10 micron, the time required to reduce the particle number by 1/3 is 50 seconds. Thus, the calculated time required for significant sorbent-ash collision is more than 10 fold the time available in a coal-fired boiler.

5.3 LIMB Simulation Tests

Calcium-based sorbents were injected near the burner (at ~1700 K) or downstream (at ~1500 K) in the BSF fired with coal to simulate the conditions in a large boiler. A number of coals with varying mineral matter contents and ash compositions were used. The weight percent (dry) of mineral matter in the coal varied from 10 percent for the Indiana No. 3 to 42 percent for the Kentucky. A detailed breakdown of the ash composition results for the tested coals is provided in Table 5-1.

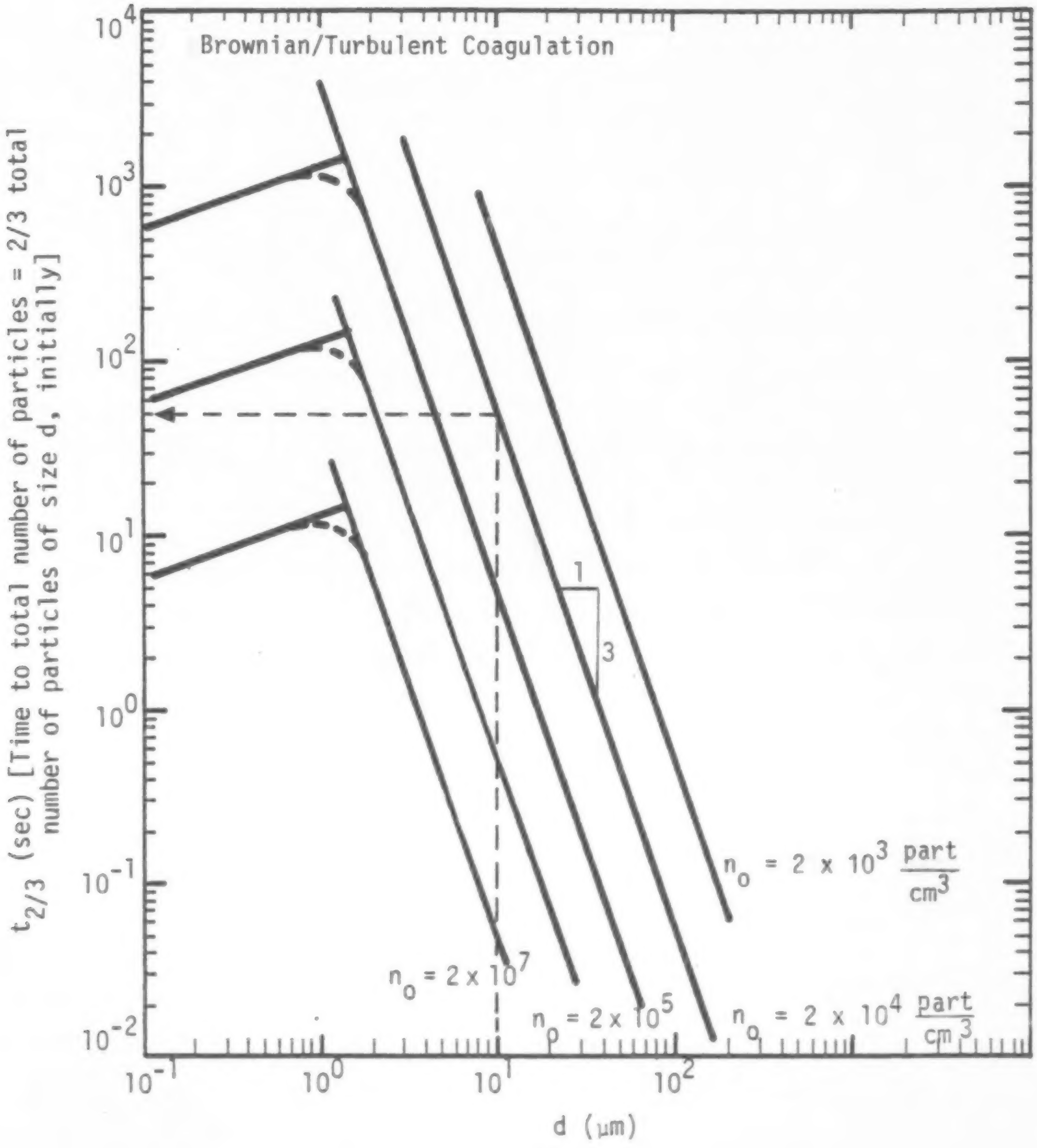

Figure 5-4. Characteristic time for coagulation for particles in turbulent flow in furnaces. (Air at 1773 K, $\varepsilon = 100\ m^2/s^3$) as function of particle size and number density.

TABLE 5-1. FUEL COMPOSITION.

Coal Name	Rank	% S (DAF)	% Ash (DRY)	Ash Composition (% of dry ash)									
				SiO_2	Al_2O_3	Fe_2O_3	CaO	MgO	K_2O	Na_2O	TiO_2	P_2O_5	SO_3
Indiana #3	HVB Bituminous	1.18	9.88	58.63	23.56	10.26	0.95	0.36	1.49	0.22	0.99	0.47	0.43
Illinois	HVC Bituminous	4.38	9.95	46.74	16.56	18.33	6.21	0.85	2.12	1.55	0.85	0.18	5.75
Kentucky		7.50	42.43	50.39	18.16	12.99	5.02	1.14	3.42	0.49	1.35	1.65	3.57
Kentucky Cleaned (1.35)*		3.04	5.18	46.59	18.88	25.60	1.18	0.80	2.67	0.92	1.44	0.41	1.06
Lower Kittanning	Medium Vol Bituminous	1.86	24.84	56.29	26.84	8.38	0.65	0.67	2.54	0.27	0.94	0.16	0.48
Lower Kittanning Cleaned (1.75)		1.06	9.65	48.51	29.82	12.39	1.16	0.59	1.75	0.40	1.10	0.20	1.15
Lower Kittanning Cleaned (1.35)		0.82	5.81	48.29	29.95	12.58	2.03	0.56	1.46	0.28	1.85	0.29	1.85

*Specific Gravity

Figure 5-5 shows the influence of fuel type on capture performance with Vicron 45-3 (calcium carbonate) and Longview (atmospheric hydrate). Comparing the sulfur capture obtained under natural gas conditions to the capture results with coal suggest the presence of mineral ash from coal firing does not influence the ability of the sorbent to capture sulfur. This finding applies equally for both injection locations and both sorbents tested and it is insensitive to coal composition. This result also supports the previous finding that the ash sorbent contacting under practical boiler conditions is limited; therefore, deactivation of the sorbent by the ash will be small.

The previous discussion has focused on deactivation of the sorbent by reaction (chemical bonding) and elimination (agglomeration) of calcium sites with the major components of the ash (i.e., aluminates and silicates); however, the ash is also metallic components (i.e., sodium, potassium) that have been shown to enhance the capture of sulfur. Table 5-2 summarizes the relative alkali metal content of the coals tested. The combined atomic ratio of alkali metals to sulfur in these fuels is approximately the same as the sodium to sulfur ratio in promoter evaluation tests where natural gas flames were doped with various alkali promoters. (See Section 6.0 for details.) In general, the natural gas tests (Section 6.0) indicate sodium enhancement of the sorbent. Unfortunately, in the case of the alkali metals present in the coal ash, the results (Figure 5-5) indicate no enhanced capture above that found for the sorbent (alone) fired with natural gas. This suggests the alkali metals were not readily available to react with the injected calcium sorbent.

5.4 Conclusions

The influence of coal mineral matter on the effectiveness of a calcitic sorbent depends heavily upon the sorbent injection conditions. If the mineral matter and sorbent are in direct contact prior to injection, then ash components can significantly reduce calcium availability and, therefore, sulfur capture. The controlling mechanism appears to involve the formation of low melting eutectics; the calcium reacts chemically with various mineral

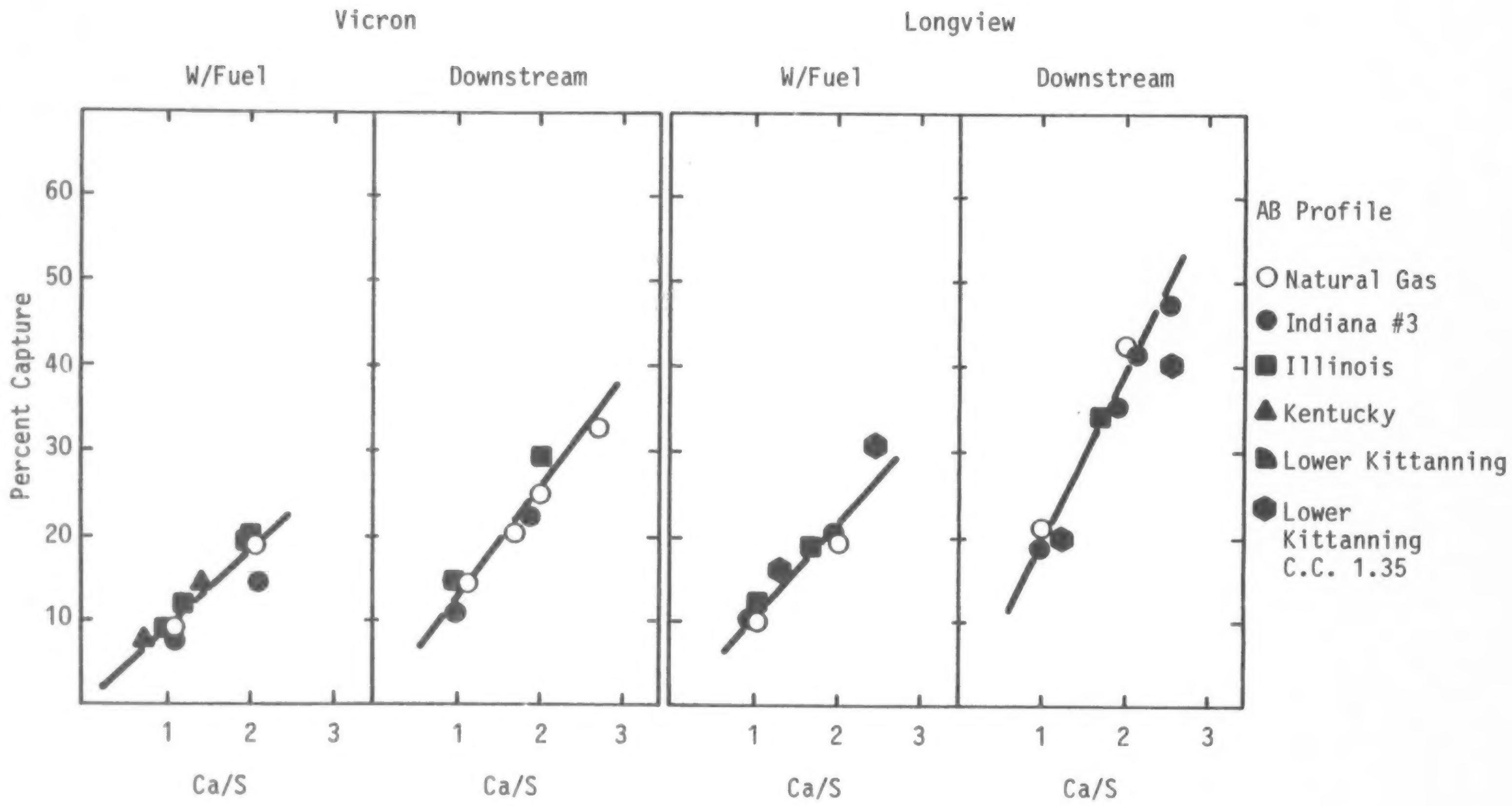

Figure 5-5. Effect of fuel type on capture with Vicron and Longview.

TABLE 5-2. S/Na RATIO COMPARISON

Fuel	$\left(\frac{S}{Na}\right)_e^*$
Natural Gas (Simulation Ca/Na = 15, Ca/S = 2)	7.5
Kentucky	6.4
Illinois	14.5
Indiana No. 3	9.6
Lower Kittanning	6.0

* $\left(\frac{S}{Na}\right)_e = \left(\frac{S}{(Na + K)}\right)$ Atomic Ratio

components and becomes unavailable for subsequent sulfation. Because of this interaction, simultaneous pulverization of the coal and limestone prior to burner zone injection is not recommended.

If the sorbent is injected separately from the pulverized coal (either with the secondary air or downstream) then essentially no sorbent deactivation due to mineral matter occurs. Particle-particle collision frequencies are simply not adequate to deactivate a significant number of sorbent particles. Therefore, the performance of the current LIMB concept (separate, downstream injection) should not be significantly degraded by the presence of mineral ash. Unfortunately, these results also suggest that the favorable alkaline metal components in the coal mineral matter are also insignificant; no measurable sorbent promotion was observed under any conditions.

EPA 3958 C 4/7

6.0 PROMOTION OF CALCIUM-BASED SORBENTS

This chapter focuses on interactions between the sorbent and possible promoters in the absence of coal ash. These complex interactions had previously been found to depend on the promoter and sorbent chemistry, and thermal environment. One of the key program objectives was to define the critical mechanisms in the promoter/sorbent interaction. To do this, hypotheses were formulated and evaluated by theoretical calculations (when appropriate) and by carefully designed experiments.

6.1 Formulation of Hypotheses

For convenience hypotheses were classified into two major categories:

- Contact Mechanism
- Sulfation Enhancement Mechanism

6.1.1 Contact Mechanism

The first major mechanistic issue is the method by which promoter-sorbent contact occurs. Initially it was postulated that promoter vaporization was the principle method of promoter contact and retention by the calcium sorbents. For simplicity, promoters were organized into volatile and non-volatile groups. In order to be classified as a volatile promoter, the promoter had to undergo at least 50 percent vaporization at the temperature of injection in a coal-fired boiler. Basic thermochemical calculations were done with the revised NASA equilibrium program; general physical properties of the promoters were extracted from the available literature (or generated experimentally when necessary) to provide the relative volatility of the promoters investigated.

6.1.2 Sulfation Enhancement Mechanism

The second category of hypotheses focuses on the mechanism by which the actual sulfation enhancement occurs. These hypotheses are of necessity somewhat more complex than the transport hypotheses because of the large number of chemical and physical modifications that may be taking place simultaneously in a promoted sorbent. Table 6-1 summarizes the possible sequential resistances which could be reduced by a promoter to enhance overall sulfur capture.

Detailed calculations of external mass transfer rate by various investigators have indicated that SO_2 diffusion from the free stream to the particle surface is unlikely to be rate controlling under the conditions of sorbent injection in pulverized coal furnaces. Hence, it is unlikely that the primary promotion mechanism relates to SO_2 diffusion to the particle and no hypothesis was proposed for this resistance.

The first major hypothesis in this category addresses the rate at which SO_2 diffuses from the particle surface through the pore or crack network within the particle. If pore mouth closure or pore diffusion is rate limiting, the addition of a promoter may react with the calcium oxide and induce chemical sintering (grain growth) which leads to an increase in the number of large pores and effectively lowers the resistance of the sorbent particle to SO_2 penetration. In addition, a limited amount of grain growth may actually enhance sulfation because although the larger pores have a slightly lower overall surface area, their tendency to close due to pore mouth plugging is reduced.

The second proposed mechanism assumes that the promoter reduces the product-layer resistance by either directly enhancing the product-layer transport rate or by altering the overall product-layer diffusion mechanism. The actual rate controlling processes for product-layer diffusion with unpromoted sorbents have not been fully identified although the possible alternatives include:

TABLE 6-1. POSSIBLE SULFATION REACTIONS

Resistance	Hypothesis of Promoter Mechanism
SO_2 Diffusion to Particle	- None expected
Pore Diffusion	- Increase macropore structure by enhancing sintering
Product-Layer Diffusion	- Reduce the diffusion resistance by altering rate-controlling mechanism (e.g., solid state to liquid diffusion)
Chemical Reaction Rate	- Operate as a catalyst - Operate as a sorbent

- Liquid diffusion
- Surface diffusion
- Knudsen diffusion
- Lattice diffusion

These diffusion processes are ordered from the lowest relative resistance to the highest. The general diffusion characteristics of calcium oxide were estimated from experimentally generated diffusivity coefficients for metallic solids and liquids with the same crystal structure (FCC) as CaO. The diffusivity coefficients for different diffusion mechanisms are provided as a function of the inverse normalized temperature in Figure 6-1. (The temperature is normalized with respect to melting temperature of the species).

The last postulated mechanism of calcium oxide enhancement by the promoter assumes a change in the chemical reaction rate with the promoter operating as a participating or a non-participating chemical catalyst. The performance of known SO_2/SO_3 catalysts as a function of temperature is summarized in Figure 6-2. The promoter may also participate as a sorbent itself, therefore, increasing sulfur capture by direct reaction to form a promoter/sulfur product.

6.2 Promoters Investigated

Past fundamental and parametric studies (13,14) have indicated that chromium, and alkali metals effectively promoted the calcium-based sorbents. Each promoter group was reviewed and evaluated experimentally and theoretically with respect to the previously proposed hypotheses. Iron (to a limited extent) was tested based on the ability of its oxides to participate as an SO_2/SO_3 catalyst.

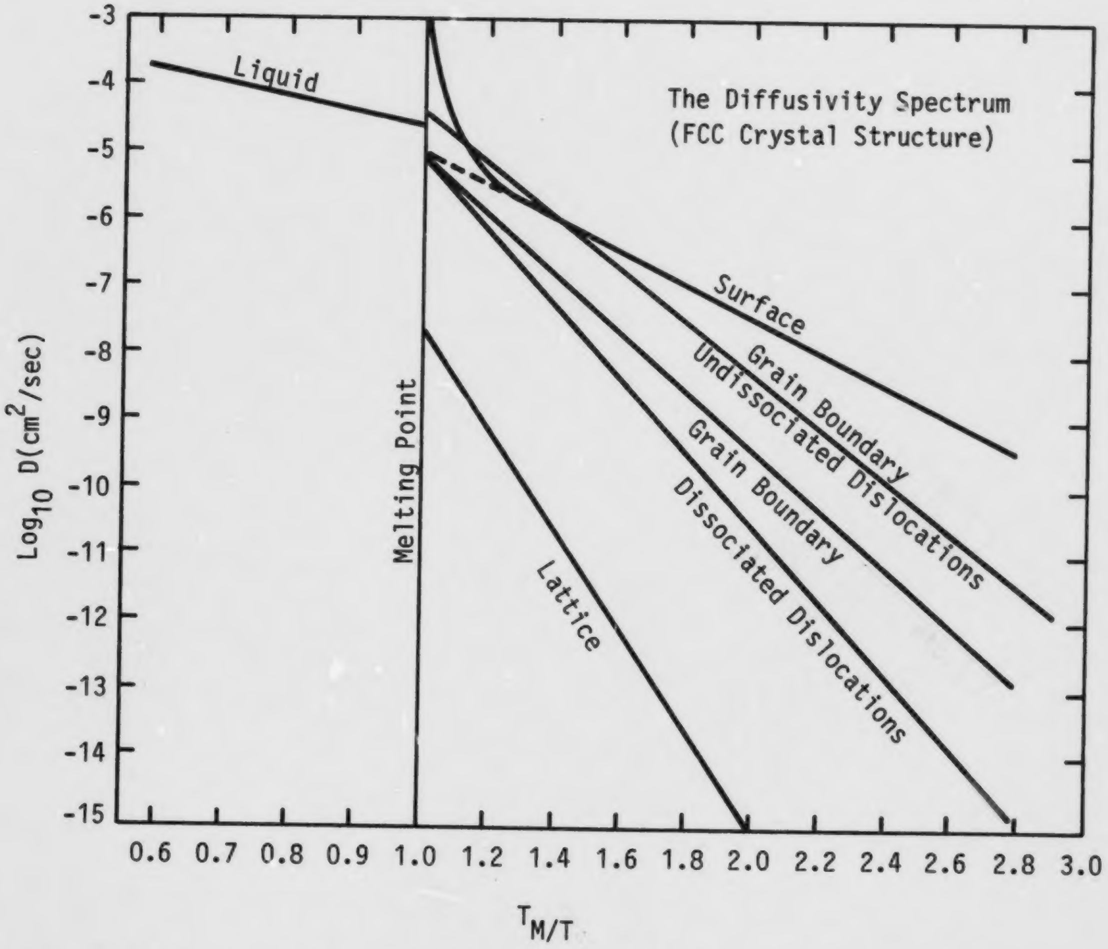

Figure 6-1. Estimation of diffusion coefficients for different diffusion mechanisms (23). From Diffusion, ASM International (formerly American Society for Metals), 1974, p 241. With permission.

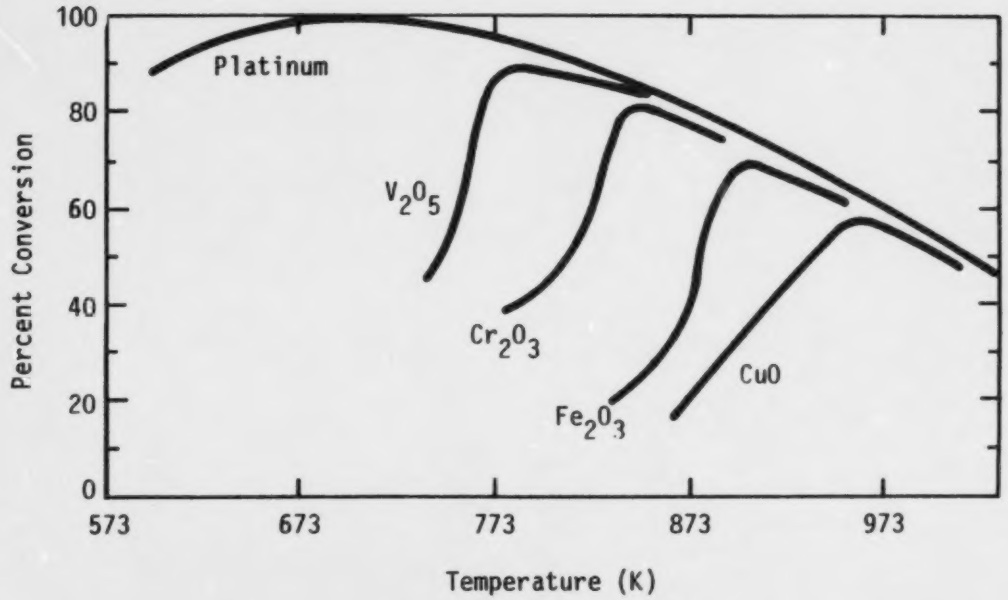

Figure 6-2. Performance of SO_2/SO_3 catalysts as a function of temperature (24). (Reprinted by permission of John Wiley & Sons, Inc., © 1981.)

6.2.1 Chromium

Previous bench scale testing (13) demonstrated that chromium oxides could greatly enhance both carbonate and hydrate sorbents. Chromium probably will not be used as a promoter (unless from the mineral matter of the coal being fired) due to the toxicity of certain chromium compounds (i.e., calcium chromate, etc.). However, by studying and understanding the chromium enhancement mechanism, it might be possible to identify other low-cost and environmentally acceptable chemical compounds capable of producing the same effect.

Equilibrium calculations (done with the NASA thermodynamic program) for conditions typically found in the boiler show that Cr_2O_3 is not a volatile promoter. The percent Cr_2O_3 vaporized as a function of stoichiometric ratio and injection temperature is depicted graphically in Figure 6-3. Based on liberal estimates of boiler combustion conditions (i.e., 1700 K, 1.25 SR) less than 1 percent of the Cr_2O_3 is vaporized. Chemical species present at equilibrium (for SR $\sim$ 1.25) are provided in Figure 6-4 as a function of temperature. Based on the calculations, the principle chromium species present is solid Cr_2O_3. At the higher temperatures other chromium oxides are present but not in significant quantities.

Potential reaction mechanisms for chromium enhancement of calcium-based sorbents assume the chromium:

- operates as a sorbent,
- physically alters the sorbent to provide improved accessibility to the calcium sites (e.g., reduces in particle size and/or increase in the number of large pores),
- increases product-layer diffusion, or

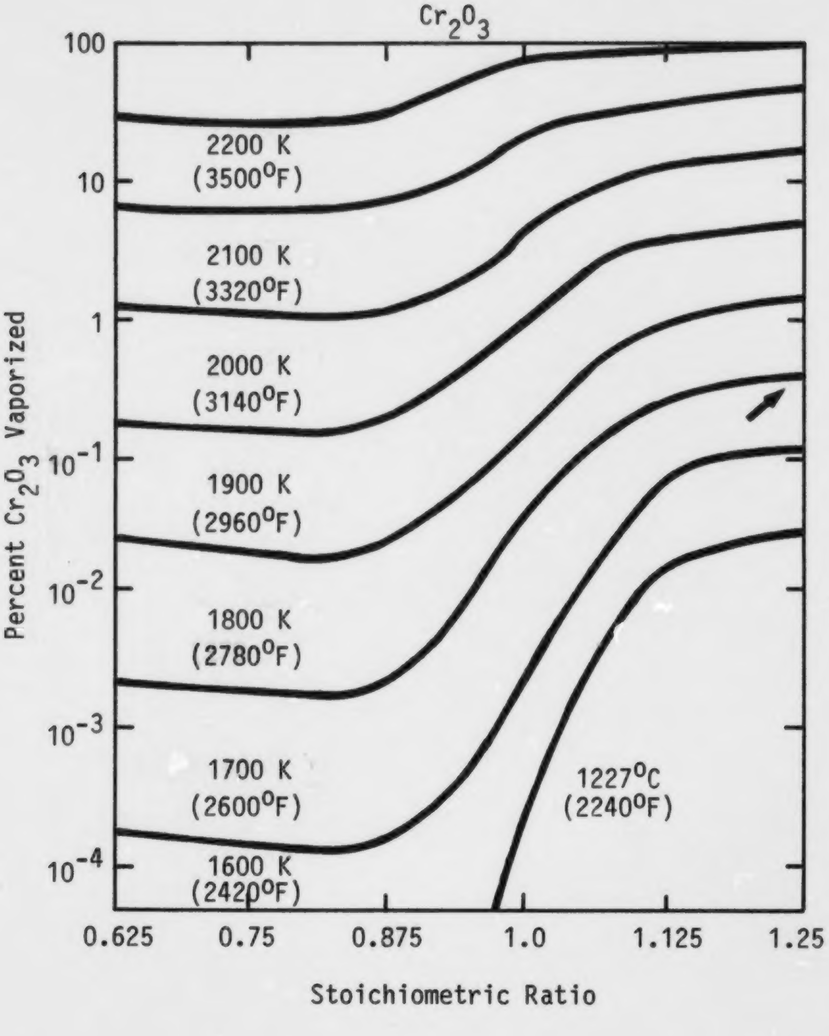

Figure 6-3. The extent of Cr_2O_3 vaporization as a function of stoichiometric ratio and temperature.

c

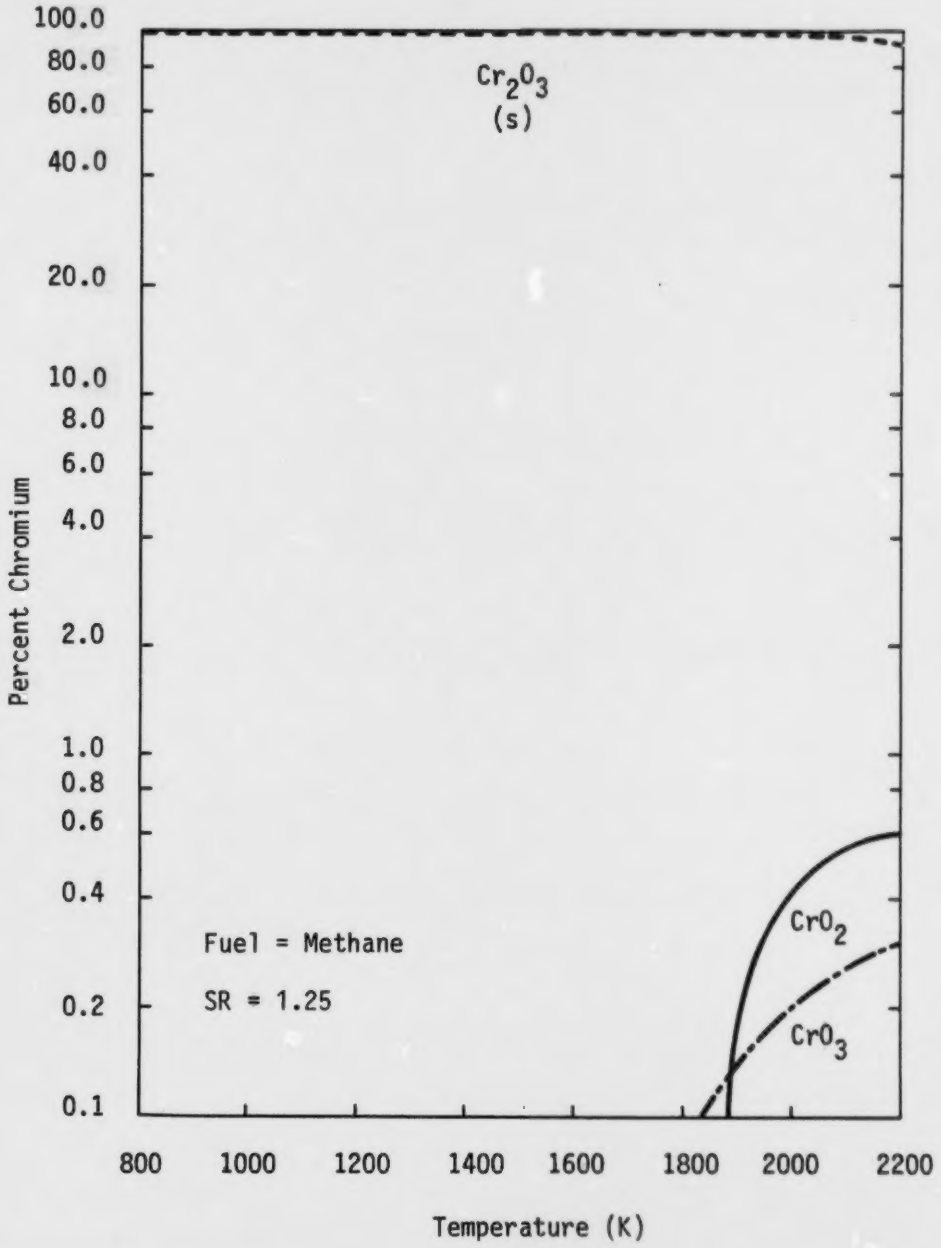

Figure 6-4. Equilibrium chromium species predicted by thermodynamic calculations.

- functions as a chemical catalyst to convert SO_2 to the more reactive SO_3.

In general, chromium promoted sorbents resulted in sulfur capture levels greatly above those obtained with calcium sorbents (without Cr) when the sorbents are injected near the burner (1700 K) region. The absolute sulfur capture levels for unpromoted sorbents are higher for downstream injection, but even here chromium promotion further enhances SO_2 capture. Figure 6-5 illustrates the influence of Cr_2O_3 addition with Vicron 45-3. (Other calcium-based sorbents show similar results). The open bars represent the capture measured with Vicron alone, and the shaded bars indicate the increase in capture that resulted from a 5 weight percent chromium addition. At both injection locations (i.e., burner and downstream), chromium promotion increases sulfur capture to approximately the same overall level (c.a. 40 percent) in spite of the very low unpromoted capture level in the near burner case (ca. 18 percent). This result suggests that, at the higher temperature, the promotion effects counterbalance the detrimental impact of thermal sintering (as seen with the calcium alone).

Increasing the bulk concentration of chromium progressively increased sulfur removal to the extent shown in Figure 6-6. The data indicate that increasing chromium concentration increased the overall sulfur removal, but that the increase in capture efficiency declined with additional promoter.

Gas-phase results from injection of Cr_2O_3 without Vicron (at 1700 K and 2000 ppm SO_2) demonstrated that Cr_2O_3 did not react to form chromium sulfate. (Examination by SEM/EDS and X-ray diffraction analytical techniques of extracted chromium oxide solids from BSF testing indicated sulfur-chromium compounds were not present.) Thermodynamic calculations confirmed the experimental results; chromium sulfates are not stable under the conditions tested. Thus, chromium does not function as an SO_2 sorbent.

Microscopic analysis (with a scanning electron microscope) of extracted solids were performed to better understand the changes in morphology of the sorbent with chromium present. Figure 6-7 presents micrographs of fired

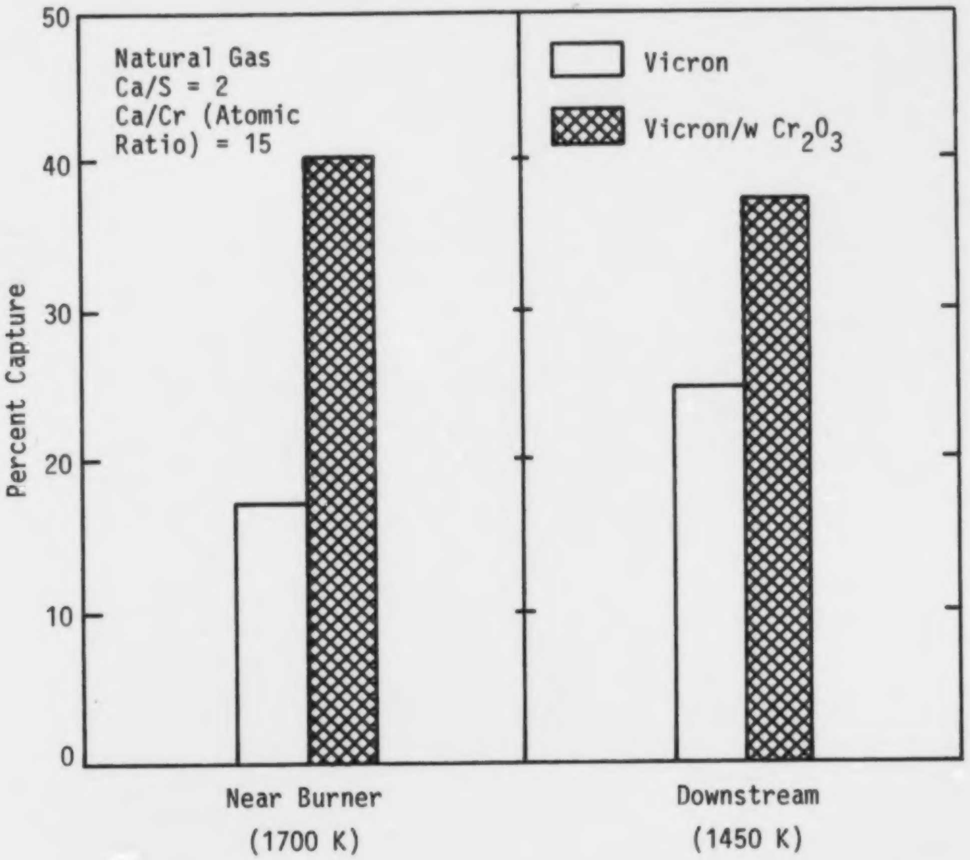

Figure 6-5. Comparison in sulfur capture between fired Vicron with and without Cr_2O_3 present at two different temperatures.

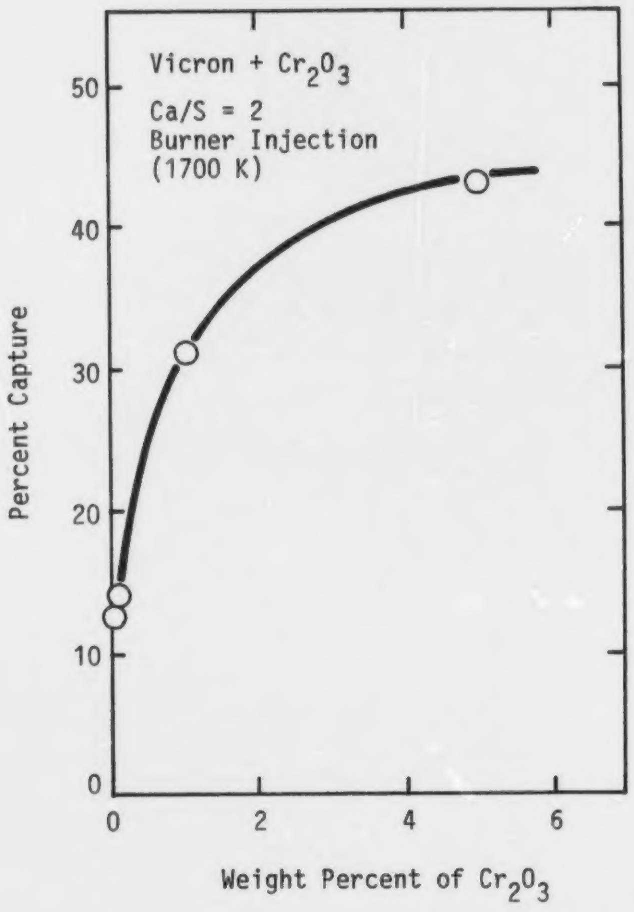

Figure 6-6. Influence of Cr_2O_3 (bulk) concentration on sulfur capture.

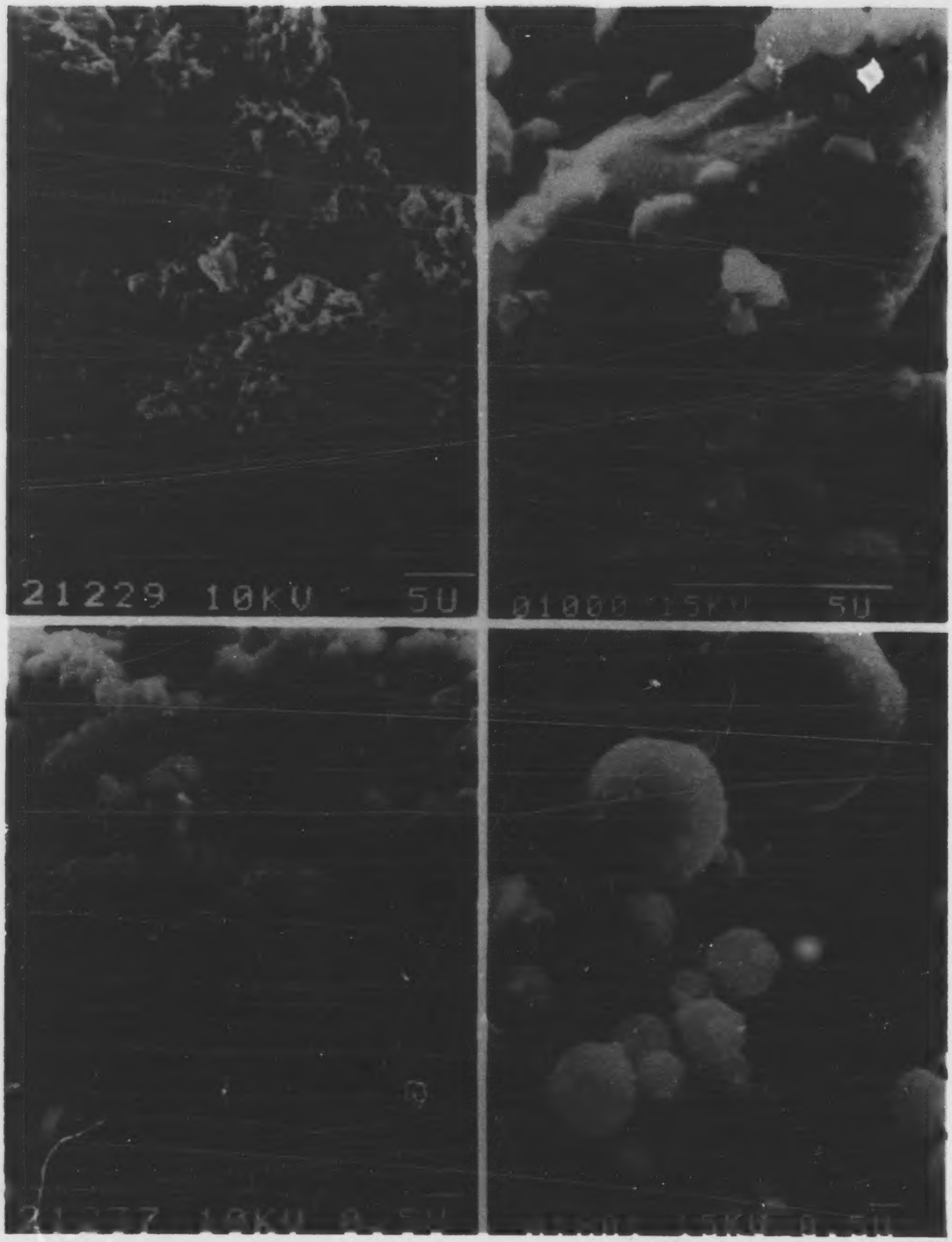
21229 10KV 5U
01000 15KV 5U
21237 10KV 0.5U
15KV 0.5U

Figure 6-7. Scanning electron micrographs of fired Vicron (21229, 21237) and Vicron with Cr_2O_3 (1000 1001).

Vicron (at 1700 K: 21229,21237) and Vicron with Cr_2O_3 (at 1700 K: 1000, 1001). The micrographs show a distinct difference in the overall shape of the particle. Fired Vicron tends to be rough, angular and contain a significant number of large pores; in contrast, the Vicron with Cr_2O_3 appears smooth with the number of large pores severely reduced and more spherical in shape. Measured B.E.T. surface areas of the two solids indicated a reduction from 12 m^2/g (for Vicron) to 4 m^2/g (for Vicron/5 percent by wt. Cr_2O_3), supporting SEM observations. Formation of spherical particles indicates the presence of a liquid phase. CaO and Cr_2O_3 separately possess high melting temperatures (2890 K and 2539 K, respectively); however, when combined, the mixture forms a low melting eutectic (based on $CaO\text{-}Cr_2O_3$ phase diagram shown in Figure 6-8). Both injection temperatures were above the theoretical temperature ($\sim$1273 K) needed to produce a liquid phase. The presence of a liquid-solid mixture has increased the diffusion of sulfur species (and calcium sites) and improved access to internal calcium sites that would be unaccessible in the solid at relatively short times.

In general, the observed particle sizes of the fired Vicron with chromium were also smaller than when the Vicron was fired alone. This might have been caused by particle fragmentation and/or chemically induced sintering. A grain on a particle might fragment (e.g., Vicron, micrograph 21237) if the mechanical strength of the grain is substantially weakened by the creation of a chromium-rich solid (or liquid) mixture. Spalling caused by chemically induced sintering of an enriched chromium solid mixture would create new reactive CaO surfaces for sulfur capture. In general, the reduction of particle size would increase calcium utilization by reducing the diffusion length required for the sulfur to reach a calcium site.

Sulfated Vicron/Cr_2O_3 solids analyzed for elemental distribution by electron dispersive spectroscopy (EDS) showed high chromium concentration associated with molten particles and high sulfur capture. Inspection of the EDS data indicates calcium in the presence of chromium is associated with a relatively high sulfur concentration. The left half of Figure 6-9 indicates the relative concentration of chromium on the solid sample given in micrograph No. 1000. The color scale below the object shows the relative

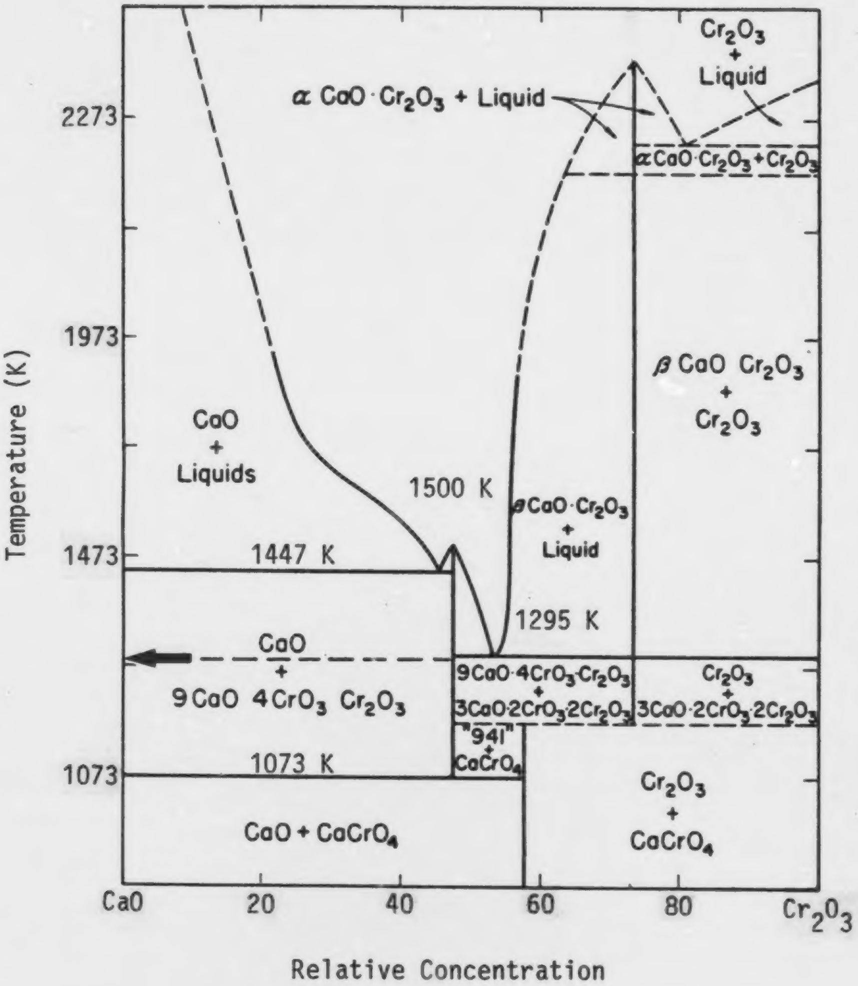

Figure 6-8. Phase diagram for CaO-Cr_2O_3 mixtures (25). The American Ceramic Society, 1964. With permission.

COLOR PHOTOS AVAILABLE FOR
INSPECTION ONLY AT EPA/AEERL

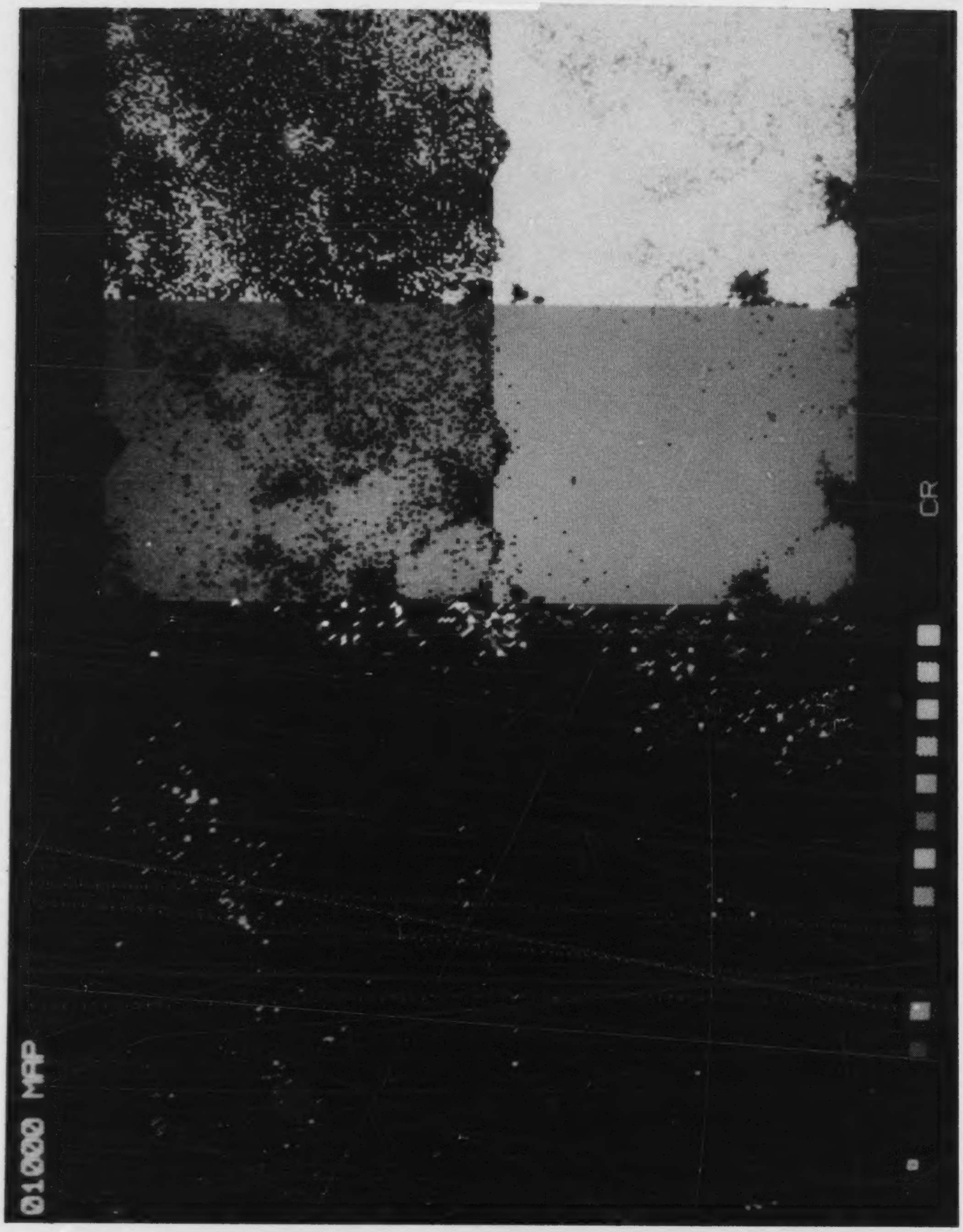

Figure 6-9. EDS analysis of chromium promoted Vicron (shown in Figure 6-7, No. 01000); chromium intensity map (left).

number of counts associated with the chromium (red to white, increasing counts). Figure 6-10 shows the corresponding map for sulfur. Comparison of the micrograph and its corresponding intensity maps shows the presence of chromium sulfur and calcium. Examination of these maps indicate the highest sulfur concentration (Figure 6-10) was found when chromium (Figure 6-9) was associated with calcium. Therefore chromium in direct contact with the calcium-based sorbent appears to enhance sulfur capture.

F 6-10
6-11
-12

The higher the concentration of chromium present, the more progressive the transformation from a rough particle to a spherical particle. For example, the upper large particle in micrograph 1001 has a lower chromium concentration (determined by EDS) and thus maintains some of the characteristics of the fired Vicron, while the particles associated with a high chromium concentration are smooth and spherical (lower spheres). Figure 6-11 summarizes the EDS analysis obtained for the sample in micrograph No. 1001 (Figure 6-7). The left half of Figure 6-11 indicates the relative concentration of chromium on the solid sample. Comparing the micrograph and its corresponding intensity map shows the higher the concentration of chromium present, the more progressive the transformation from the rough particle to a spherical particle. The right half of Figure 6-11 shows the element distribution and composite (lower right corner map).

While the chromium must be in sufficient quantities and intimate contact with the calcium to effectively promote an increase in capture, the sulfur capture also follows closely the amount of calcium present. A line-scan analysis (from a microprobe) of sulfated Vicron particles (extracted from BSF) indicates that sulfur content (bold line on Figure 6-12) traced the relative changes in calcium (dotted line). Once a sufficient amount of chromium was present (for enhancement), further chromium did not increase sulfur capture. Diffractograms (from X-ray diffractometry) of the solids indicates the formation of the chemical species $CaSO_4$, $CaCrO_4$, CrO_3, and Cr_2O_3. (These chromium species are in agreement with those specified in the phase diagram). This supports the gas-phase data which indicated no direct reaction to form chromium sulfates.

COLOR PHOTOS AVAILABLE FOR
INSPECTION ONLY AT EPA/AEERL

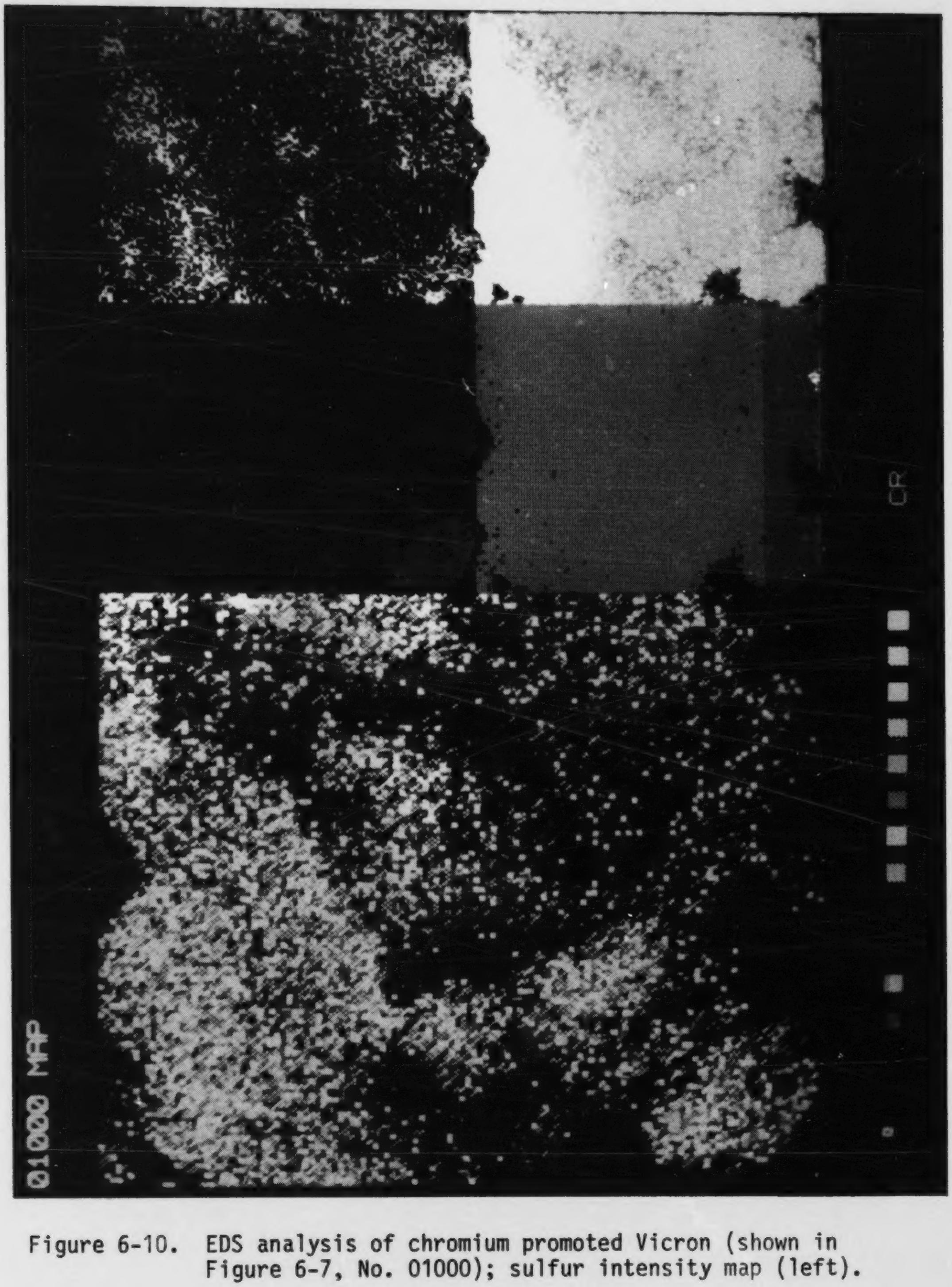

Figure 6-10. EDS analysis of chromium promoted Vicron (shown in Figure 6-7, No. 01000); sulfur intensity map (left).

COLOR PHOTOS AVAILABLE FOR
INSPECTION ONLY AT EPA/AEERL

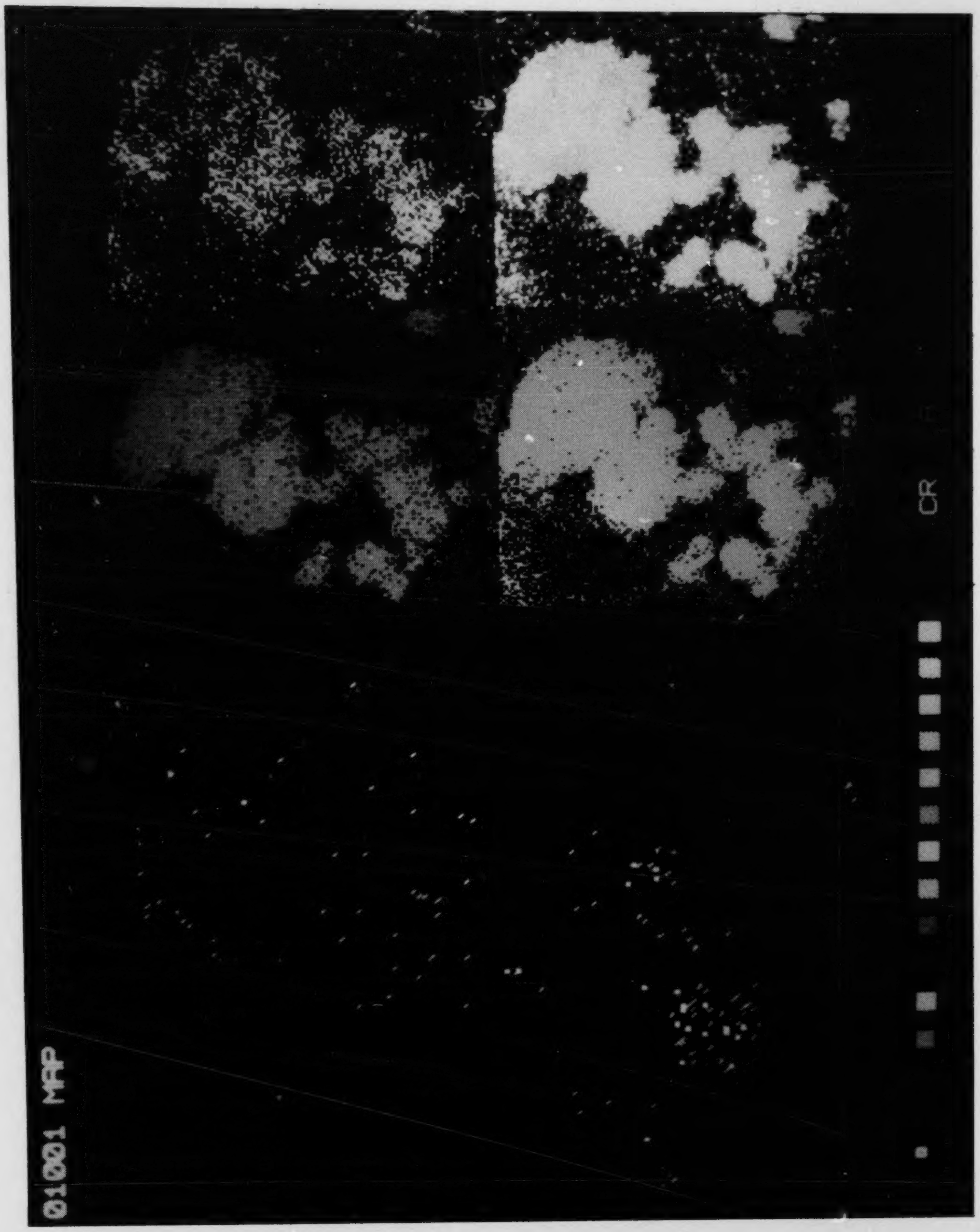

Figure 6-11. EDS analysis of chromium promoted Vicron (shown in Figure 6-7, No. 01001; chromium intensity map (left).

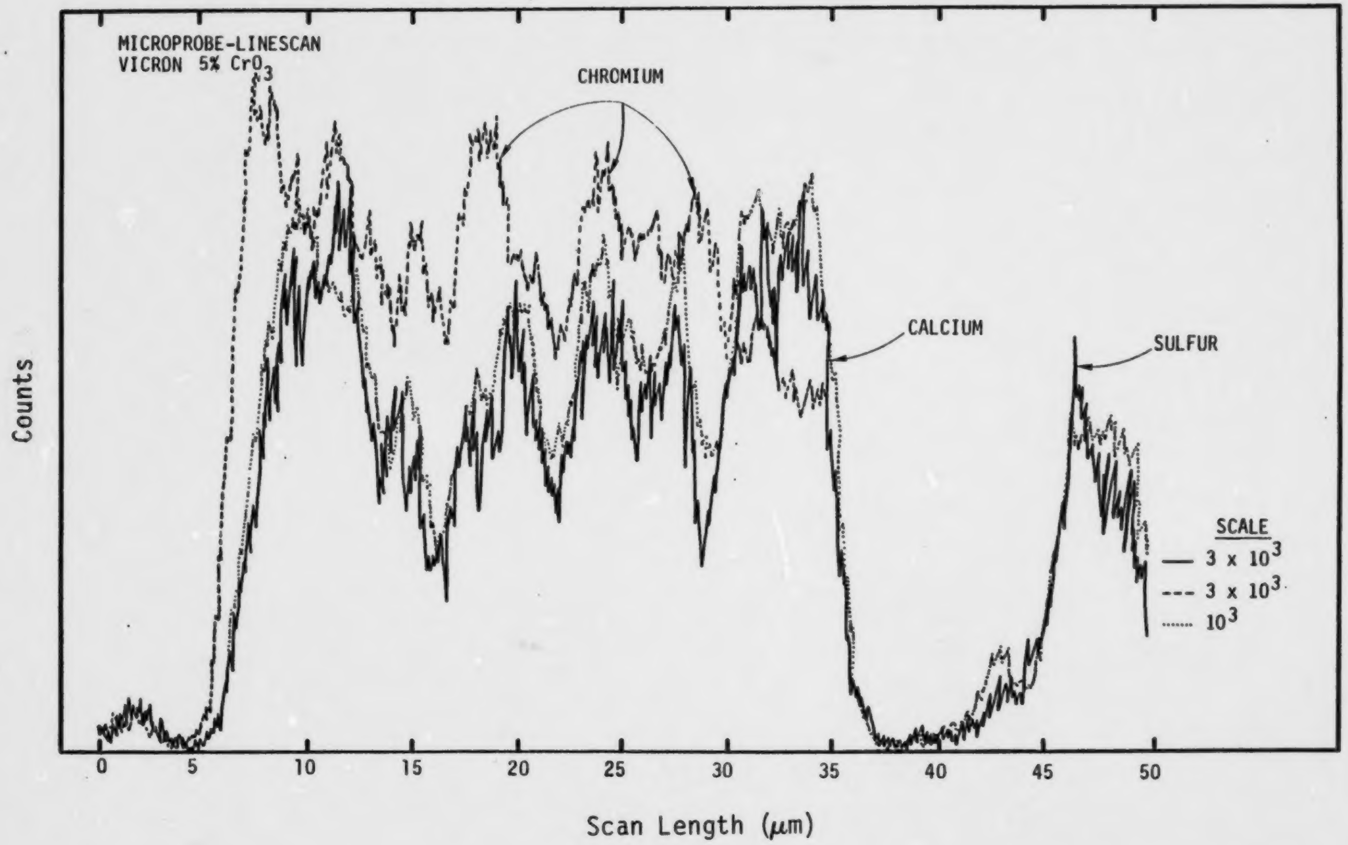

Figure 6-12. Line-scan of Ca, Cr, and S from a microprobe of a sulfated Vicron (with Cr_2O_3) sample.

Reduced injection temperatures reduced the chromium distribution on the sorbent and limited $CaCrO_4$ formation. The solid analysis results discussed thus far have been primarily based on the burner injection of Vicron (with Cr_2O_3); analysis of extracted solids from tests of downstream injection reflected similar but less extensive changes. These samples contained some spheres, but also a large number of rough and angular particles with only localized patches of chromium. Figure 6-5 indicates that the lower temperature injection produced a small enhancement with chromium present. The preceding arguments suggest that chromium must be in intimate contact with calcium to provide a large enhancement; therefore, the smaller overall enhancement at the lower temperature is probably due to less effective distribution of the chromium.

Evaluation of Catalytic Activity Hypothesis

Since chromium oxides are present, the enhancement with Cr_2O_3 might be due to the formation (and subsequent reaction with CaO) of the more reactive SO_3. While Cr_2O_3 is a known SO_2/SO_3 catalyst, its effectiveness has a negative dependence with increasing temperature (8); for temperatures of 1145-1475 K the SO_3 conversion from SO_2 is reduced to less than 10 percent. Differentiating the relative importance of physical and chemical catalysis mechanisms is difficult under the thermal conditions typically used for sorbent evaluation. Therefore, to avoid producing significant physical changes in the sorbent and to enhance the local catalytic conversion of SO_2 to SO_3 from 10 to 50 percent, experimental studies were conducted at a temperature of 1023 K. The reduction in the experimental temperature also reduced the kinetic rate for sulfation which allowed the chemical species produced (or eliminated) to be tracked as a function of time. The 1023 K temperature was determined to be above the temperature needed to ensure that only calcium sulfate was the favored reaction product (not calcium sulfites or sulfides).

An EPA investigation (14) to determine the impact of Cr_2O_3 as an SO_2/SO_3 catalyst used Cr_2O_3 powder placed above calcium oxide. (The materials were physically separated.) In principle, the Cr_2O_3 layer was to produce SO_3 for subsequent reaction with the calcium oxide layer. Their results showed no increase in sulfur capture. The present study also indicated that chromium must be in intimate contact with the sorbent to potentially be effective in obtaining additional sulfur capture. The dynamic X-ray diffractometer (DXRD) was used to determine the importance of precontacted chromium as an SO_2/SO_3 catalyst. Cr_2O_3 evaporated on a precalcined Vicron (to ensure intimate contact with the sorbent) was reacted isothermally under a simulated combustion gas (e.g., 2000 ppm SO_2). The results are shown in Figure 6-13. At short times (1-25 min.), the results indicate no significant difference in overall rate and ultimate sulfur capture. (If the chromium had operated as an SO_2/SO_3 catalyst, the initial rate of sulfation would have been higher). The capture performance during the times between 25 and 75 minutes of the experiment yielded calcium utilizations slightly lower than those obtained with unpromoted CaO which suggests that chromium physically blocked potential CaO sites. The slight increase in the capture performance with the promoted Vicron at 110 minutes is believed to have been caused by chromium penetrating the CaO crystal matrix. ($CaCrO_4$ was detected in the solid phase after 110 minutes). The dotted line indicates the level of utilization expected beyond 110 minutes if the chromium penetration/reaction had not occurred.

Scanning electron microscopy with EDS analysis indicated that chromium-rich calcium sorbent effectively captured sulfur. Figure 6-14 contains the high resolution photographs (micrograph No. 33310, 33305, and 33306) of the reacted, chromium-evaporated sorbent compared to the reacted sorbent without the promoter (micrograph No. 10703). The calcined Vicron did not change drastically after reaction in the diffractometer; the sorbent maintained its angular characteristics. In general, the most significant change in the unpromoted sorbent was the formation of crack networks. In contrast, the promoted sorbent attained a "glassy" appearance upon completion of the sulfation experiment in the diffractometer; this suggests the presence of a liquid phase during the experiment. This confirms the diffractometer results which indicate a reaction occurred. There was also a well defined crystalline structure present which is shown clearly in Figure 6-14 (micrograph No. 33310 and 33306). This structure may be due to chemically induced sintering of the calcium matrix by low concentrations of chromium (less than the amounts needed to generate a liquid phase). EDS results for micrograph

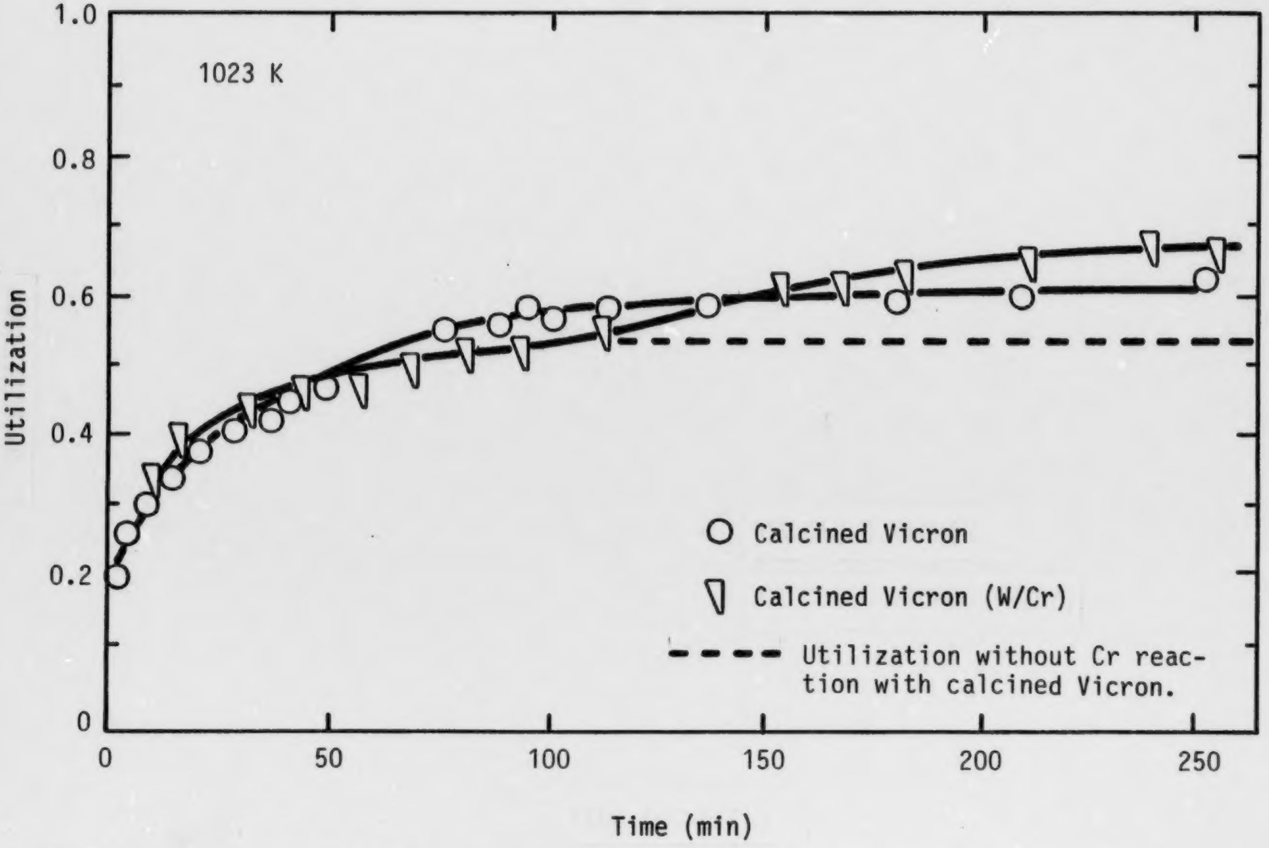

Figure 6-13. Influence of kinetic rate on sulfation and ultimate capture on a chromium promoted calcine.

J

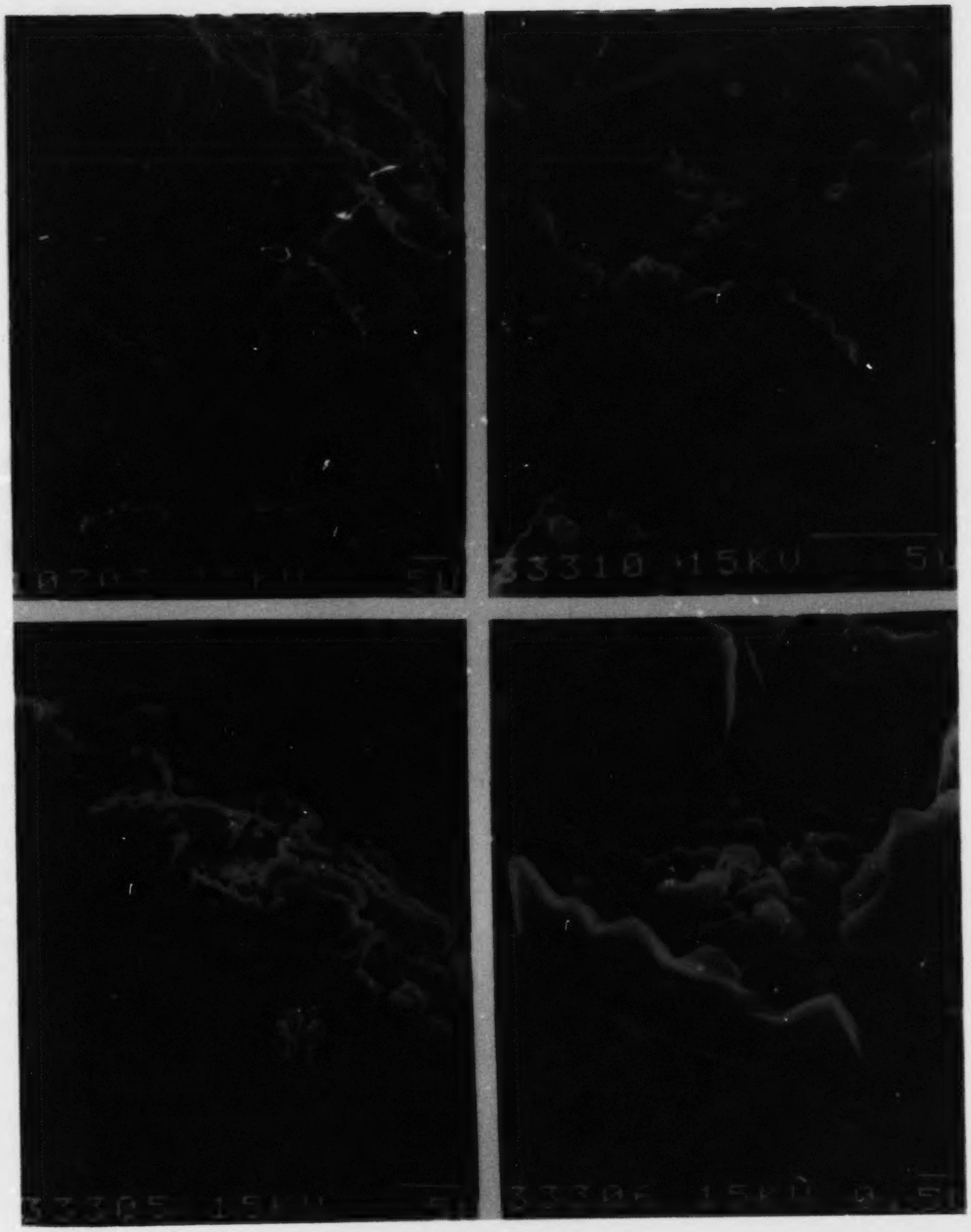

Figure 6-14. Morphology of sulfated chromium promoted calcine (Micrographs No. 10703--0% Cr; No. 33310, 33305, and 33306--Ca/Cr 16).

No. 33305 in Figure 6-15 show the relative sulfur content of the different types of morphology. The glassy (i.e., liquid) phase contained a significant amount of sulfur.

F6-15
-16
-17
-18

In summary, chromium/sorbent contact was found to be a prerequisite for enhancement. Chromium deposited (without reaction) on the calcium-based sorbents (e.g., Cr_2O_3) did not measurably improve sulfur removal; this suggests that catalysis of SO_2 to SO_3 by Cr_2O_3 is not important in improved sulfur capture. It is clear that chromium penetrates the calcium oxide crystal structure (e.g., $CaCrO_4$ formed), suggesting that the enhancement mechanism is a physical alteration of the sorbent. Accessibility to calcium sites may be increased by reducing the effective particle size and forming a liquid-solid mixture (at the surface) which substantially increases product-layer diffusion rates.

6.2.2 Alkali Metals

In general, the alkali metals (as a group) have also been shown to promote calcium-based sorbents. Figure 6-16 summarizes the sulfur capture with lithium, sodium, or potassium premixed with Vicron 45-3 compared to sulfur removal by Vicron alone. In these cases with premixed powders, the capture efficiencies were highest for the potassium and sodium promoted sorbent. Because the chemistry of the alkali metals is similar, promotion of calcium-based sorbents by sodium was extensively studied to determine the mechanism of alkali metal promotion.

Vaporization calculations for Na_2CO_3 and $NaHCO_3$ suggest that, unlike Cr_2O_3, the alkali species are volatile promoters (i.e., unstable at the injection temperature). Figure 6-17 summarizes the percent Na_2CO_3 vaporized as a function of stoichiometric ratio and temperature. It is clear at 1500 K (typical downstream injection temperature), the additive may be completely vaporized. Thermodynamic calculations suggest gaseous NaOH is the major chemical species present in the thermal environment at both burner and downstream injection. The equilibrium chemical species present (at SR = 1.26) are illustrated in Figure 6-18 as a function of temperature. (Note:

COLOR PHOTOS AVAILABLE FOR
INSPECTION ONLY AT EPA/AEERL

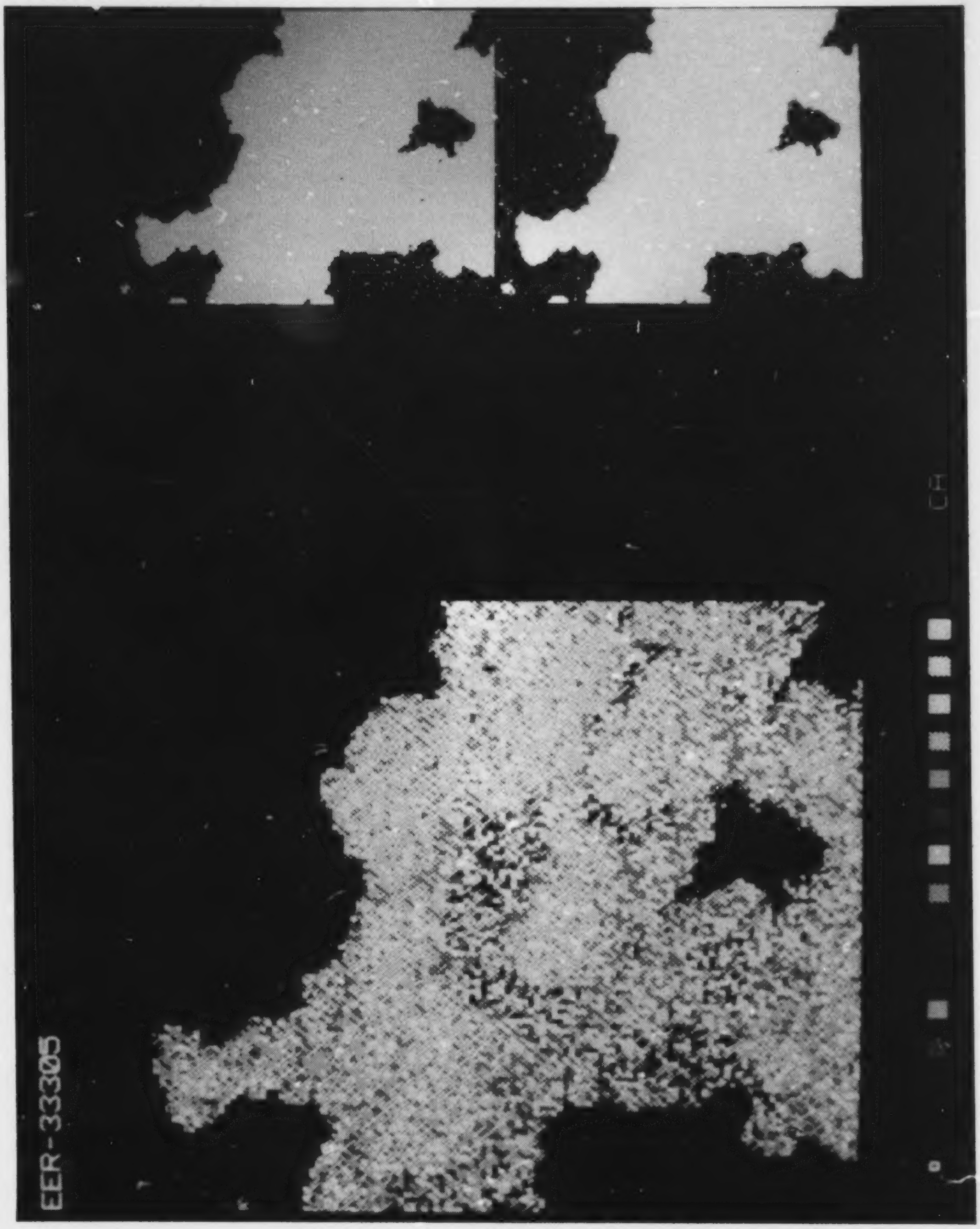

Figure 6-15. EDS analysis of sulfated chromium promoted calcine (shown in Figure 6-14, No. 33305); sulfur intensity map (left).

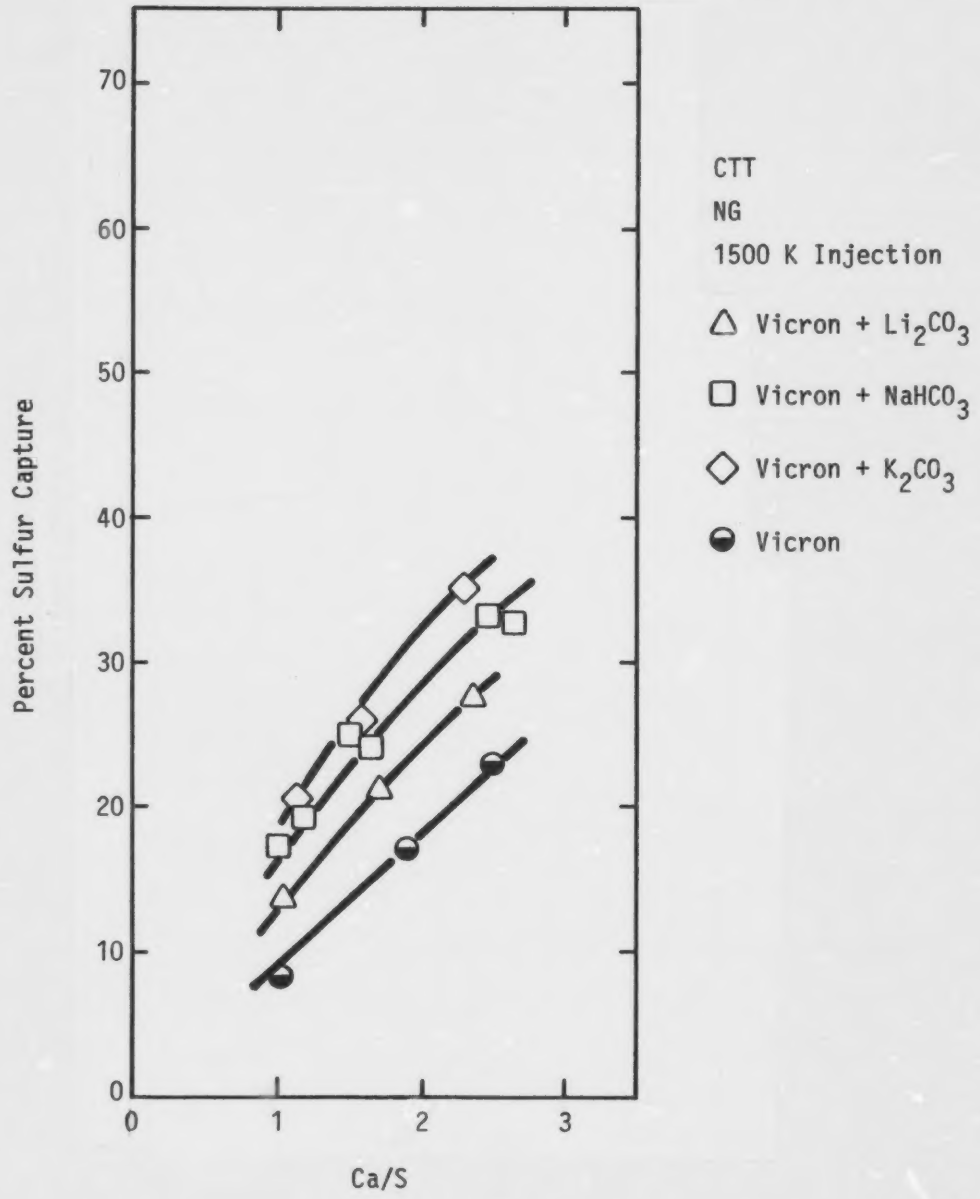

Figure 6-16. Summary of sulfur capture with alkali metals.

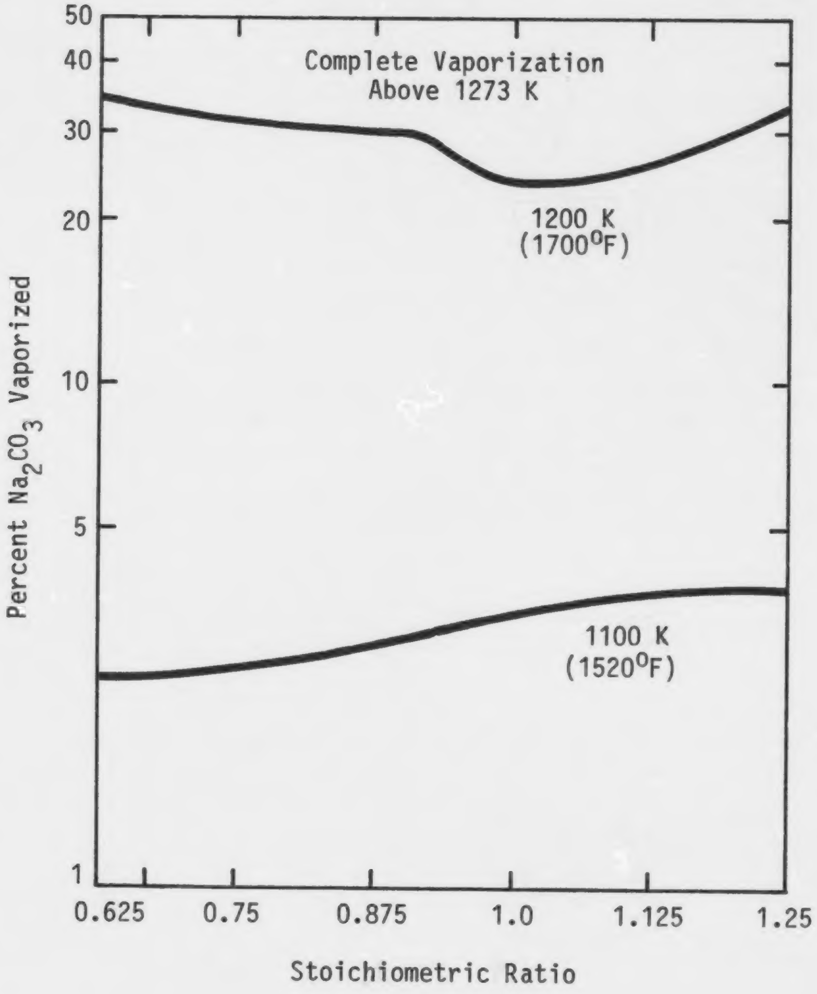

Figure 6-17. The extent of sodium vaporized.

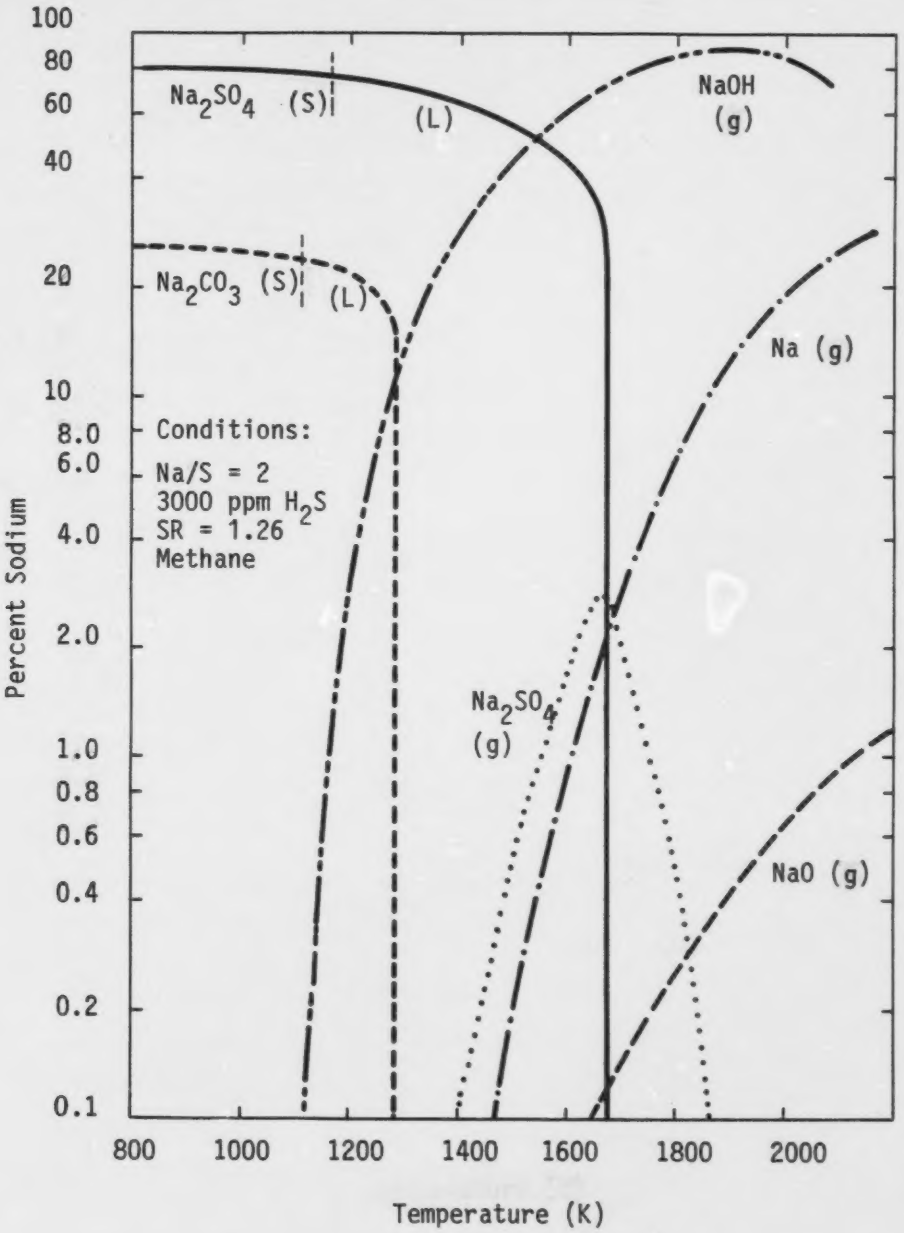

Figure 6-18. Equilibrium sodium species predicted by thermodynamic calculations.

With sulfur present, the thermodynamic calculations suggest the presence of sodium sulfate.)

Potential reaction mechanisms for sodium enhancement of calcium-based sorbents assume that the sodium:

- operates as a sorbent,
- physically alters the sorbent to provide improved accessibility to the calcium sites (e.g., reduction in particle size and/or increase in the number of large pores), or
- increases product-layer diffusion.

The influence of sodium promoted Vicron on sulfur capture is summarized in Figure 6-19. The open symbols represent the capture measured with the Vicron alone, and the solid symbols represent capture that resulted from sodium promoted sorbent (i.e., Ca/Na = 14.8 atomic). For both injection locations (i.e., burner and downstream), the increase in sulfur capture by the promoted sorbents was significant. The sulfur capture with the promoted limestone at high temperature injection (1700 K) was equivalent to the capture at the lower temperature (1450 K). At the higher temperature, the promotion effects with sodium counterbalance the detrimental impact of thermal sintering. Injection of sodium bicarbonate alone (at 1700 K and 2000 ppm SO_2) also decreased the SO_2 emissions suggesting that sodium compounds can react directly with sulfur to produce sodium sulfate. However, the overall increase in sulfur capture with the promoted sorbent is greater than can be explained due to formation of sodium sulfate alone. (The shaded area in Figure 6-19 represents the capture enhancement possible if all of the available sodium reacted to form sodium sulfate).

The impact of sodium concentration on sulfur capture efficiency is summarized in Figure 6-20. As the sodium concentration increased the overall sulfur removal increased linearly. The surface concentration of sodium on fired Vicron changed the sorbent's morphology. High-resolution photographs

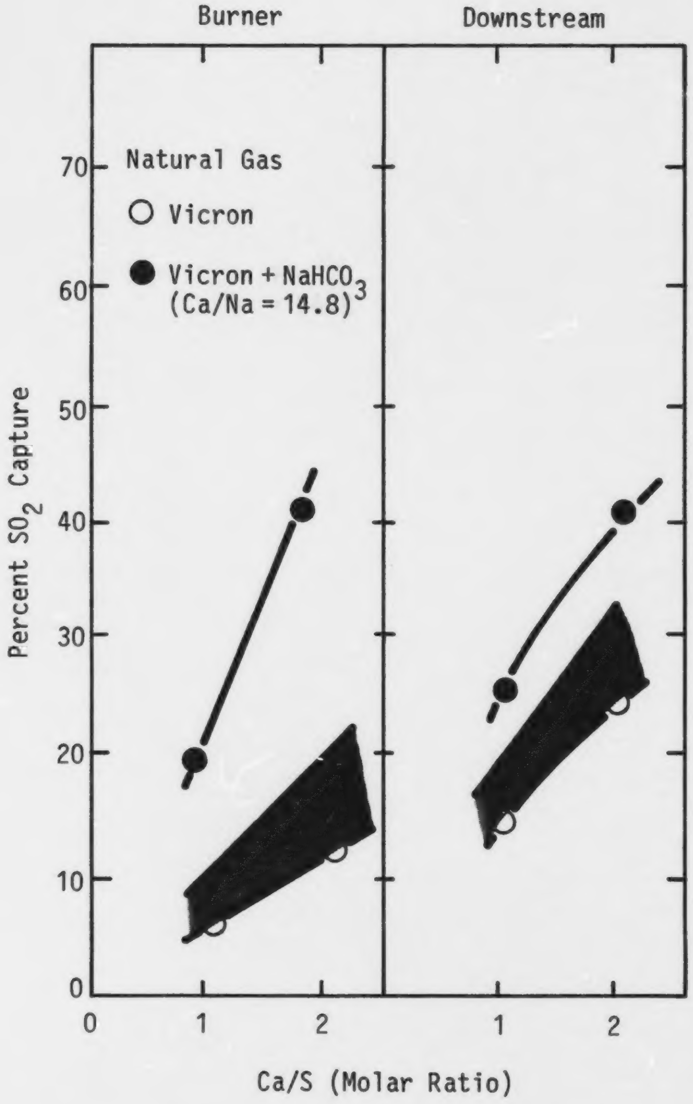

Figure 6-19. Comparison in sulfur capture between fired Vicron with and without $NaHCO_3$ present at two different temperatures.

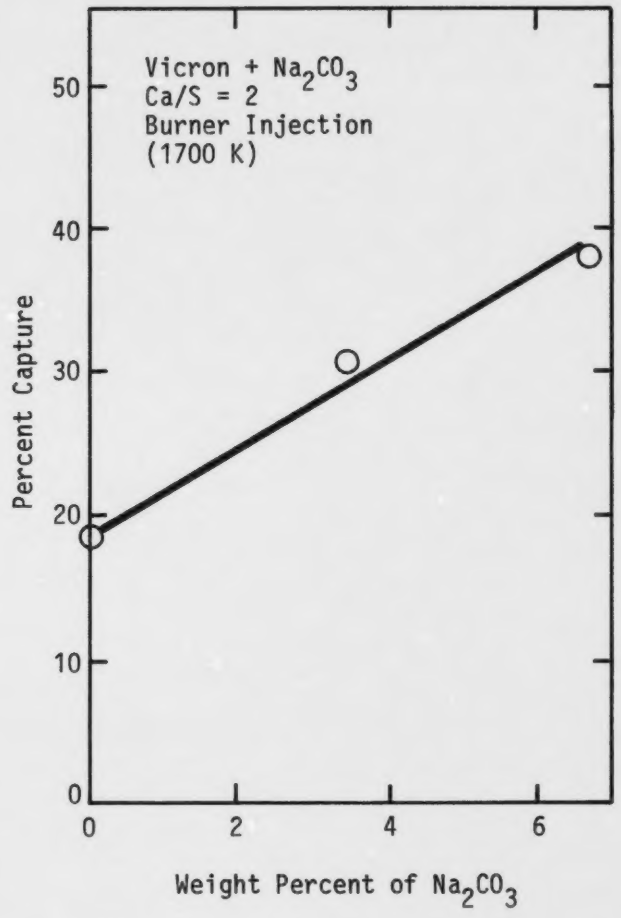

Figure 6-20. Influence of Na_2CO_3 (bulk) concentration on sulfur capture.

shown in Figure 6-21 indicate that, as the sodium concentration on the sorbent surface increased, there was a reduction in the observed particle size. A closer examination of micrograph No. 20001 (in Figure 6-21) suggests that the presence of sodium also produces more cracks on the particle surface. Measured B.E.T. surface area of sodium promoted sorbents (from this work and others (14)) showed a decrease in surface area relative to the unpromoted sorbent when injected under similar conditions. While this appears to contradict the increase in cracks observed on the surface of the promoted sorbent, it may only indicate a physical rearrangement of the solid phase. The presence of sodium in the CaO matrix is believed to induce chemical sintering which reduces the smaller pores that are responsible for the majority of the measured surface area. The large cracks produced and the observed increase in fragmentation are believed to be caused by differences in the local sintering rates of the sodium enriched CaO and the unpromoted CaO. These cracks are relatively large, increasing the accessibility of the interior CaO sites to SO_2. While it is true the additional large cracks (or pores) increase the overall surface area, this increase is not enough to counter the loss of surface from the reduction of the smaller pores. Thus the measured B.E.T. surface area decreases.

To identify the interaction of sodium with CaO, sodium coated CaO particles (calcined Vicron) were placed in the dynamic X-ray diffractometer under a simulated combustion gas at 1023 K. These results (Figure 6-22) show that the sodium promoted CaO increased both the overall rate of sulfation and ultimate sulfur capture. Micrographs of extracted sodium promoted solids compared to sulfated unpromoted particles are shown in Figure 6-23 (micrograph No. 10720 no sodium; micrographs No. 99918, 99916, and 99915, sodium present). The promoted CaO reacted with CaO which reduced the observed particle size and caused the formation of a liquid phase. EDS analysis indicates better sulfur capture coincides with the presence of the liquid phase.

In summary, the sodium compounds tested readily vaporize at combustion temperatures. The sodium appears to react with the CaO matrix to induce particle fragmentation and large cracks, thereby increasing the number of

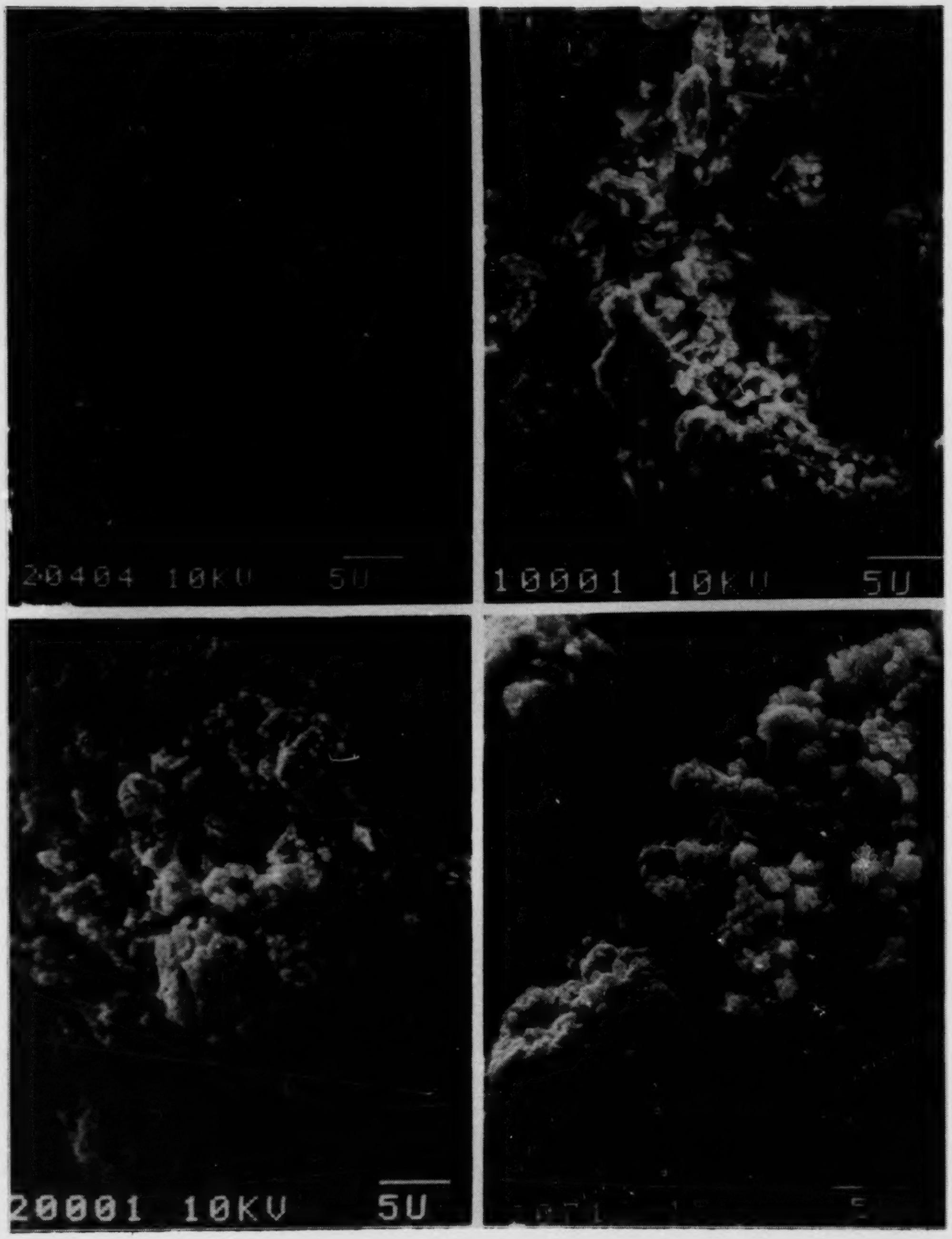
20404 10KV 5U
10001 10KV 5U
20001 10KV 5U

Figure 6-21. Influence of sodium (surface) concentration on surface morphology of a fired Vicron (Micrograph No. 20404--0% Na; No. 10001--6% Na; 20001--12% Na; and No. 20712--12% Na atomic).

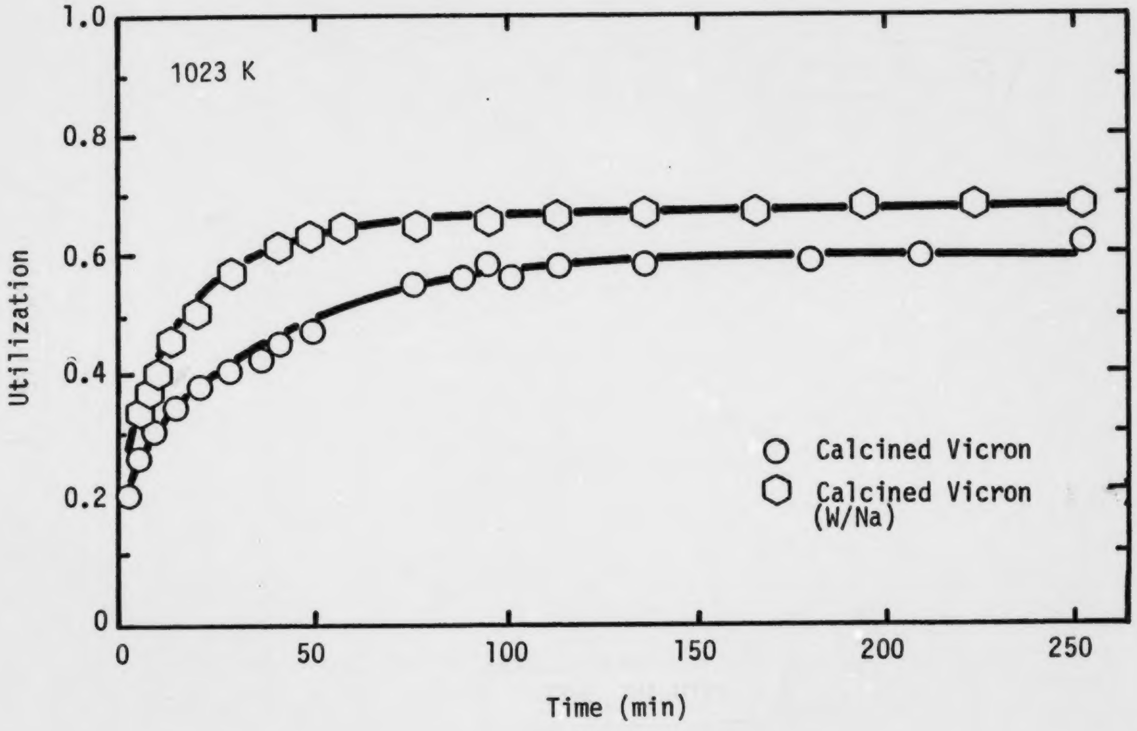

Figure 6-22. Influence of kinetic rate on sulfation and ultimate capture on a sodium promoted calcine.

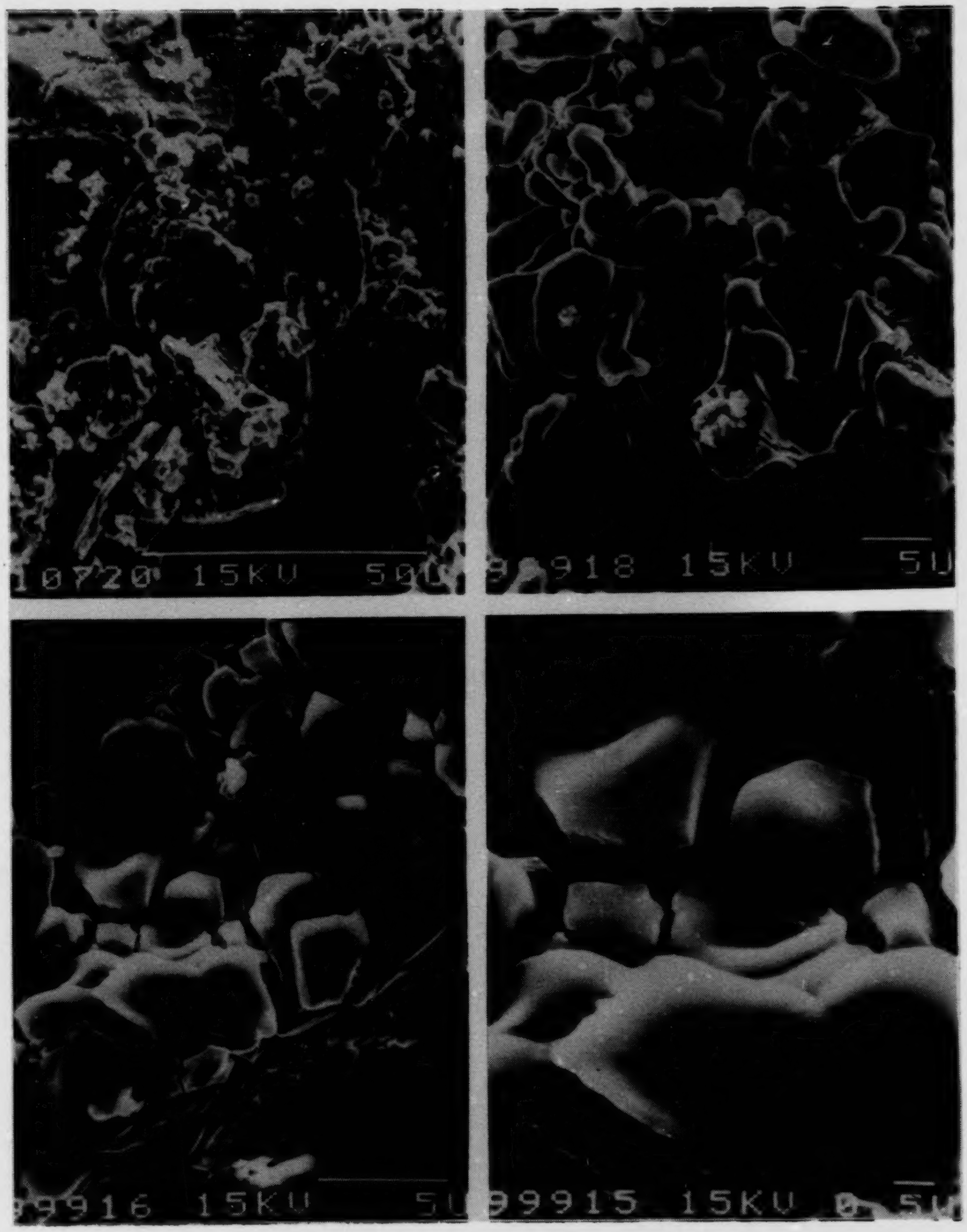
10720 15KV 50U
99918 15KV 5U
99916 15KV 5U
99915 15KV 5U

Figure 6-23. Morphology of sulfated sodium promoted calcine (Micrographs No. 10720--0% Na; No. 99916; 99918; and 99915--Ca/Na = 25 atomic ratio).

calcium sites that are readily available. The sodium impregnated calcium oxide produces a liquid mixture that is highly mobile and reactive at the conditions tested. In addition, the sodium compounds can react directly with the sulfur species; part of their enhancement potential is due to their ability to function as sorbents themselves.

6.2.3 Iron

The success of a transition metal (i.e., chromium) as an effective promoter, the need for an environmentally acceptable additive, and previous reports of promotion effects measured in fluidized beds (26) suggested the investigation of iron compounds. The BSF and the CTT were used to evaluate the influence of contacting method (i.e., premixed powders, vaporization, and iron in the water of hydration) injection location, and fuel composition (natural-gas and coal firing) on iron promotion. Figure 6-24 summarizes results of premixed powders of Fe_2O_3 and Vicron 45-3 for both burner and downstream injection, while Figure 6-25 illustrates results from a promoted pressure hydrate with $Fe(NO_3)_3$ added to the hydration water. Sulfur capture was not enhanced by the addition of iron to the calcium-based sorbents under any of the conditions tested.

The dynamic X-ray diffractometer was used to investigate the lack of reactivity of iron promoted (Fe_2O_3 evaporated) calcined Vicron. The iron, in intimate contact with the sorbent (a condition known to be a prerequisite for Na and Cr enhancement), was reacted isothermally at 1023 K under a simulated combustion gas (e.g., 2000 ppm SO_2). These results are provided in Figure 6-26. The results indicate that the performance of the iron additive produced significantly lower sulfur capture than the precalcined Vicron without iron. Investigation of the sulfated solids revealed that the physical morphology of the sorbent appeared unchanged compared to the precalcined Vicron. High resolution photographs of the sulfated iron impregnated precalcine are provided in Figure 6-27 (iron containing calcine in micrographs No. 33412, 33421, and 33413; sulfated calcine without iron, in No. 10700). The areas of relatively high iron concentrations produced signs of early spalling much like the morphology seen with sodium and chromium promotion.

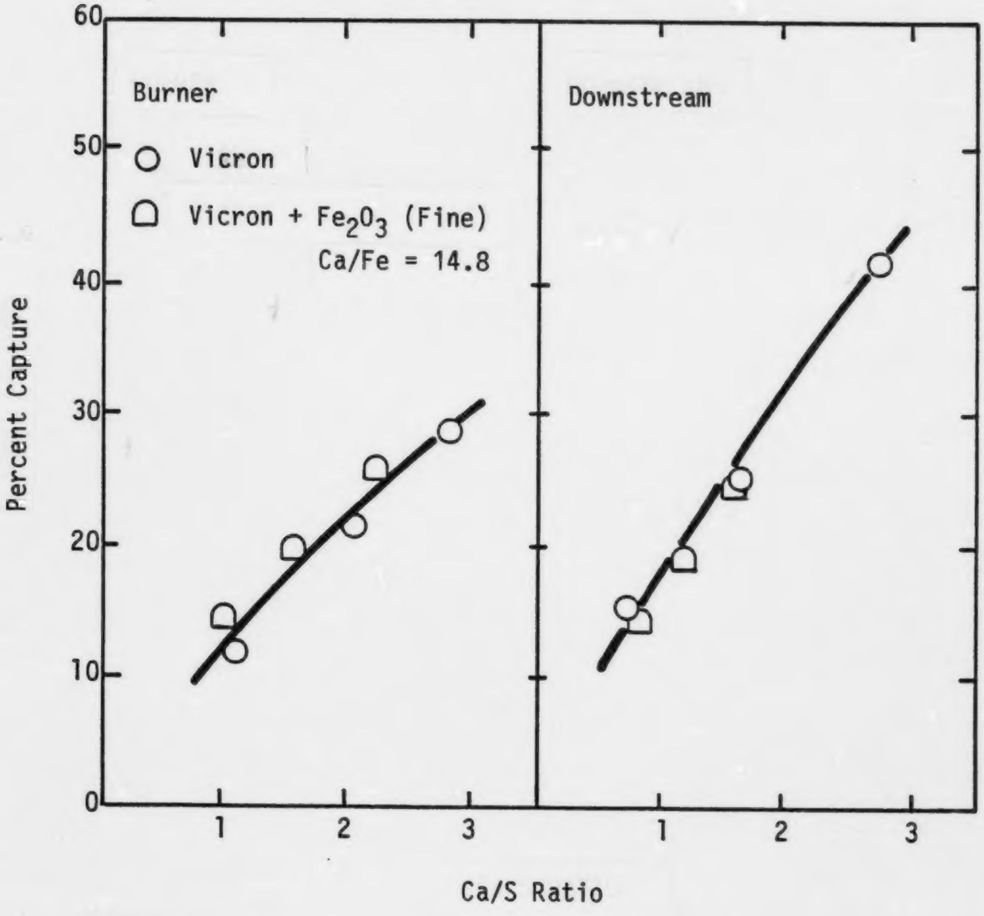

Figure 6-24. Sulfur capture between fired Vicron with and without Fe_2O_3 present at two different temperatures.

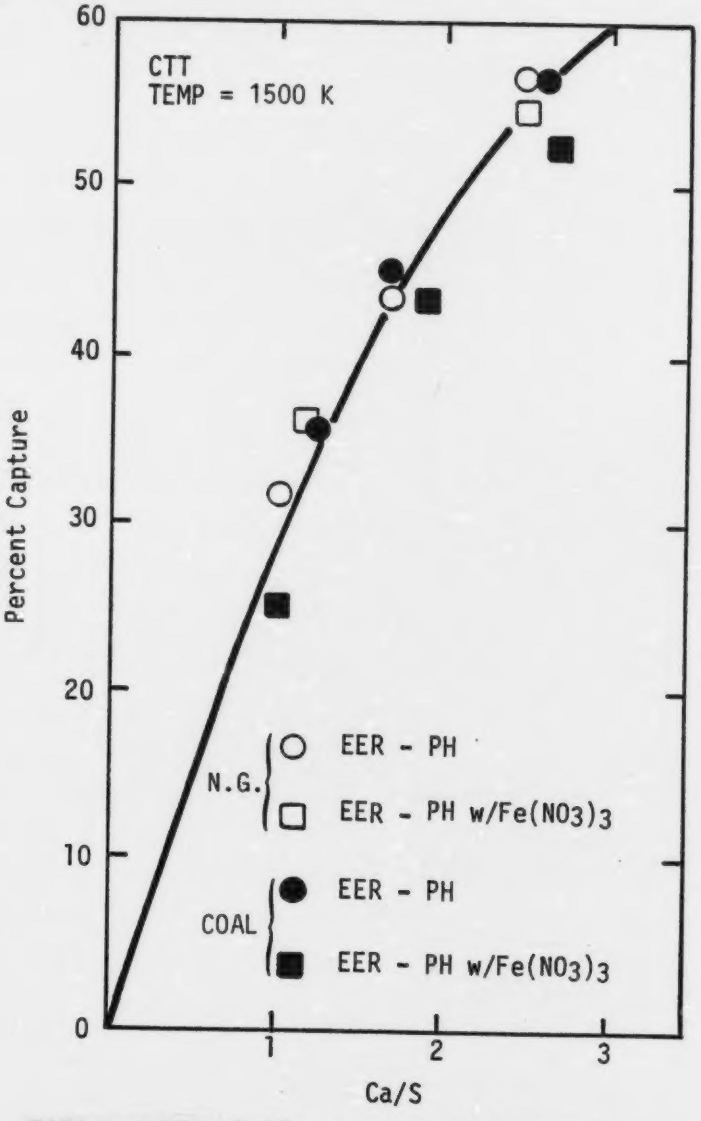

Figure 6-25. Sulfur capture between pressure hydrate with and without Fe present for two fuels.

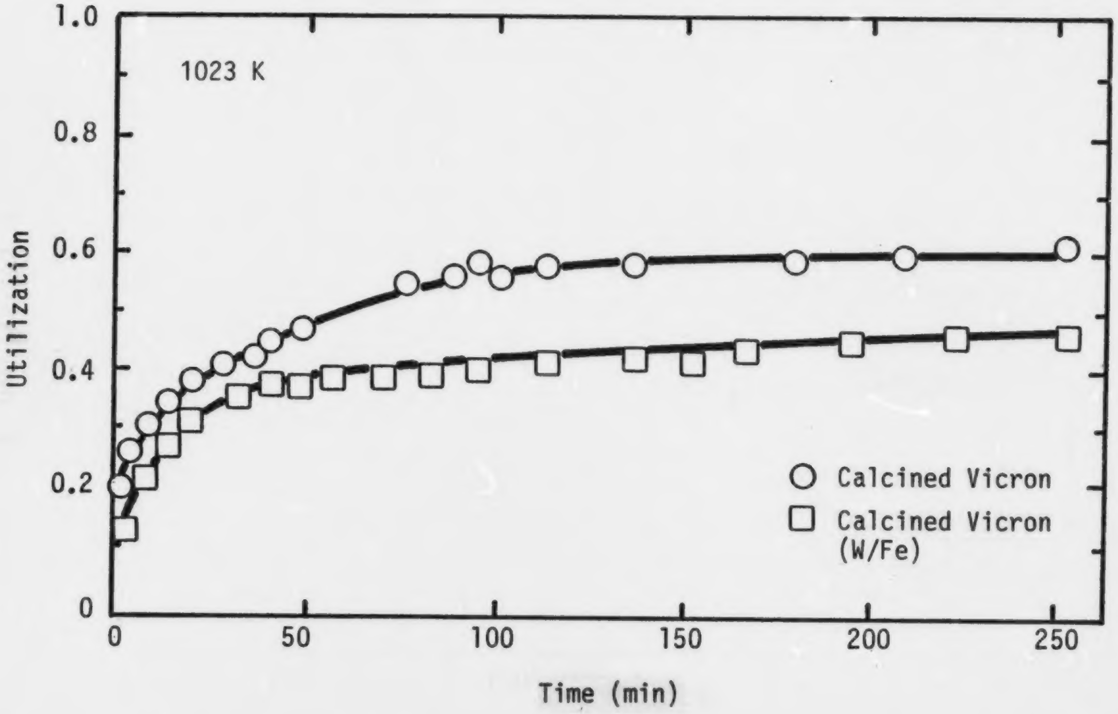

Figure 6-26. Influence of kinetic rate and ultimate sulfur capture with an iron promoted calcine.

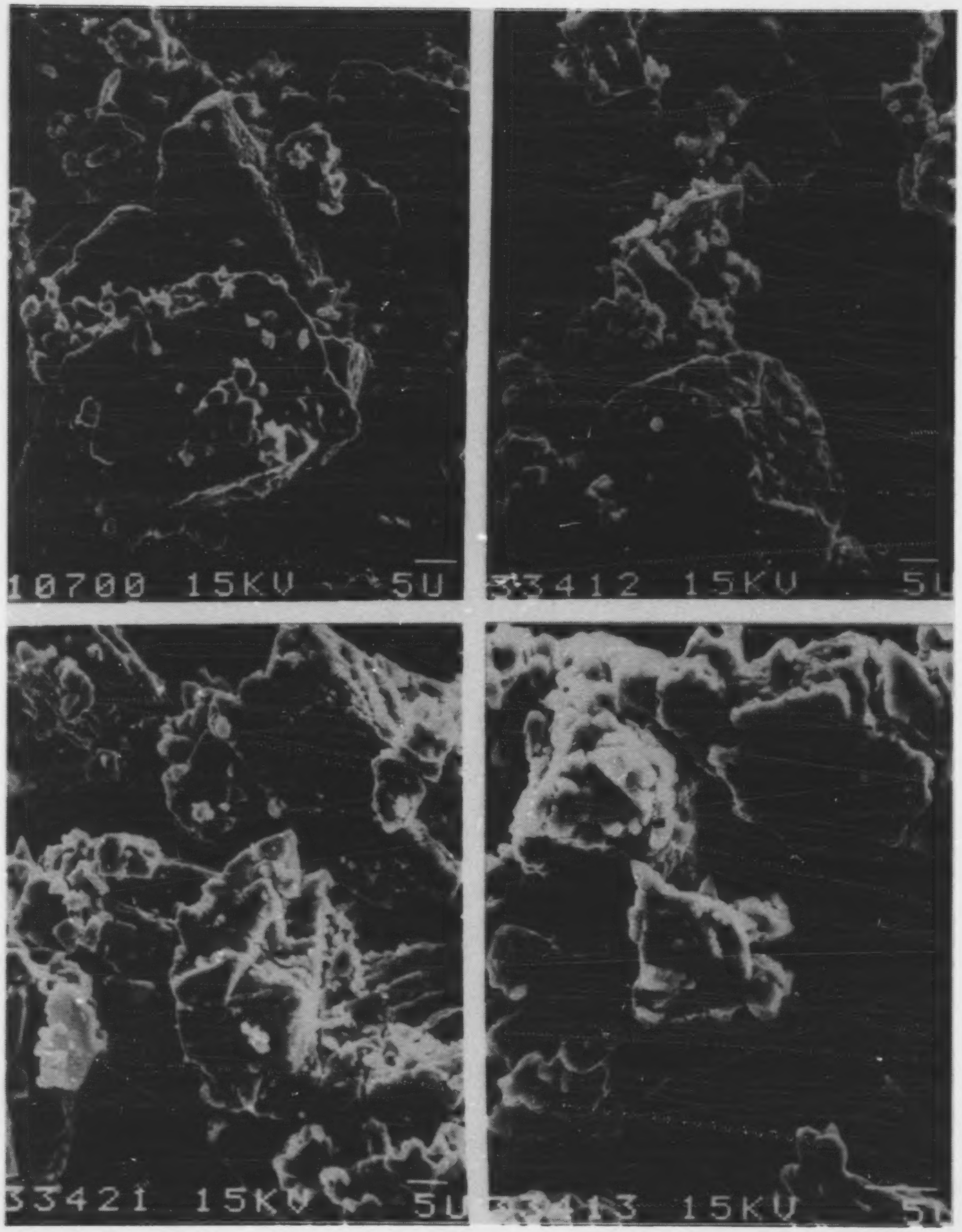
10700 15KV 5U
33412 15KV 5U
33421 15KV 5U
33413 15KV 5U

Figure 6-27. Morphology of sulfated iron promoted calcine (Micrographs No. 10700--0% Fe; No. 33412, 33421, and 33413--Ca/Fe = 16 atomic ratio).

However, no liquid phase was detected during the detail examination of the sulfated sample containing iron. The EDS analysis of the sample pictured in micrograph No. 33413 is illustrated Figure 6-28 which shows an intensity map for the relative sulfur content (left) with the associated distribution maps for the elements: sulfur, calcium, and iron (right). The relative concentration of sulfur was lower with the presence of iron. It is believed that the iron did not penetrate into the CaO matrix as effectively as sodium and chromium, and, therefore, physically blocked potential CaO sites instead of generating new and more reactive surfaces for sulfur capture. (Diffraction results from the calcine indicated no iron/calcium compounds were formed.)

In summary, iron does not promote calcium-based sorbents under the conditions typically found in combustion boilers. Detail studies of the Fe promoted solids did not reveal the significant changes in particle morphology recorded previously for sodium and chromium promotion.

6.3 Conclusions

Chromium series transition elements and alkali metals effectively increase the ability of calcium based sorbents to capture SO_2. The primary enhancement mechanism is not chemical catalysis of the SO_2 to SO_3 reaction step; rather, these materials react chemically with the CaO to produce local, physical changes in the sorbent which enhance sulfur capture. In particular the promoters induce particle fragmentation, the creation of large cracks and grain growth (pore enlargement), all of which serve to increase the accessibility of the interior Ca and to decrease the rate of site loss by pore mouth plugging. In addition the promoters often produce low melting eutectics with CaO and the liquid phase probably enhances transport of the sulfur to unreacted CaO.

The alkali metals also react directly with SO_2 to produce sulfate products, therefore, part (but not all) of their enhancement is due to their ability to function as sorbents themselves. The chromium compounds do not exhibit this behavior.

COLOR PHOTOS AVAILABLE FOR
INSPECTION ONLY AT EPA/AEERL

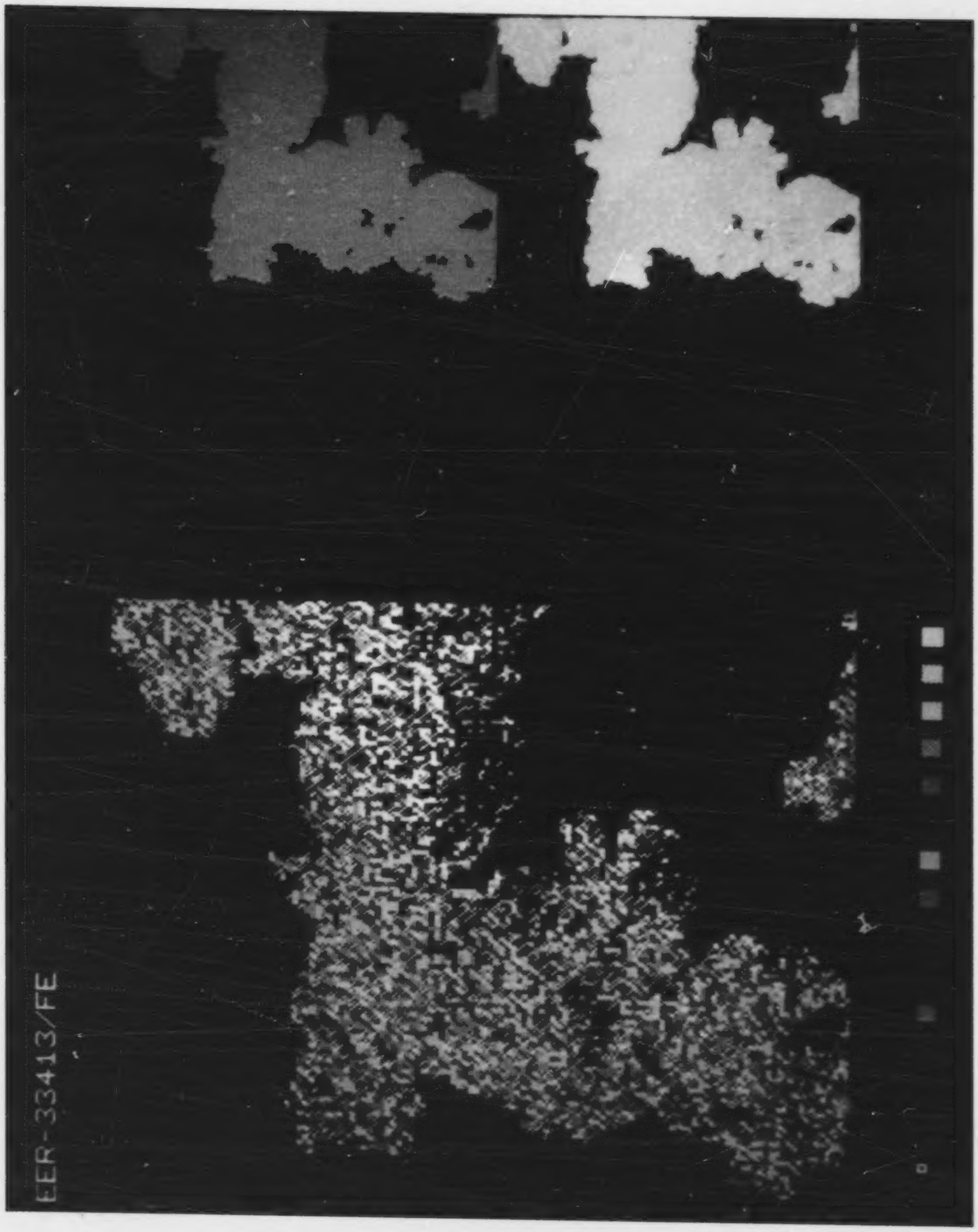

Figure 6-28. EDS analysis of sulfated iron promoted calcine (shown in Figure 6-27, No. 33413); sulfur intensity map (left).

Iron does not promote calcium-based sorbents under typical high temperature injection conditions. Detailed analysis of iron promoted solids indicated no physical changes in particle morphology occur with iron promotion.

7.0 PROMOTER/COAL ASH

The third program objective was to define the mechanisms which are important in the promoter/mineral ash interaction. From the results presented in Section 5, the presence of mineral ash did not significantly change the sulfur capture by the calcium-based sorbents. This chapter examines the impact of the mineral ash on promoted sorbents.

7.1 Promoter/Ash Interaction

The testing in this portion of the program was focused on two additives which represented the two primary promoted classes, namely sodium bicarbonate and Cr_2O_3. The capture levels achieved with each of the additives are shown in Figure 7-1 for two sorbents and two injection locations. These capture levels were obtained with natural gas or coal firing at a Ca/S ratio of 2.0. The solid bars represent the baseline sorbent capture (without additive in either gas or coal firing) and the open bars indicate additional capture with the additives in a natural gas system. Enhancement with $NaHCO_3$ was relatively constant at 15 to 20 percent for both sorbents and injection locations, while with Cr_2O_3, the enhancement varied from 12 percent with Vicron injection downstream to about 37 percent with Longview injection at the burner. Figure 7-1 also provides a direct comparison of the enhanced capture levels for Indiana coal. The most striking feature of this plot is the incremental decrease in capture for coal with the sodium runs; the Cr_2O_3 results are varied. In general, the coal capture was only slightly lower than the gas capture for Cr_2O_3 except for Longview at the burner where a significant decrease in capture occurred. Unfortunately, the presence of the coal ash greatly reduced the enhancement by the $NaHCO_3$ at all conditions. The remaining portions of this section examine the mechanisms associated with these effects. Sodium promotion is considered because its promotion effect was the most severely retarded by the mineral matter.

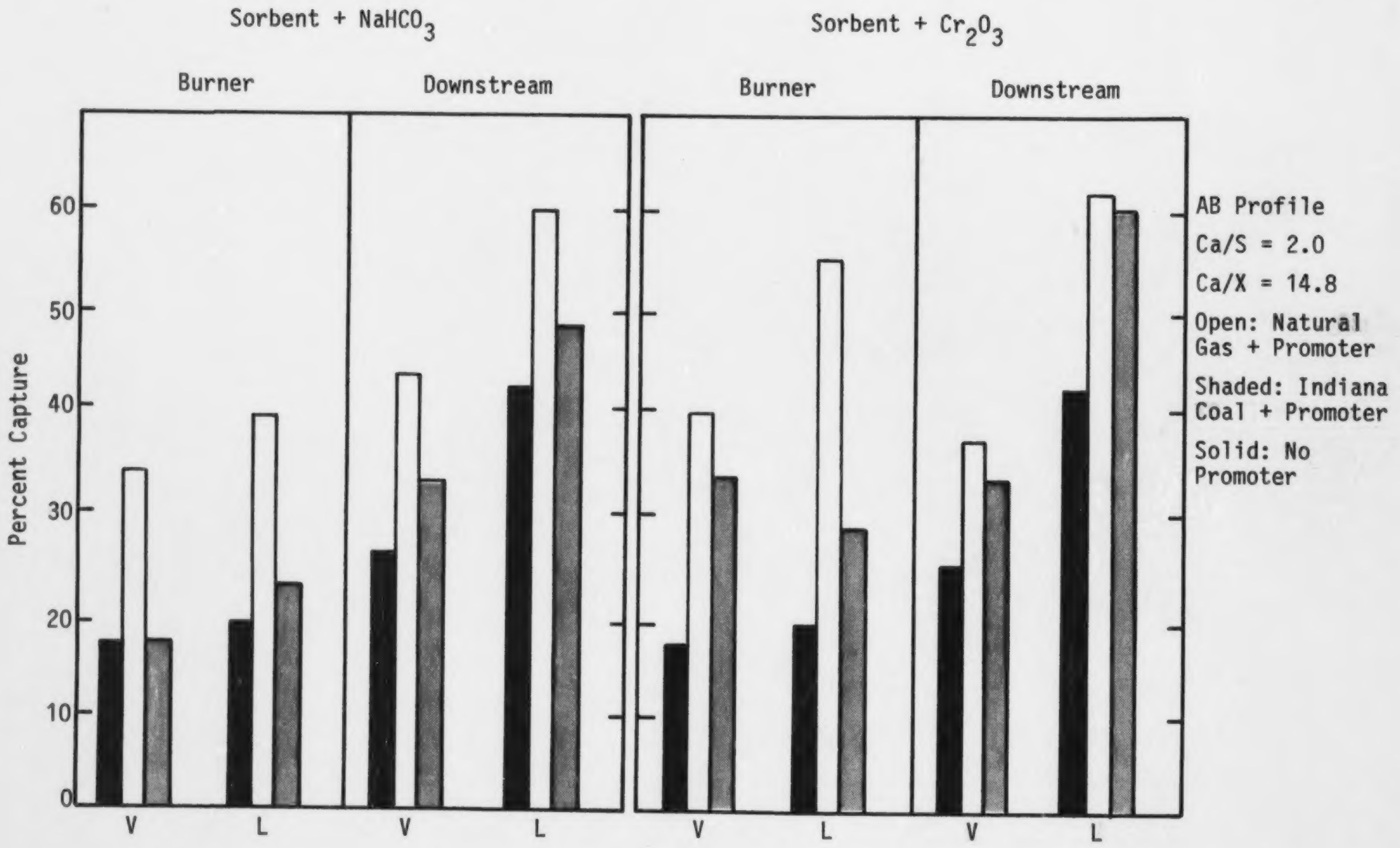

Figure 7-1. Enhancement comparison between coal and gas.

7.1.1 Sodium/Ash Interaction

In order to determine whether the reduction in enhancement for the sodium additives was specific to Indiana coal, two other coals were tested with Vicron and $NaHCO_3$. Figure 7-2 shows that for injection at the burner, a substantial decrease in capture occurred for the Kentucky and Illinois coals as well although the extent of the decrease was dependent on the coal composition. Thus, the coal mineral matter/promoter interaction seems to apply to different fuel types. The results of experiments designed to decouple the sorbent/additive/ash system effects are shown in Figure 7-3. In the left hand plot, the Vicron plus $NaHCO_3$ data for natural gas and Indiana coal are presented as a function of the Ca/S ratio. The open squares represent a coal simulation in which the fuel was natural gas and the sorbent and ash were fed through two different feeders. The circles represent a normal natural gas case (without ash). The addition of coal ash dramatically reduces the effectiveness of the $NaHCO_3$ promotion and hence overall capture (to the level of the actual Indiana #3 coal data). These results suggest that introduction of ash provides additional reactive sites and surface for condensation of sodium which reduces sodium that can react with calcium. The middle plot again shows that the ash does not have a great effect on the ability of Vicron itself (without a promoter) to capture when the two materials are injected separately. The right hand plot in Figure 7-3 shows the results of tests where $NaHCO_3$ was injected as a sorbent alone (no ash) at the burner and again separately with fly ash and SiO_2. Clearly, the sodium bicarbonate was very effective as a sorbent when injected into the gas flame; but when either fly ash or SiO_2 was introduced, the capture was dramatically reduced. The mass flowrates of the ash and SiO_2 were maintained at the same rate of ash input as from the Indiana No. 3 coal. Overall, the data shown in Figure 7-3 show that the interaction is most pronounced between the $NaHCO_3$ and the ash.

Figure 7-4 shows the results of the actual coal runs where $NaHCO_3$ was injected at the burner and downstream. For burner injection, the coal capture dropped off to very low levels just as was the case in the simulation

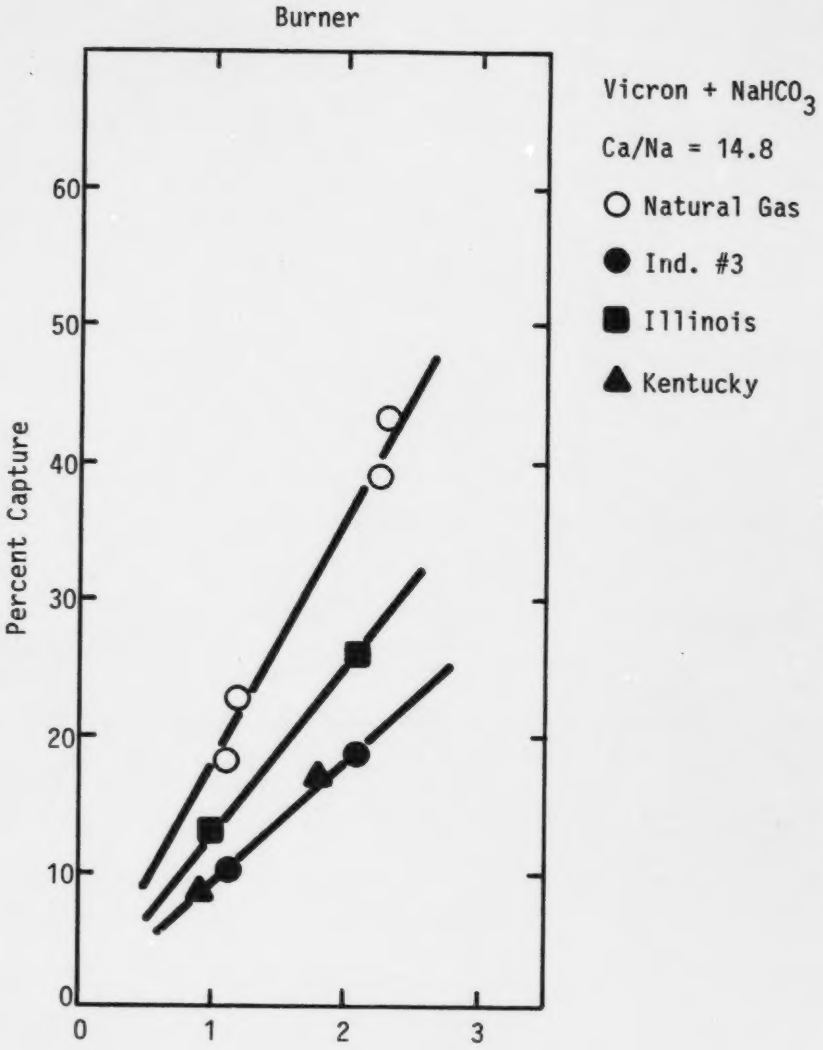

Figure 7-2. The effect of coal mineral matter on NaHCO$_3$ enhancement.

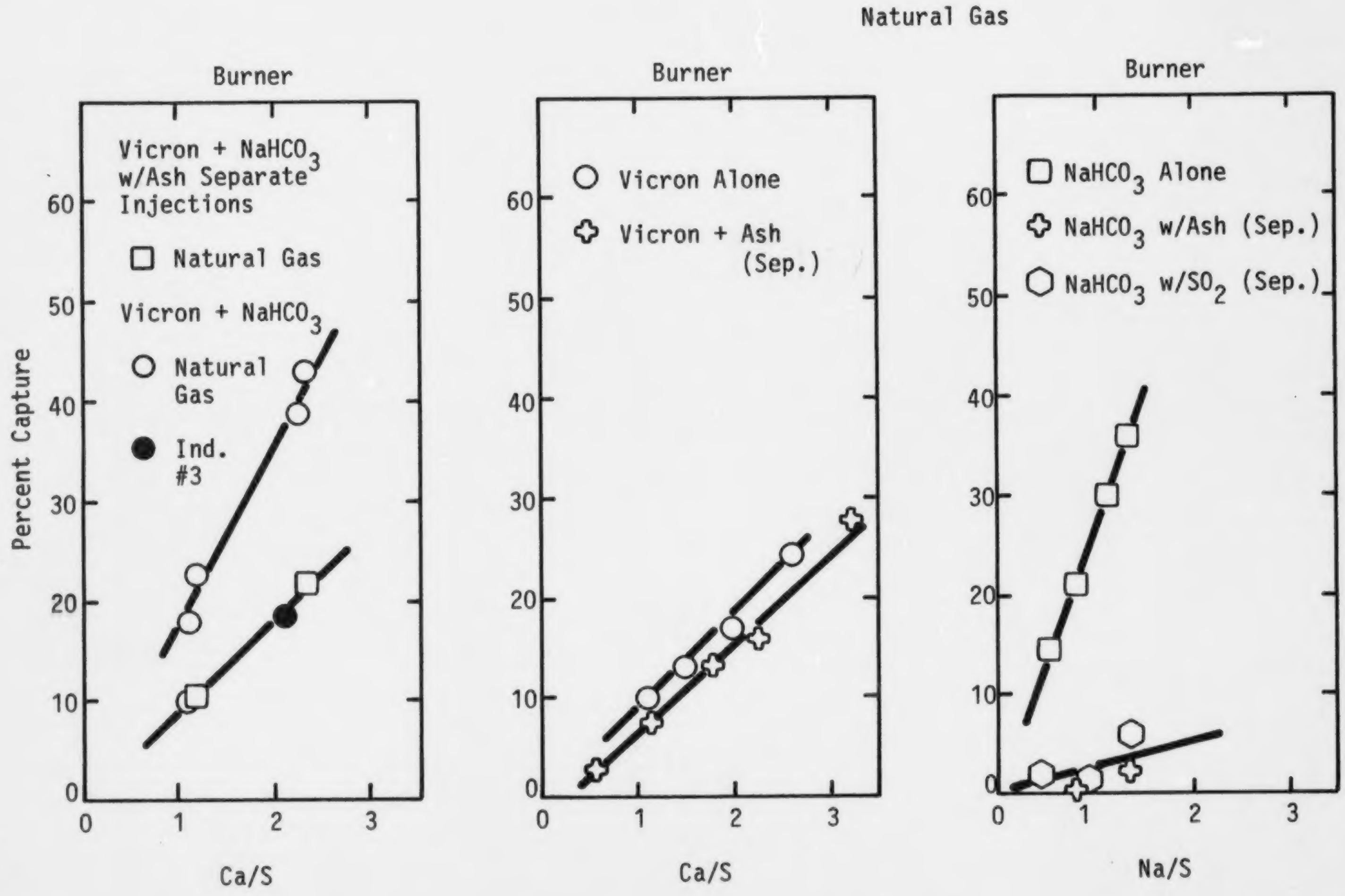

Figure 7-3. The effect of coal ash on $NaHCO_3$.

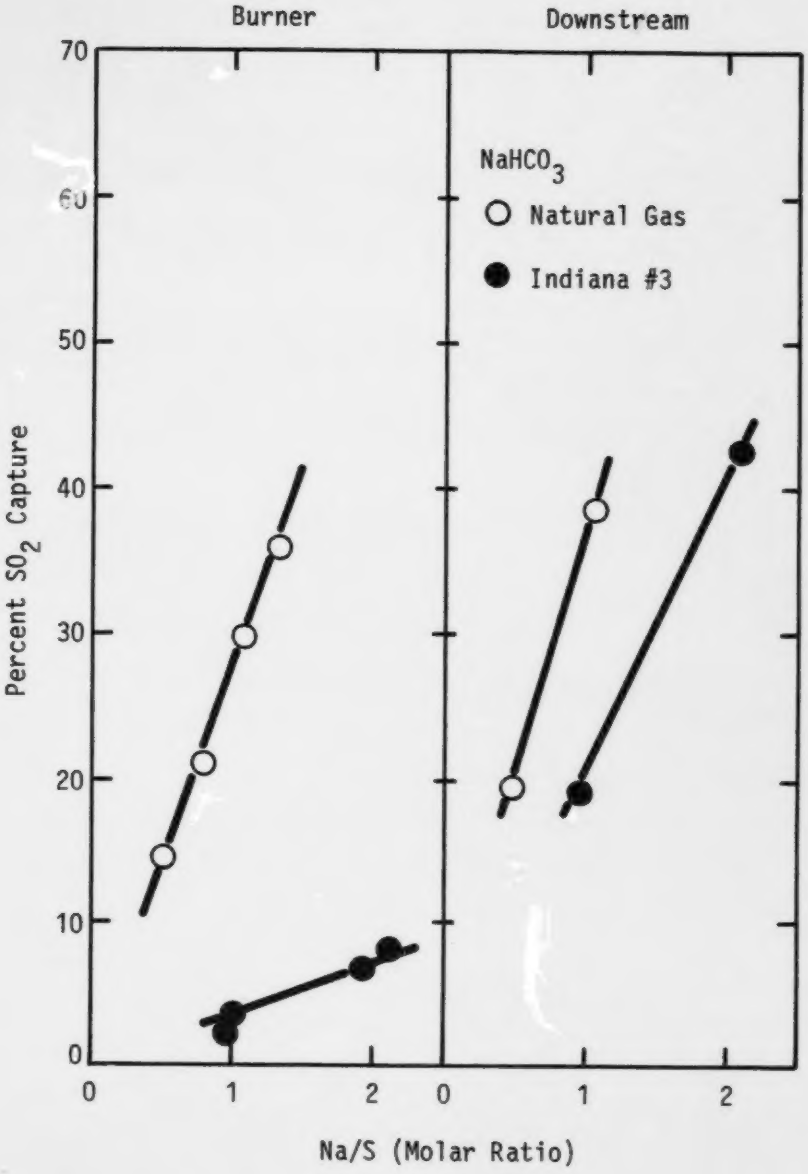

Figure 7-4. NaHCO$_3$ capture with coal and gas.

experiment (Figure 7-3c). For downstream injection, sulfur reduction by the sorbent with coal was only half the capture level with natural gas. The data in Figure 7-4 and selected X-ray diffraction analysis on extracted solids support a chemical reaction mechanism with sodium and ash. (Based on thermochemical calculations shown in Figure 6-17, vaporization of sodium should be complete.)

The extracted solids containing the sorbent, ash, and sodium were examined by SEM, EDS, and X-ray diffraction. A high resolution photograph is presented in Figure 7-5 with its corresponding elemental spectrum and distribution maps shown in Figure 7-6 and Figure 7-7, respectively. In addition, intensity maps of a number of elements (with associated distribution maps) are provided in Figures 7-8 through 7-11. (Intensity maps are located to the left above a color bar; red, lowest number of counts to white, highest number of counts. Distribution maps are associated with the element with the same color; element labels are located below the maps at the right.)

The elements present in the sample are labeled in the spectrograph (Figure 7-6). Based on the EDS analysis, the calculated calcium utilization is 12 percent corresponding to the capture efficiency of the unpromoted sorbent. Inspection of the relative elemental concentration of the particles pictured in Figure 7-8 indicates clearly that the sodium is uniformly distributed over the ash and sorbent suggesting relatively uniform condensation of the sodium as expected. X-ray diffraction results indicate that sodium silicates are present in the extracted solids. Calcium (Figure 7-9) is associated with sulfur (Figure 7-10) only if it is not found with the ash (i.e., silicon, Figure 7-11). This is consistent with X-ray diffraction results which show that if the calcium reacts with the ash to form calcium silicates the calcium is not available to react with sulfur. The same is true for sodium; the sodium which condenses on the ash reacts with it and is not available for subsequent sulfation.

Initial attempts to correlate the data on the basis of SO_2 baseline or percent ash in the coal proved fruitless. One parameter that was tried was ash to additive mass ratio entering the furnace. This parameter takes into

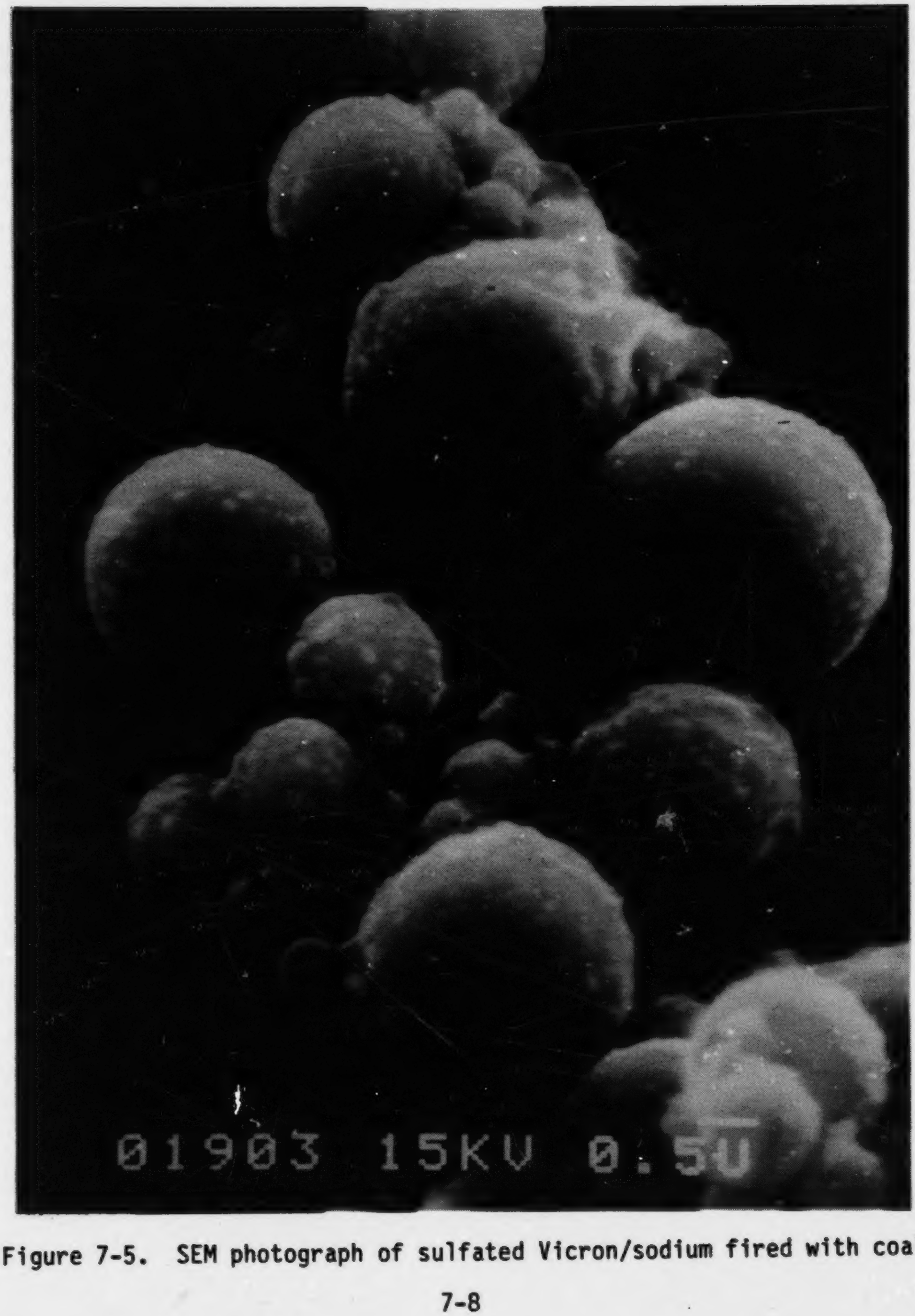
01903 15KV 0.5U

Figure 7-5. SEM photograph of sulfated Vicron/sodium fired with coal.

COLOR PHOTOS AVAILABLE FOR
INSPECTION ONLY AT EPA/AEERL

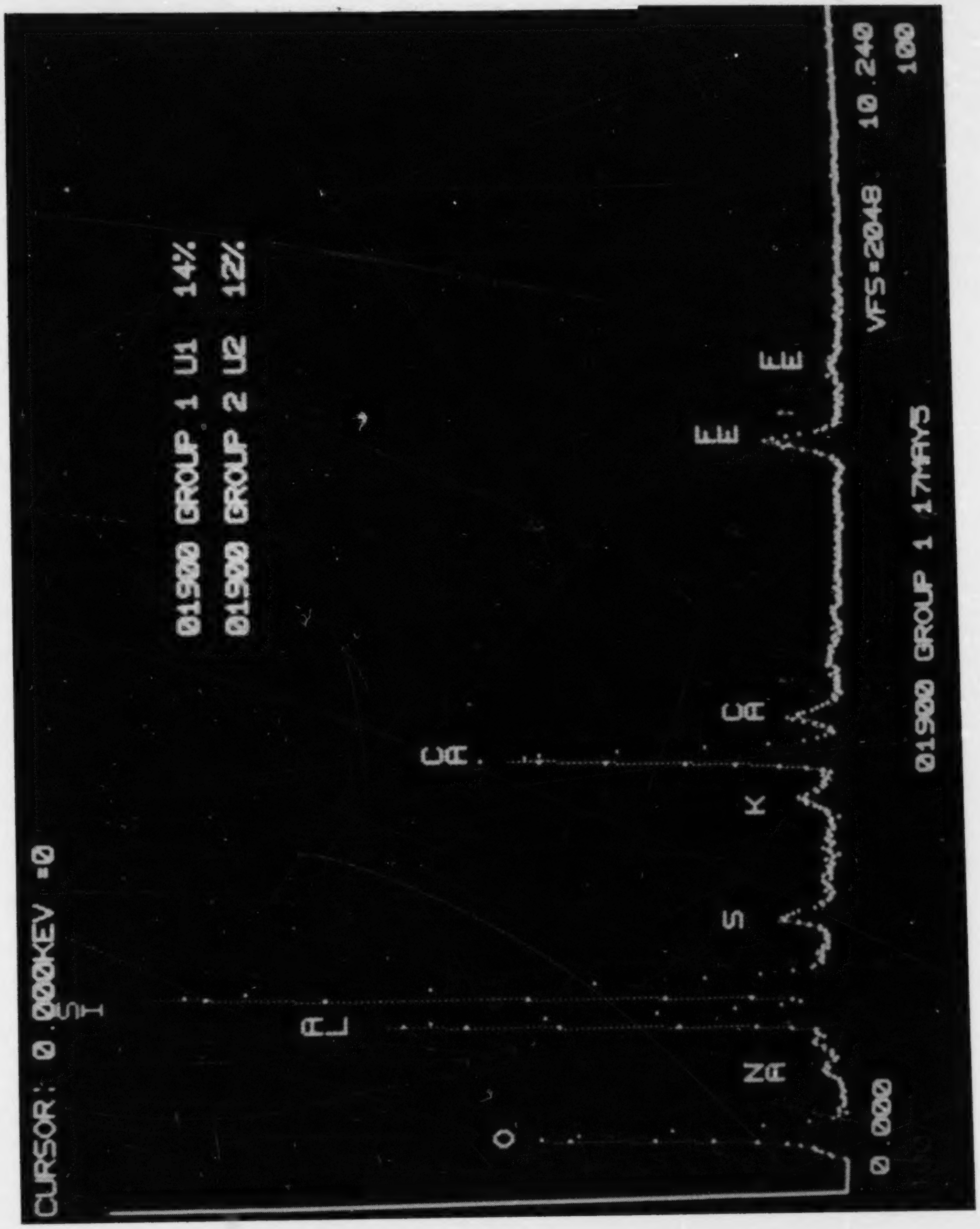

Figure 7-6. Spectrograph from EDS analysis of NA promoted Vicron fired with coal (see Figure 7-5).

COLOR PHOTOS AVAILABLE FOR
INSPECTION ONLY AT EPA/AEERL

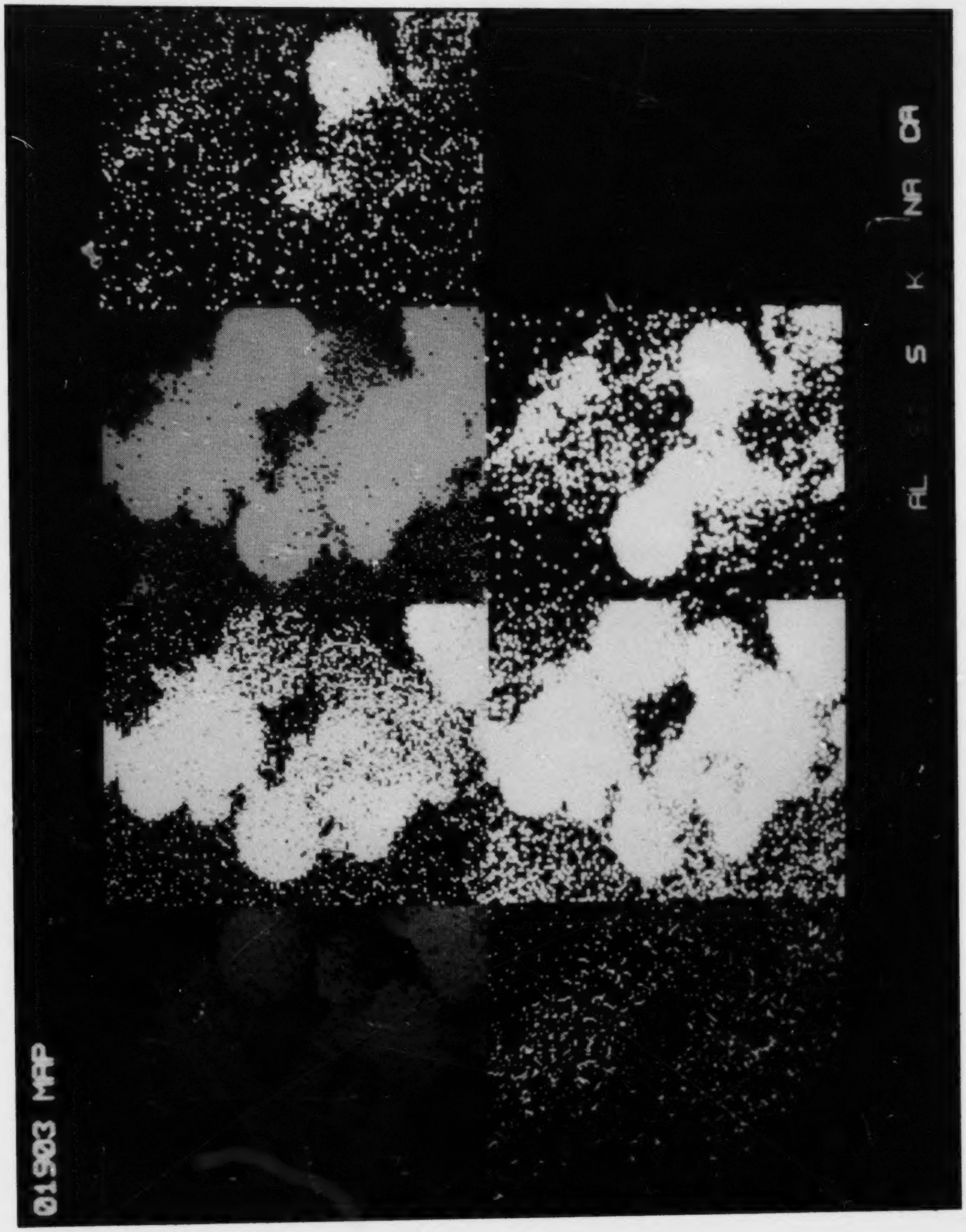
AL
SI
S
K
NA
CA
01903 MAP

Figure 7-7. Elemental distribution maps from EDS analysis of Na promoted Vicron fired with coal (see Figure 7-5).

COLOR PHOTOS AVAILABLE FOR
INSPECTION ONLY AT EPA/AEERL

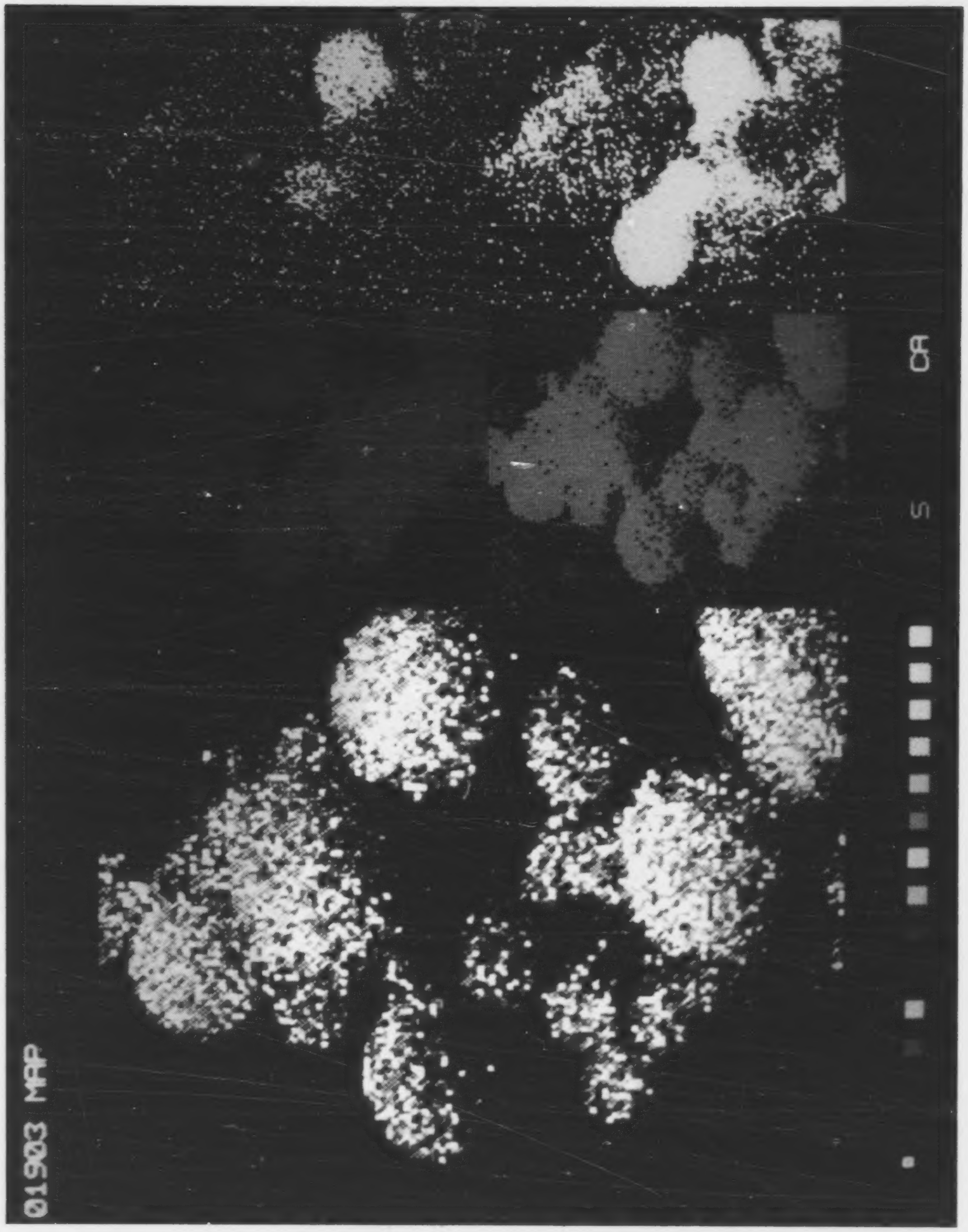

Figure 7-8. Sodium intensity map (left0 from EDS analysis of Na promoted Vicron fired with coal (see Figure 7-5).

COLOR PHOTOS AVAILABLE FOR
INSPECTION ONLY AT EPA/AEERL

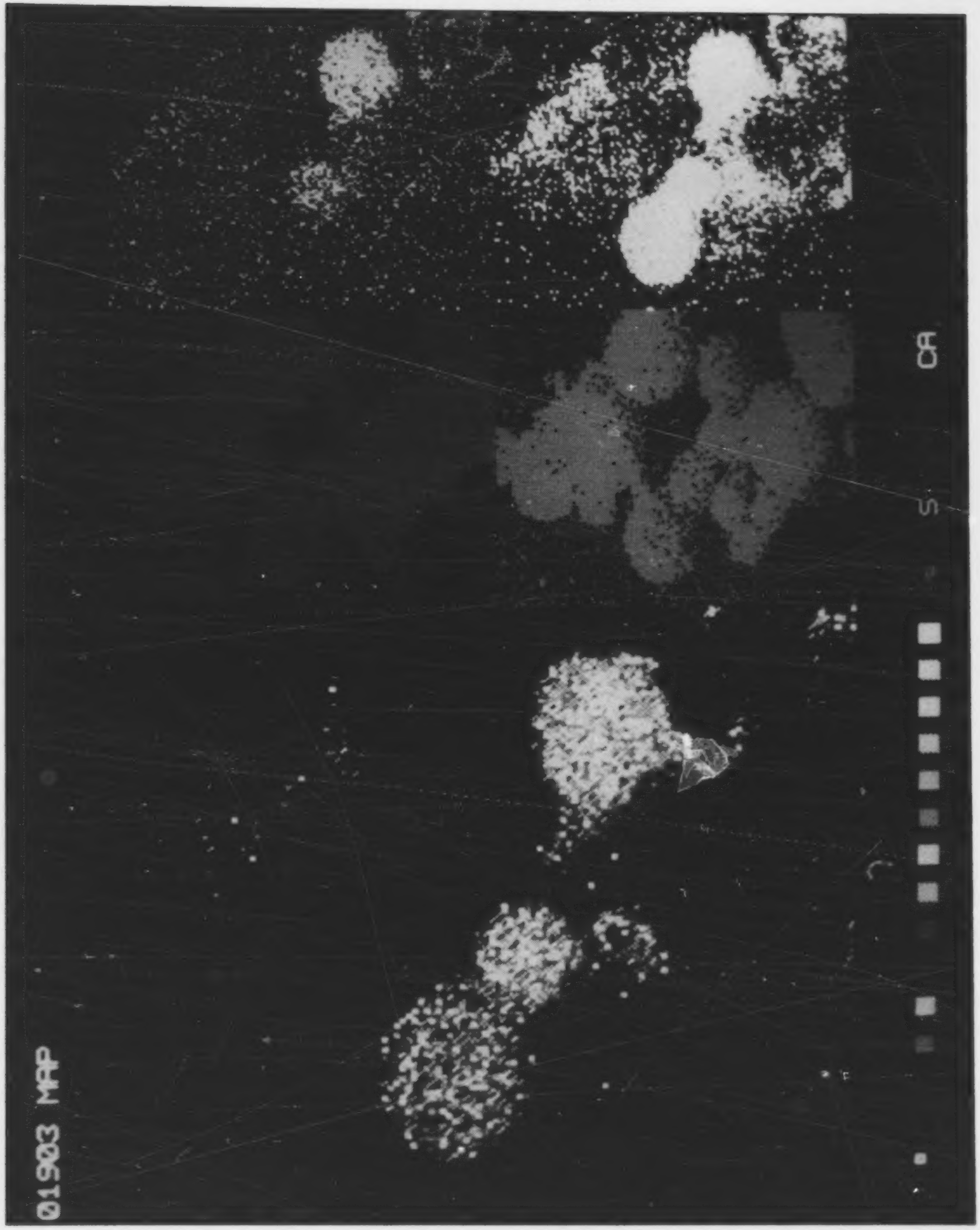

Figure 7-9. Calcium intensity map (left) from EDS analysis of Na promoted Vicron fired with coal (see Figure 7-5).

COLOR PHOTOS AVAILABLE FOR
INSPECTION ONLY AT EPA/AEERL

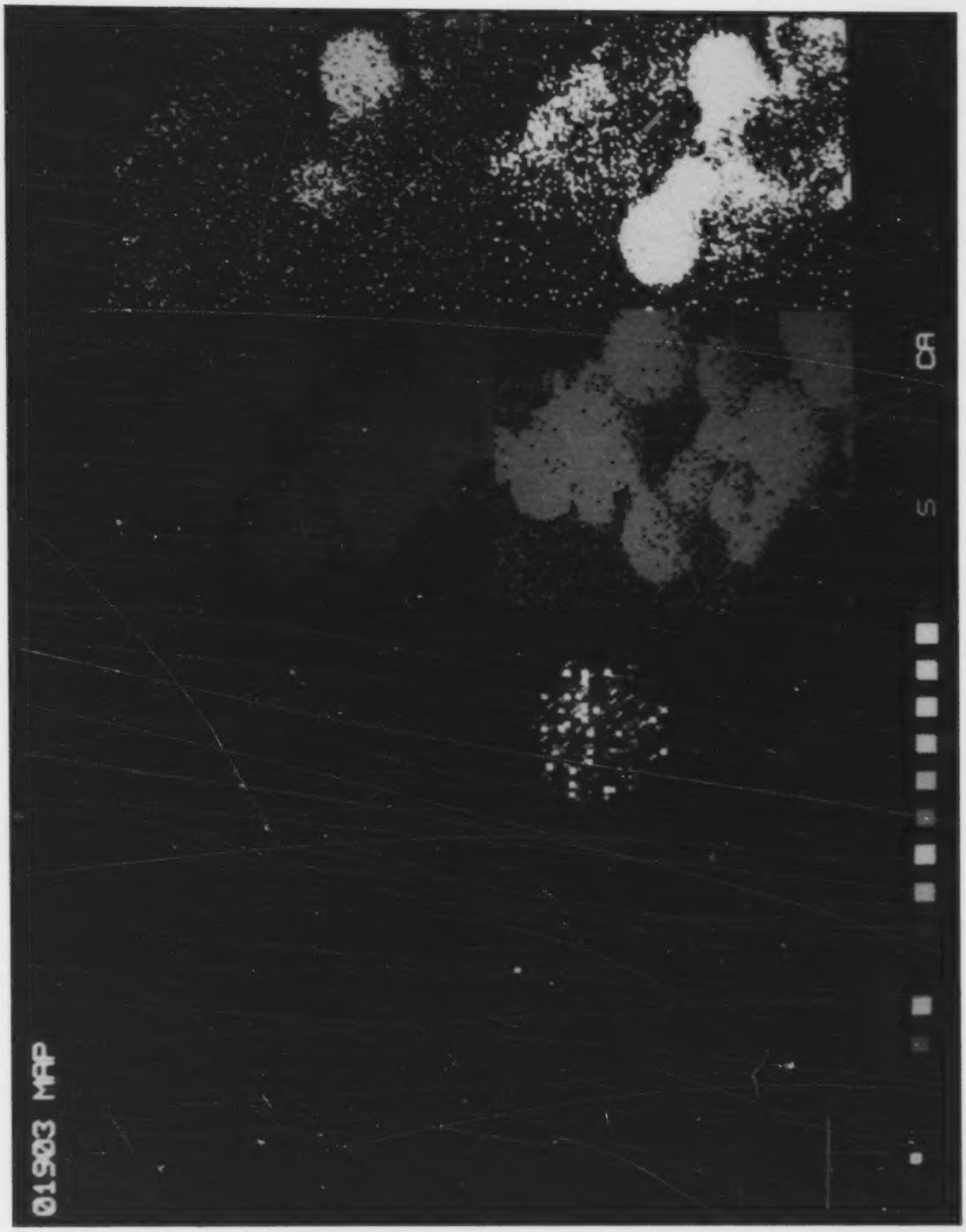

Figure 7-10. Sulfur intensity map (left) from EDS analysis of Na promoted Vicron fired with coal (see Figure 7-5).

COLOR PHOTOS AVAILABLE FOR
INSPECTION ONLY AT EPA/AEERL

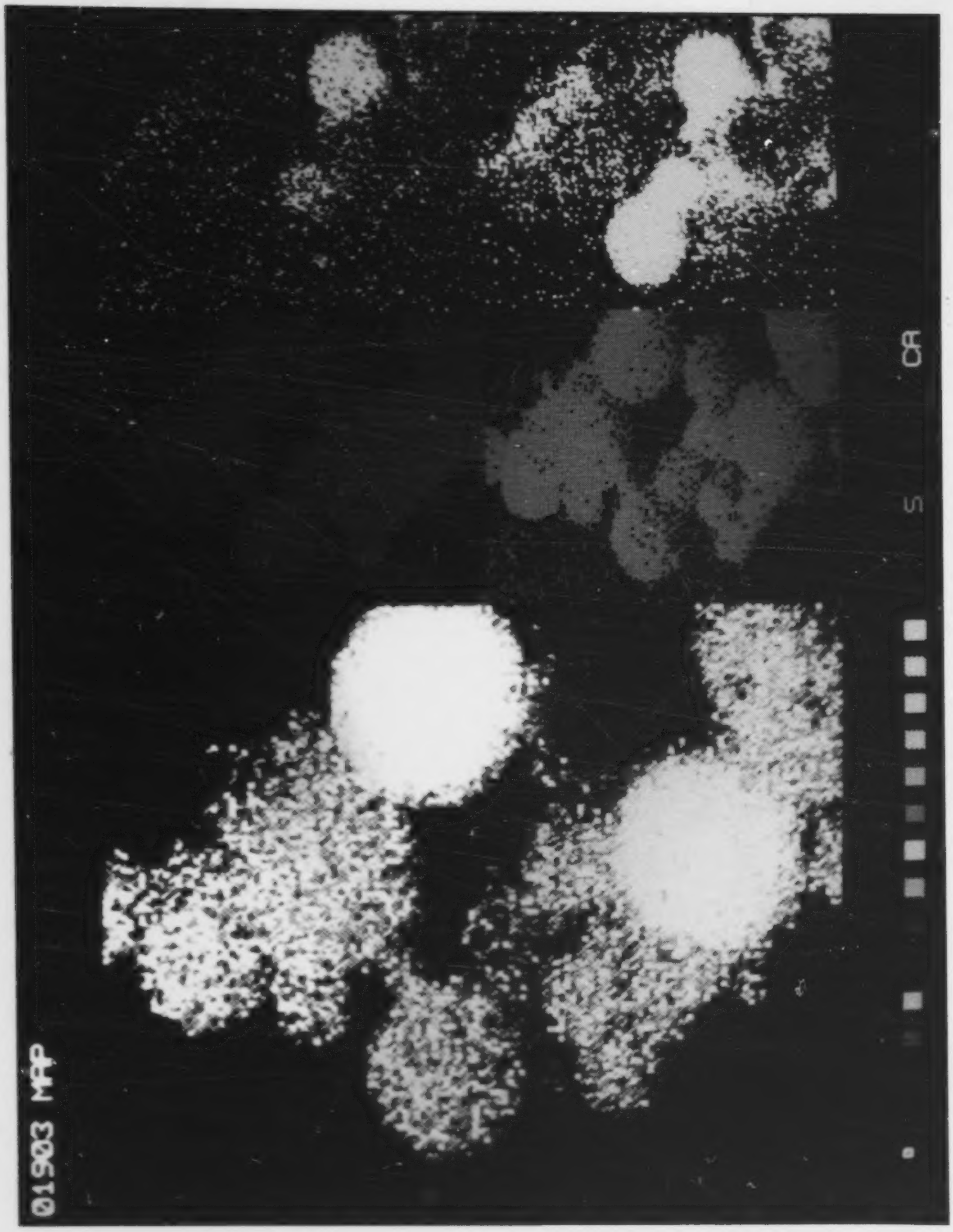

Figure 7-11. Silicon intensity map (left0 from EDS analysis of Na promoted Vicron fired with coal (see Figure 7-5).

account the relative concentration of both species and is also indirectly tied to the sulfur level in the coal since Ca/additive ratio was constant and Ca/S ratio determines the sorbent feed rate. Figure 7-12a illustrates the capture data for all of the fuels correlated with respect to ash/$NaHCO_3$ mass ratio for both injection locations. For sodium, the percent capture decreased correspondingly with increasing ash/$NaHCO_3$ ratio and the curves appear to reach an asymptote at higher ratios. The ash reduced sodium availability by direct chemical reaction with the silicates and by providing sites for condensation of the sodium species.

7.1.2 Chromium/Ash Interaction

The effect of coal mineral matter on Cr_2O_3 enhancement is shown in Figure 7-13 for burner injection with Vicron and Longview. The sorbents were tested with natural gas and four coals. The sulfur capture with both sorbents, was better in the natural gas (ash free) environment. In the gas experiments, 55 percent capture was obtained with burner injection of the promoted Longview sorbent and 40 percent was obtained with promoted Vicron. The extent of the coal ash influence was somewhat dependent on the specific coal and sorbent although the promoter was consistently more effective with the Illinois coal than with the Kentucky coal.

A coal simulation experiment (similar to the $NaHCO_3$ experiments) was performed by separately injecting Vicron plus Cr_2O_3 and fly ash during natural gas combustion. The purpose of the experiment was to determine if ash alone could account for the reduction in capture enhancement that was observed between gas and coal. Figure 7-14 shows the natural gas and Indiana coal lines for promoted Vicron injected at the burner. When fly ash was injected separately, the reduction was even a little lower than the coal line as indicted by the cross symbols. These data confirm that mineral matter can reduce the effectiveness of Cr_2O_3 as a promoter of sulfur capture although the effect is not as dramatic as with $NaHCO_3$ (Figure 7-3a).

In view of the results in Figure 7-14, it was decided to test the effectiveness of Cr_2O_3 on several raw coals and their respective cleaned

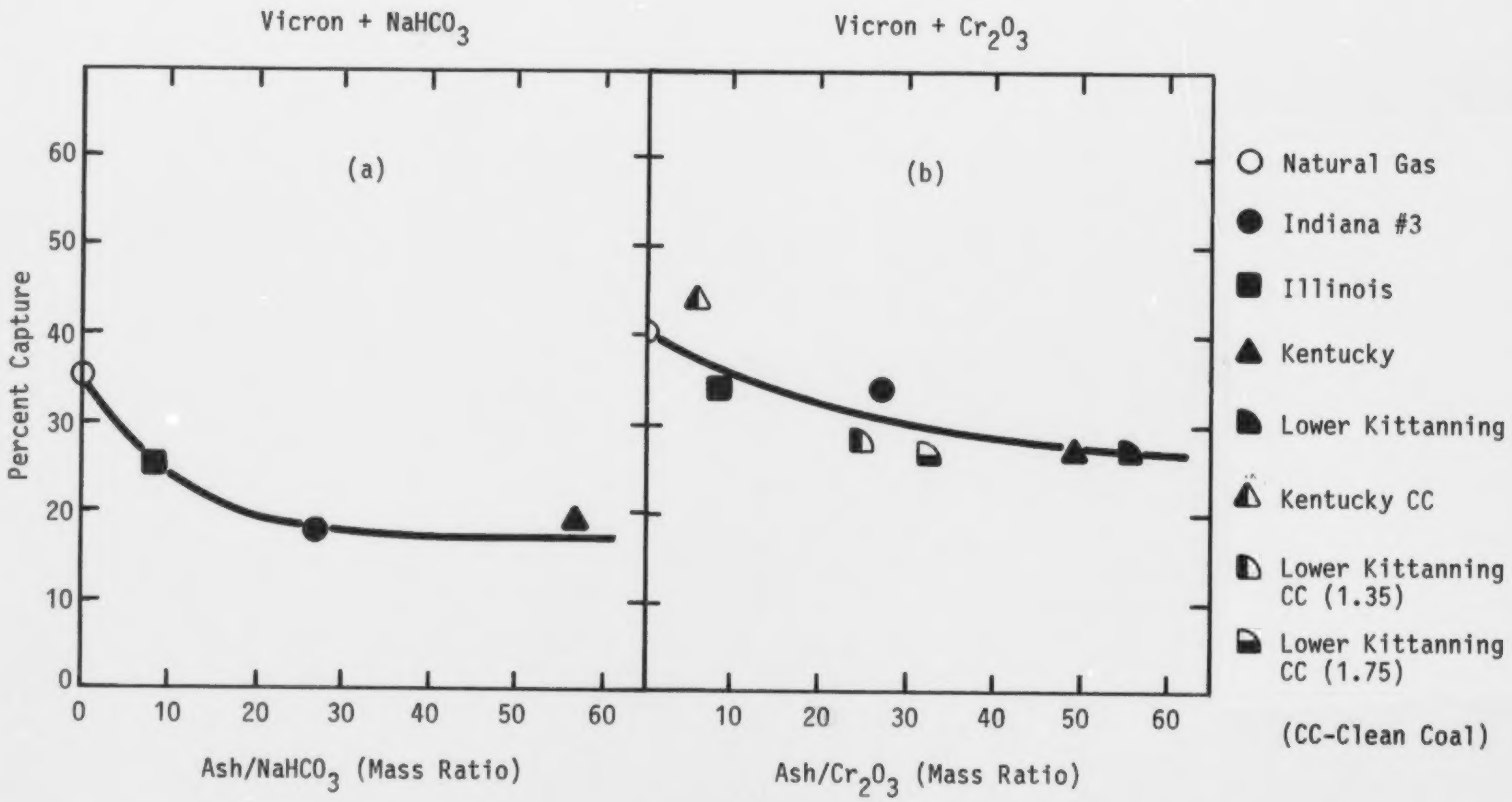

Figure 7-12. Capture correlation.

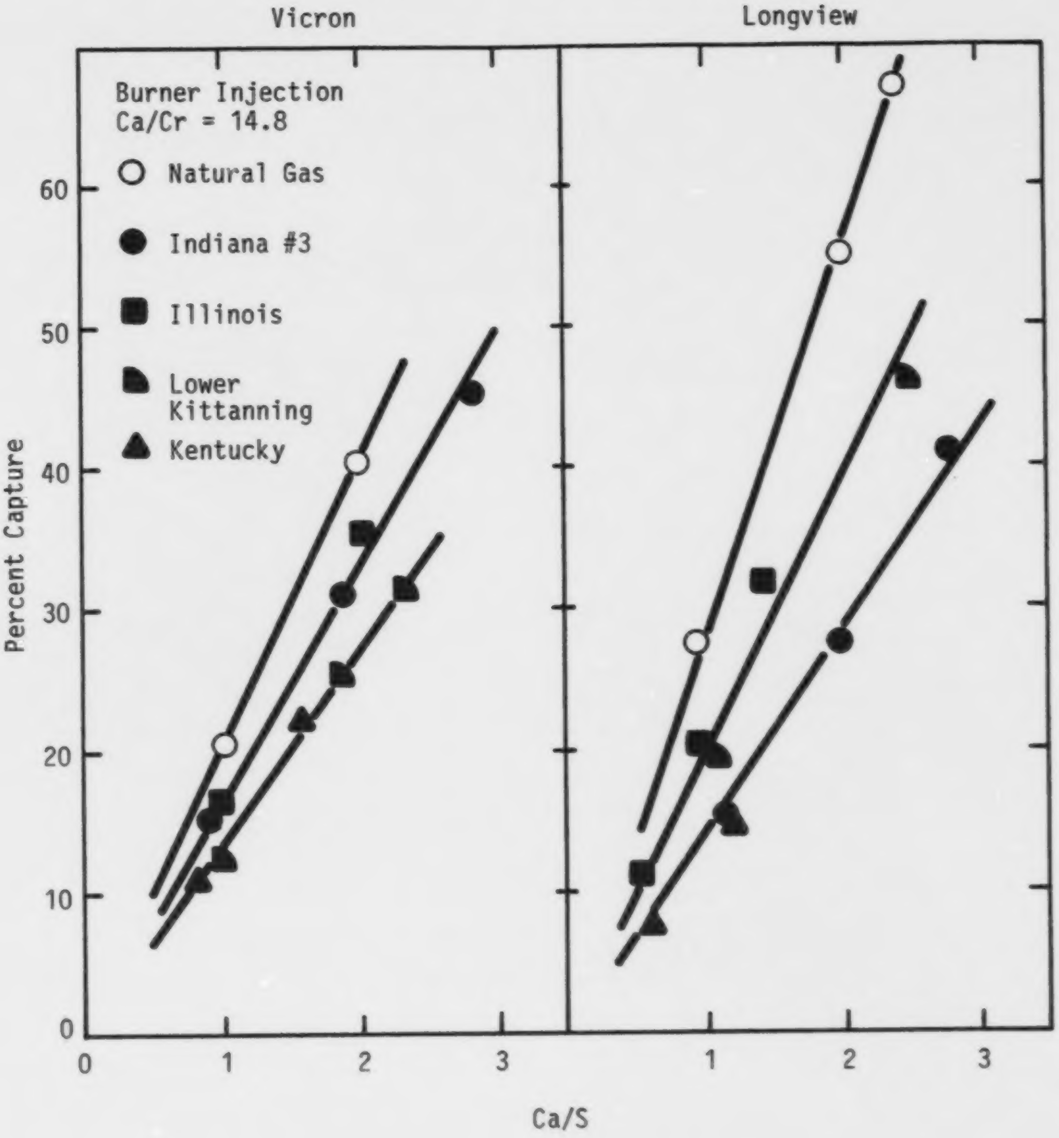

Figure 7-13. The effect of coal mineral matter on Cr_2O_3.

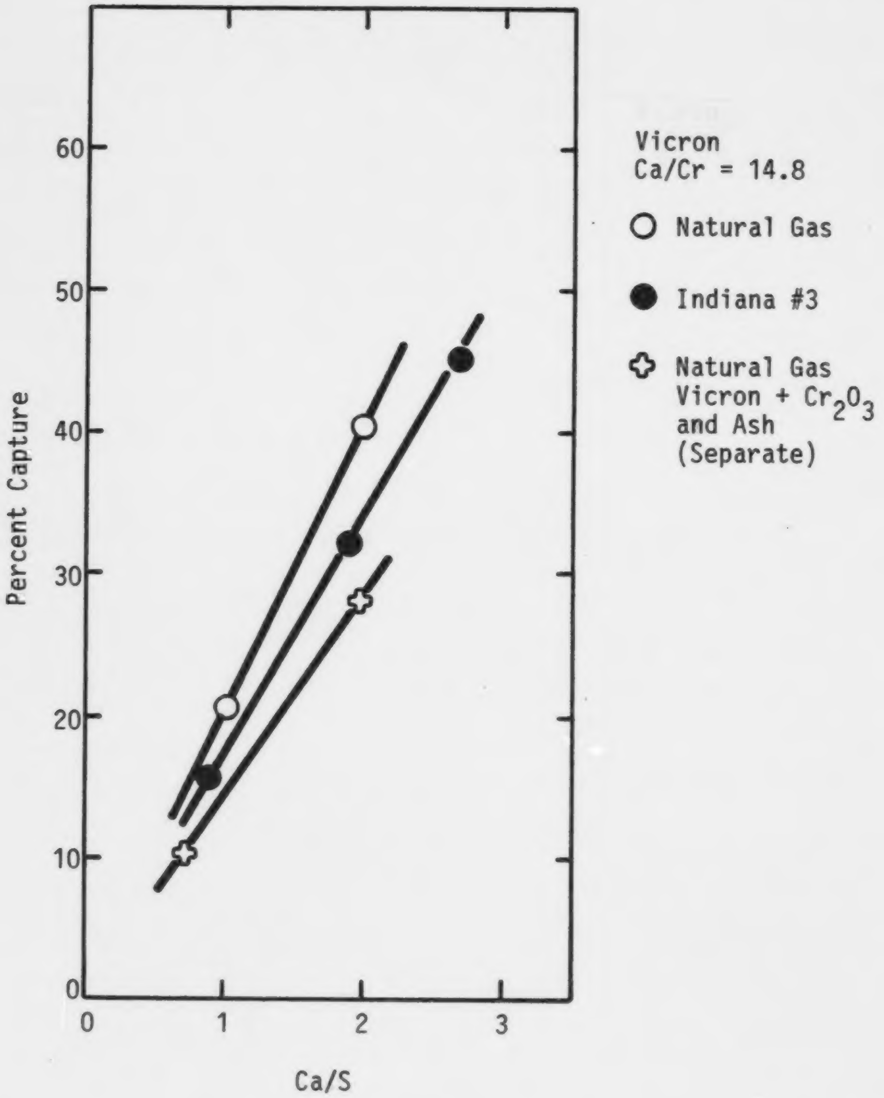

Figure 7-14. The effect of coal ash on Cr_2O_3 enhancement.

coals from which much of the ash had been removed. Figure 7-15 shows the results for the two chromium enhanced sorbents injected at the burner. Each sorbent was run with the Kentucky and the Kentucky cleaned coal and with the lower Kittanning and two levels of cleaned Kittanning coal. The coal and ash analysis data for each fuel are shown in Table 7-1. For the Kentucky coals, the results are as expected with the cleaned coal giving much higher capture than the raw coal. Again the effect was attributed to the presence of mineral matter in the coal. For the lower Kittanning coals, however, the results were initially somewhat surprising in that the coal cleaning had no effect on sulfur capture. Detailed examination of the coal analysis data indicated that with the Kentucky coal, cleaning reduced the ash by 80 percent and the sulfur by only 23 percent. Hence at Ca/S = 2 and Ca/Cr = 14.8, the overall ash/promoter ratio decreased by 65 percent. However, with the Lower Kittanning coal, cleaning (s.g. = 1.35) reduced the ash by 50 percent and the sulfur by 54 percent. In this case the overall ash/promoter ratio actually increased slightly (by 8 percent); consequently, coal cleaning did not improve the effectiveness of the promoter.

Figure 7-12b illustrates the capture data for all of the fuels correlated with respect to ash/Cr_2O_3 mass ratio. For burner injection, the percent capture decreased correspondingly with increasing mass ratio and the curve appears to reach an asymptote at higher ratios. The correlation failed for downstream injection of the chromium promoted sorbents. The reduction at the higher temperature is believed to be caused by a reaction with chromium and calcium which forms a low melting eutectic mixture (see Section 6) and subsequently allows the loss of chromium components to the gas-phase. Once in the gas phase, ash particles compete with the calcium particles as condensation sites.

As with the sodium promoter, the extracted solids containing the sorbent, ash, and chromium were examined by SEM, EDS and X-ray diffraction. A high resolution photograph is presented in Figure 7-16 with its corresponding elemental spectrum and distribution maps shown in Figure 7-17 and Figure 7-18, respectively. In addition, intensity maps of each of the

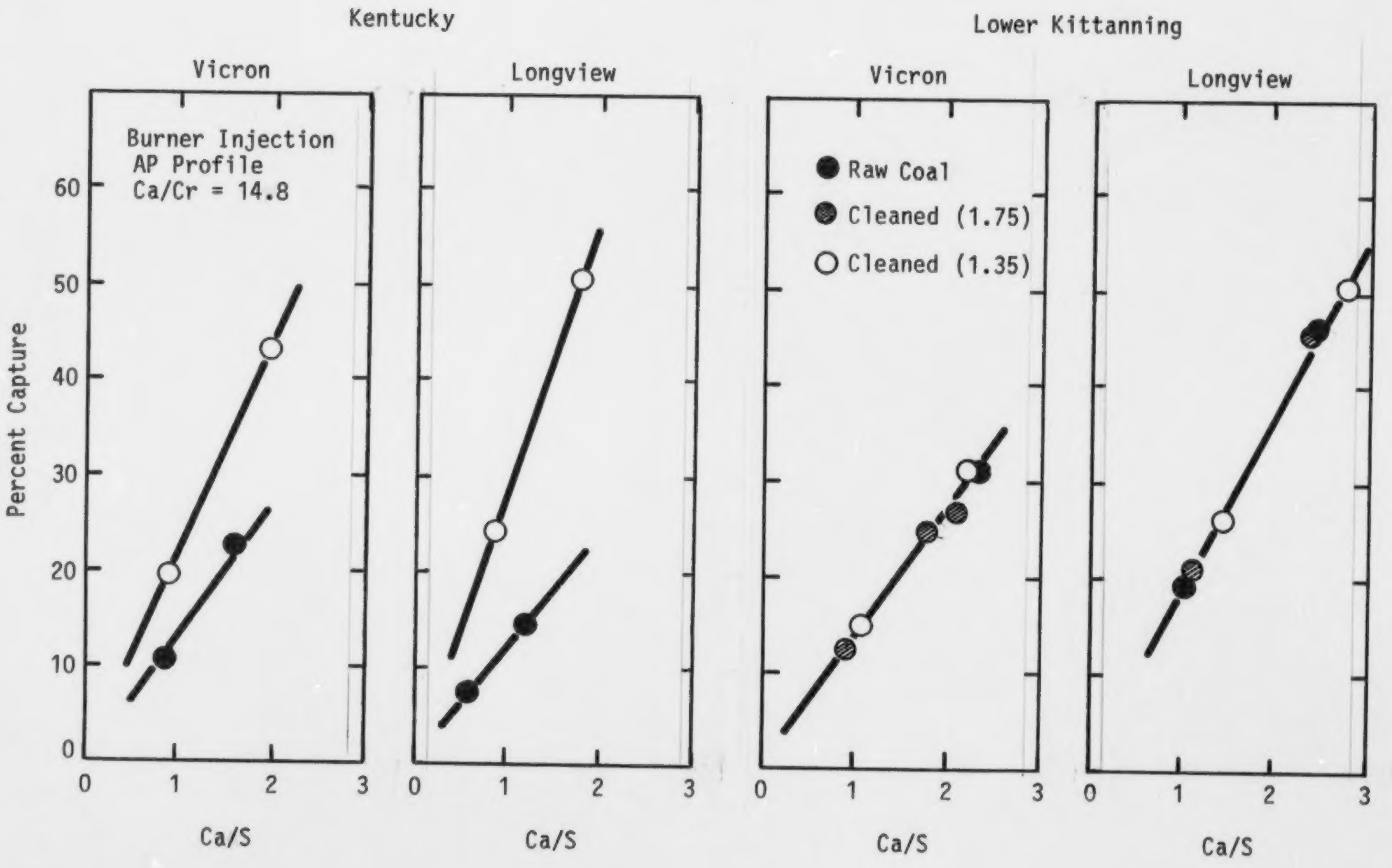

Figure 7-15. Influence of coal cleaning.

TABLE 7-1. FUEL ANALYSIS

	Indiana #3	Illinois	Lower Kittan-ning	Lower Kitt. C.C. (1.75)	Lower Kitt. C.C. (1.35)	Kentucky	Kentucky C.C. (1.35)	Natural Gas
Proximate, %(As Received)								
H_2O	7.97	6.61	1.65	1.80	1.21	33.06	3.56	-
Volatile Matter	33.02	38.70	22.23	20.28	21.12	27.82	40.73	100
Fixed Carbon	50.25	45.61	60.29	69.94	69.72	36.74	48.84	-
Ash	8.76	9.08	15.83	7.98	7.95	31.88	6.60	-
Ultimate, % (Dry)								
Carbon	71.32	69.13	72.46	82.35	82.74	51.42	73.87	72.15
Hydrogen	4.57	4.83	4.29	4.48	4.49	3.52	5.17	23.04
Nitrogen	1.33	1.16	1.05	1.27	1.16	1.00	1.37	1.84
Sulfur	1.22	3.87	1.68	0.97	0.76	3.31	2.55	-
Oxygen	12.04	11.29	4.42	2.80	2.80	7.69	10.18	0.59
Ash	9.52	9.72	16.10	8.13	8.05	33.06	6.86	-
HHV (Btu/lb)	12,545	14,114	11,510	14,238	14,820	7,762	13,519	22,714
Ash								
SiO_2	58.41	51.28	51.67	40.88	39.68	52.53	42.92	-
Al_2O_3	23.96	18.39	26.40	25.15	24.44	21.21	19.05	-
Fe_2O_3	10.39	16.90	10.25	23.34	25.25	10.94	25.92	-
CaO	1.60	4.97	1.61	2.46	2.65	3.76	4.17	-
MgO	0.14	0.95	1.08	0.82	0.81	1.90	0.33	-
K_2O	1.45	1.82	2.39	1.32	1.47	3.20	1.81	-
Na_2O	0.20	0.82	0.28	0.34	0.34	0.64	1.08	-
TiO_2	0.96	0.77	1.32	2.26	2.10	1.30	1.08	
P_2O_5	0.54	0.26	0.21	0.32	0.35	0.72	0.39	-
SO_3	0.43	4.93	1.49	2.27	2.48	4.68	2.43	-

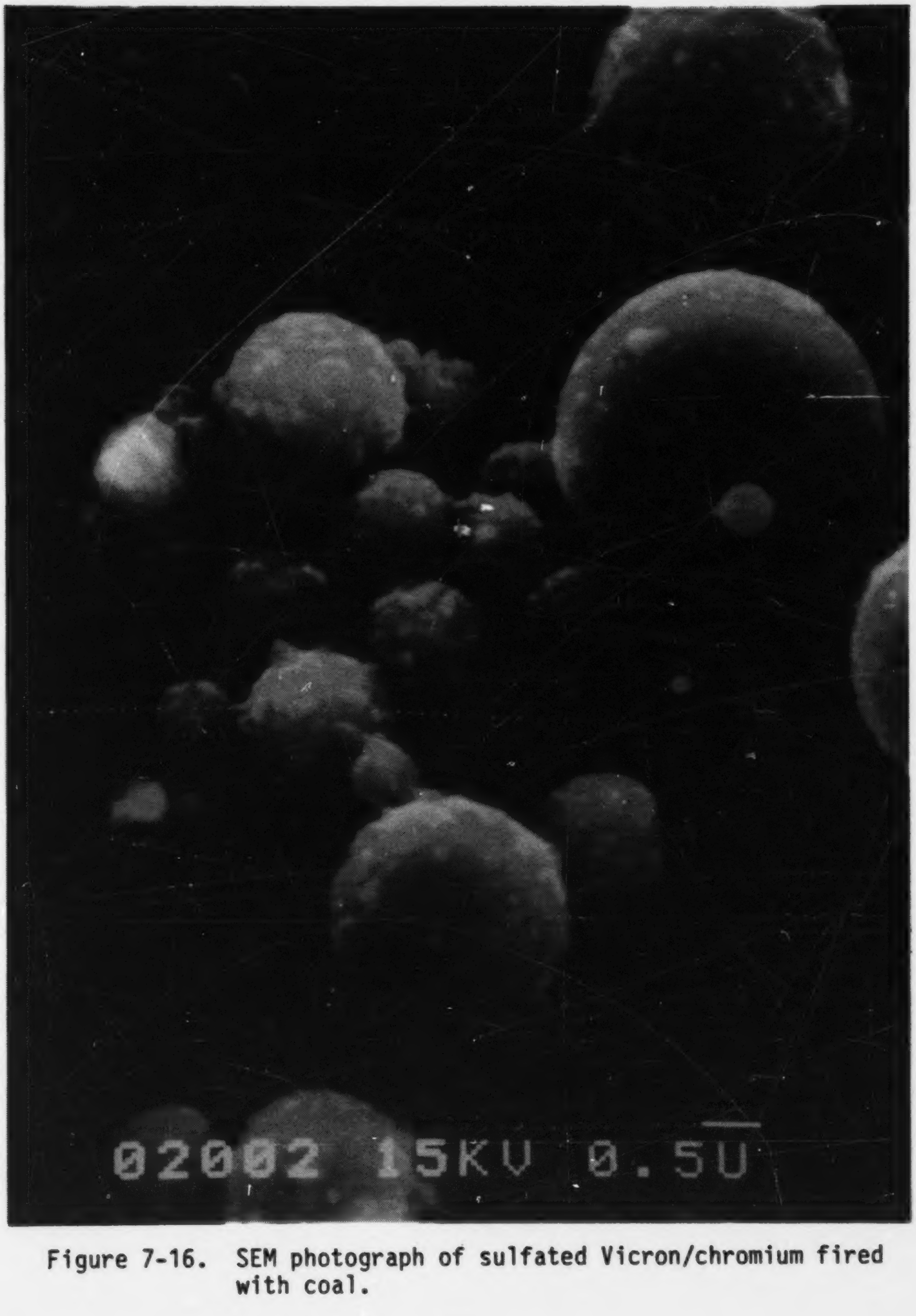
02002 15KV 0.5U

Figure 7-16. SEM photograph of sulfated Vicron/chromium fired with coal.

COLOR PHOTOS AVAILABLE FOR
INSPECTION ONLY AT EPA/AEERL

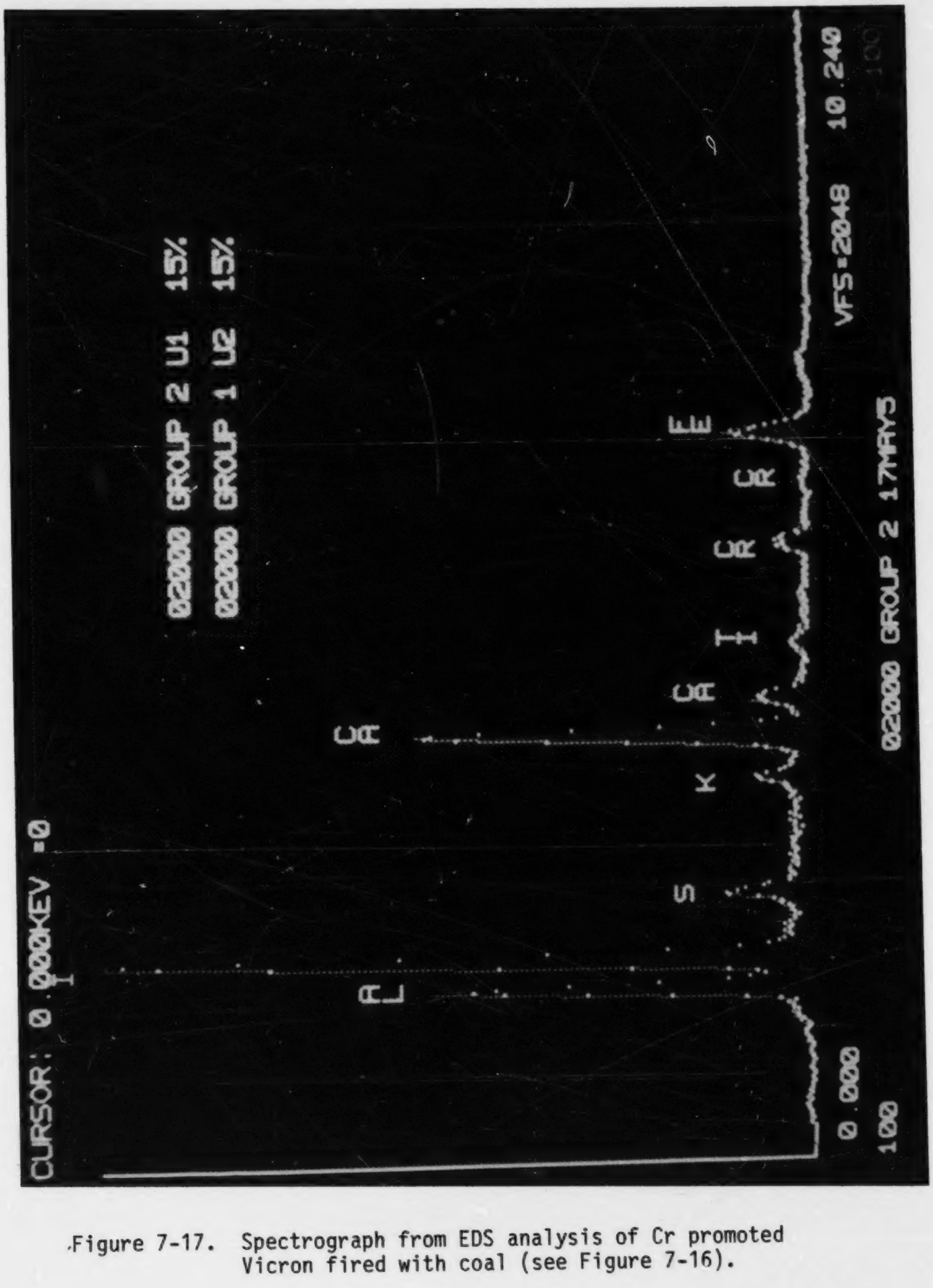

Figure 7-17. Spectrograph from EDS analysis of Cr promoted Vicron fired with coal (see Figure 7-16).

COLOR PHOTOS AVAILABLE FOR
INSPECTION ONLY AT EPA/AEERL

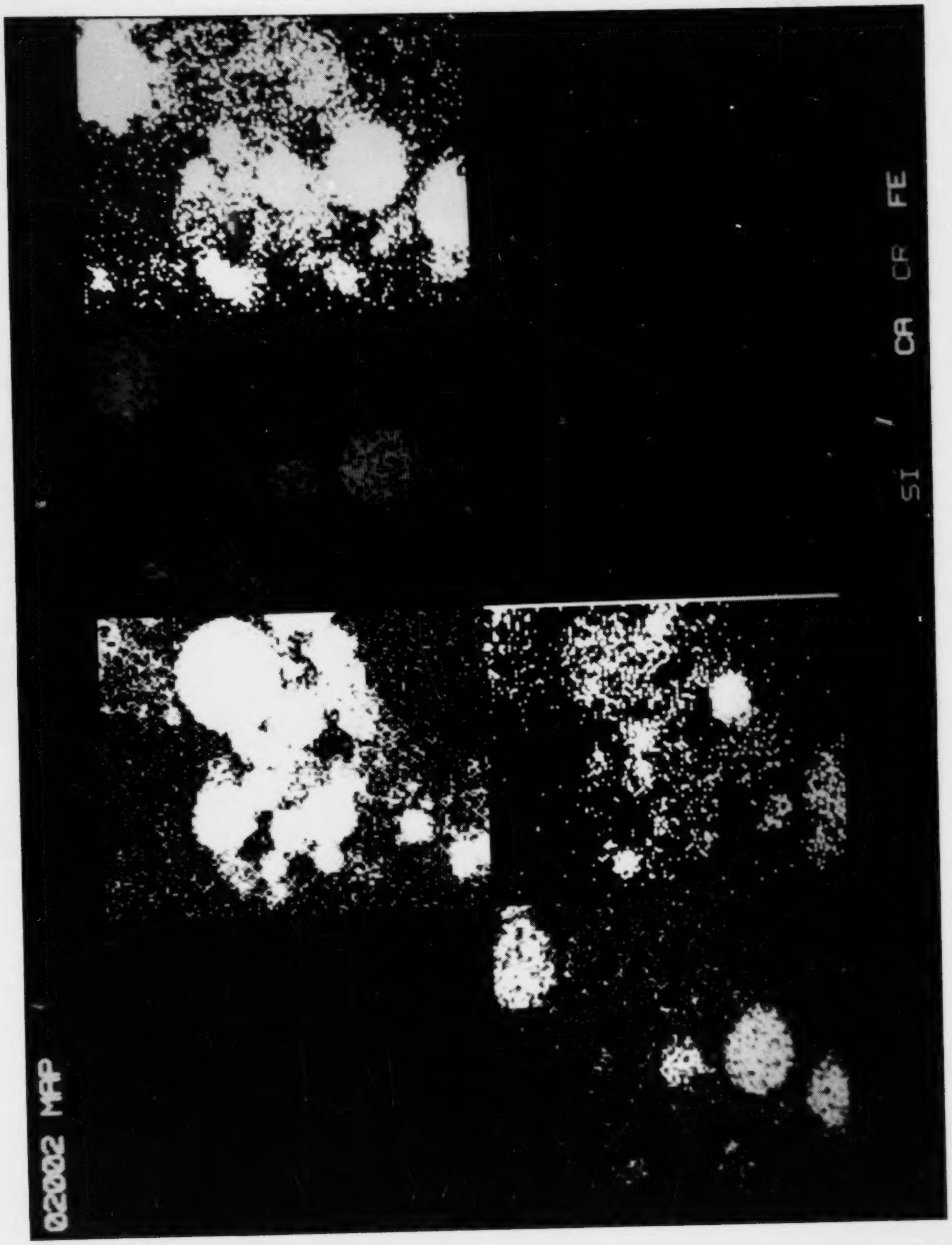
SI / CA CR FE
02002 MAP

Figure 7-18. Elemental distribution maps from EDS analysis of Cr promoted Vicron fired with coal (see Figure 7-16).

elements present (with associated distribution maps) are provided in Figures 7-19 through 7-22.

The elements present in the sample are labeled in the spectrograph (Figure 7-17). Inspection of the relative elemental concentration of the objects pictured in Figure 7-18 indicate clearly that the chromium did not uniformly distribute over the ash and sorbent (like sodium) as shown in Figure 7-19. The decrete distribution of chromium on calcium sorbent confirms chromium is not significantly vaporized at the conditions tested. Calcium (Figure 7-20) is associated with enhanced sulfur capture (Figure 7-21) if found with chromium. As discussed in Section 6, the chromium reacts with the calcium in order to promote sulfur capture. In general the chromium was found to be associated with the calcium and not the ash. If the ash (i.e., silicon, Figure 22) is associated with calcium, sulfur capture is reduced.

7.2 Sodium Condensation on Ash and Sorbent Particles

A series of computer simulations was performed for the purpose of studying the probable behavior of sodium additives (likely to be used in promoter technology) in the presence of both submicron and coarse ash particles, and sorbent particles. Items addressed in some fashion in this modeling included:

- The effects of varying coal composition
- The effects of varying sorbent type
- The effects of varying Ca/S mole ratio
- The effects of varying sorbent surface area available for condensation.

In order to perform these calculations in a manner most representative of the actual combustion conditions, a number of input parameters were necessary. The important parameters include the type of coal burned, the combustion conditions (stoichiometric ratio and temperature profile), the

COLOR PHOTOS AVAILABLE FOR
INSPECTION ONLY AT EPA/AEERL

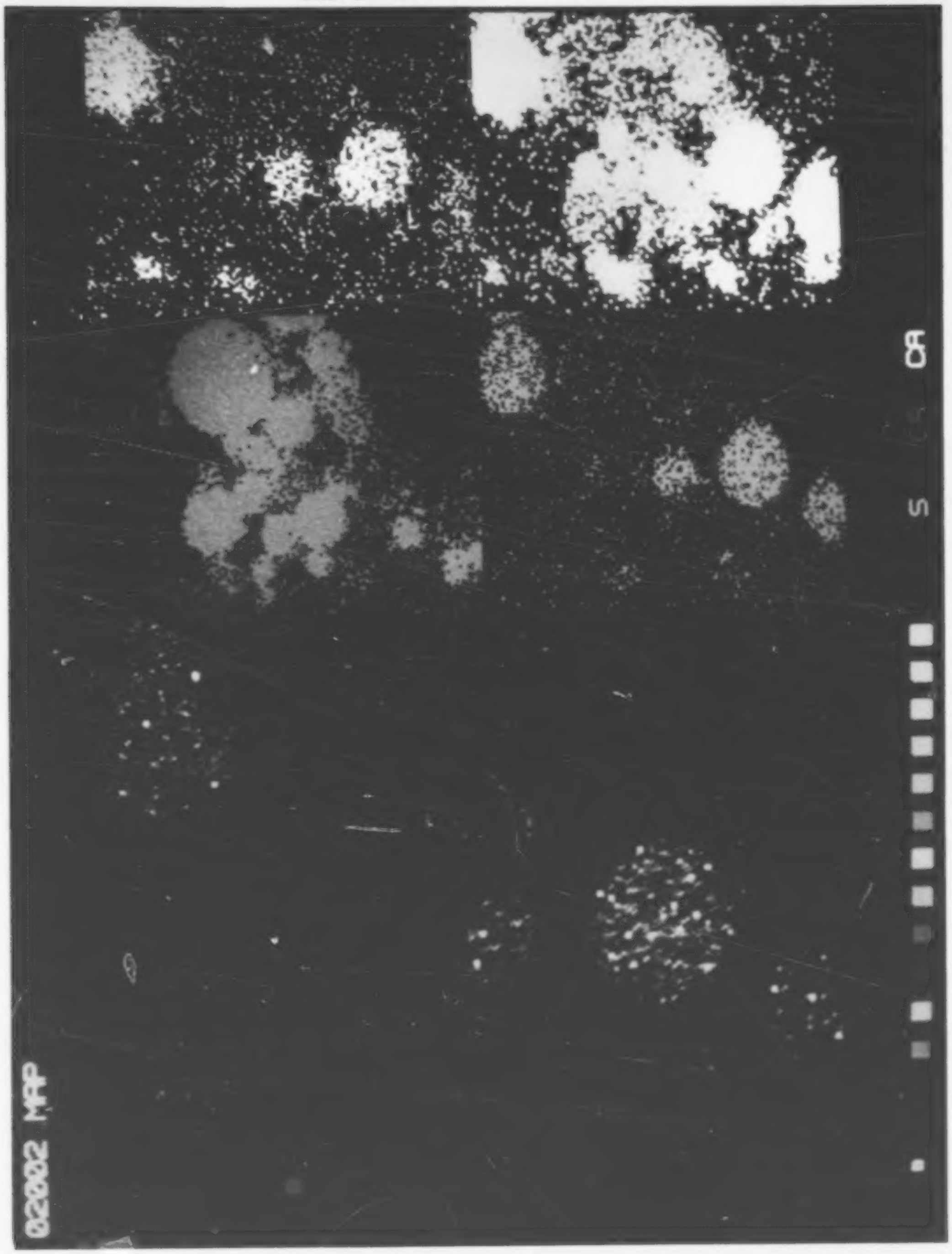

Figure 7-19. Chromium intensity map (left) from EDS analysis of Cr promoted Vicron fired with coal (see Figure 7-16).

COLOR PHOTOS AVAILABLE FOR
INSPECTION ONLY AT EPA/AEERL

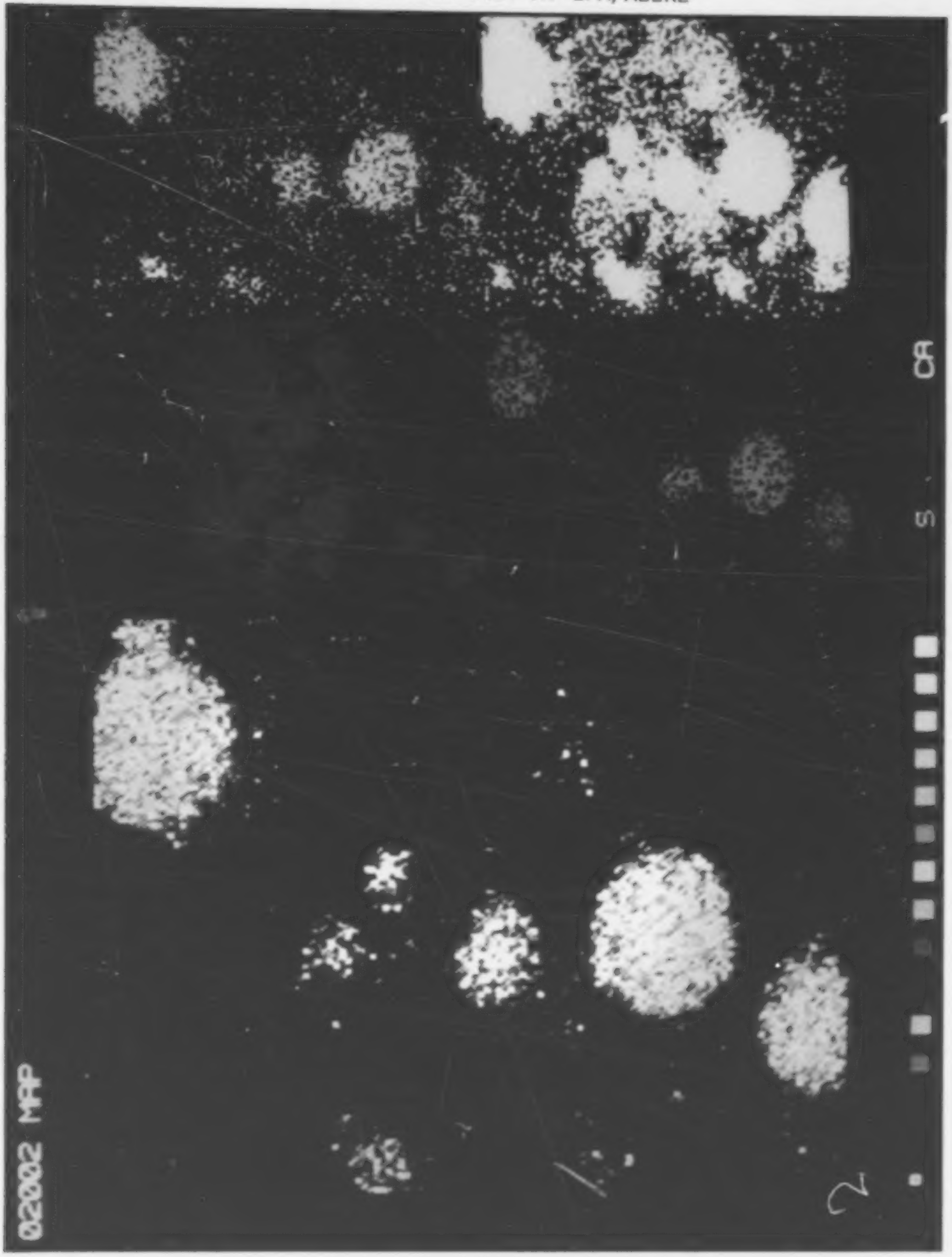

Figure 7-20. Calcium intensity map (left) from EDS analysis of Cr promoted Vicron fired with coal (see Figure 7-16).

COLOR PHOTOS AVAILABLE FOR
INSPECTION ONLY AT EPA/AEERL

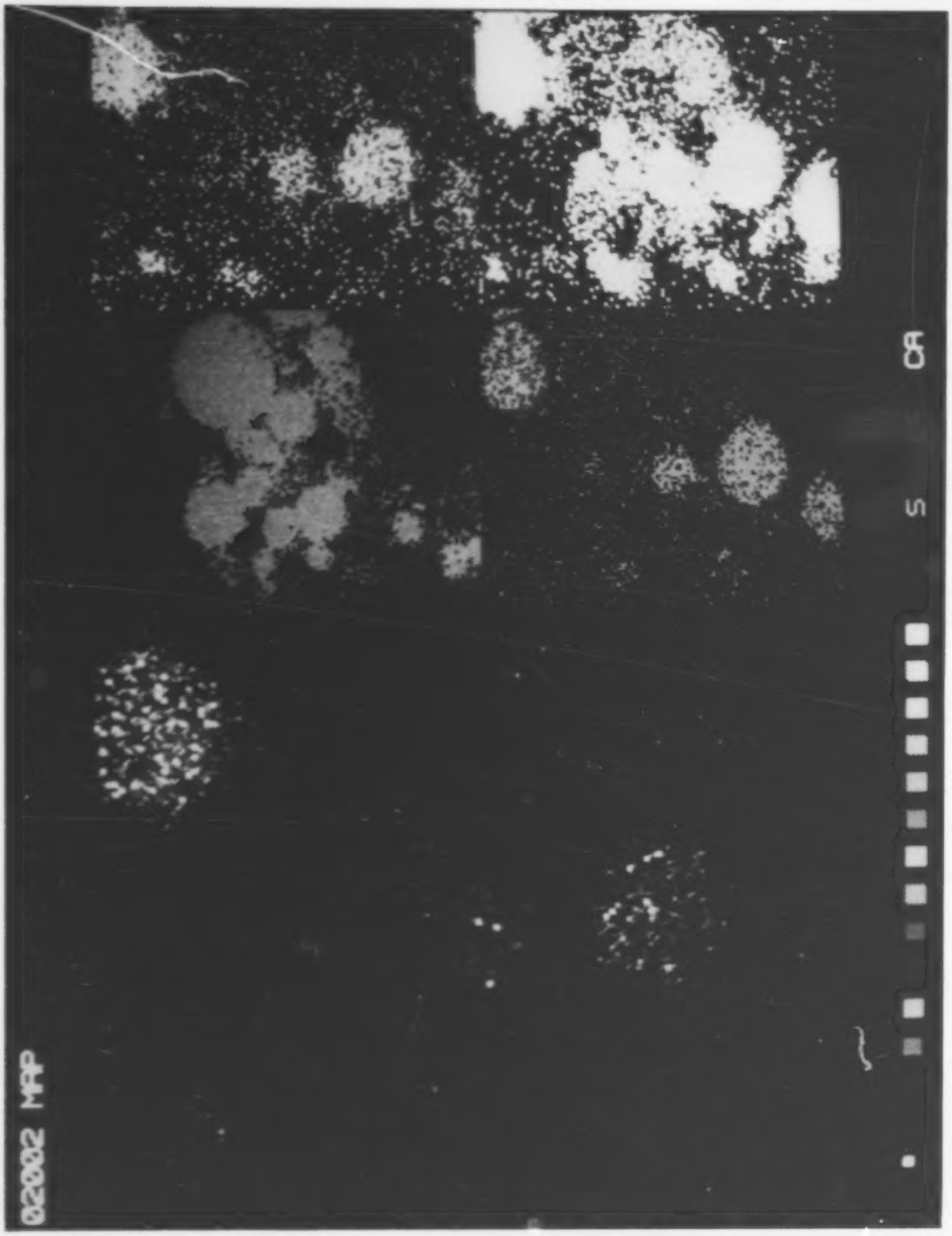

Figure 7-21. Sulfur intensity map (left) from EDS analysis of Cr promoted Vicron fired with coal (see Figure 7-16).

COLOR PHOTOS AVAILABLE FOR
INSPECTION ONLY AT EPA/AEERL

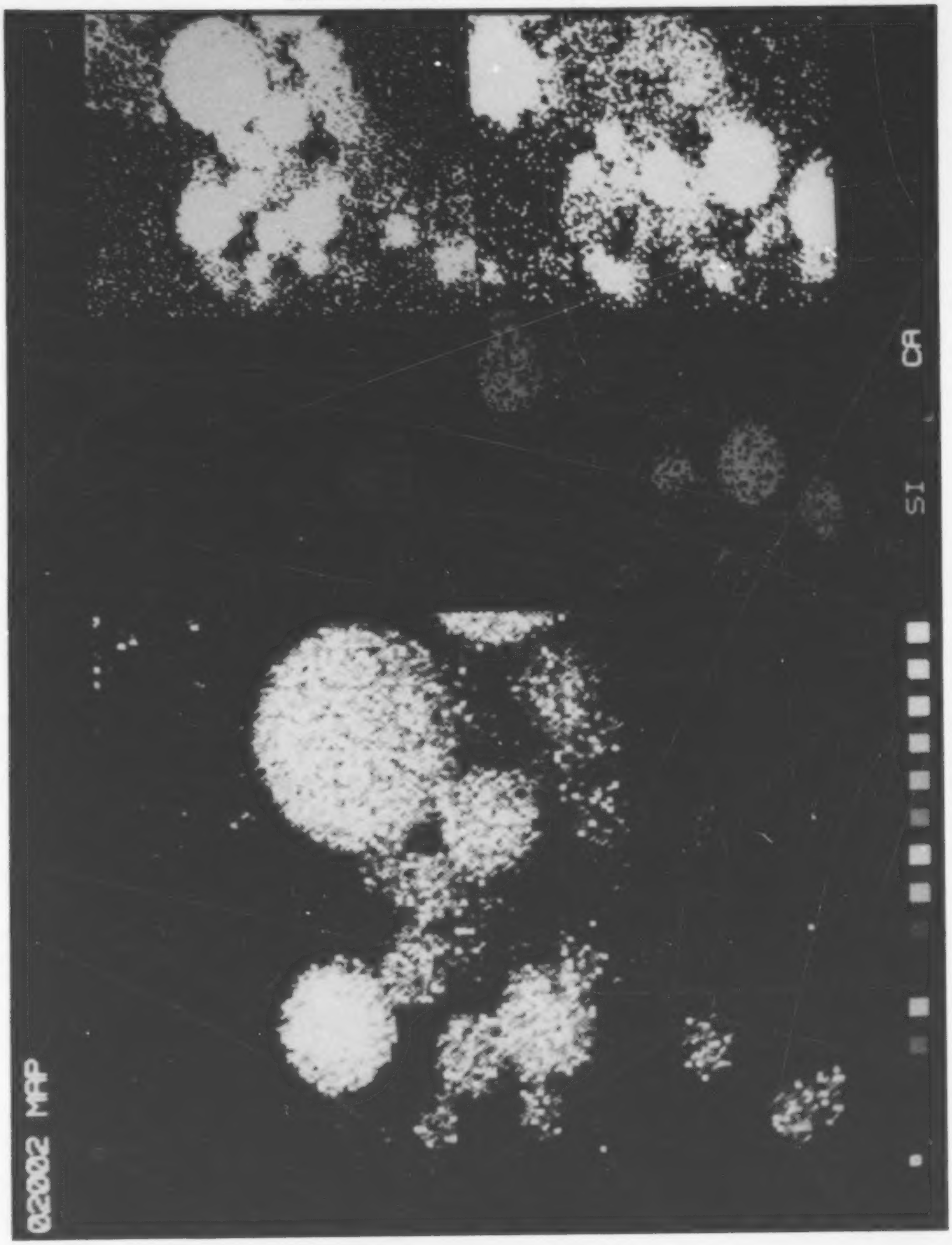

Figure 7-22. Silicon intensity map (left) from EDS analysis of Cr promoted Vicron fired with coal (see Figure 7-16).

resultant ash distribution, the sorbent type, the particle size distribution, and the ratio of additive to sorbent utilized. Listed below are the assumed values of the parameters for each of the simulations presented.

7.2.1 Coal Type

All simulations were performed on one of two types of coal; a Kentucky seam 11 and an Indiana No. 3. Both were assumed to be burned under a stoichiometric ratio of 1.2, and to follow a temperature profile described by the standard American Boiler Profile. (Characteristic temperature quench rate in the sulfation window is ~333 K/s).

The Kentucky seam 11 is composed of 42.94 percent C, 4.32 percent S, and 42.43 percent ash, on a dry basis. The ash analysis indicates that 0.49 percent of the ash is Na_2O. The Indiana No. 3 coal is composed of 72.16 percent C, 1.06 percent S, and 9.88 percent ash, on a dry basis. Approximately 0.22 percent of the ash is Na_2O.

7.2.2 Ash Distributions

From the given ash and carbon content, it was determined that at a representative temperature of 1700 K, the Kentucky coal liberated 14.92 g ash/m^3, while the Indiana coal liberated 2.07 gr ash/m^3 at that same temperature. Ash size distributions were based on measurements from the University of Arizona in a bench scale combustor. Lacking better data, it was assumed that all ash from the coals combusted fell into one of two size ranges (at least with regard to the potential condensation sites for vapor sodium species).

Experimental data from the University of Arizona facility indicate that approximately 5 percent of the total ash content of the coal ends up in the submicron mode. While these particles are likely the product of nucleation followed by coagulation late in the char burnout process, it was assumed that the submicron aerosol seen by the condensing sodium was an evolved aerosol with a mean of approximately 0.2 microns. Additionally, a coarse mode aerosol, comprised of the remainder of the ash, was assumed to be characterized by a mean at approximately 5.0 microns. For simplicity, the initial ash distributions were assumed to be adequately represented by log-normal distributions with the reported mean particle sizes. Table 7-2 summarizes the coal and ash characteristics (both calculated and assumed) from the Kentucky and Indiana coals.

7.2.3 Sorbents

Two sorbents were considered in these simulations. The first sorbent considered was the Vicron 45-3 calcite, composed of 40 percent calcium and having a mean diameter of 12 microns. The second sorbent was the Longview commercial hydrate, with 48.8 percent calcium and a mean particle size of about 4 microns. For simplicity, the initial distributions for the sorbents were assumed to follow the log-normal form with the reported mean particle size.

At a Ca/S ratio of 2.0, the sorbent concentration for the Vicron at 1700 K is 9.4 and 1.38 g/m^3 in air for the Kentucky and Indiana coals, respectively. For the Longview under the same conditions, the sorbent concentration is 8.72 and 1.13 g/m^3 in air for the Kentucky and Indiana coals, respectively. Table 7-3 summarizes important characteristics of the sorbents.

7.2.4 Additive Characteristics

Assuming a Ca/Na mole ratio of 15 and a Ca/S ratio of 2, the mass ratio of sodium additive to sodium in the coal is 2.67 and 6.36 for the Kentucky and Indiana, respectively. The corresponding concentrations of additive sodium at 1700 K are 0.145 and 0.021 g Na/m^3 for the Kentucky and Indiana coals, respectively. Although the ratio of additive to ash sodium is of order one to ten in both cases considered, it is assumed that most of the sodium in the coal is probably tied up as silicate and hence not available for vaporization. Table 7-4 summarizes the characteristics of the additive.

TABLE 7-2. COAL CHARACTERIZATION

	Kentucky Seam #11	Indiana #3
Dry Basis:		
Wt % C	42.94	72.16
Wt % S	4.32	1.06
Wt % Ash	42.43	9.88
	Ash Characterization	
g Na/g C	3.6×10^{-3}	2.2×10^{-4}
	@ SR = 1.2	
Total Ash Concentration @ 1700 K (g/m^3)	14.92	2.07

TABLE 7-3. SORBENT CHARACTERIZATION

	Vicron 45-3	Longview
Wt % Ca	40	48.8
Mean Diameter; μm	12	4
d(0.01); μm	~1.0	~0.5
d(0.99); μm	~45	~100

TABLE 7-4. ADDITIVE CHARACTERIZATION

@ S/Na Mole Ratio = 7.5		
	Kentucky	Indiana
$\frac{\text{g Na Additive}}{\text{g C}}$	9.6×10^{-3}	1.4×10^{-3}
$\frac{\text{Na Additive}}{\text{Na Ash}}$	2.67	6.36
$\frac{\text{g Na Additive}}{\text{m}^3}$	0.145	0.021

(@ 1700 K; SR = 1.2)

7.2.5 The Simulations

The simulations reported below have examined only the physical behavior of the aerosol evolution process. No attempt has been made to incorporate chemically mediated mechanisms, such as surface reactions, which may enhance or reduce the sodium condensation process. Basically, the following scenario was considered:

An initial ash aerosol, comprised of two modes, and a unimodal sorbent evolve in the presence of Na which, by virtue of its vapor pressure, is found predominantly in the vapor phase. The ash is represented by a submicron mode (formed by nucleation and condensation of less volatile species such as Si oxides) and a coarse mode (formed by fragmentation of the char as it burns, exposing large mineral inclusions). The sorbent is represented by it's measured particle size distribution prior to injection. As the ash and sorbent evolve in time through the furnace, following a prescribed temperature profile (the American Boiler profile), they coagulate among themselves and with each other. As the furnace temperature drops, the equilibrium vapor pressure of the volatile sodium species drops, and eventually the sodium will either condense on existing particles or nucleate to form new particles. Preliminary screening runs indicated that it is far more likely that the sodium will condense on existing particles rather than nucleate to form new particles. Further, it was observed that once the equilibrium vapor pressure dropped below the actual vapor concentration of the sodium, the condensation was almost instantaneous. After passing through this temperature regime, coagulation was the only process that significantly affected the evolving aerosol distribution. Therefore, as far as the evolution of the sodium is concerned, the critical point is that point at which the vapor pressure passes through the equilibrium vapor pressure, whereupon the sodium condenses on the existing aerosol particles.

There is some question regarding just what form the sodium is likely to be in at the time of condensation to the particle phase. The additive itself is a bicarbonate, $NaHCO_3$ which decomposes at 543 K to the hydroxide, NaOH. However, it is considered likely that the reaction with gaseous sulfur-containing species results in the formation of the sulfate, Na_2SO_4, which then subsequently condenses. Since the thermodynamics of condensation depends strongly on the species of concern, it is obviously quite important to know what form the Na takes prior to condensation (see Figure 6-1). For the simulations performed, it was assumed that the sulfate form predominated. As will be discussed, quite different behavior would be seen if the condensing form would be the hydroxide or even the oxide.

Equilibrium vapor pressures for the sulfate and hydroxide as function of temperature were converted into equation form. For the sodium sulfate, the vapor pressure (in atmospheres) as a function of temperature (in degrees K) is given by the expression

$$p = 2.11 \cdot 10^5 \exp(-3.41 \cdot 10^4/T).$$

For the NaOH, the expression is

$$p = 3.35 \cdot 10^4 \exp(-1.73 \cdot 10^4/T).$$

In the simulations, four "components" are followed: the submicron ash aerosol, represented in all figures by the squares (□), the coarse mode ash, represented by the circles (○), the sorbent, represented by the triangles (△), and the condensed sodium species, represented by the diamonds (◇). Table 7-5 summarizes the simulations conducted. Briefly, all runs marked 01 or 02 correspond to the Kentucky coal. All runs marked 03, 04, and 05 correspond to the Indiana coal. The results are presented in the form of fraction of a given material found greater than the stated size. Hence, all curves for all species begin at 1.0 on the ordinate and proceed to zero as the particle diameter increases. These plots indicate for each species where the majority of that species is found in the size spectrum. Simulations represent the aerosol just after the "condensation threshold" has been crossed. Table 7-6 lists the temperatures at which this threshold is crossed for each of the simulations performed. For the Kentucky coal, the resultant sodium concentration dictates that condensation of the sodium sulfate occurs in the temperature range 1645 to 1740 K, depending on the Ca/S ratio. For

TABLE 7-5. SIMULATIONS PERFORMED

Run	Ca/S Ratio	Initial Na Vapor Cond. (kg/m^3)	Initial Ash (Sub- m) (kg/m^3)	Initial Ash (Coarse) (kg/m^3)	Initial Sorbent (kg/m^3)	Coal	Sorbent
1. 01	2	14.5 x 10^{-5}	0.746 x 10^{-3}	14.174 x 10^{-3}	9.40 x 10^{-3}	Ky	Vicron
2. 01a	1	7.25 x 10^{-5}	0.746 x 10^{-3}	14.174 x 10^{-3}	4.70 x 10^{-3}	Ky	Vicron
3. 01b	3	21.75 x 10^{-5}	0.746 x 10^{-3}	14.174 x 10^{-3}	14.10 x 10^{-3}	Ky	Vicron
4. 02	2	14.5 x 10^{-5}	0.746 x 10^{-3}	14.174 x 10^{-3}	7.72 x 10^{-3}	Ky	Longview
5. 02a	1	7.25 x 10^{-5}	0.746 x 10^{-3}	14.174 x 10^{-3}	3.86 x 10^{-3}	Ky	Longview
6. 02b	3	21.75 x 10^{-5}	0.746 x 10^{-3}	14.174 x 10^{-3}	11.58 x 10^{-3}	Ky	Longview
7. 03	2	2.1 x 10^{-5}	0.1035 10^{-3}	1.9665 10^{-3}	1.38 x 10^{-3}	Ind	Vicron
8. 03a	1	1.05 x 10^{-5}	0.1035 10^{-3}	1.9665 10^{-3}	0.69 x 10^{-3}	Ind	Vicron
9. 03b	3	3.15 x 10^{-5}	0.1035 10^{-3}	1.9665 10^{-3}	2.07 x 10^{-3}	Ind	Vicron
10. 04	2	2.1 x 10^{-5}	0.1035 10^{-3}	1.9665 10^{-3}	1.13 x 10^{-3}	Ind	Longview
11. 04a	1	1.05 x 10^{-5}	0.1035 10^{-3}	1.9665 10^{-3}	0.565 10^{-3}	Ind	Longview
12. 04b	3	3.15 x 10^{-5}	0.1035 10^{-3}	1.9665 10^{-3}	1.695 10^{-3}	Ind	Longview
13. 05a	2	2.1 x 10^{-5}	0.1035 10^{-3}	1.9665 10^{-3}	172.5 x 10^{-3}	Ind	Vicron
14. 05b	2	2.1 x 10^{-5}	0.1035 10^{-3}	1.9665 10^{-3}	47.09 x 10^{-3}	Ind	Longview

TABLE 7-6. CRITICAL CONDENSATION TEMPERATURES

Simulation Runs	As Na_2 SO_4 (K)	Residence (sec)	As NaOH (K)	Residence (sec)
01, 02	1705	~1	955	~3
01a, 02a	1645	~1	920	~3
01b, 02b	1740	~1	980	~3
03,04,05a,05b	1545	~1-1/4	860	~3.2
03a, 04a	1500	~1-1/4	830	~3.2
03b, 04b	1575	~1-1/4	880	~3.2

the Indiana coal, the sodium sulfate condensation temperature is in the range 1500 to 1575 K. If the condensed species was in fact NaOH rather than the sulfate, the condensation temperature would drop significantly; to the 920-980 K range for the Kentucky and 830-880 K for the Indiana coal. These threshold condensation temperatures correspond to residence times in the furnace from about 1 sec for the sodium sulfate formed during combustion of the Kentucky coal to about 3.2 sec for the NaOH formed during combustion of the Indiana coal. After that point, the vapor sodium species have condensed on the existing aerosol.

In all cases, varying the Ca/S ratio within a specific coal type and sorbent type produced very minor changes in the fractional distribution of the additive. Obviously, increasing the sorbent will in fact decrease the additive concentration relative to the sorbent, but little effect on the mass fraction distribution of the additive is seen. These observations can be made by comparison between the "EEROxa and EEROxb" runs, where x is 1 to 4. (Results shown in Figure 7-23 through 7-36).

The major effect of changing from the Vicron to the Longview sorbent is to reduce the amount of additive condensed on the submicron ash, in favor of condensation on the sorbent. This is due to the fact that the Longview sorbent has a smaller mean particle size (4 micrometers, compared to 12 micrometers for the Vicron), and hence a higher surface area to mass ratio. This can be seen by comparing figure sets 1 to 2 (for the Kentucky coal) or sets 3 to sets 4 (for the Indiana coal). For example, looking at Figure 7-23 (labelled EER01; Kentucky/Vicron; Ca/S = 2), approximately 10 percent of the sodium condenses on particles greater than 1 micrometer, meaning that 90 percent condensed on the submicron particles. By comparison, the data in Figure 7-26 (EER02; Kentucky/Longview; Ca/S = 2) show that approximately 20 percent of the sodium condensed on the larger particles, while 80 percent fell in the submicron range.

On a relative mass basis, the effect of coal type on the size distribution of condensed additive is rather minimal, in spite of the fact that the ash concentration for the Kentucky coal is a factor of 7 greater

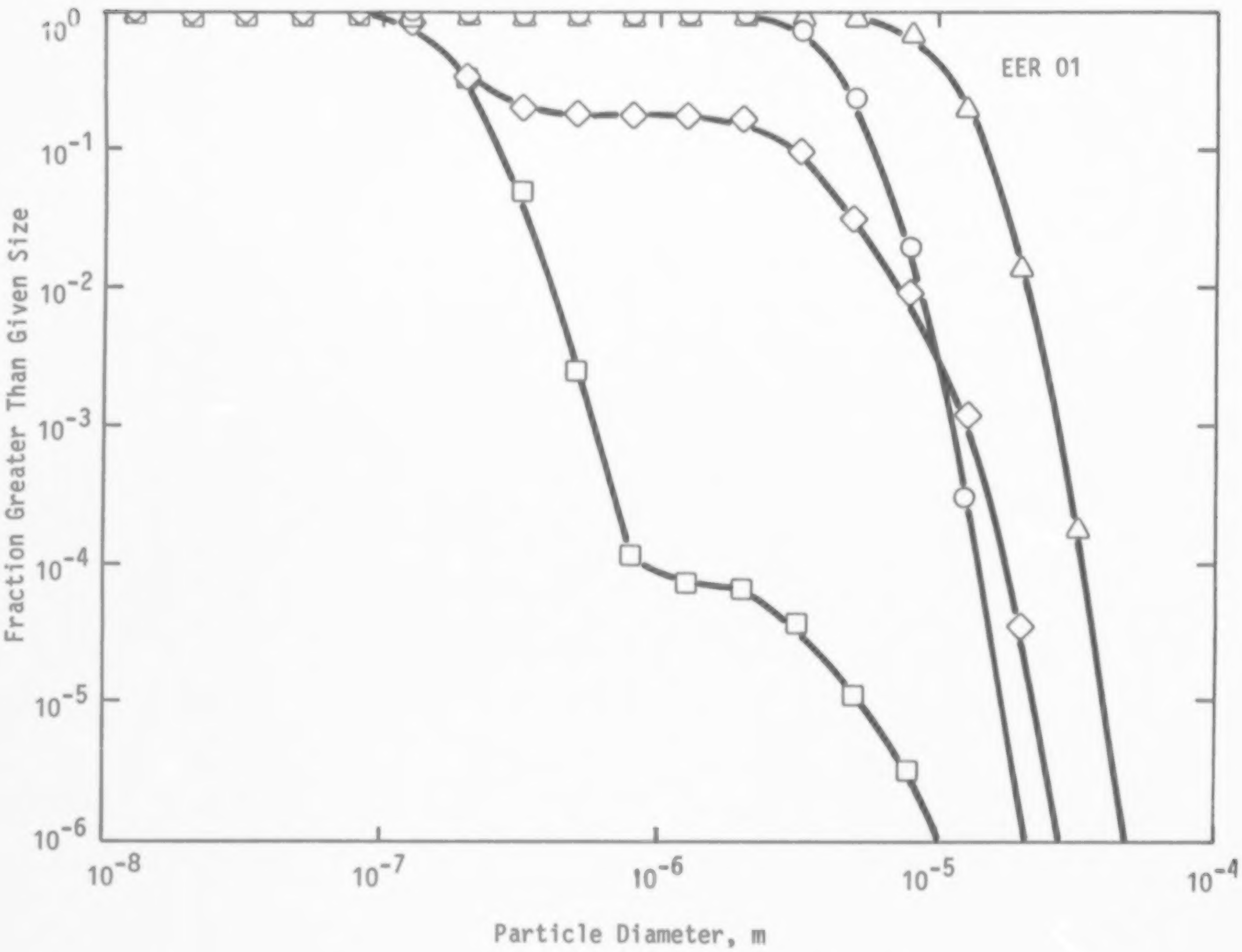

Figure 7-23. Simulation EER01.

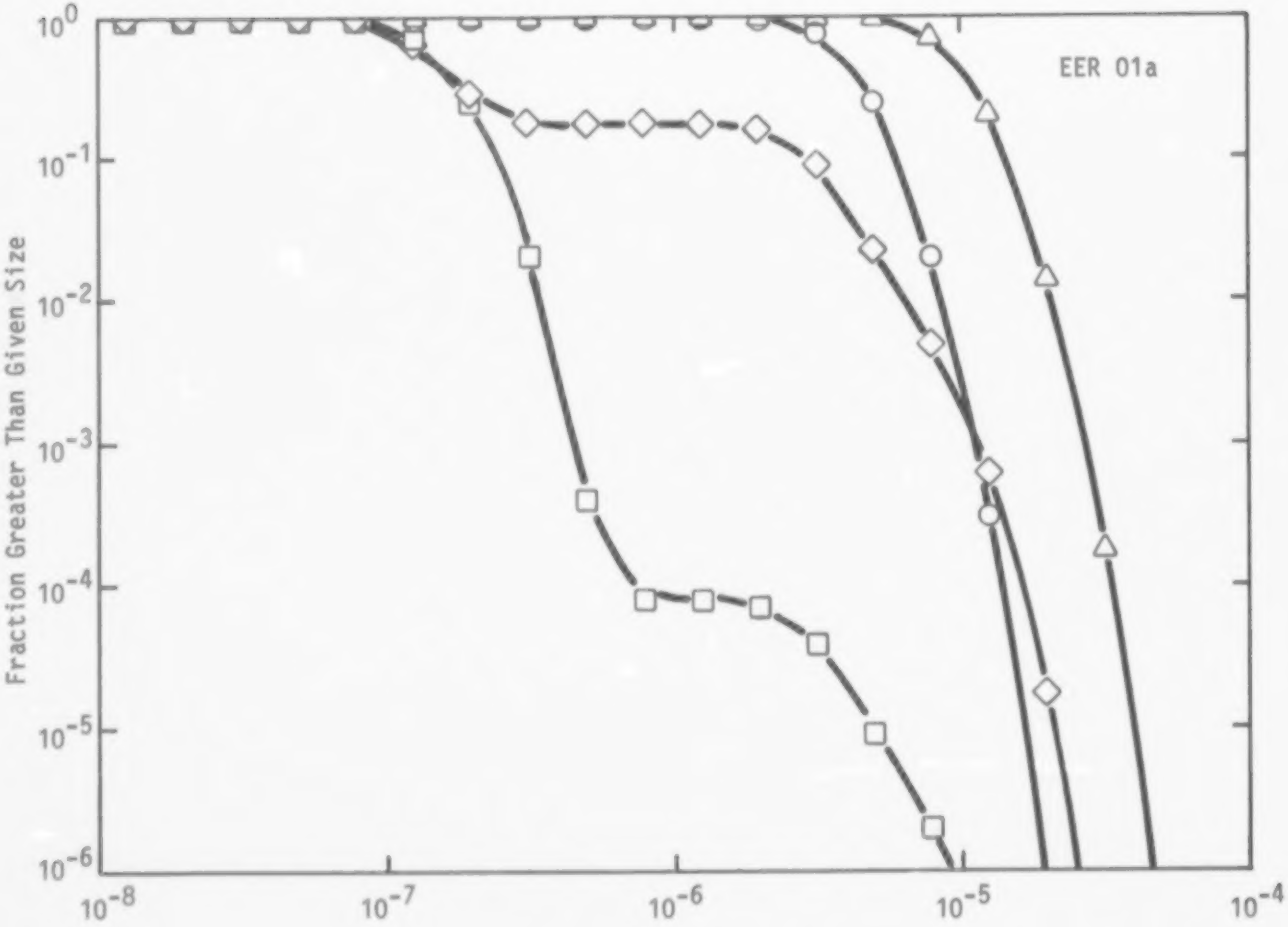

Figure 7-24. Simulation EER01a.

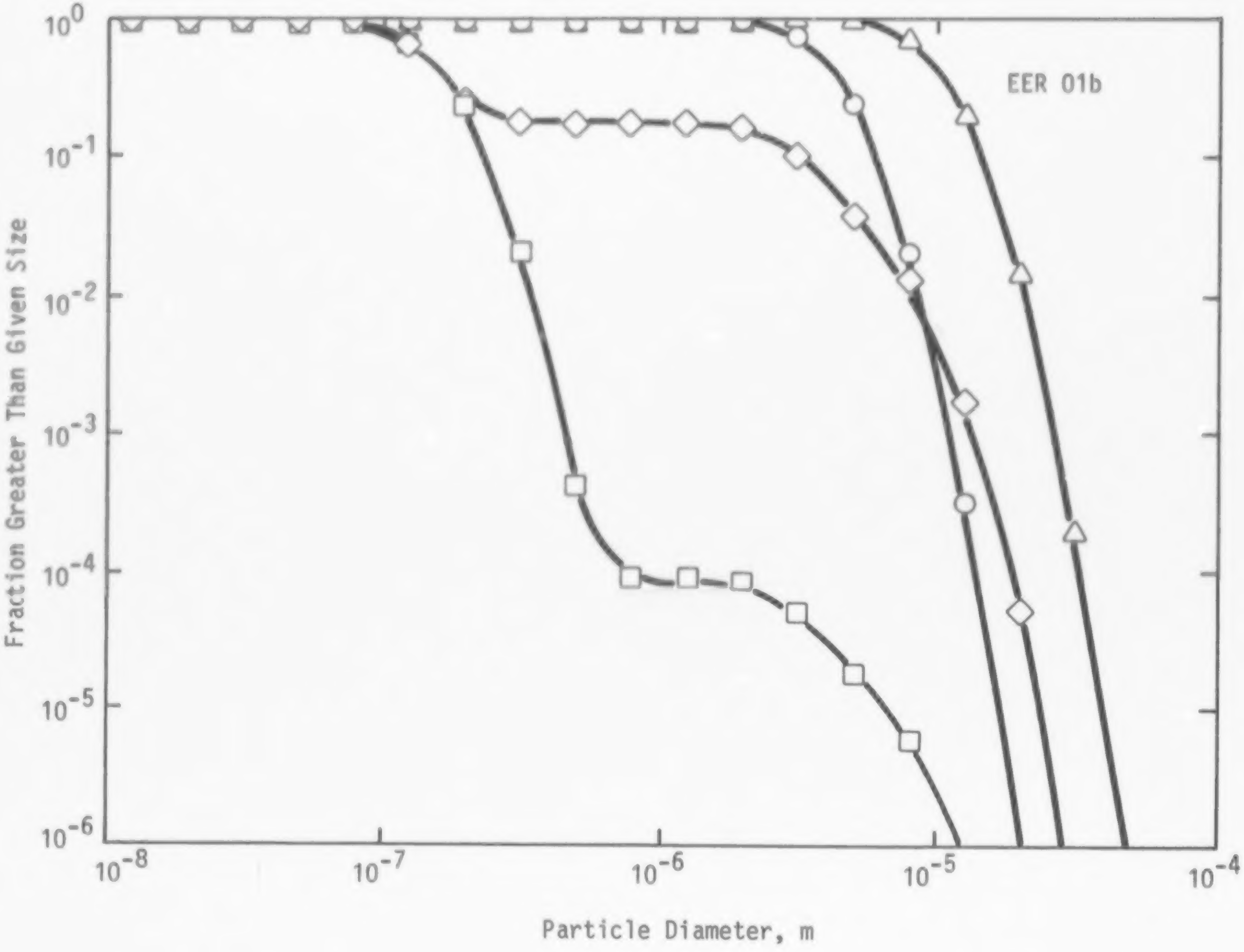

Figure 7-25. Simulation EER01b.

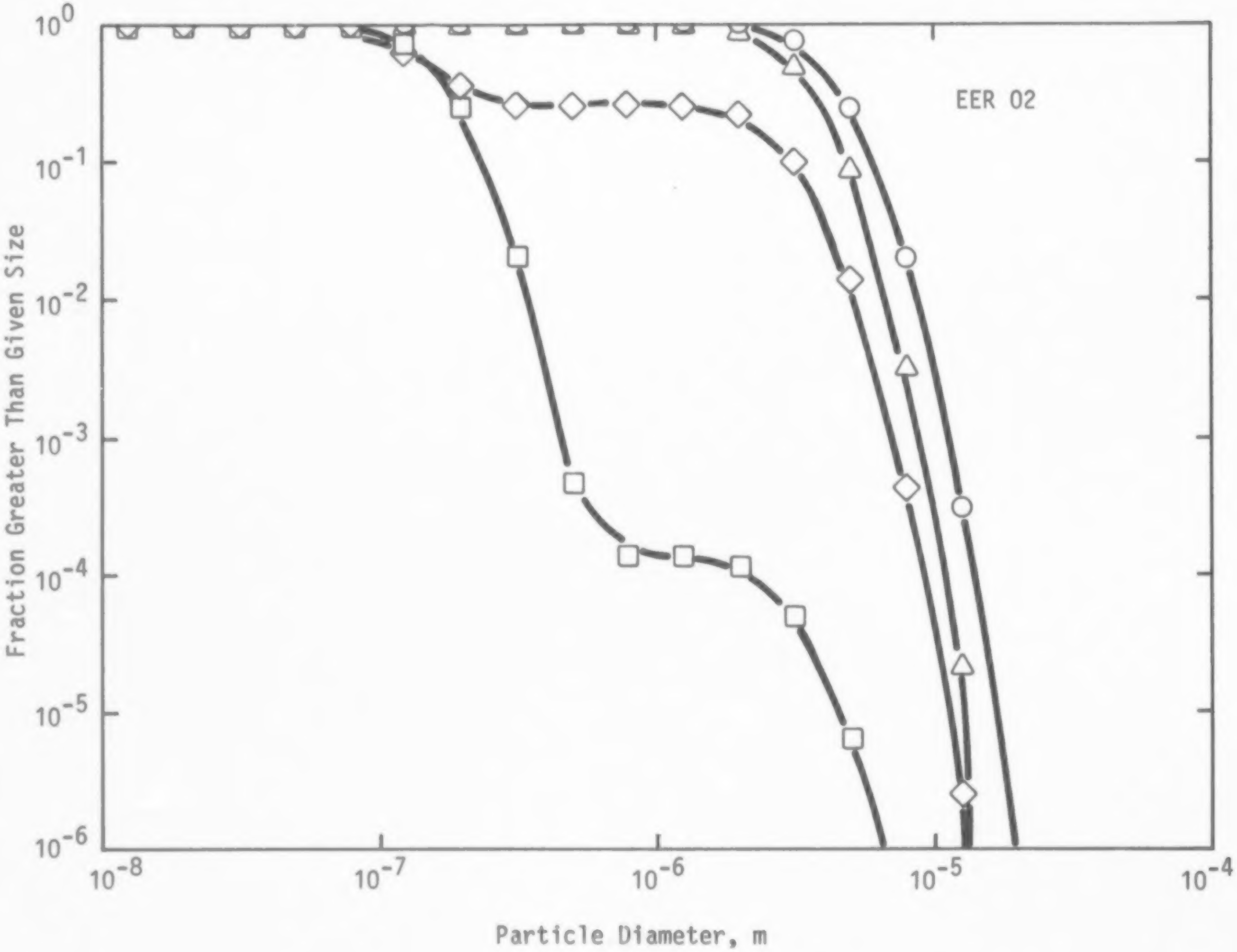

Figure 7-26. Simulation EER02.

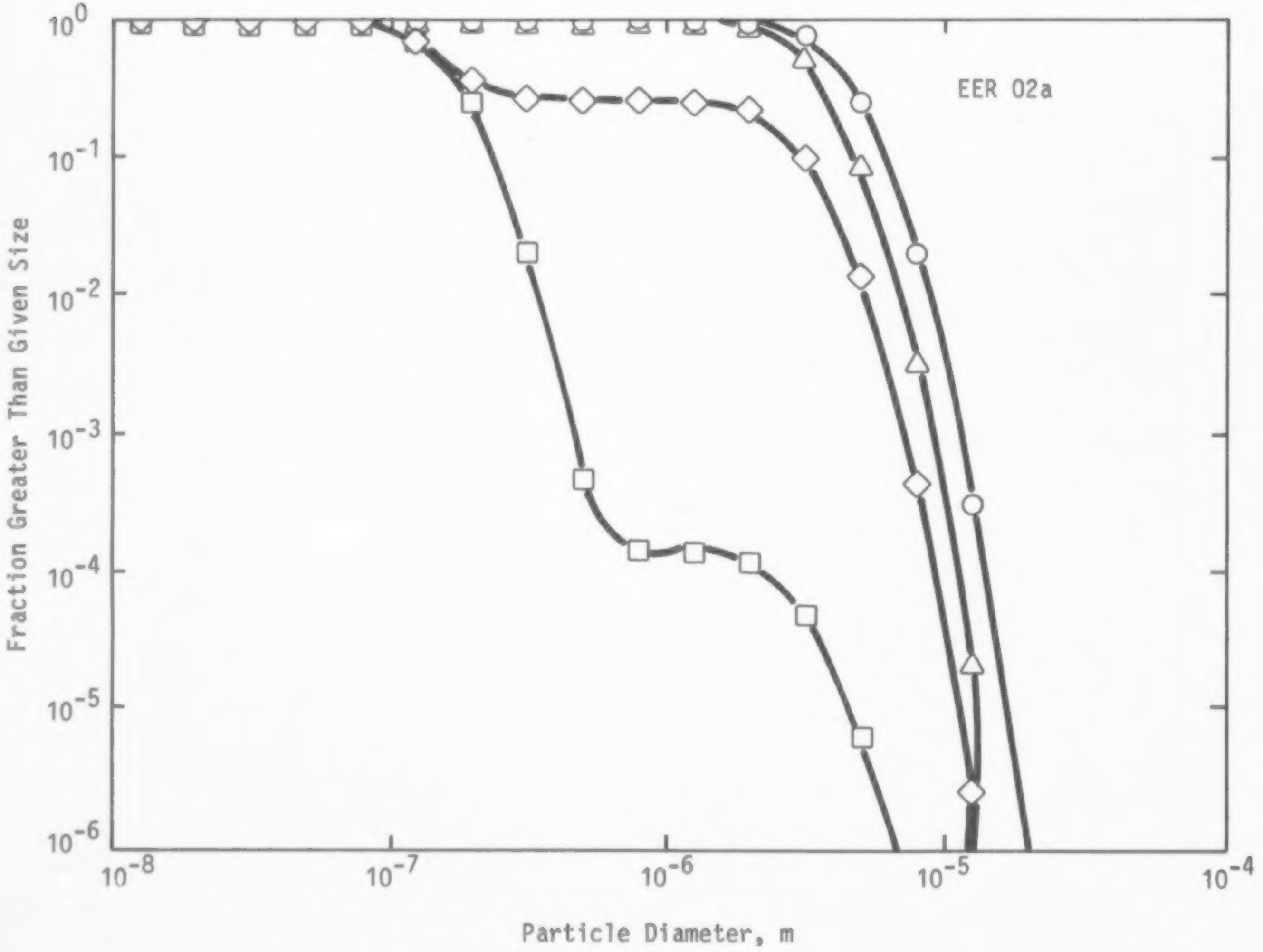

Figure 7-27. Simulation EER02a.

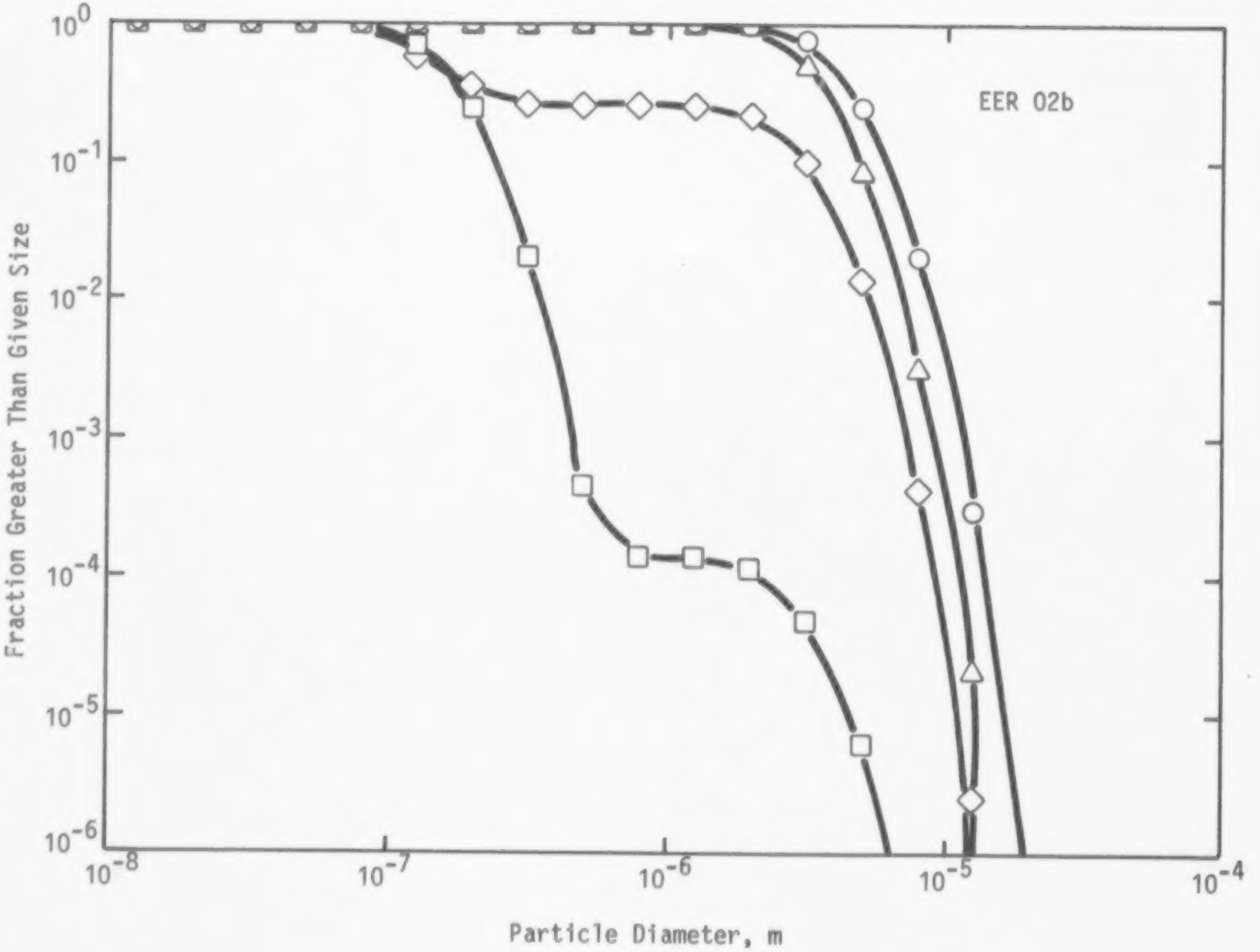

Figure 7-28. Simulation EER02b.

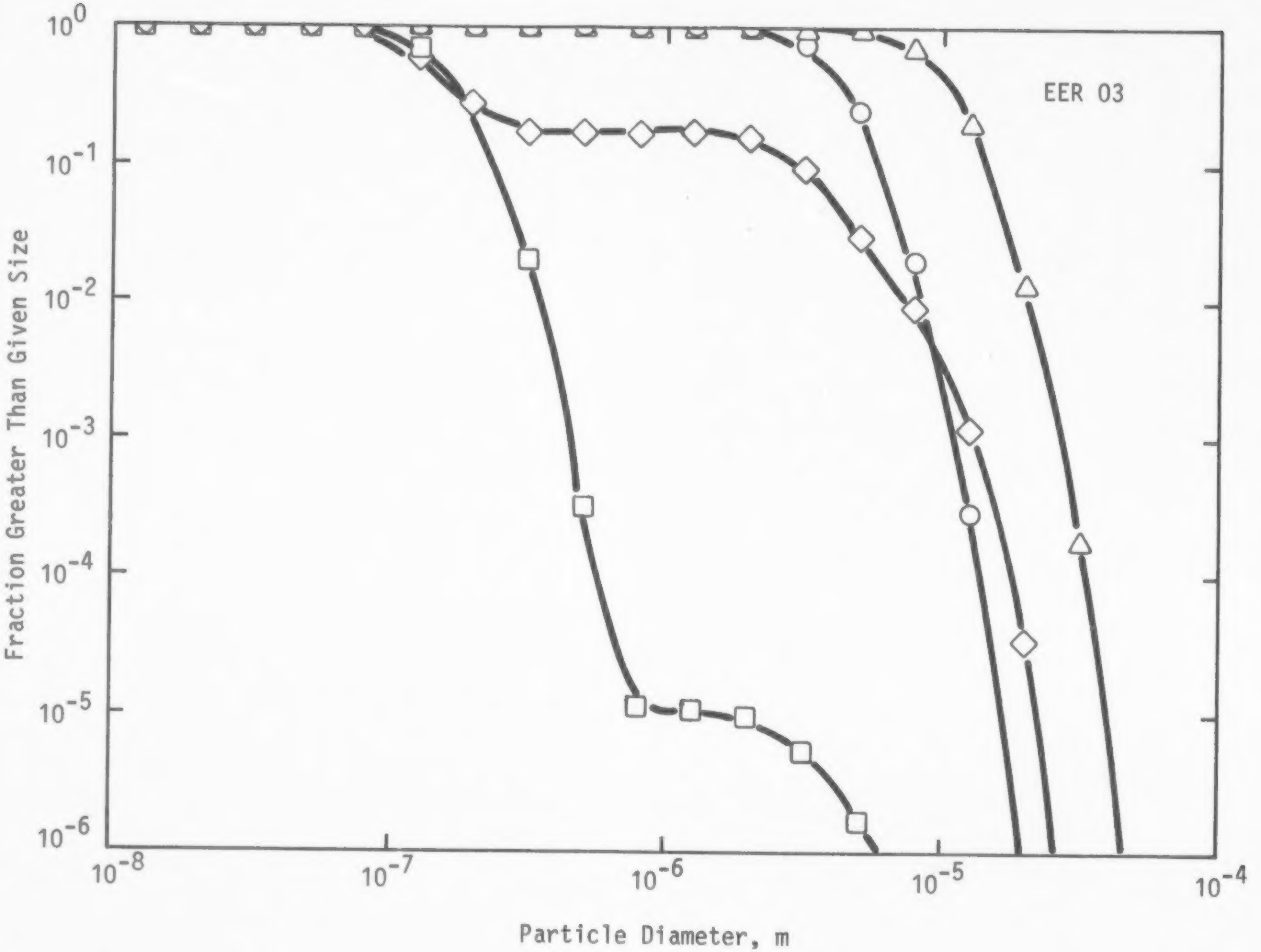

Figure 7-29. Simulation EER03.

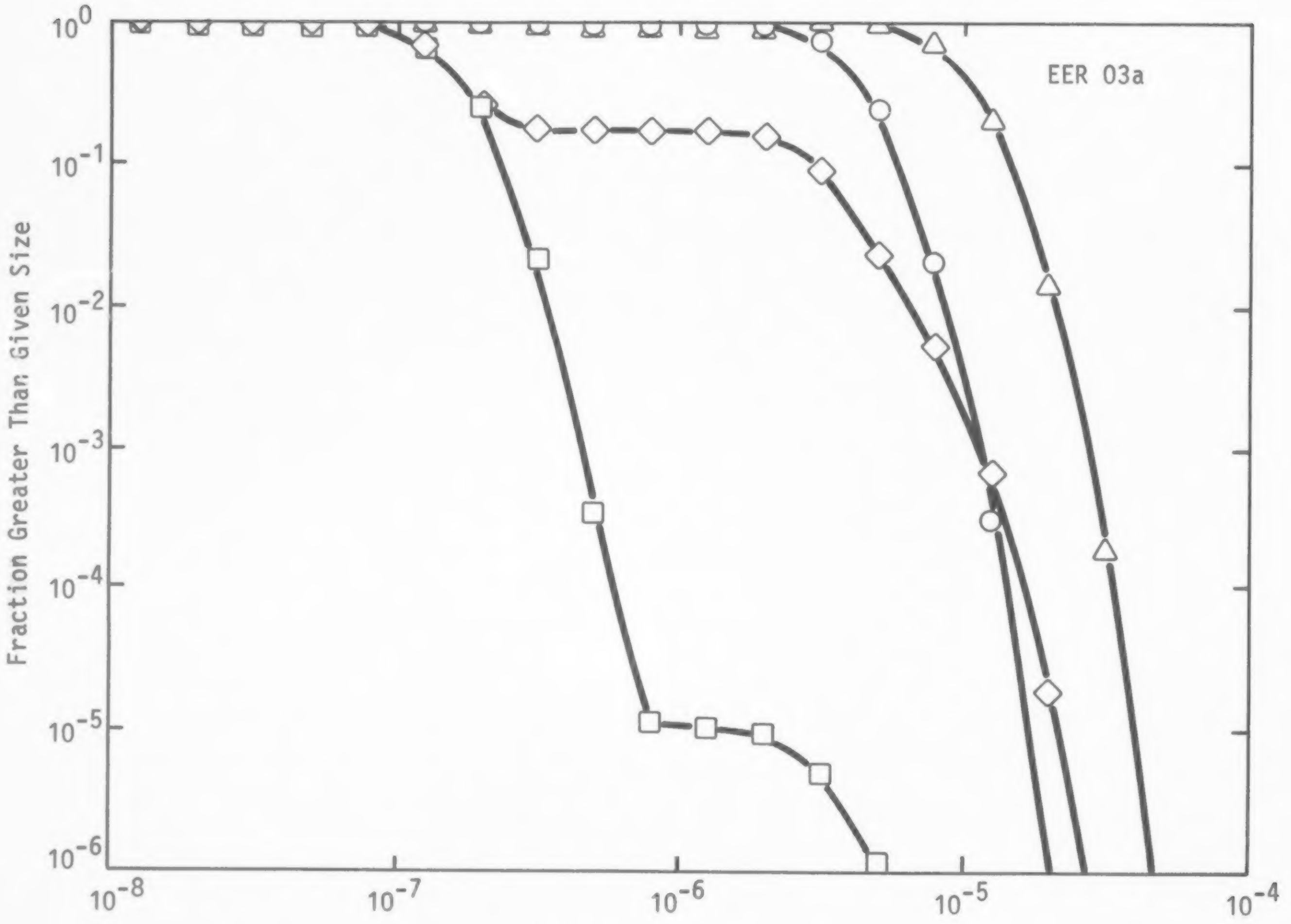

Figure 7-30. Simulation EER03a.

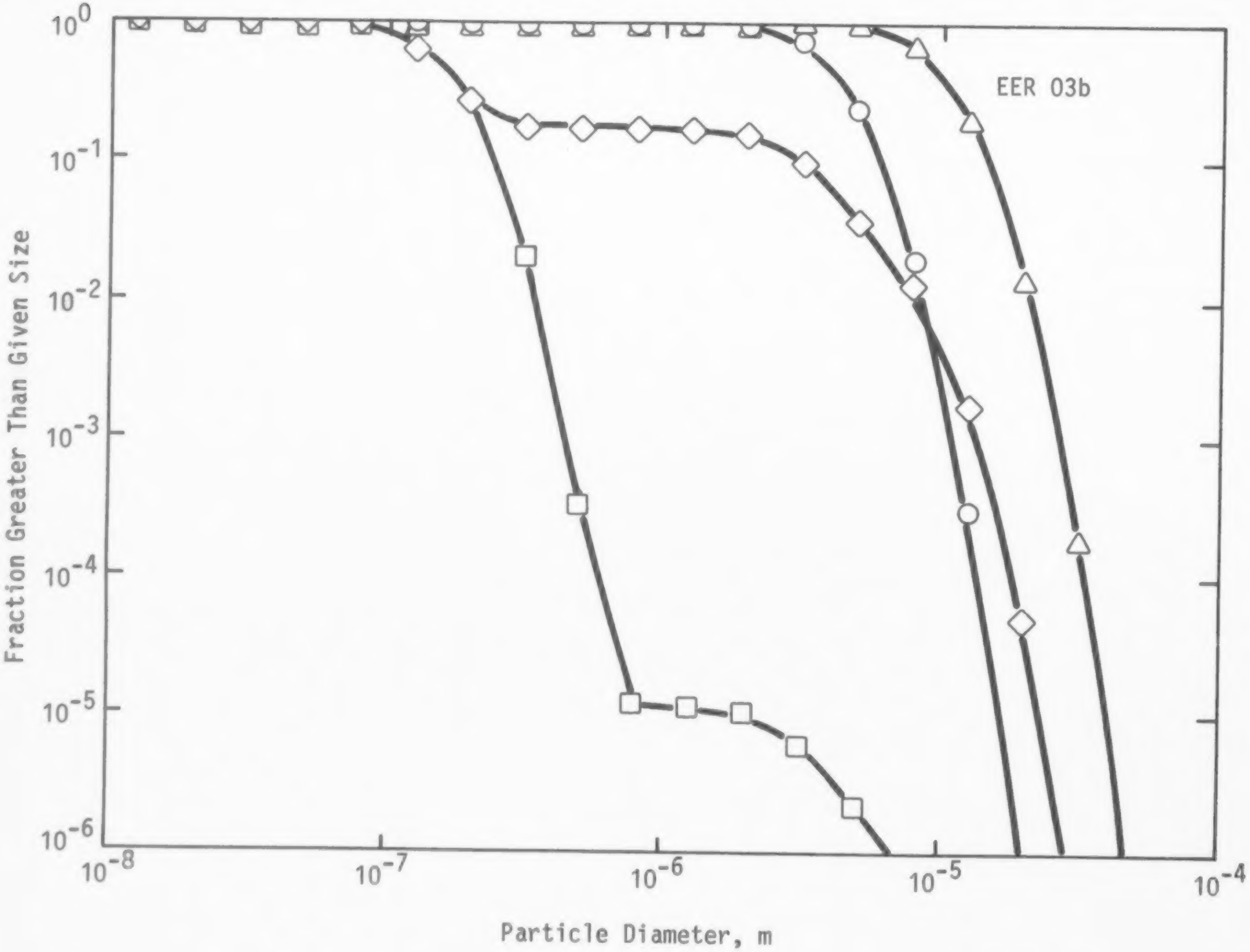

Figure 7-31. Simulation EER03b.

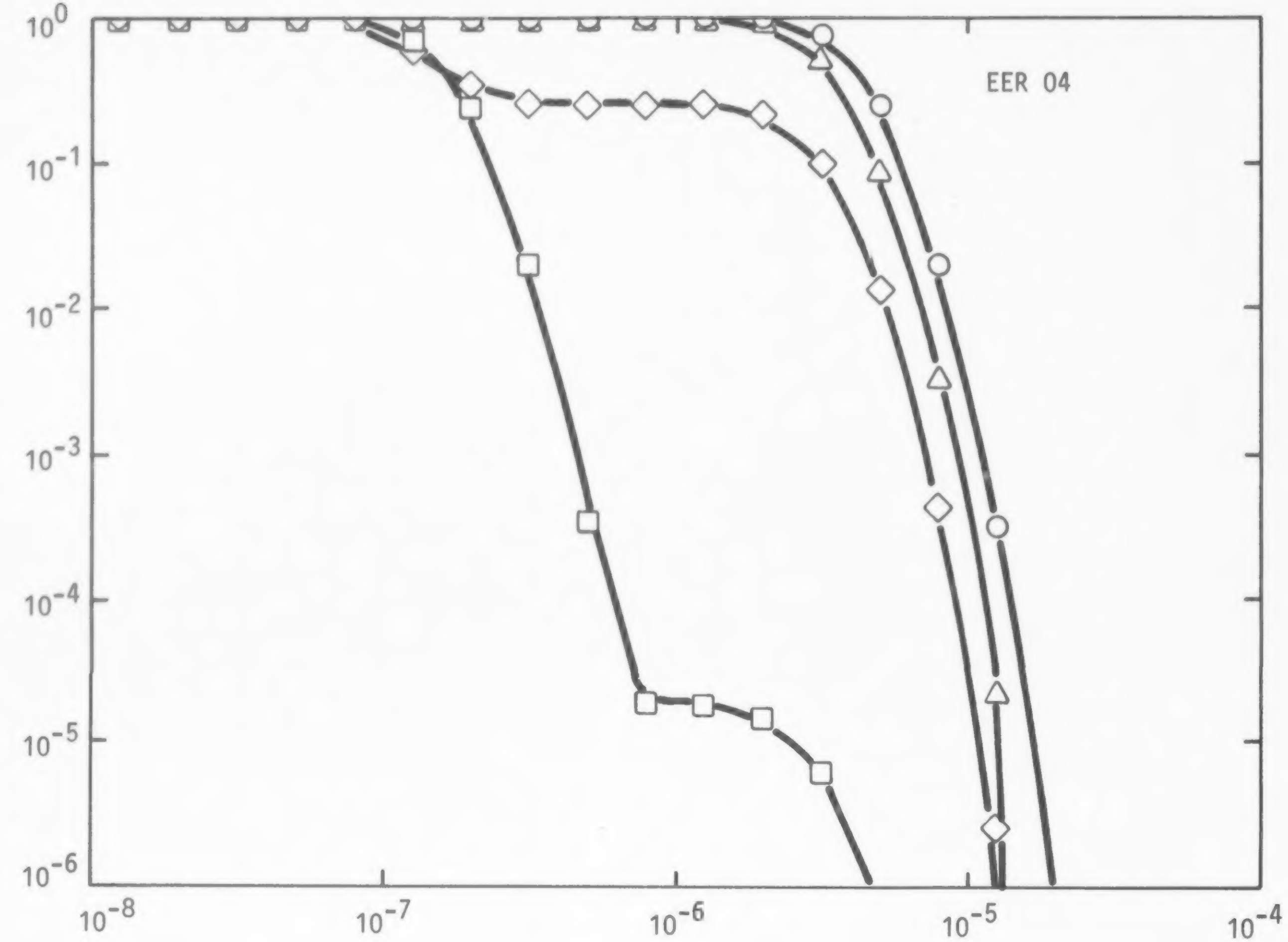

Figure 7-32. Simulation EER04.

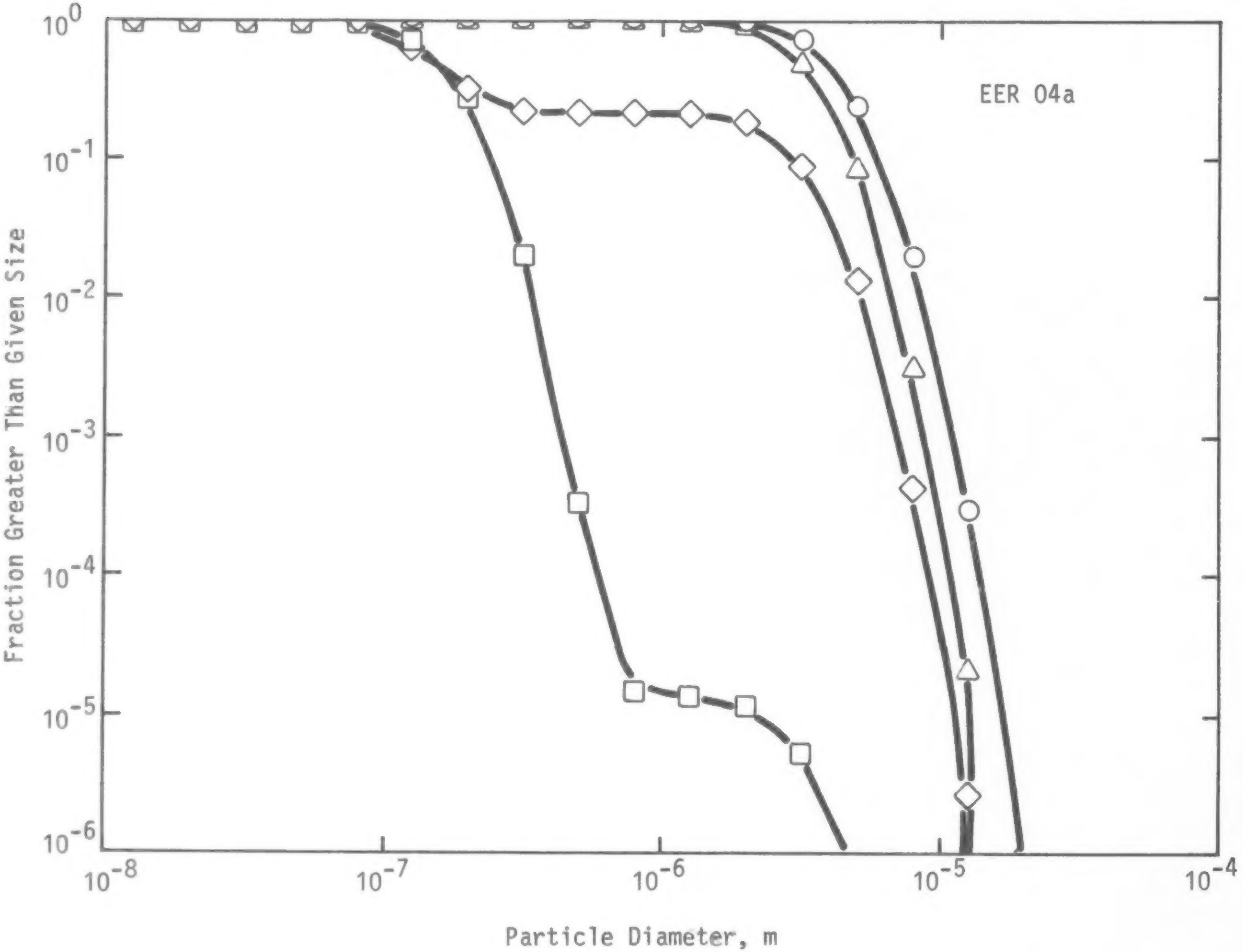

Figure 7-33. Simulation EER04a.

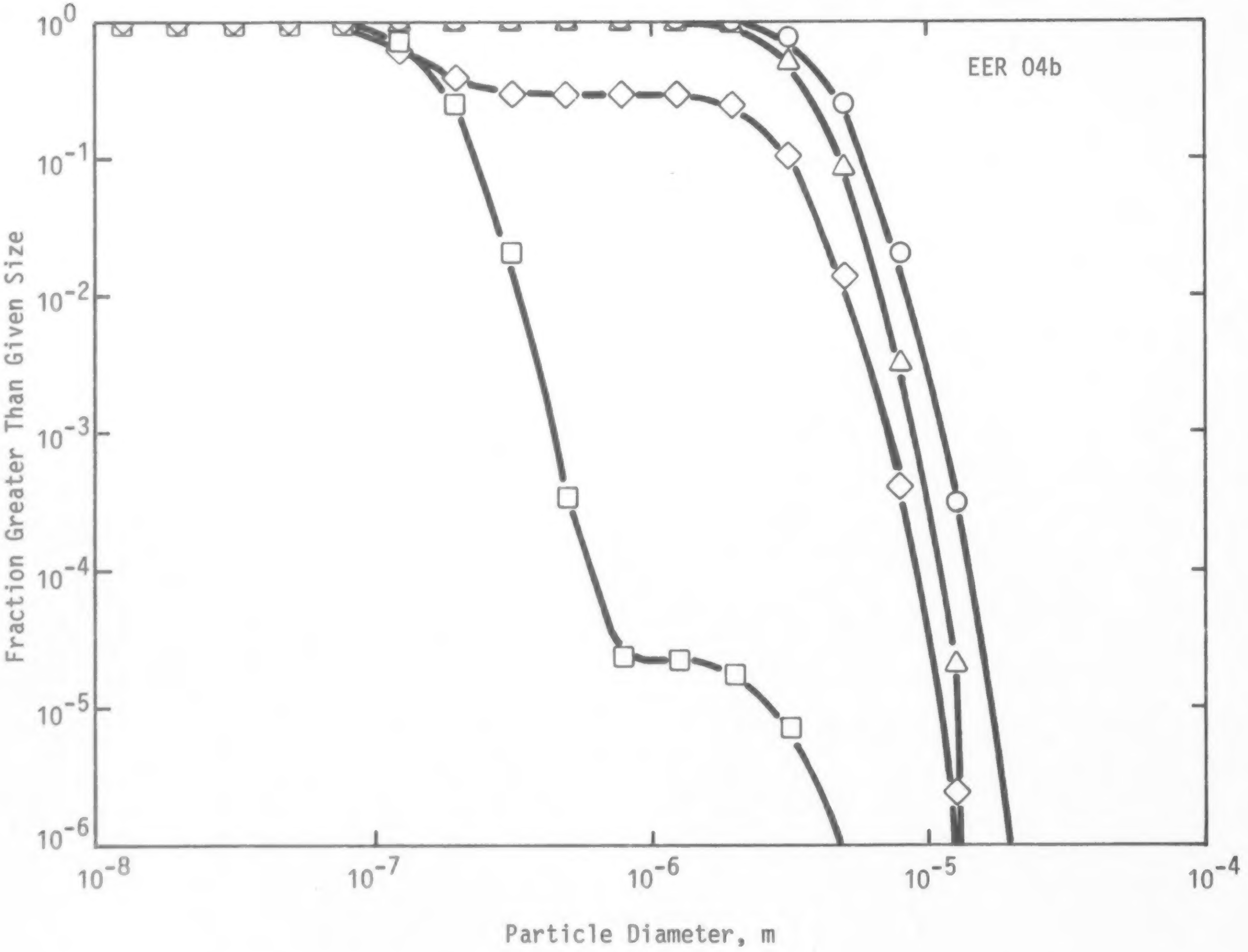

Figure 7-34. Simulation EER04b.

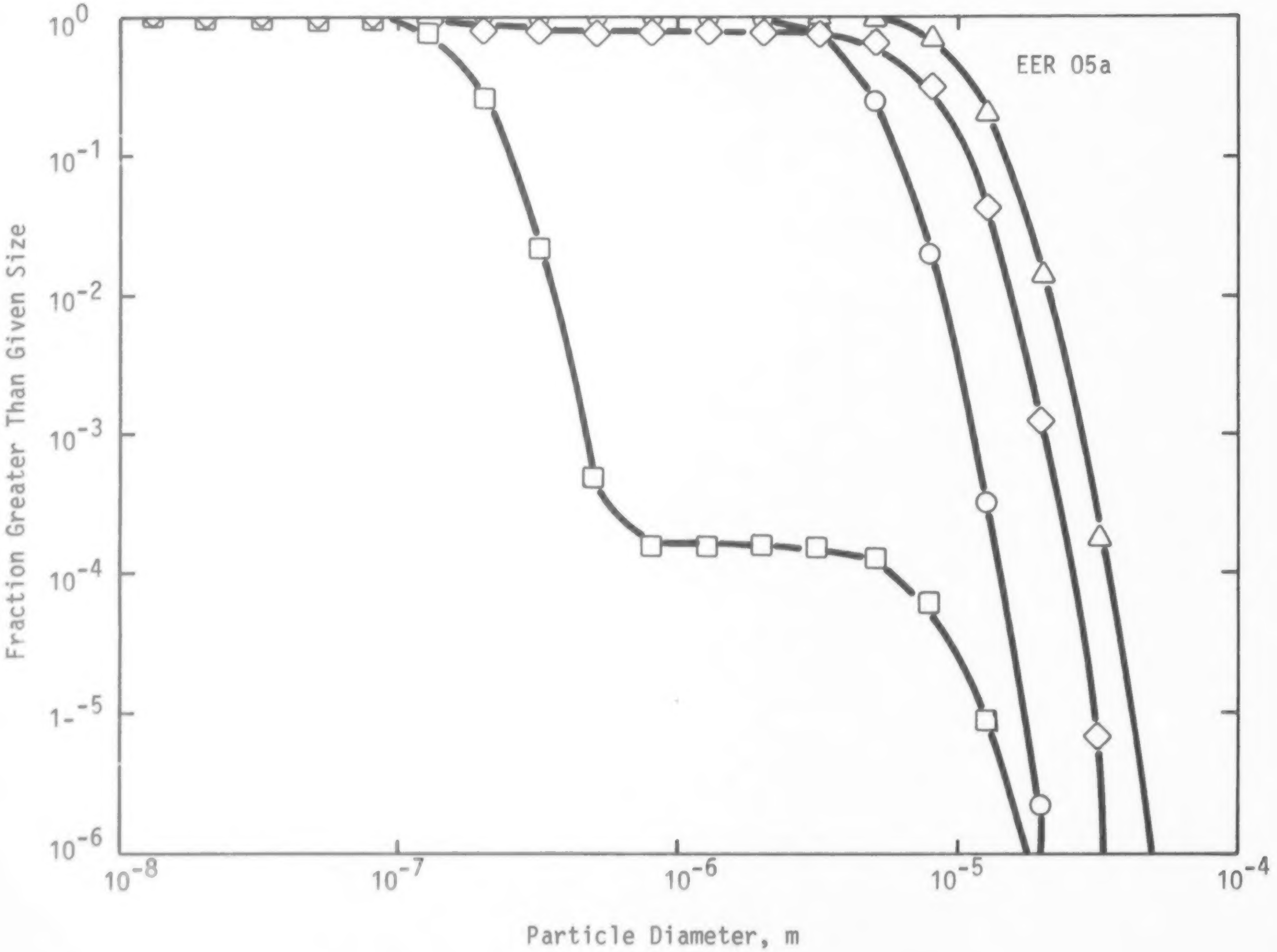

Figure 7-35. Simulation EER05a.

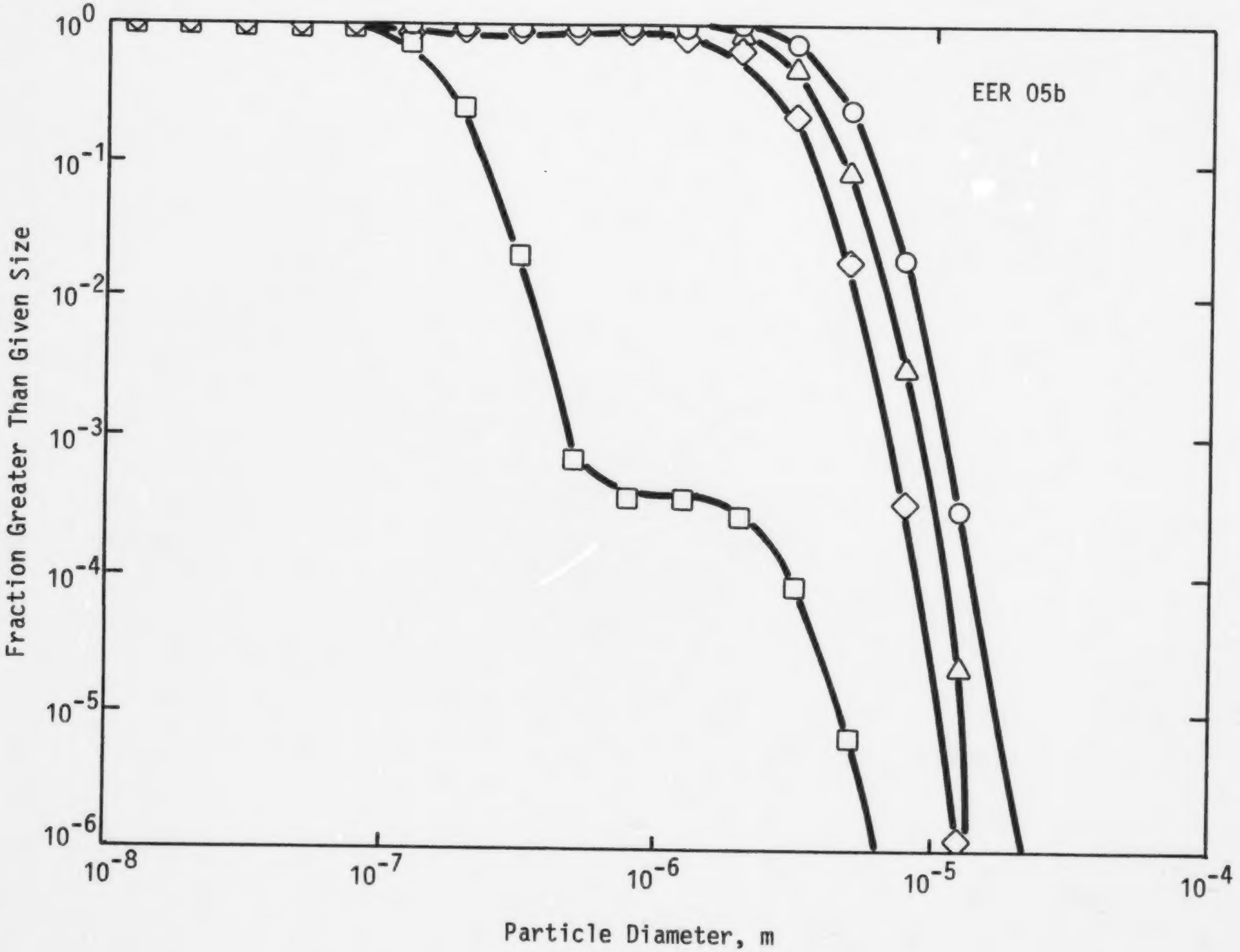

Figure 7-36. Simulation EER05b.

than that for the Indiana coal. The probable explanation for this behavior is that the required additive concentration also goes up by about a factor of 7 for the Kentucky compared to the Indiana coal. This coincidence is due to the fact that the ash-to-sulfur ratios in both coals is about the same, and sodium additive concentration is directly related to the sulfur content of the coal.

By far the largest effect on the sodium additive disposition as a function of particle size is seen in the output from runs "eer05b" (shown in Figure 7-36). Here, the "effective surface area" equivalent mass of sorbent, given a BET surface area of 25 square meters/gram, is input to the model. This simulation effectively allows sodium to condense not only on the outer spherical shell of the sorbent, but also on the surface area within the sorbent pores as well. Run 05a (Figure 7-35) corresponds to a Vicron sorbent and an Indiana coal, and 05b to a Longview sorbent and an Indiana coal. In both cases, 80-90 percent of the sodium condenses on the larger particles. It is obvious that this condensation is taking place on the sorbent itself, because the steepest changes in the mass fraction distributions are seen in the neighborhood of the sorbent's mean diameter (12 micrometers for the Vicron and 4 micrometers for the Longview).

In conclusion, it is apparent that the submicron ash aerosol can act as a major competitor for additive condensation. A major question to be addressed is to what extent the internal surface area of the sorbent is truly available for condensation. As stated initially, only physical phenomena have been examined here, and other phenomena, such as chemical reactions which may enhance condensation, have not been considered.

7.3 Conclusions

The effectiveness of promoted sorbents for SO_2 control may be significantly less in actual, coal-fired systems than in SO_2-doped, natural gas tests due to the presence of the submicron ash aerosol. The enhancement associated with the more volatile promoter, sodium bicarbonate, was almost completely eliminated when used with bituminous coal. External contact between the promoted sorbent and coal is not required; separate injection still leads to deactivation. EDS analysis confirmed the presence of sodium on the mineral ash as well as the sorbent, suggesting that the controlling contacting mechanism is vaporization and uniform sodium condensation. Condensation modeling calculations indicated that more than 90 percent of the added sodium could condense on the submicron ash aerosol if the sorbent particles were large and internal surface area was not available. X-ray diffractograms indicated that the condensed sodium reacted with refractory oxides present in the coal ash to form sodium silicates, thereby effectively reducing the sodium available for direct reaction with SO_2.

Coal ash has less influence on the promotion effect of chromium, a relatively non-volatile promoter. EDS analysis indicated that the chromium was primarily associated with the calcium; little chromium was found with the ash. Since the primary contacting mechanism for chromium promotion appears to be direct contact (due to premixing, hydration, etc.), the submicron ash has far less opportunity to block the promotion process than with sodium. Increasing the ash/promoter ratio, decreased overall capture for both sodium and chromium enhancement.

In conclusion, the effectiveness of sodium promotion is reduced in coal-fired systems because sodium condensation on the submicron ash aerosol greatly decreases the amount of sodium which actually reaches the calcium sorbent and the benefits to sorbent morphology are decreased correspondingly. In addition, part of the sodium which condenses on the ash reacts to form silicates and is, therefore, unavailable for direct sulfation. The submicron ash aerosol can also consume chromium and reduce its enhancement effect; however, this impact is smaller because only a small fraction of the chromium is ever vaporized.

PART IV. PROCESS EVALUATION

8.0 SULFATION RATES FOR DOPED SORBENTS

A parametric study examining the influence sorbent type, promoter, temperature, and reaction time on the sulfation kinetics was performed in the DXRD. First, a discussion of the sulfation kinetics for Vicron (without a promoter) is provided followed with a discussion on the results for the doped sorbents.

8.1 Reaction Kinetics for Vicron Sulfation

The kinetics of limestone sulfation are complicated by the occurrence of diffusional limitations created by the $CaSO_4$ product. The latter is made more difficult in this situation because the $CaSO_4$ can act to block pores as well as to "cover" unreacted CaO. As a result it is not meaningful to derive classical reaction rate expressions for the sulfation reaction and a complete treatment of the diffusional processes was beyond the scope of this program. Thus the approach taken here was to explore the effects of the typical reaction kinetic parameters (temperature and SO_2 concentration) and to obtain some information on the magnitude of the rates associated with low sulfation conversion (chemical reaction controlled) as well as those associated with higher conversions where diffusional processes would be expected to be limiting. Finally, because high temperatures contribute to increased sintering rates as well as to increased sulfation rates, a separate study of the sintering phenomena was also undertaken.

During the course of the investigation it was also found necessary to conduct separate experiments using our TGA/GC system. The TGA/GC system was chosen since it is compatible with fairly large sample sizes ($\sim$1 gram) and these are needed in order to determine BET areas and pore size distributions. The procedure here was to load the 1 gram samples on the 3 cm diameter basket and, after calcining and equilibrating at temperature, to expose the sample to the simulation gas. At the conclusion of the run the sample was removed and then subjected to BET and pore size analysis using a Quantachrom Autosorb 6 instrument. Separate sintering experiments were also conducted on calcined Vicron samples. In this case 1 gram samples were placed in a temperature controlled muffle furnace (923-1123 K) and allowed to remain at temperature for times ranging from 10 minutes to 2 hours. Upon removal from the furnace they too were subjected to BET analysis and loss of surface area was taken as a measure of the extent of sintering.

8.1.1 Effect of Calcination

Although the comparison experiments were all run on samples which had been pre-calcined, calcination and sulfation will take place simultaneously during actual combustor applications. Thus, preliminary calcination experiments were conducted in an N_2 environment as well as in the presence of the simulation gas in order to determine whether the occurrence of sulfation would inhibit calcination. In addition, there is a mechanistic question related to whether SO_2 can react directly with $CaCO_3$ ($CaCO_3 + SO_2 + 1/2\ O_2 \longrightarrow CaSO_4 + CO_2$) or whether it must first decompose to CaO. The results of these experiments are shown in Figure 8-1. As can be seen, in an N_2 atmosphere, the $CaCO_3$ totally disappears in less than 10 minutes whereas only 20 percent has reacted in the presence of the simulation gas after about 40 minutes. Because there is 8 percent CO_2 in the simulation gas ($P_{CO_2} \simeq .04$ atmosphere), the calcination rate would be expected to be slower and, since over 50 percent of the reacted $CaCO_3$ formed $CaSO_4$ at the end of 40 minutes, it is likely that some portion of the SO_2 is reacting directly with the $CaCO_3$. Consequently, it is not possible to determine whether simultaneous sulfation inhibits calcination.

8.1.2 Effect of Surface Area

In a gas-solid reaction, the rates would be expected to be proportional to the total surface area of the solid. Thus a major objective in the preparation of solid sorbents is to create as high a surface area as possible. Table 8-1 shows the results of BET measurements on three of the solid sorbents: the Vicron baseline, the pressure hydrate baseline and the

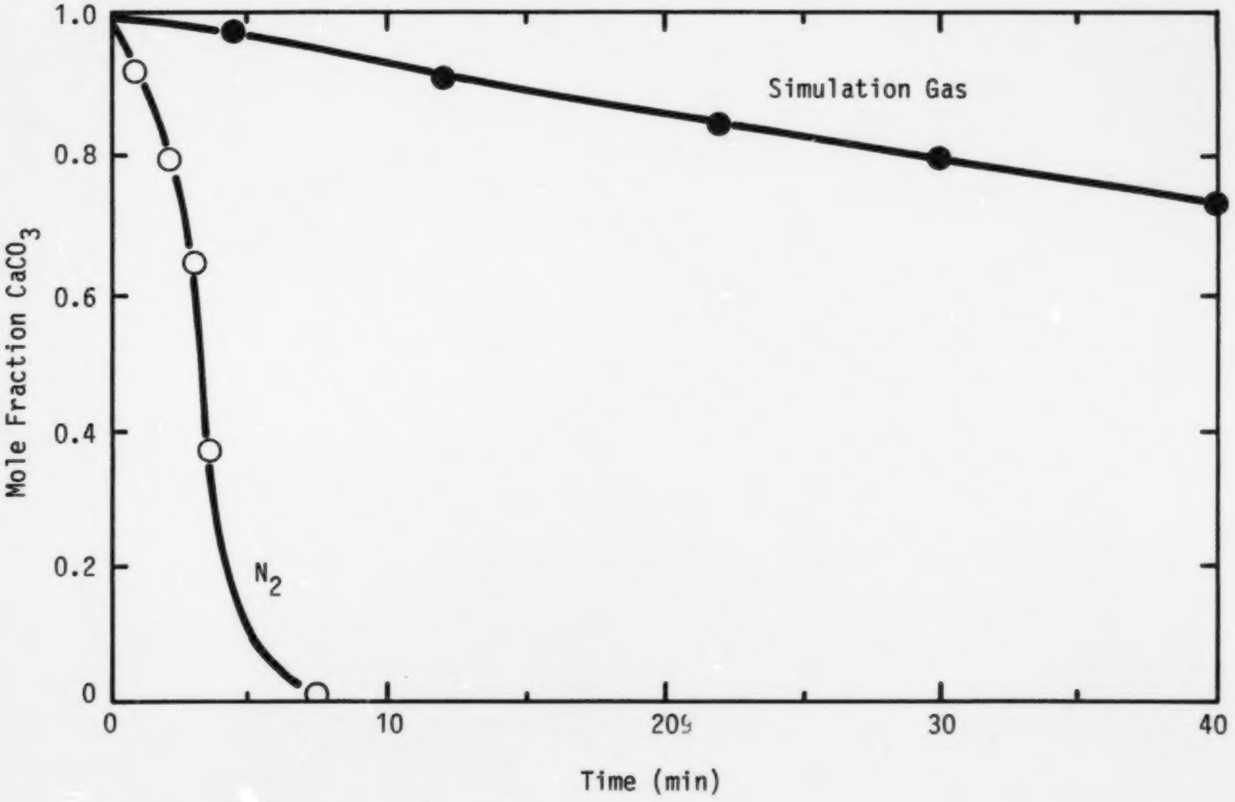

Figure 8-1. Vicron calcination rates (T = 923 K).

TABLE 8-1. BET MEASUREMENTS ON SELECTED SAMPLES

Sample	BET Area m^2/g	Pore Volume	
		cc/g	% by Pores < 100 A°
Vicron			
Uncalcined	0.8	0.006	16
Calcined[a]	35	--	--
100% Sulfated	1.5	0.013	13
Baseline Pressure Hydrate			
Unreacted	73	0.237	62
CrO_3 Pressure Hydrate			
Unreacted	49	0.353	24
76% Sulfated	2.3	0.05	4
100% Sulfated	1.2	0.009	13

[a] At 1163 K for 5 minutes.

chromium doped pressure hydrate. In addition, BET measurements were also conducted on three samples which had previously been sulfated on a TGA unit at 1023 K in the presence of the simulation gas. As can be seen, the pressure hydration process produces a baseline surface area which is almost twice that of calcined Vicron and this is due to the high percentage of pore volume which is contributed by the smaller pores. It is interesting that when the same process is used on the CrO_3 doped sample, the pore size distribution shifts to larger pores and there is a concomitant loss of surface area. As expected, the reacted samples all show an extreme loss in pore volume and surface area although it is difficult to determine the conversion level at which the largest pores become blocked.

8.1.3 The Effect of SO_2 Concentration

Figure 8-2 shows the formation of $CaSO_4$ for Vicron when exposed to SO_2 concentrations between 500 and 15,000 ppm (6% O_2, remainder N_2). As can be seen, there is a steady increase in rate as the SO_2 concentration is raised to 10,000 ppm but the rate drops significantly when the SO_2 concentration is raised to 15,000 ppm. Although not shown in Figure 8-2, these experiments were repeated and the drop in rate from 10,000 ppm SO_2 to 15,000 ppm SO_2 is a repeatable phenomenon. The explanation may very well be attributed to pore mouth plugging where the shape of the curves in Figure 8-2 are due to a competition between the rates of plugging and pore diffusion. At the lowest SO_2 concentration (500 ppm), the initial reaction rates are slow and the SO_2 is able to diffuse into the pores at a rate which is faster than the plugging rate since the latter is proportional to the initial reaction rate. Thus, the shape of the 500 ppm curve does not display the sharp knee characteristic of the transition from reaction rate control to diffusion control. However, as the SO_2 concentration is raised to 10,000 ppm, there is a clear indication of diffusion control. At 15,000 ppm, the global sulfation rate is reduced due to very rapid initial sulfation at the outer surface of the particle which leads to severe pore mouth plugging. Thus, in this case, diffusion is the controlling mechanism right from the start of the experiment.

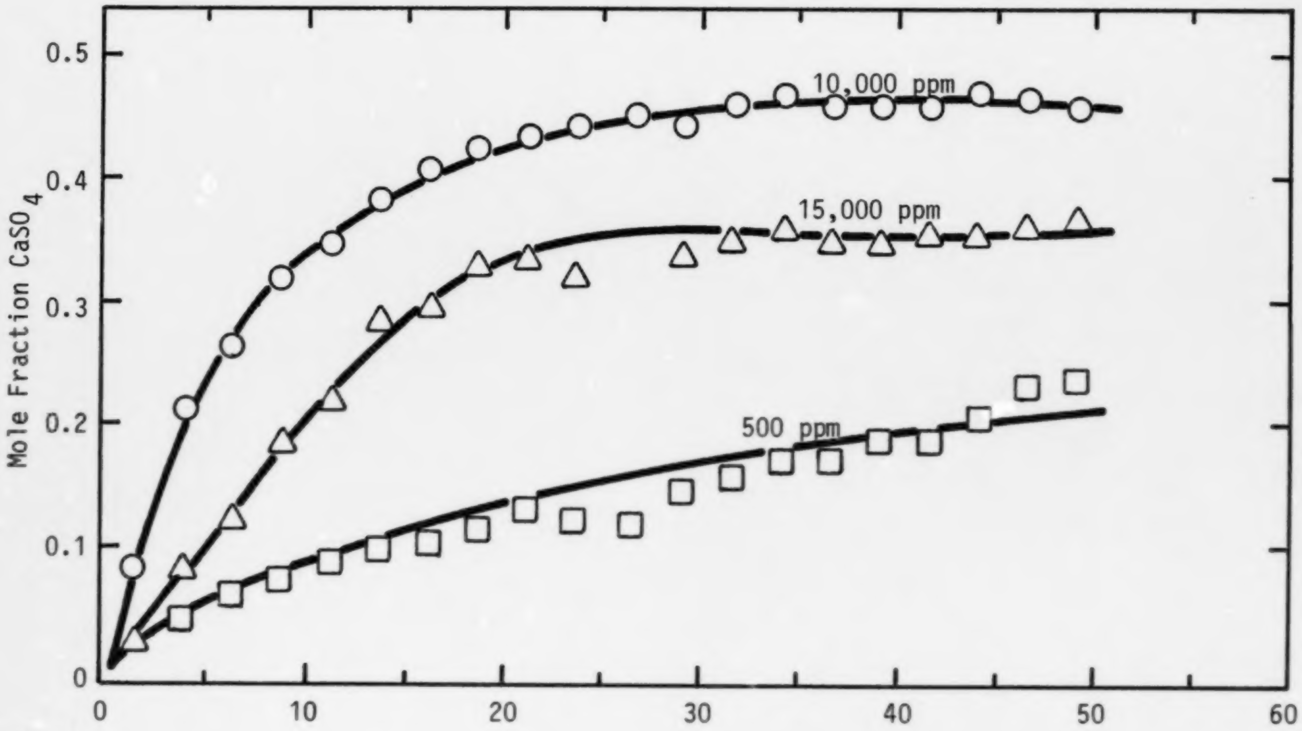

Figure 8-2. Vicron sulfation as a function of SO_2 concentration ($6\%\ O_2$, remainder N_2, 923 K).

A selected number of experiments were also run at 923 K with 8 percent CO_2 in the gas and variable SO_2 concentration. Although recarbonation was apparent, the sulfation rates were very similar to those presented in Figure 8-2. In fact, at the highest SO_2 concentration (14,300 ppm), the rates of sulfation and recarbonation were similar up to a concentration of about 20 percent mole fraction. At that point, the calcite was observed to partially decompose so that it reached an equilibrium value of 10 mole percent. This behavior is apparently due to local changes in the surface temperature as the exothermic sulfation and recarbonation reactions take place. In any case, there was little evidence that recarbonation inhibited sulfation, at least up to 40 percent $CaSO_4$ formation.

8.1.4 The Effect of Temperature

As can be seen from Figure 8-3, there was only a moderate increase in the Vicron sulfation rate when the temperature was raised from 923 K to 1083 K in the presence of the simulation gas. Even though the shape of the conversion curves indicates that diffusion becomes controlling after about 20 percent conversion, the temperature effects were expected to be much stronger than that which was observed (since solid state diffusion is an activated phenomenon).

8.1.5 Sintering

One of the questions which arose out of the temperature data shown in Figure 8-3, is whether the temperature dependence of sintering was much stronger than the temperature dependence of sulfation. Consequently, a separate set of sintering experiments were conducted using loss of BET area as a measure of the sintering rate. Figure 8-4 shows the results of these experiments over a temperature range of 997 K to 1163 K.

Since the experiments were run by placing uncalcined Vicron in a furnace, there is a competition between calcination (which increases surface area) and the sintering process. As a result, the surface area of the freshly calcined sample was determined by back extrapolating the data to a

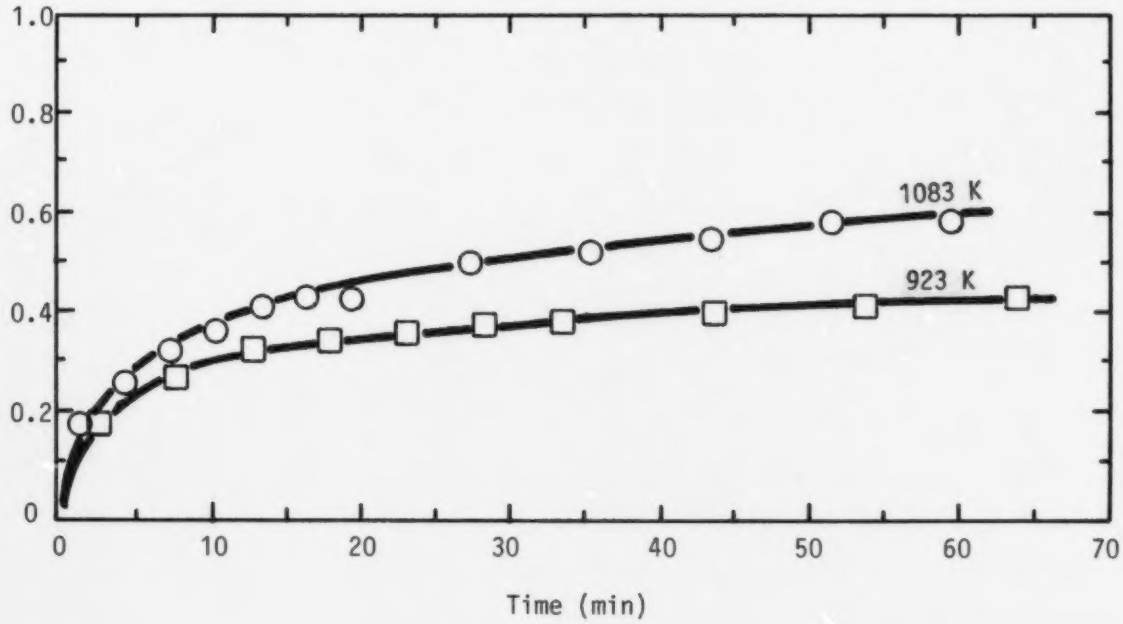

Figure 8-3. Vicron sulfation as a function of temperature (simulation gas).

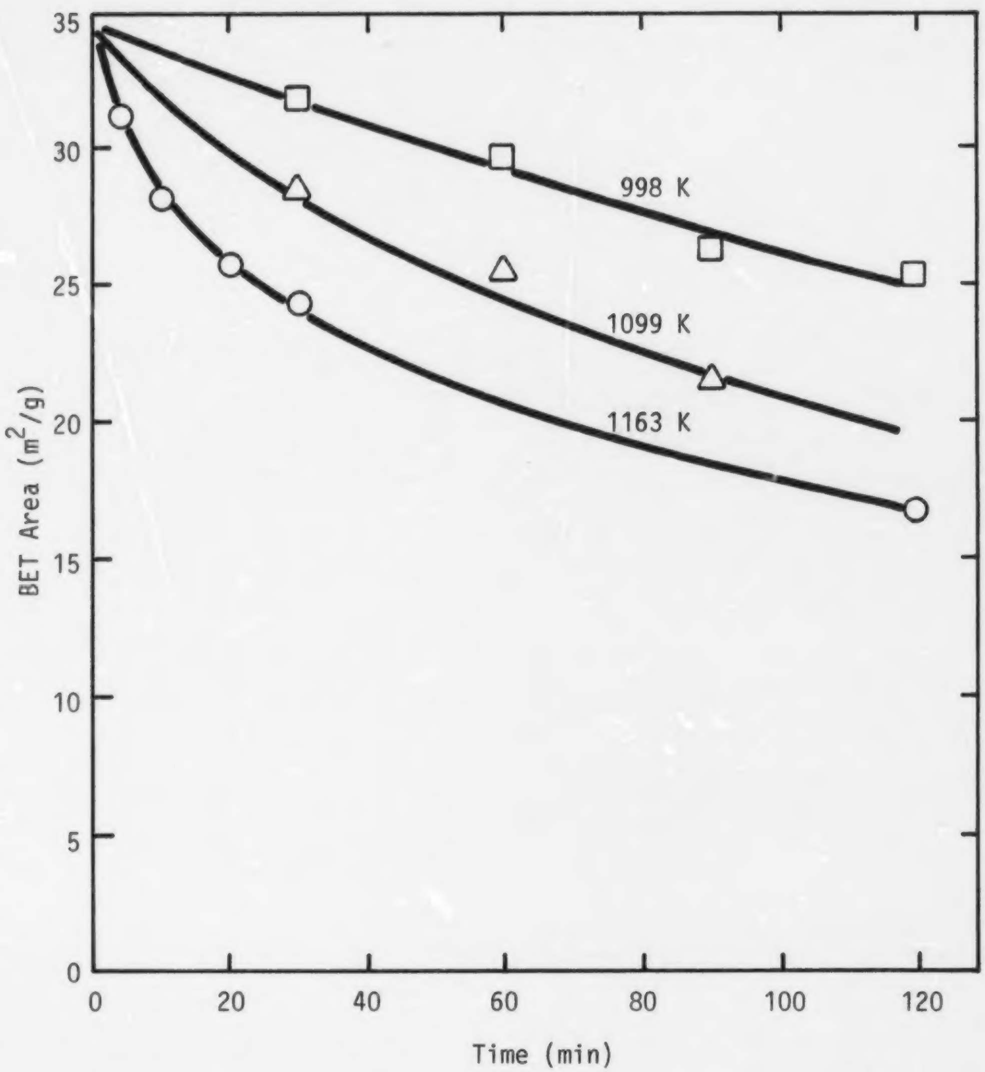

Figure 8-4. Vicron sintering as a function of temperature.

common point of intersection (~35 m^2/g). Although at first glance it would seem that the surface area reduction is small at the temperatures of interest (923 K-1083 K), it should be kept in mind that Borgwardt's shrinking core model predicts that the apparent rate constant will be proportional to the square of the BET area (this will be discussed later). Consequently, the sintering data were fit to a typical sintering kinetic model

$$\frac{dA}{dt} = -k_s A^n \tag{8.1}$$

$$k_s = k_{s_o} \exp\left[\frac{-E_s}{RT}\right] \tag{8.2}$$

When this was done, a reasonable fit to the data was obtained with

$$n = 5$$

$$k_{s_o} = 2.22 \times 10^{-4} \ (m^2/g)^{-4} \ min^{-1}$$

$$E_s = 22.3 \ KCal/mole$$

The high order of the sintering reaction is not unusual and values for supported catalysts typically range from 2 to 22 (27).

Reaction Rate Analysis. The rates of sulfation can be limited by chemical reaction, pore diffusion and/or grain diffusion. Because of the shape of the curves shown in Figures 8-2 and 8-3, chemical reaction rates would not be expected to be limiting in these experiments. If pore diffusion is limiting, then the SO_2 reactants will have a difficult time in reaching unreacted CaO grains which are present within the CaO particles. Once the SO_2 does not reach the grains (by pore diffusion mechanisms), then the reaction may proceed either under chemical reaction control or under the control of SO_2 diffusion through the $CaSO_4$ product layer.

Borgwardt et al. were able to model the sulfation of calcined limestone by assuming grain diffusion limitations which fit the classical shrinking core model

$$F(x) = k_d t \tag{8.3}$$

where

$$F(x) = 1-3(1-x)^{2/3} + 2(1-x) \tag{8.4}$$

$$k_d = 2530\ A^2(P_{SO_2})^{.62} \exp\left[\frac{-36600}{RT}\right] \tag{8.5}$$

with P_{SO_2} in atmospheres, the initial surface area, A_o, in M^2/g and k_d in sec^{-1} units. Thus a plot of the functional dependence on conversion, F(x), versus time should be linear.

We also attempted to fit our data according to the grain diffusion model presented above. In addition, we added corrections to equation (8.2) in order to account for sintering. This correction accounts for the fact that grain growth would accompany sulfation and the diffusion path would become longer. With this correction, equation (5) becomes

$$F(x) = k_d{}'\ F(t) \tag{8.6}$$

where

$$F(t) = (1 + k_s\ A^4\ t)^{-1/2} t \tag{8.7}$$

and k_s is the sintering rate constant (Eq. (8.2)) and A_o is the initial surface area. Note that F(t) = 1.0 in the absence of sintering.

In all of the experiments conducted here, the grain diffusion model was only able to fit the data (F(x) vs F(t) was linear) up to a CaO conversion of about 50 percent. Furthermore, the sintering correction was found to be important only at the highest temperature (1083 K) where F(t) dropped to .75 at 40 minutes reaction time. On the basis of this analysis it is believed that pore diffusion was probably a contributing factor to the global reaction rate. The calcines used by Borgwardt et al. had particle sizes of approximately 1μ whereas our particle sizes were on the order of $10\ \mu$. Thus it is very likely that the progression of pore mouth plugging served to slow down the sulfation rates to even a greater extent than the occurrence of product layer diffusion on individual grains. In fact, the relatively low dependence on temperature and P_{SO_2} which was observed indicates that pore diffusion was dominant during most of the reaction time. Thus, the occurrence of a straight line fit to equation (8-6) at conversions less than 50 percent is simply a fortuitous result.

8.2 Reaction Kinetics for Doped Sorbents

Experiments were designed to examine three parameters thought to be important to the sulfation rate; they were dopant type, sorbent type, and temperature.

8.2.1 Effect of Dopant and Sorbent Type

A direct comparison of the sulfation of the various doped samples prepared by both pressure hydration and evaporation was conducted at 923 K in the simulation gas. The procedure for both sets of samples was the same, after the sample was mounted on the heating strip, each was heated from room temperature to 923 K in one minute's time in flowing N_2. Although both sets had been pre-calcined it should be noted that the $Ca(OH)_2$ formed during the pressure hydrating was observed to decompose at about 450-773 K which was immediately accompanied by the formation of calcite. The latter was attributed to the recarbonation of CaO from the trace CO_2 present in the N_2 (~300 ppm). Since this was not observed in the evaporatively prepared samples,either CO_2 reacts directly with the $Ca(OH)_2$ or the CaO formed from $Ca(OH)_2$ decomposition is more reactive than the CaO in the evaporatively prepared samples. For comparison purposes, the baseline Vicron samples were also sulfated under the same conditions. However, in this case the Vicron was calcined by holding it at 998 K for one hour in flowing N_2 before being exposed to the simulation gas. An XRD scan at this point confirmed that complete calcination had taken place prior to the sulfation experiment.

Figure 8-5 shows a comparison of the sulfation of the calcined Vicron baseline with the three evaporatively prepared doped samples. Notice that both the sodium and chromium doped samples reach a higher $CaSO_4$ conversion

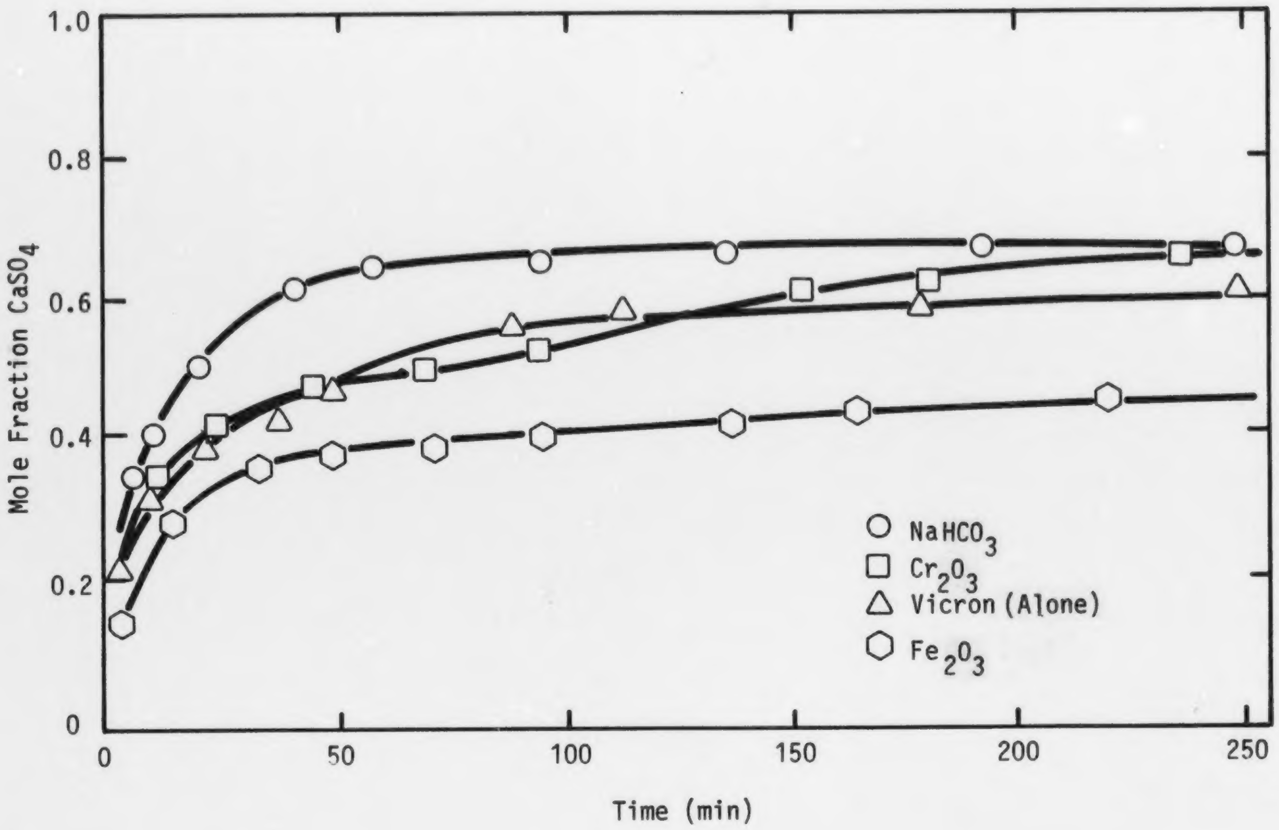

Figure 8-5. Sulfation of evaporatively doped limestone (simulation gas, T = 923 K).

and the initial sulfation are of the sodium sample is much higher than any of the other samples. The iron sample was by far the poorest performer. Figure 8-6 shows a similar comparison for the pressure hydrate samples. Except for the baseline, all of the pressure hydrates perform better than the evaporative samples, particularly the iron sample. Once again, the sodium and chromium samples were superior.

In an effort to gain insight into the difference exhibited by the various dopants, selected samples were also subjected to electron microprobe analysis (EMP) and Scanning Electron Microscopy. The EMP analysis of the sulfated samples indicated that there was no correlation between the presence of the dopant and the presence of the sulfur. In fact, there were a number of situations where the dopant was present only on the outer surfaces of the CaO grains but yet the sulfur was distributed uniformly throughout the grain. In addition, there was clear evidence that $CaCrO_4$ was present in all the chromium doped pressure hydrate samples, both before and after sulfation. Although it was not possible to obtain an accurate concentration of this compound, it appears that its concentration did not change during sulfation. In most cases there was also clear evidence of a $CaSO_4$ "shell" surrounding the unreacted CaO. This is consistent with the DXRD results shown in Figures 8-5 and 8-6 where there is clear evidence of diffusion limited reactions for conversions greater than about 30 percent. Based on these results it is likely that the dopants produce a more stable macropore void fraction; one that is less susceptible to pore mouth plugging. Another plausible explanation is the enhancement of product-layer diffusion through the sulfated shell. Both mechanisms are possible as discussed in Section 6.

8.2.2 Effect of Temperature

Two of the most effective dopant samples, the chromium and sodium pressure hydrates, were also sulfated at temperatures up to 1083 K and compared to the sulfation of the baseline Vicron over the same temperature range. Because sintering was expected to be of significance in these experiments, all of the experiments were conducted by first exposing the

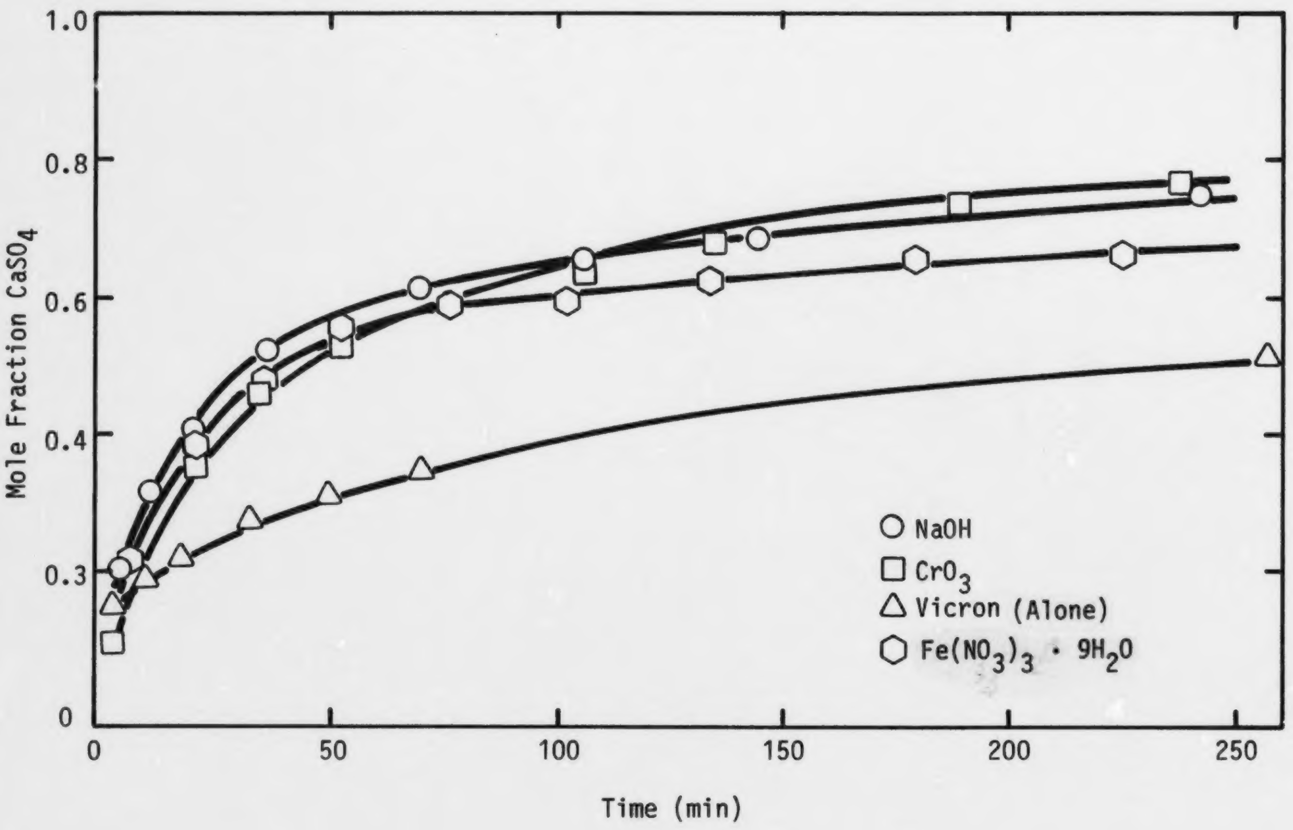

Figure 8-6. Sulfation of doped pressure hydrate limestone (simulation gas, T = 923 K).

samples to 998 K in flowing N_2 for one hour to insure that all started from the same base point.

Figures 8-7 and 8-8 show the time varying formation of $CaSO_4$ as a function of temperature for the sodium and chromium doped samples, respectively. Note that in the case of sodium, the rate increases substantially between 923 and 978 K but only slightly at higher temperatures. It is conceivable that we are experiencing an evaporative loss of sodium at the higher temperatures and/or the rate of sintering above 973 K increases faster than the rate of sulfation. However, as Figure 8-8 shows, the rate of $CaSO_4$ formation in the chromium doped sample increases steadily with temperature, reaching almost 90 percent conversion by the end of the run at 1083 K. It is interesting that while the sodium doped samples were superior at 923 K, it is the chromium doped samples which perform better at 1083 K.

The advantage of using dopants is apparent when Figure 8-3 is compared to the effects of temperature observed in both the sodium and chromium doped pressure hydrates (Figures 8-7 and 8-8). However, since the effect of temperature is much stronger when dopants are used, this would question whether the effects of dopants are really due to enhanced solid state diffusion. That is, if ionic substitution does take place, the apparent activation energy would be expected to decrease, not increase as these data indicate.

Figure 8-9 compares the sodium and chromium doped samples with the Vicron baseline at 1083 K. It is interesting that the initial rate of sulfation is actually higher for the Vicron than it is for the sodium doped sample. However, diffusion limitations take over at a relatively low conversion (20 percent) in the Vicron sample and the sodium doped sample ultimately gives a higher conversion. Another interesting observation here was that the Vicron sample experienced some recarbonation at temperatures as high as 1023 K. However, neither the sodium or chromium doped samples recarbonated once the temperature reached 973 K.

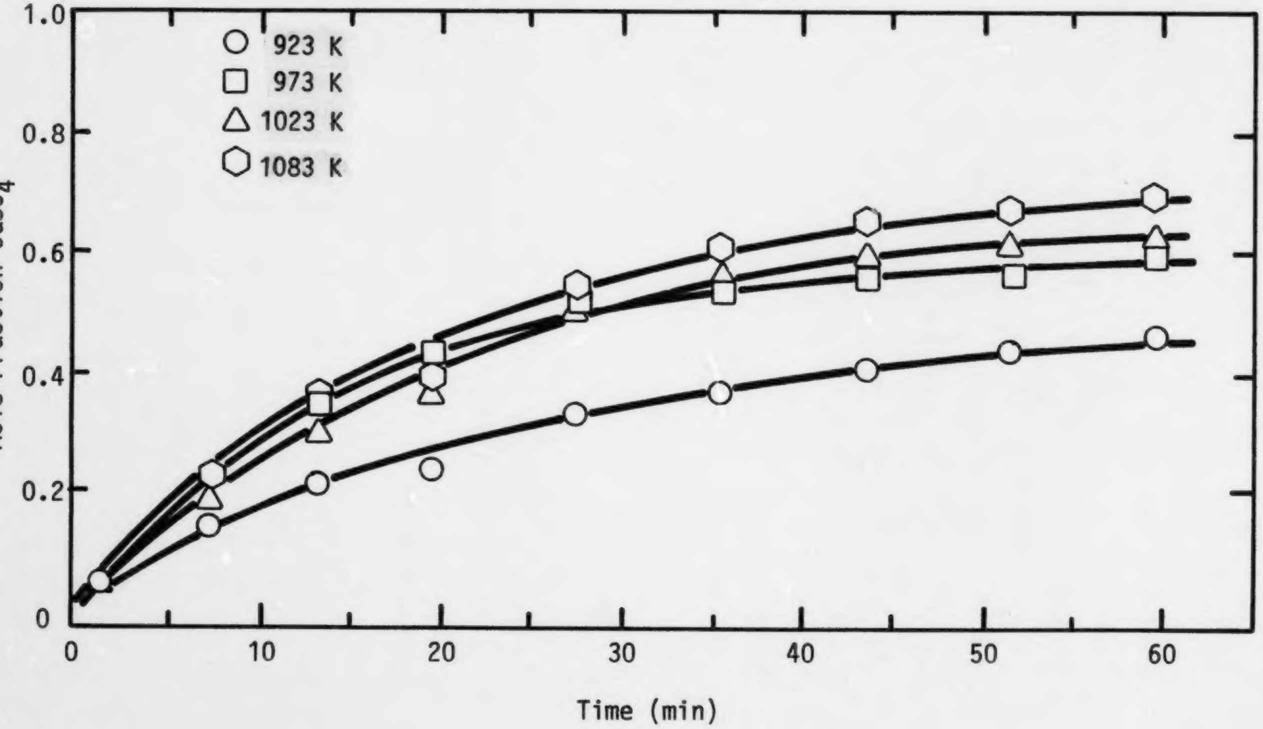

Figure 8-7. Sulfation of sodium doped pressure hydrate sample as a function of temperature (simulation gas).

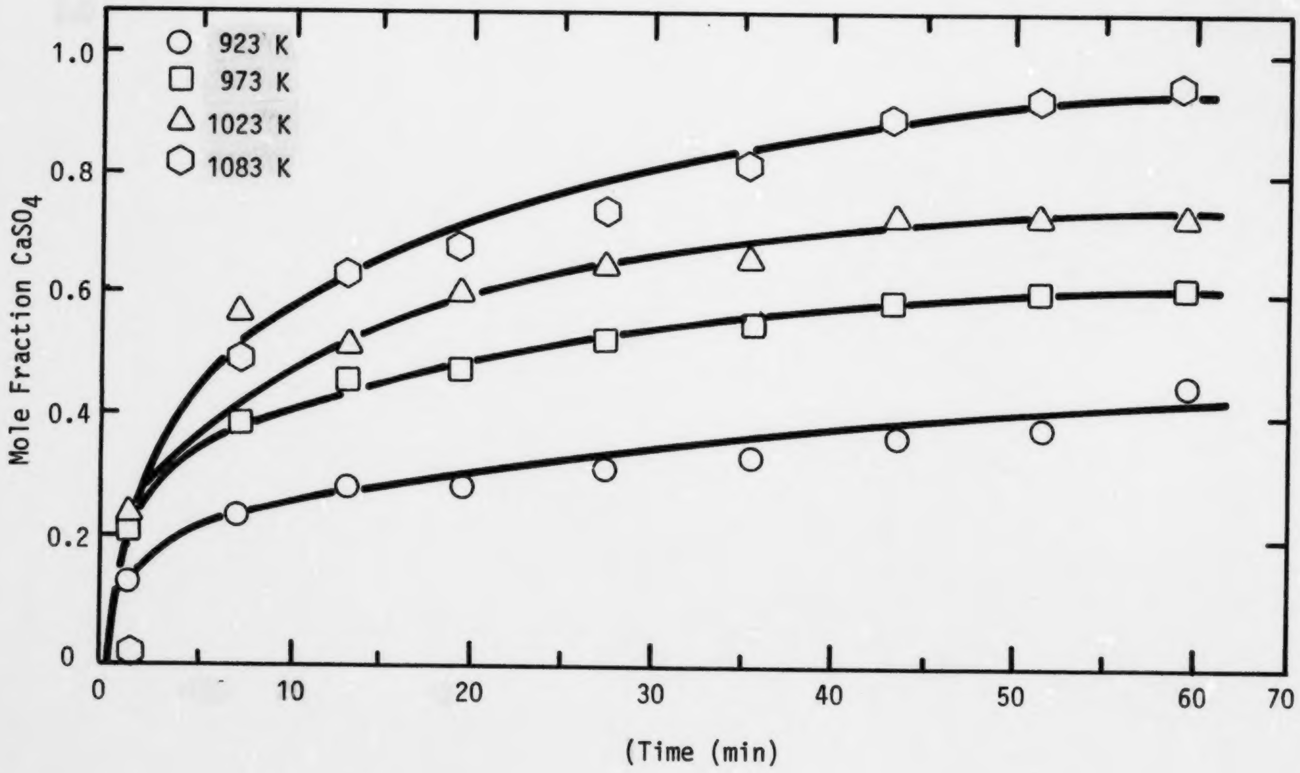

Figure 8-8. Sulfation of chromium doped pressure hydrate sample as a function of temperature (simulation gas).

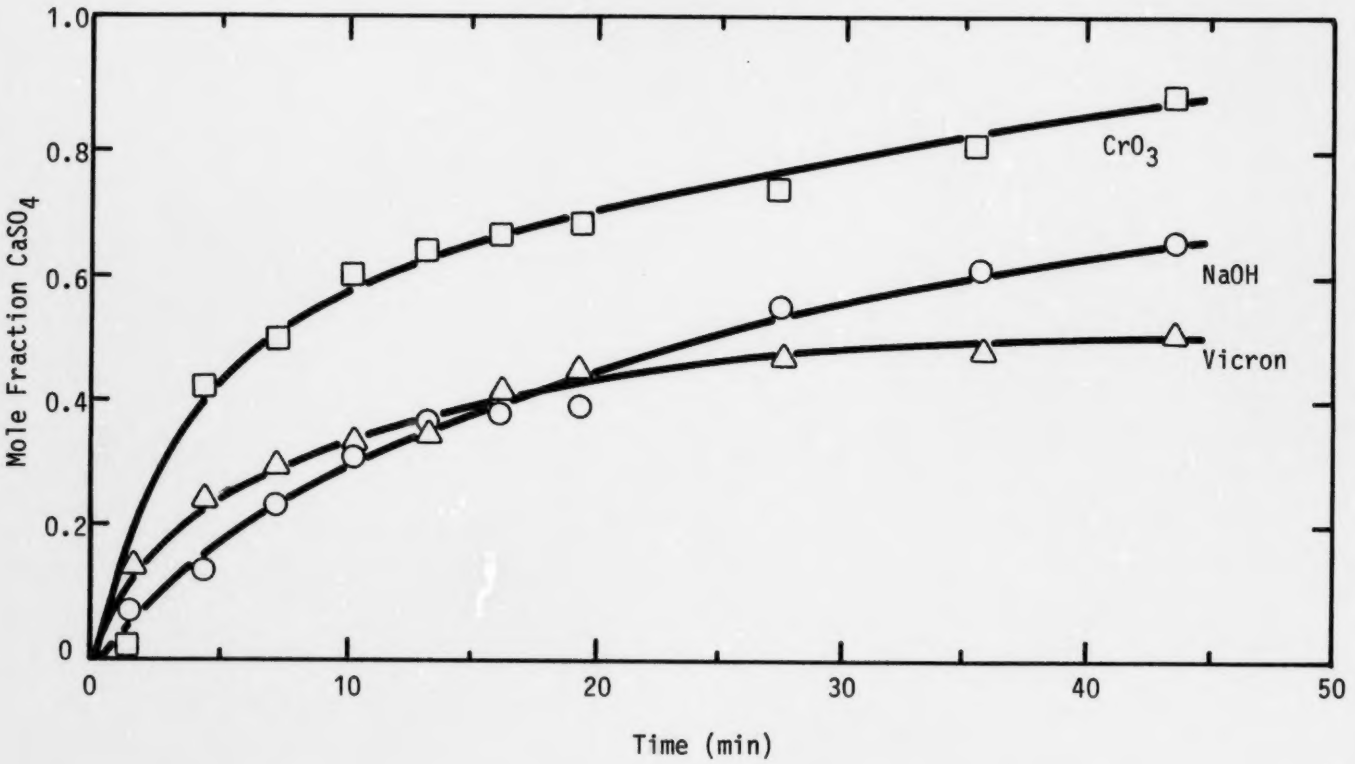

Figure 8-9. Sulfation comparisons for pressure hydrate samples at 1083 K (simulation gas).

8.3 Conclusions

The Vicron sulfation rates measured in this study were generally lower than those reported earlier by Borgwardt et al. This is attributed to pore diffusion limitations in our particles relative to those used by Borgwardt (10).

In all cases except for the iron-doped, evaporatively prepared limestone, dopants increased both the initial rates and final conversions of the sulfation. Pressure hydrate prepared dopants were superior to those prepared by evaporative techniques. There was a much stronger sulfation temperature dependence for the pressure hydrate samples than for either the evaporative samples or the baseline Vicron. While the sodium pressure hydrate sample was superior at 923 K, the chromium pressure hydrate performed better at 1083 K.

The fact that the dopants caused enhanced sulfation even in the presence of strong pore diffusion effects, is cause for questioning whether they simply act to increase grain diffusion rates. In addition, their higher dependency on temperature is inconsistent with the lowering of the activation energy which would be expected for increased ionic mobility. It is believed that they also act as structural promoters which maintain the access of SO_2 to CaO grains.

9.0 PARAMETRIC STUDY ON PREMIXED POWDERS AND SPECIAL DOPED SORBENTS

This program focused on two promoters: alkali-metals (e.g., sodium) and chromium. Enhancements with sodium-promoted sorbents have been relatively constant at 15 to 20 percent for the sorbents tested, while the increase in sulfur capture for chromium-doped sorbents varied from 12 percent to 37. From an environmental position, chromium and some chromium oxides are toxic; therefore, chromium must be retrievable to be considered a viable promoter. Unfortunately, it has not been possible to effectively encapsulate the chromium (or the Cr-oxides) in a retrievable solid. Thus, the alkali-metals were selected for further study. This section provides a description of the parametric study which was conducted to evaluate alkali promotion with premixed powders. Three other specially designed dopant/sorbent combinations were also evaluated: sodium deposited carbonates, sodium promoted calcines, and promoted hydrates. (a detailed description of the dopant/sorbent generation methods is provided in Section 4.)

9.1 Premixed Powders (A Parametric Study)

The most direct method to combine the dopant with the sorbent is premixing a powdered promoter with a calcium-based sorbent before introduction into the boiler. Upon injection the additive interacts with the sorbent in the manner described in Section 6.

9.1.1 Comparison of Combustion Facilities

To assure the process results are comparable between test facilities, a series of tests was conducted with similar experimental conditions. Figures 9-1 and 9-2 show a comparison of identical tests run in the BSF and CTT with natural gas and Indiana No. 3 coal, respectively. The quench rate for both facilities was similar and the sampling locations to determine sulfur capture were at approximately the same downstream temperature. For all of the runs, independent of fuel or injection location, the capture was similar between the two furnaces. These data indicate the capability of these two furnaces to produce the same experimental result. These results also suggest

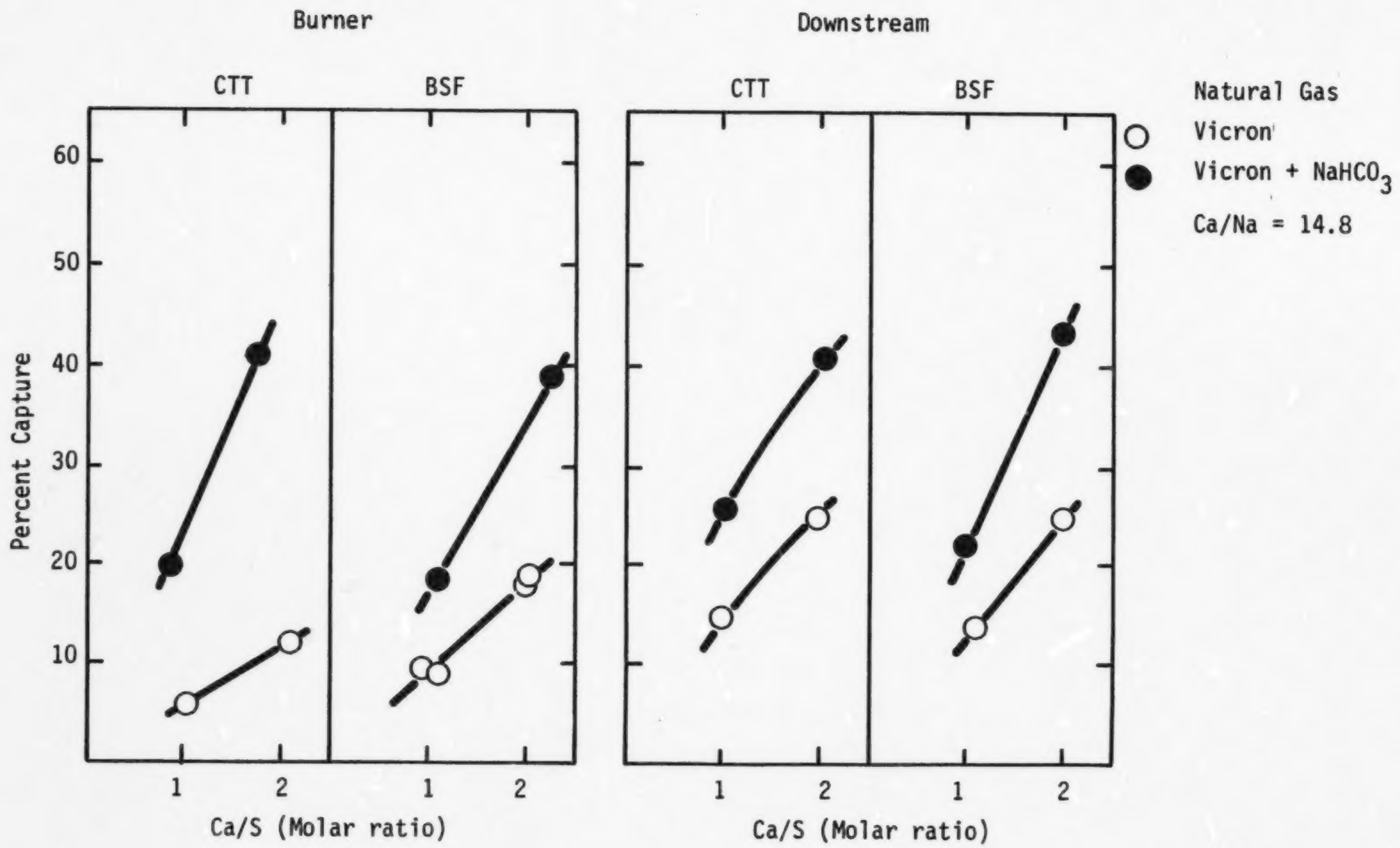

Figure 9-1. BSF vs. CTT comparison for gas.

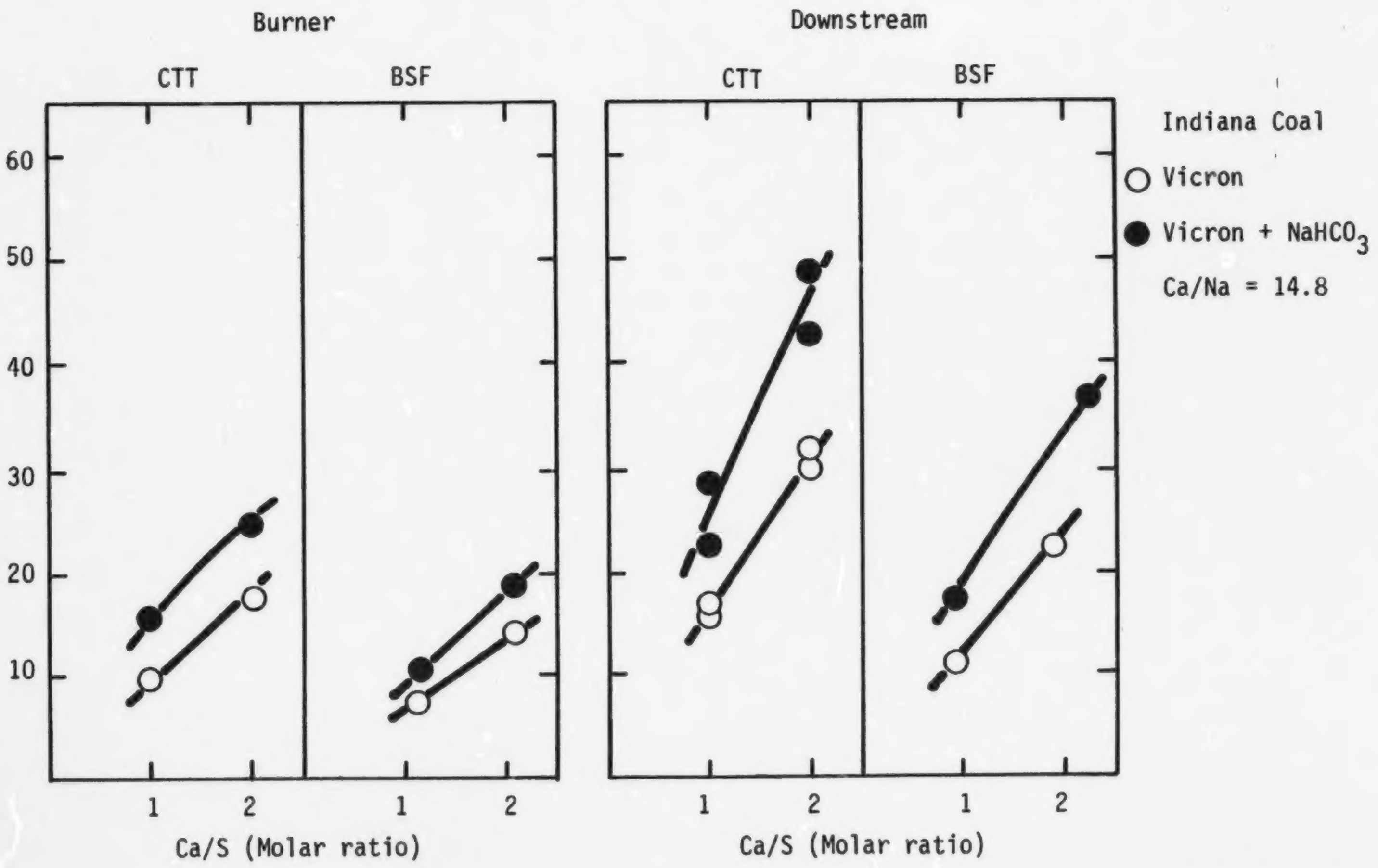

Figure 9-2. BSF vs. CTT comparison for coal.

the promotion effect seen with the addition of sodium is independent of scale.

9.1.2 Sodium Chemical Form and Size

To investigate the SO_2 capture enhancement effects of sodium based compounds, two promoter sorbent mixtures were prepared. Mixtures of Vicron with $NaHCO_3$ and Vicron with Na_2CO_3 were prepared such that the molar ratio of calcium to sodium was 14.8 to 1 (Ca/Na = 14.8). These two mixtures were compared to the performance of raw Vicron. The capture data at Ca/S = 2 is presented in Figure 9-3. For burner injection, the addition of $NaHCO_3$ to Vicron substantially increased the SO_2 capture by a factor of four when natural gas was used as the fuel. When the sorbents were injected downstream, improvements in the SO_2 capture were observed with both promoters. However, the Na_2CO_3 did not appear to enhance the Vicron as effectively as the $NaHCO_3$.

When it became apparent that $NaHCO_3$ was more effective than Na_2CO_3, it was important to determine what inherent properties of the additives that caused the difference in sulfur capture. Measurement of the mean particle size for $NaHCO_3$ and Na_2CO_3 indicated a significant difference; therefore, the effect of particle size was examined. The left side of Figure 9-4 shows a particle size analysis for the two additives and indicates that the raw Na_2CO_3 (labeled "coarse") was at least an order of magnitude larger than the $NaHCO_3$ that was used in the testing. It was postulated that particle size could affect the extent of vaporization and, hence, limit sodium dispersion. Na_2CO_3 was, therefore, reduced to a particle size comparable to the $NaHCO_3$. The hatched symbols (labeled "fine") show that the Na_2CO_3 particle size after grinding. The right side of Figure 9-4 shows downstream capture data for the two particle sizes of Na_2CO_3 mixed with Vicron. For the smaller particle size, the capture increased to the same level as for the $NaHCO_3$. Thus the apparent superiority appears to be due to the difference in particle size of commercially available materials. These data suggest that decreasing the promoter particle size can increase the effectiveness of the material by enhancing its ability to distribute uniformly over the sorbent.

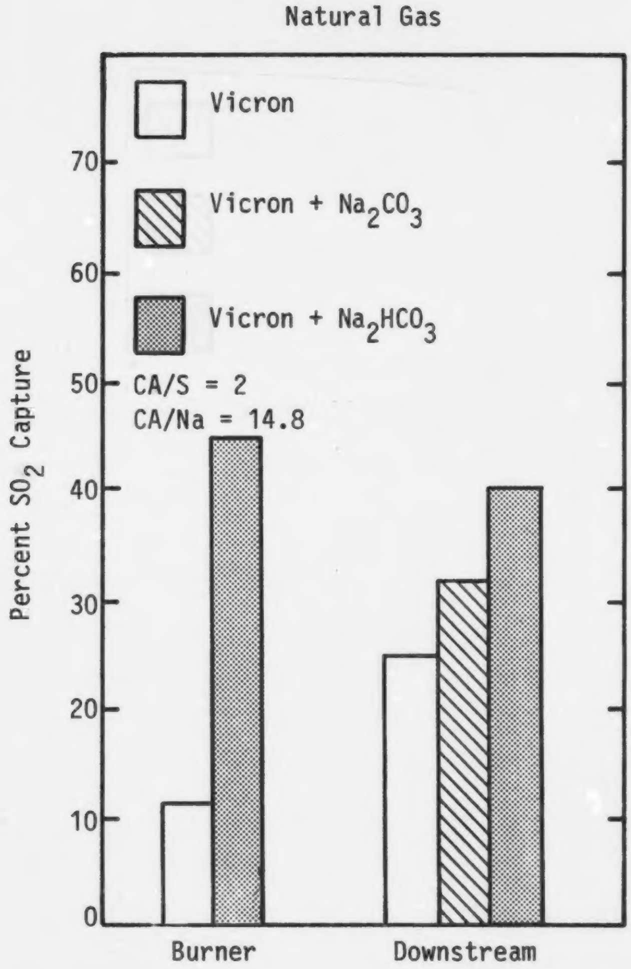

Figure 9-3. Capture enhancement with Na-based additives.

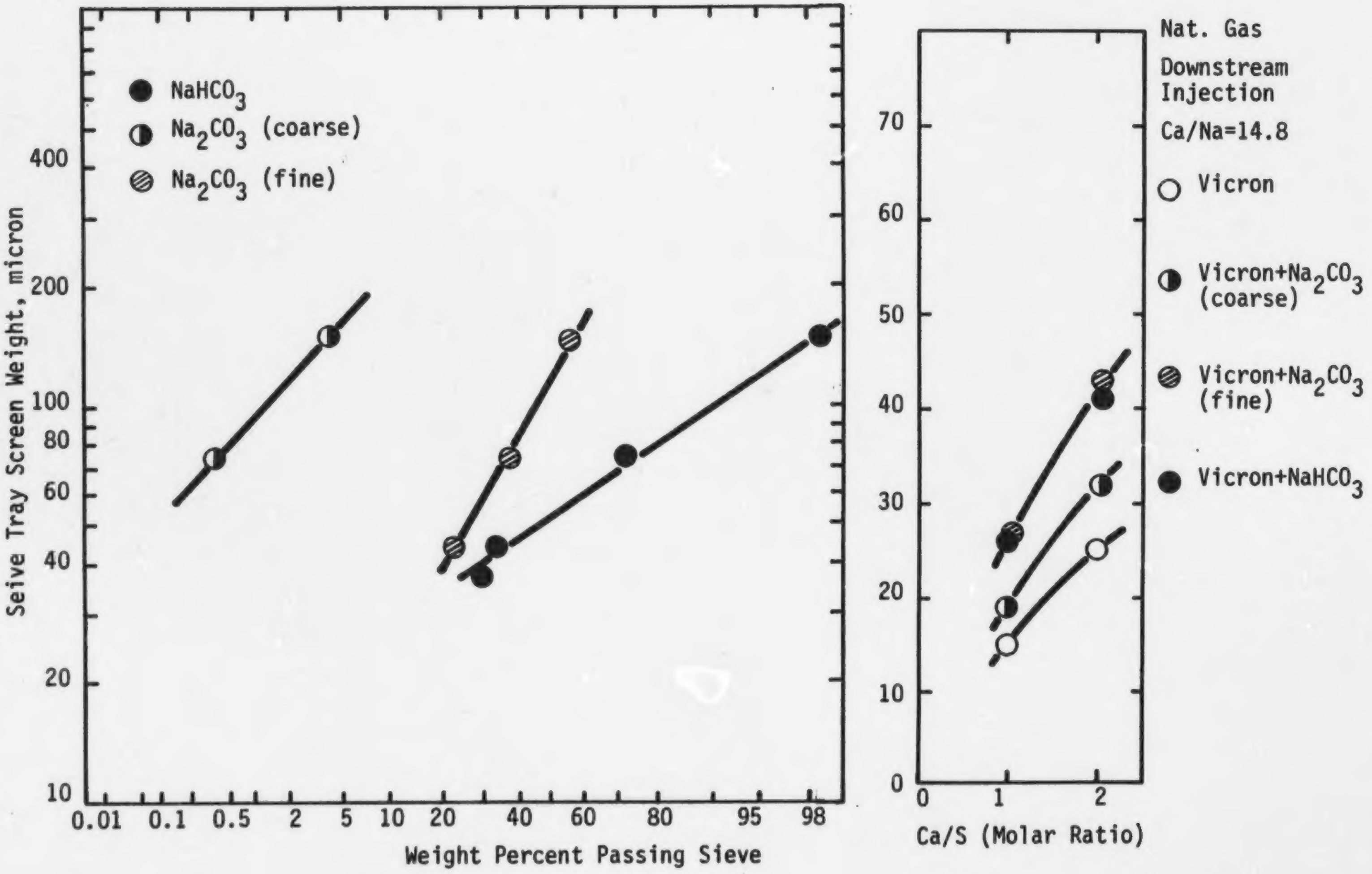

Figure 9-4 . Influence of additive particle size.

9.1.3 Injection Temperature and Location

A parameter found to greatly influence the overall capture of calcium based sorbents (without promoter) is the injection temperature. Sorbent injected at 1700 K (burner injection) is severely sintered before calcium sulfate is thermodynamically stable. Injection of the sorbent at the beginning of the sulfation window (approximately 1500 K) produces higher sulfur removal. Figure 9-5 summarizes the impact of injection temperature on sulfur capture when sodium is present with Vicron. Several injection schemes were tested including premixed and separate injection of sodium and Vicron. The sulfur capture of the injection combinations is compared to sulfur capture with burner injection (injection at secondary air port) and downstream injection of Vicron alone. As was expected, the sodium promoted Vicron produced greater capture than Vicron alone. The left graph (Figure 9-5) shows sulfur capture to be approximately the same for Vicron injected at the burner regardless of whether the sodium bicarbonate was mixed with the Vicron prior to the burner injection, or injected separately downstream. In the case of downstream injection of Vicron (right graph), the data show similar results indicating capture levels comparable for both separate and premixed injection of the $NaHCO_3$. These results suggest the location of sodium injection is not important as long as the relatively volatile sodium promoter is allowed to vaporize and react with the calcium. In addition, these data indicate that sodium promotion can "eliminate" the detrimental effects of high temperature sintering. The raw Vicron alone performs much poorer with burner zone injection than downstream injection. However, sodium promotion eliminates this effect.

Fig 5

9.1.4 Sorbent Type

Sulfur capture for different types of sorbents (i.e., calcitic carbonates, hydroxides, and dolomitic sorbents) is not usually the same (under similar conditions). Therefore a series of tests was performed in the BSF to compare overall sulfur capture for a variety of sorbent types premixed with $NaHCO_3$. Four sorbents:

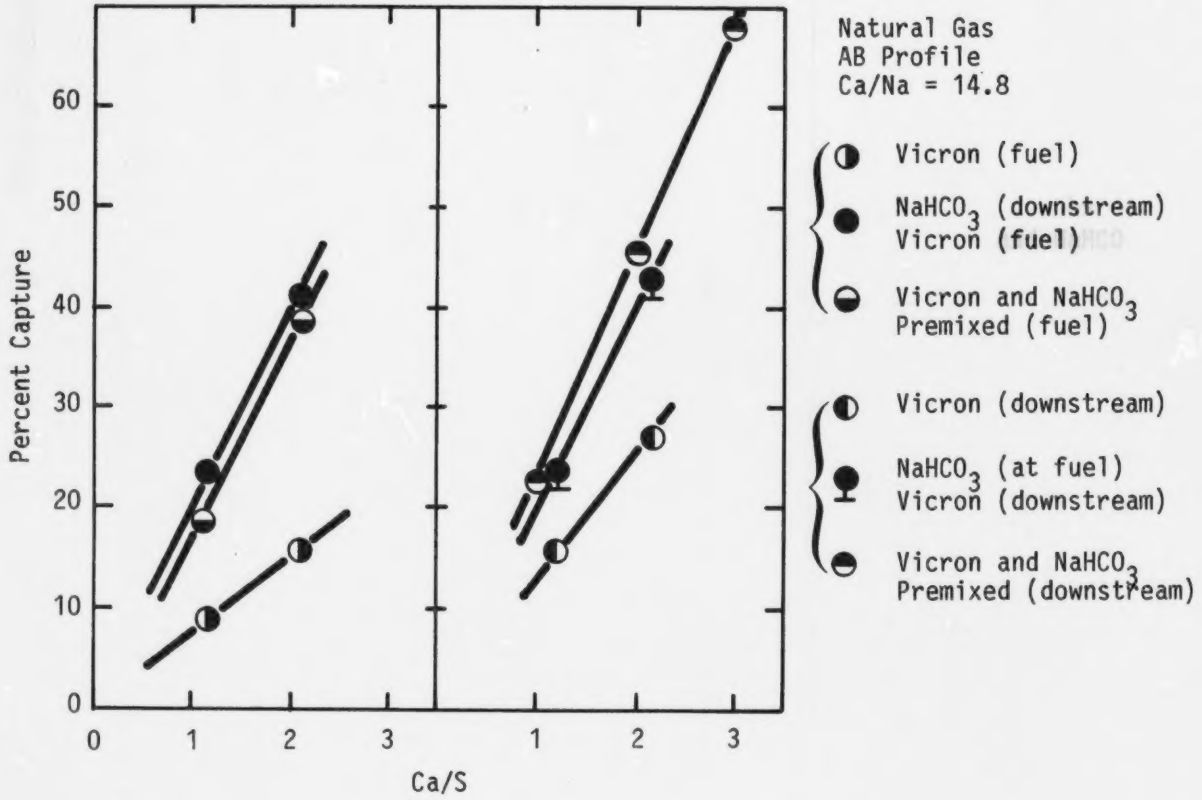

Figure 9-5. Injection locations (e.g., temperature) of sodium and Vicron on sulfur capture.

BSF to compare overall sulfur capture for a variety of sorbent types premixed with $NaHCO_3$. Four sorbents:

- Vicron ($CaCO_3$),
- Longview hydroxide ($Ca(OH)_2$),
- Dolomite-D3002 ($CaMg(CO_3)_2$), and
- Genstar Dolomitic Pressure Hydrate ($CaMg(OH)_4$),

were premixed with $NaHCO_3$ and injected downstream in the BSF. The tests included injecting the sorbents without a promoter to elucidate the effectiveness of the promoter/sorbent combination. The experimental results are summarized in Figure 9-6. For all sorbents tested the sodium doped sorbent outperformed their unpromoted counterparts in the removal of sulfur. There was a substantial (80 percent) increase in sulfur uptake measured relative to the unpromoted level with Vicron. The increases in sulfur capture with Longview, Dolomite, and Genstar were 50, 33, and 20 percent, respectively. Based on the work presented in Section 6, it is believed sodium reacts into the CaO matrix to cause fragmentation and pore widening, both of which result in improved accessibility of the interior CaO sites. The largest percent change would have been expected to occur with the carbonates rather than the hydrates due to the fact the hydrates are already relatively small and contain a large number of macropores. However, this alone does not explain the relatively small change measured with dolomite (a carbonate). The "dolomitic" carbonate has magnesium within the crystalline matrix and the magnesium itself effectively induces chemical sintering resulting in fragmentation and pore mouth widening at temperatures corresponding to those found in the boiler. The magnesium in effect functions in the same manner as sodium; therefore, the result of sodium impregnation is not as dramatic. (Since the magnesium does not react with SO_2, its presence also tends to keep the pores from blocking.)

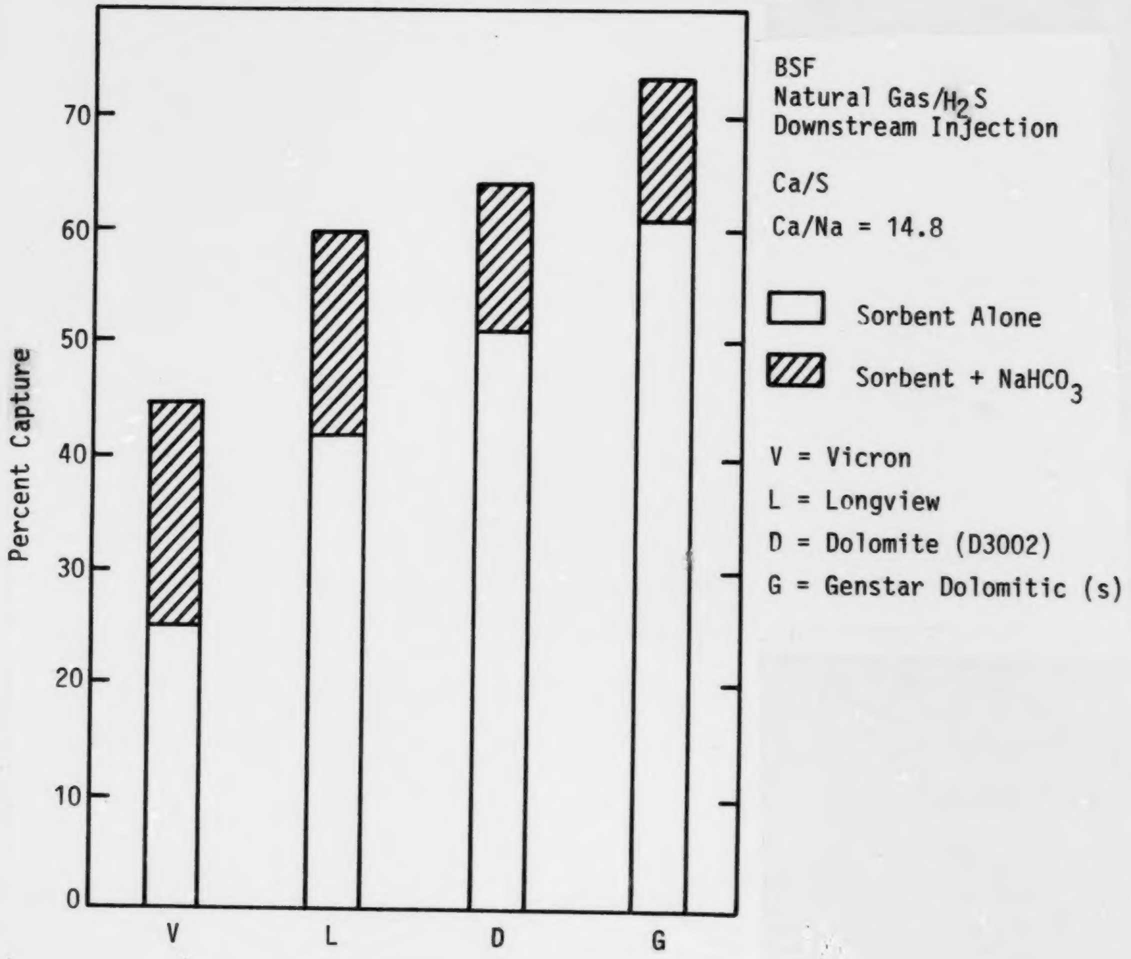

Figure 9-6. Sulfur capture of sodium bicarbonate premixed with a variety of calcium-based sorbents.

9.2 Special Sorbents

A major problem is the elimination of sodium by the coal ash as shown in Section 7. In general, sodium is a relatively volatile promoter; once sodium is in the gas phase, reaction with (or condensation on) the ash is possible. Three special sorbents were designed to improve sodium retention on the calcium, therefore effectively reducing sodium loss to the ash. These sorbent/promoter combinations were manufactured in bench scale facilities to obtain sufficient quantities of the doped sorbent for CTT testing.

9.2.1 Sodium Deposited Carbonates

The deposition of sodium on the carbonate was achieved by using the rotary kiln (see Section 4). During the manufacturing process the temperature of the kiln was maintained at approximately 533 K to avoid calcination. (For a true comparison, the unpromoted Vicron experienced the same kiln conditions except no sodium was present.) High resolution photographs of Vicron, and sodium doped Vicron shown in Figure 9-7 (micrograph No. 43900 and 44303, Vicron; No. 45602 and 44904, Vicron with Na) indicate no significant change between the sorbents' surface morphology. This suggests the sodium condensed on the surface and did not chemically react with the sorbent. The Ca/Na atomic ratio for the doped sorbent was approximately 26 (Table 9-1).

CTT fired with coal was used to evaluate the sodium doped carbonate. The tests included examining the sulfur capture for three different injection temperatures, 1533 K, 1410 K, and 1255 K. The results shown in Figure 9-8 indicate the sodium doped sorbent did show an increase in sulfur capture for all injection temperatures tested. Sulfur capture with the unpromoted Vicron was reduced with decreasing temperature; performance ranged from 30 percent for units 1533 K to 10 percent for 1255 K. The incremental increase between the promoted and unpromoted Vicron is shown to be temperature dependent; the lower the injection temperature, the smaller the change in capture. At the injection temperature of 1533 K the results indicate approximately a 15 percent increase in sulfur capture with the doped carbonate (for coal, at Ca/

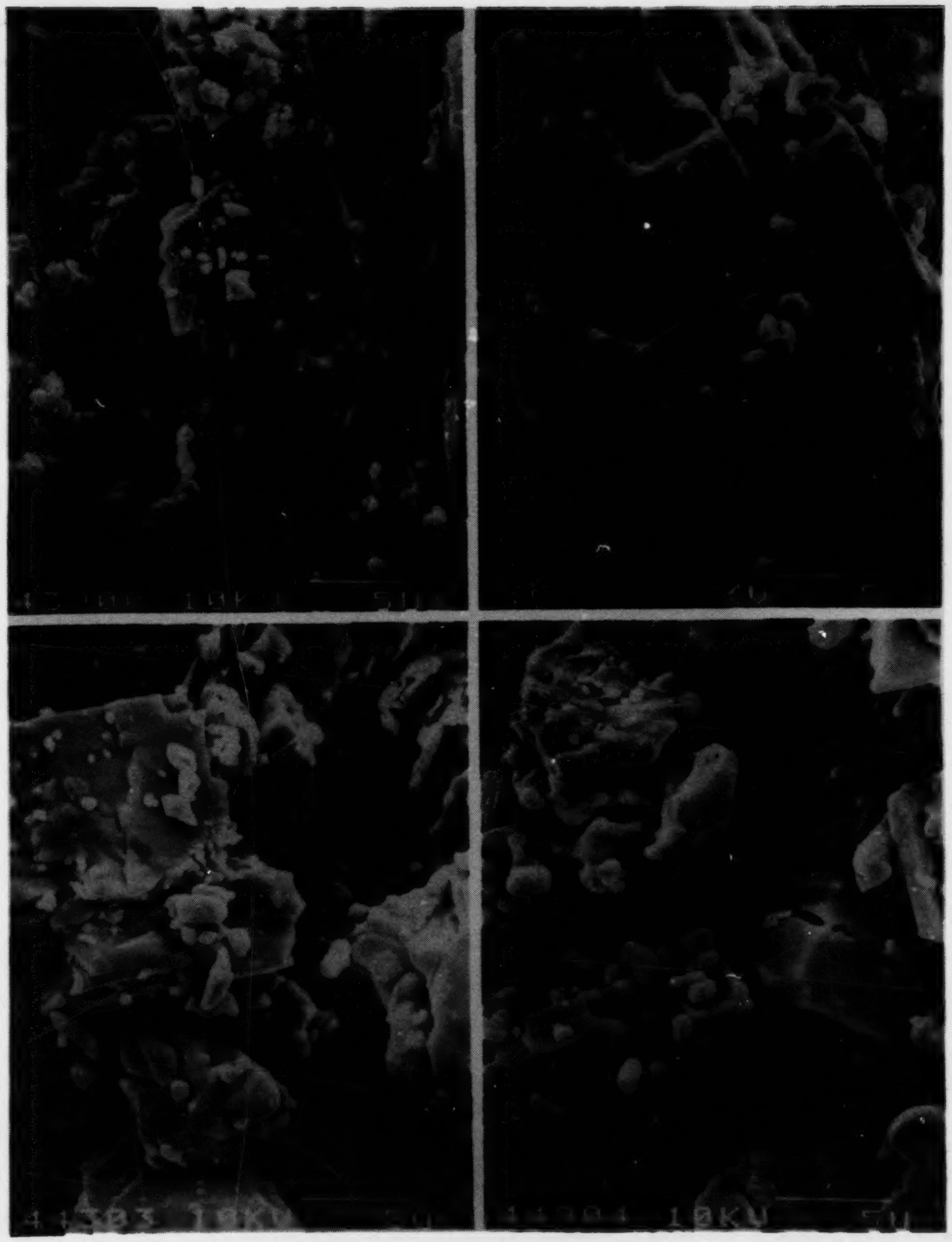
44303 10KV 5U
44904 10KV 5U

Figure 9-7. Kiln fired carbonate (Micrograph No. 43900, and 44303--no Na; No. 45602, and 44904--Na).

TABLE 9-1. CHARACTERISTICS OF KILN-PRODUCED SORBENTS

Conditions	Surface Area (m^2/g)	Weight Percent					Calculated Percent $CaCO_3$	Ca/Na (Atomic Ratio)
		Ca	C	H	N	Na		
Raw Vicron	0.76	39.38	11.98	0.01	0.00	-	101.5	-
533 K, No Na	0.82	37.76	11.79	0.04	0.00	-	104.2	-
533 K, W/Na	0.74	37.66	11.46	0.05	0.00	0.810	101.6	26.7
1060 K, No Na	0.72	39.84	9.80	0.01	0.00	-	82.1	-
1055 K, W/Na	0.58	38.87	10.29	0.07	0.00	1.00	88.4	22.3
1322 K, No Na	-	66.4	0.50	0.09	0.00	-	2.5	-
1322 K, W/Na	1.22	63.7	0.16	0.02	0.00	0.63	0.8	58
1161 K, W/Na	1.25	65.2	0.17	0.00	0.00	0.45	0.9	83

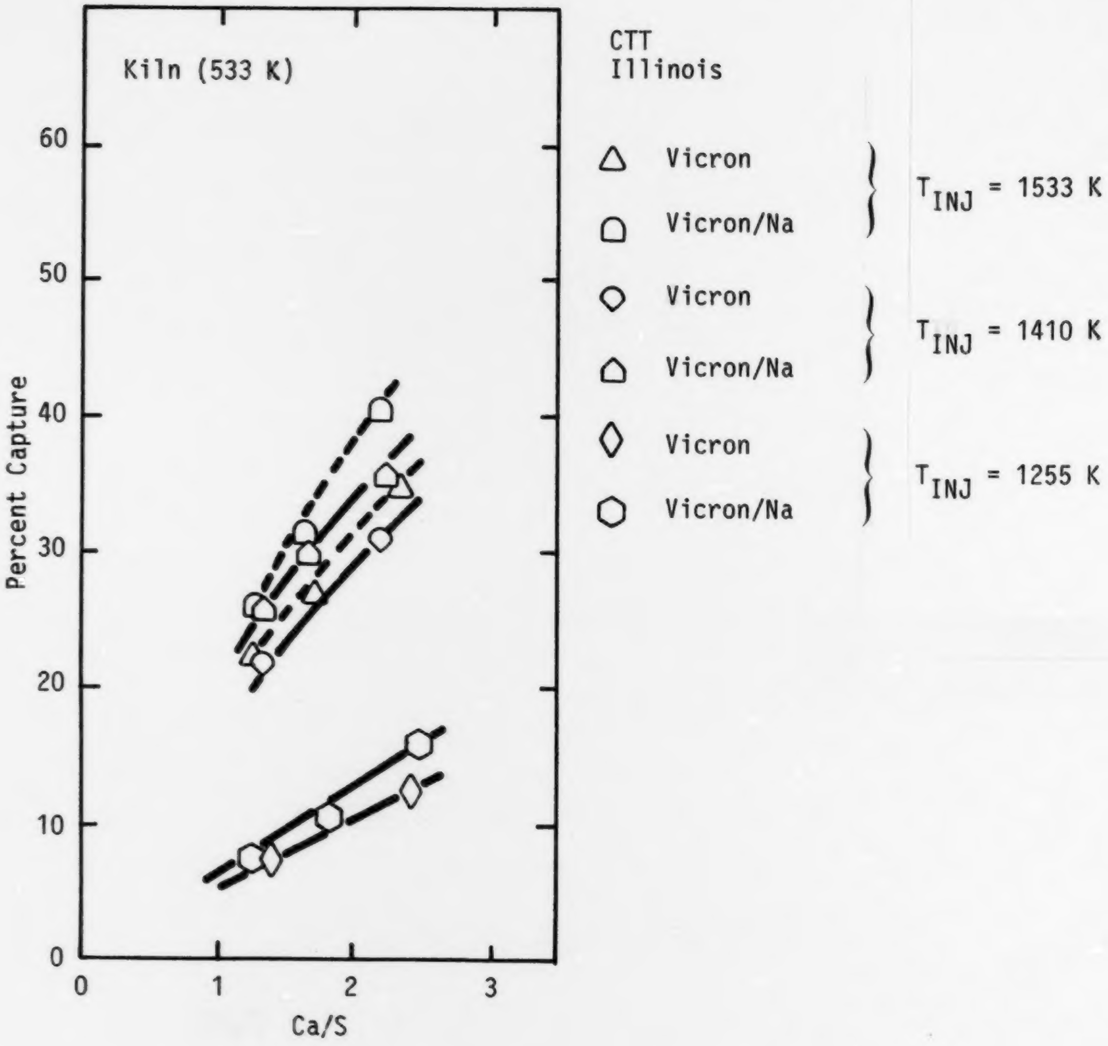

Figure 9-8. Sulfur capture with sodium promoted carbonates.

S = 2). Unfortunately, the increase in capture contains a substantial capture value for sodium (as a sorbent) of 11 percent.

9.2.2 Promoted Calcines

In order to reduce sodium reaction with ash in the boiler, the sodium was allowed to react with the sorbent (without ash present) prior to injection into the boiler. Again the rotary kiln was used to manufacture the promoted sorbent. Vicron/$NaHCO_3$ was the calcium sorbent/promoter combination produced. The objective was to generate a highly reactive calcine with a reasonably open interior. To achieve this, a calcine with a surface area of approximately 25 m^2g was to be generated and reacted with sodium. The sodium would tend to react on the exterior producing local sintering which would cause fragmentation and pore widening (grain growth).

Several attempts to produce the desired doped calcine (and corresponding undoped calcine) were not completely successful. In all cases, especially, the measured BET surface areas were approximately 1 m^2/g (see Table 9-1). At the lowest temperature, 1033 K, calcination was not complete even though the carbonate is unstable at 1033 K. It is believed the thermal decomposition was effected by the presence of CO_2 in the relatively thick kiln bed. The presence of CO_2 increases the effective thermal decomposition temperature and increases the sintering rate of CaO. High resolution photographs of kiln fired Vicron (with sodium) shown in Figure 9-9 (micrograph No. 44900 and 44901, 44902 and 44903) indicate there were small changes between the calcine generated at 1033 K. (Only the differences are presented). Based on examination of these samples and other calcium sorbents, it is believed there was limited reaction of the sodium with the parent $CaCO_3$ which produced the morphology shown in micrographs No. 44901, 44902, and 44903.

Results from sulfation of the calcines produced at 1033 K (shown in Figure 9-10) show significant enhancement (based on the measured Ca/Na = 22 atomic). With the presence of sodium, sulfur capture increased by 16 percent (with coal, at Ca/S = 2). If all the sodium reacted to form sodium sulfate there would have been only a 14 percent increase over the capture of the

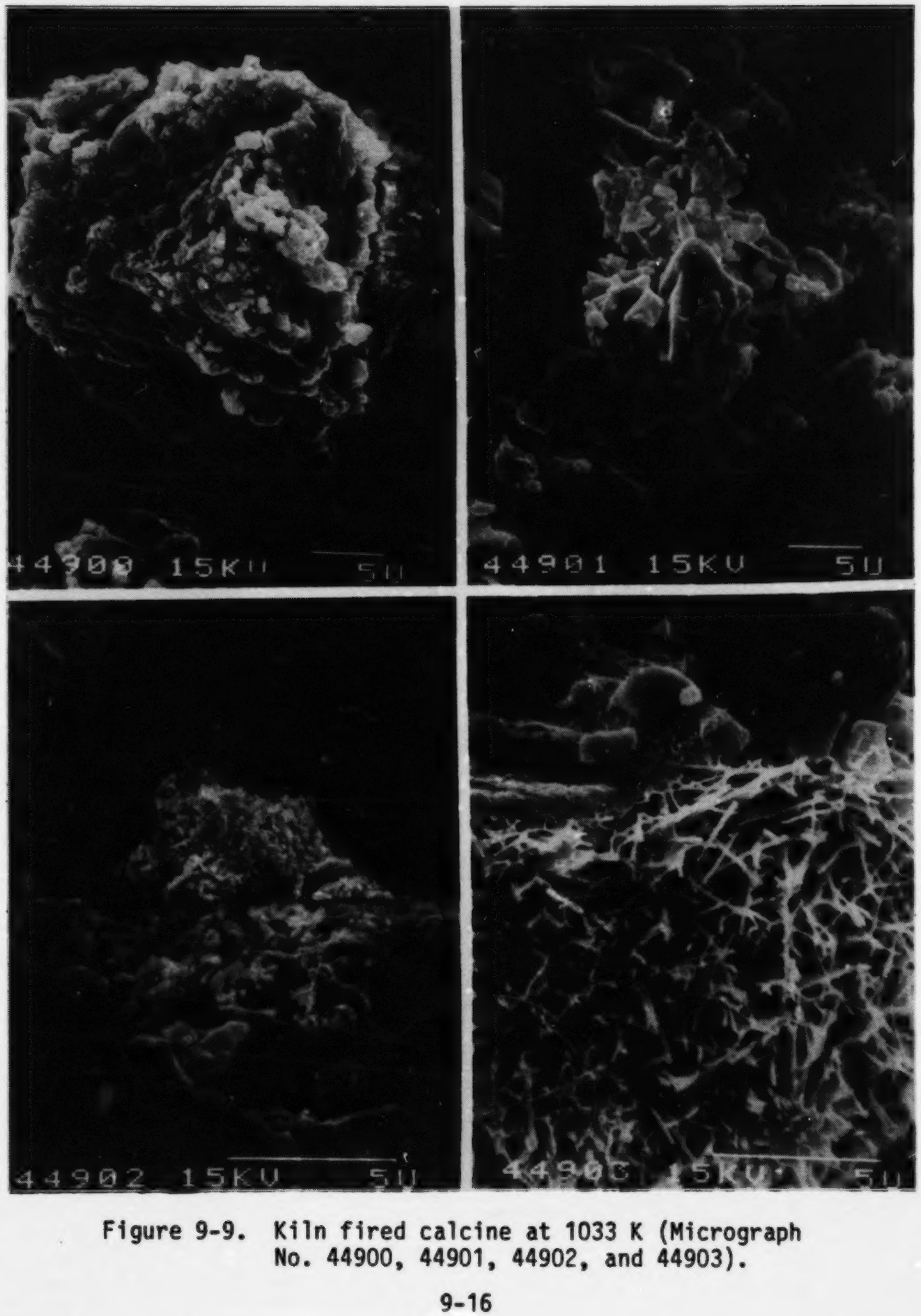
44900 15KV 5U
44901 15KV 5U
44902 15KV 5U
44903 15KV 5U

Figure 9-9. Kiln fired calcine at 1033 K (Micrograph No. 44900, 44901, 44902, and 44903).

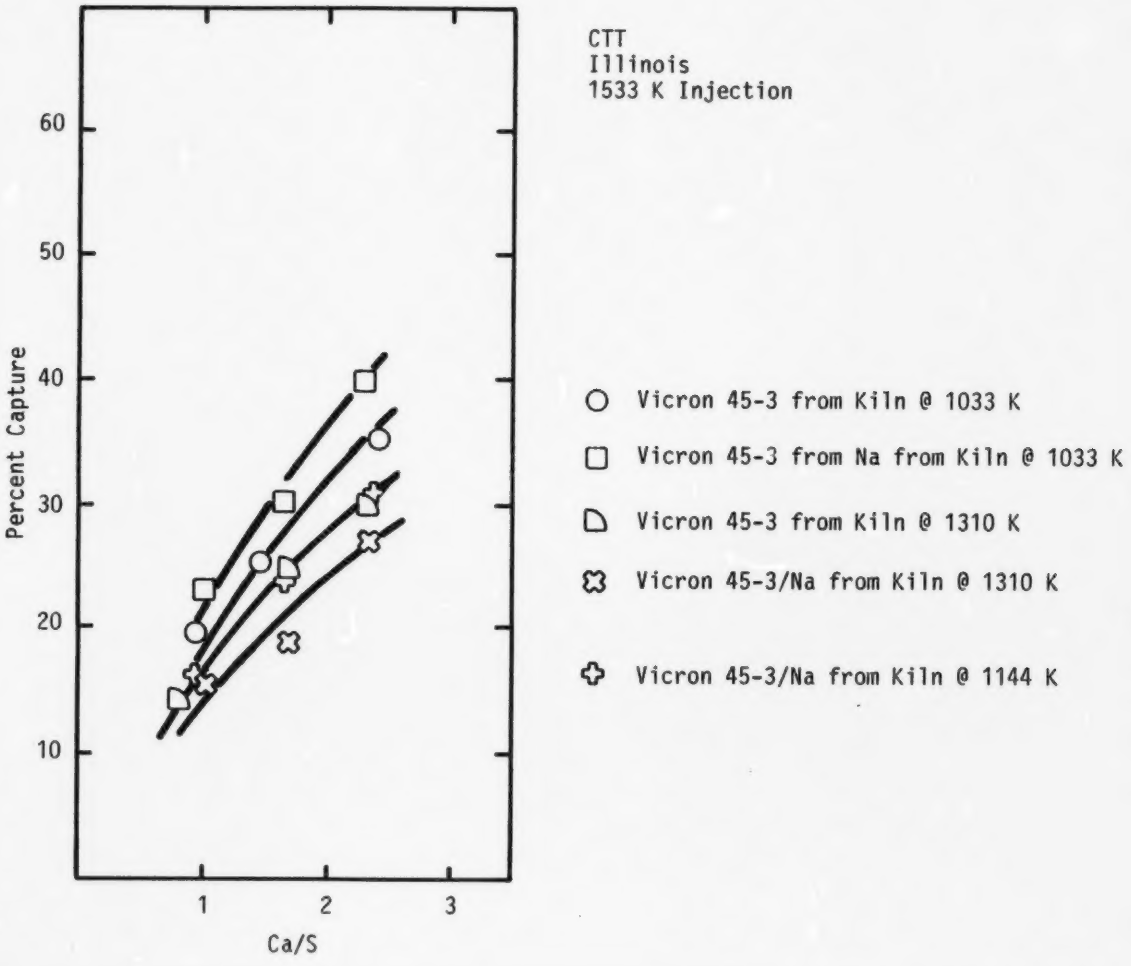

Figure 9-10. Sulfur capture with sodium promoted calcines.

unpromoted calcine. The promotional value of the sodium was not evident with only a 16 percent increase in sulfur capture. The results were similar to the sulfur captures achieved with the doped carbonate. This is not surprising; since the sorbent was only approximately 15 percent calcined (Table 9-1), it functions as a carbonate.

To provide fully calcined stones, the kiln bed temperature was increased; while an increase in the temperature increased the decomposition rate, it also increased the sintering rate of the generated CaO. Unfortunately, low BET surface areas for these calcines were measured (as summarized in Table 9-1). Also at higher temperatures ($T > 1100$ K), the amount of sodium that reacted with the calcium sorbent was substantially reduced due to the tendency for the vaporized sodium to remain in the gas phase (even through the bulk gas velocity remained relatively constant). This is evidenced by the high measured Ca/Na ratio for the doped sorbent generated at both temperatures, 1310 K and 1144 K, (e.g., 1161 K - Ca/Na = 83 atomic). High resolution photographs of kiln fired Vicron (with sodium) at 1310 K, shown in Figure 9-11 (micrograph No. 47204 and 47103--no Na; No. 47002 and 47001--Na), indicate the calcines were extensively sintered (note the characteristic large grains, and the large number of macropores). For the sodium promoted calcine, a large number of particles appear torn apart as depicted in Figure 9-11, thus the observed particle size was smaller.

Examination of the results from sulfation of the high temperature calcine (shown in Figure 9-11) indicate a significant enhancement (based on the measured Ca/Na = 58 atomic). With the presence of sodium, sulfur capture increased by 26 percent (with coal, at Ca/S = 2). If all the sodium reacted to form sodium sulfate there would have been only a 7 percent increase over the capture of the unpromoted calcine instead of the measured 26 percent. In general the sodium reacted with CaO to further fragment the calcine particles as illustrated by photographs of the sodium doped calcine.

It is believed, based on these results, that if the 25 m^2/g calcine could have been produced the ultimate capture would have been greater than

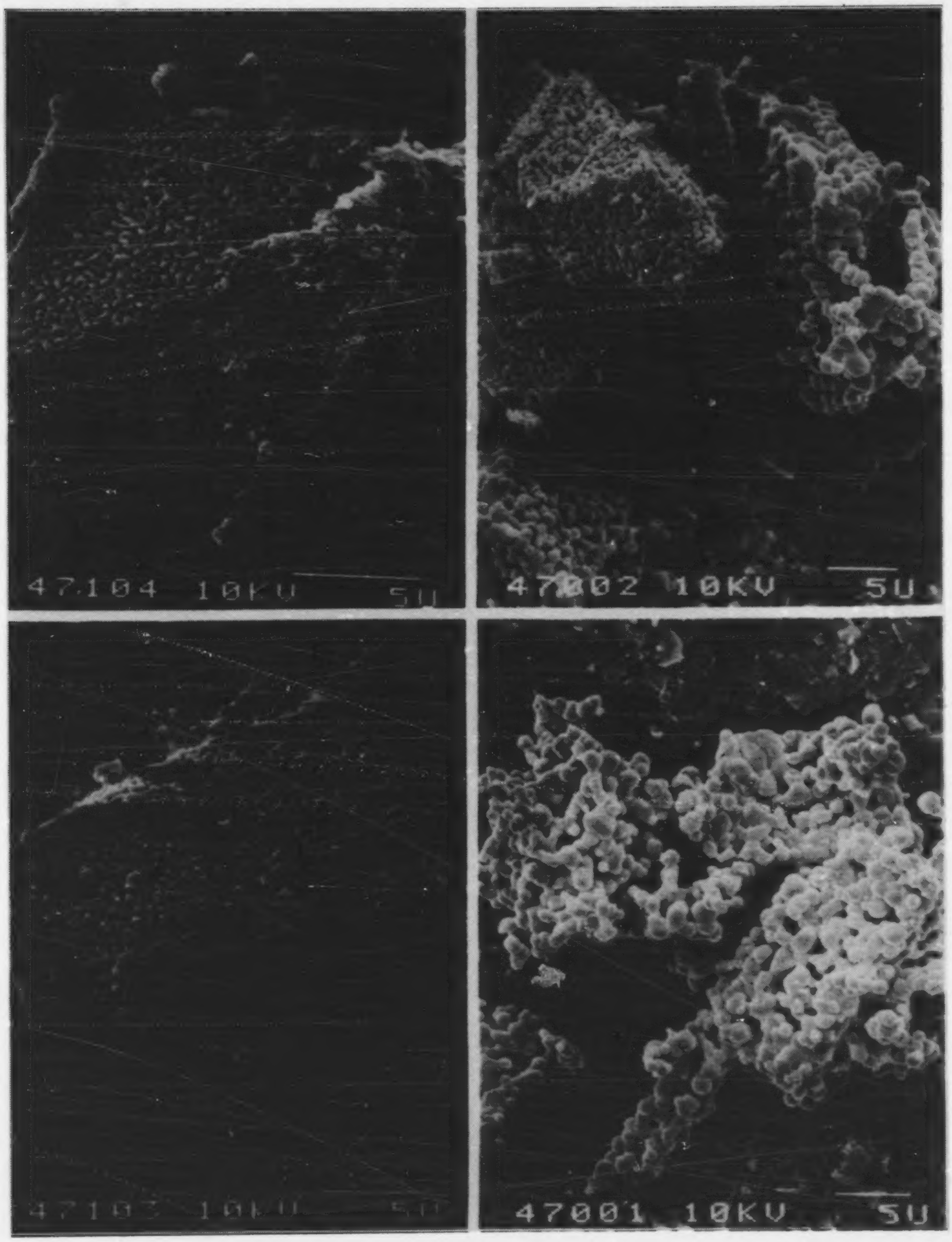
47104 10KV 5U
47002 10KV 5U
47103 10KV 5U
47001 10KV 5U

Figure 9-11. Kiln fired calcine at 1310 K (Micrograph No. 47104 and 47103--no Na; No. 47002 and 47001--Na).

40 percent with an incremental increase (above unpromoted capture) greater than 25 percent.

9.2.3 Promoted Hydrates

The third doped sorbent was prepared by dispersing (and to a limited extent, reacting) the promoter during hydration of the CaO. This allowed a fine dispersion of the promoter on (and within) the calcium matrix. The ability of the hydrates to capture sulfur is superior to the carbonates, therefore the addition of the dopant offers outstanding potential capture performance.

Three water soluble additives were tested: NaOH, CrO_3, and $Fe(NO_3)_3$. The materials were manufactured (as described in Section 4) then injected in CTT at 1500 K to determine the capture performance of the doped sorbents. Results of the evaluation of doped pressure hydrates in the CTT fired with coal and natural gas are summarized in Figures 9-12 and 9-13.

The pressure hydrate doped with sodium did enhance sulfur capture as shown in Figure 9-12; the sulfur capture increased by 17 percent at a Ca/S = 2. Only a 10 percent increase in sulfur removal would be expected if the added sodium functions as a sorbent. In general the hydrate particles are smaller and more porous (i.e., they contain a large number of macropores); therefore, the ability of the sodium to improve the already open, stable hydroxide is decreased. With coal as the fuel, the influence of sodium on sulfur capture is reduced. Based on results in Section 7, vaporized sodium is eliminated from possible reaction with the sorbent by reaction and/or condensation on the coal ash.

The results (shown in Figure 9-13) for iron impregnated hydrate indicated capture levels comparable to the unpromoted pressure hydrate for both coal and gas. This is not unexpected, in general, iron impregnated sorbents were found not to promote sulfation of the calcium sorbents (Section 6). That is not the case for the manufactured chromium doped pressure hydrate, the overall capture level is significantly higher at 75 percent than

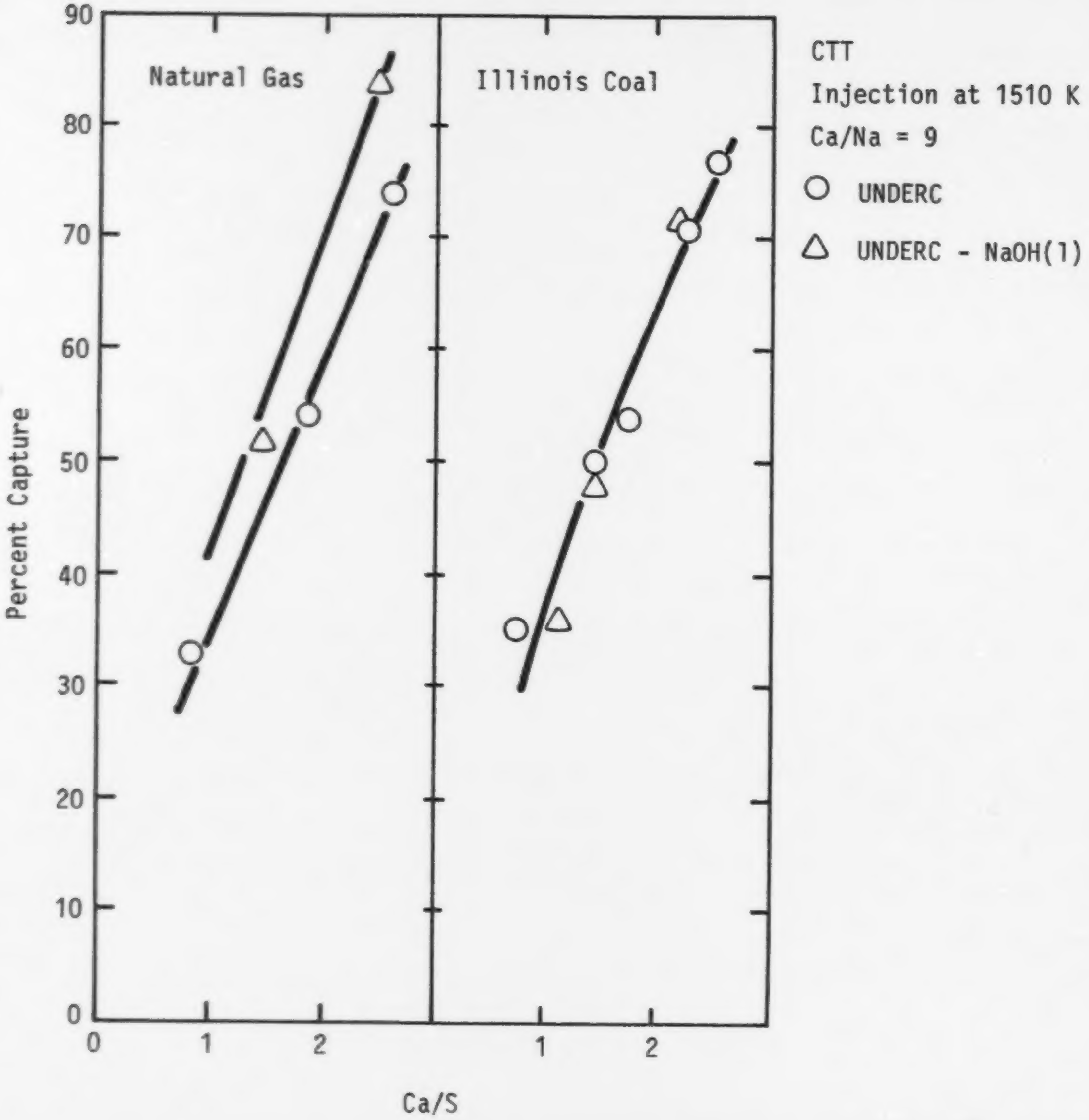

Figure 9-12. Sulfur capture with sodium promoted pressure hydrates.

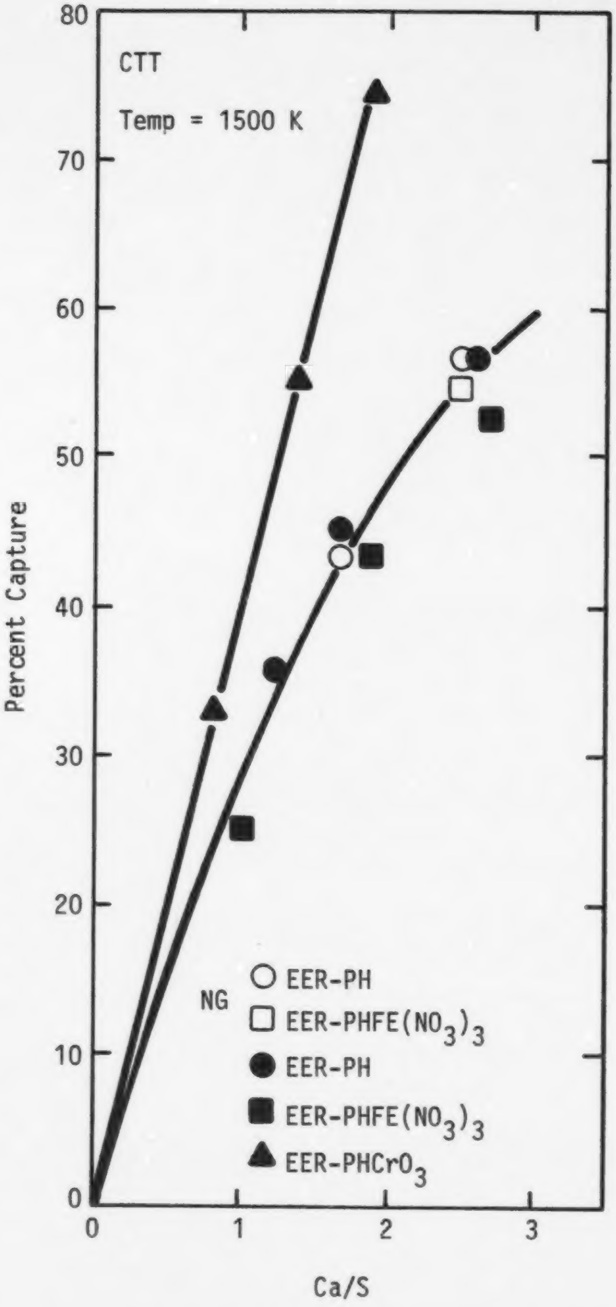

Figure 9-13. Sulfur capture with promoted pressure hydrates.

the unpromoted capture of 50 percent (at Ca/S = 2). The substantial increase is believed to be due to the formation of the reactive low melting $CaO-Cr_2O_3$ eutectic mixture. Photographs of sulfated pressure hydrate containing chromium are shown in Figure 9-14. Three distinct morphologies associated with this hydrate, they are:

- granular (upper left, No. 50054),
- granular/eutectic mixture (lower left, No. 50054; and 50053), and
- eutectic mixture (right side, No. 50054).

Figure 9-15 provides results of an EDS analysis for micrograph No. 50054. The figure includes a sulfur intensity map (left) with distribution maps for sulfur, calcium and chromium (right). Based on the EDS analysis, sulfur was found to associate with the presence of the eutectic mixture. It is important to point out that merely contacting chromium and calcium without reaction is not sufficient to enhance sulfur capture as discussed in detail in Section 6. Chromium and the calcium appear not to have reacted at the upper left and therefore the amount of sulfur present is relatively small.

9.3 Conclusions

These parametric studies examined the influence of sodium type, sodium particle size, injection location, and sorbent type on sulfur capture of a premixed sodium/sorbent combination. Particle size of the sodium promoter was found to be relatively important in effectively vaporizing and dispersing the promoter on the sorbent (i.e., larger particles more difficult to vaporize). Sodium need not be injected with the calcium to be effective in promoting sulfur capture due to the instability of the compounds at the injection temperatures (i.e., 1700 K, and 1500 K). Calcium sorbents when combined with sodium produced an increase in sulfur capture; capture enhancements ranged from 50 percent for Vicron to 20 percent for Genstar Type S.

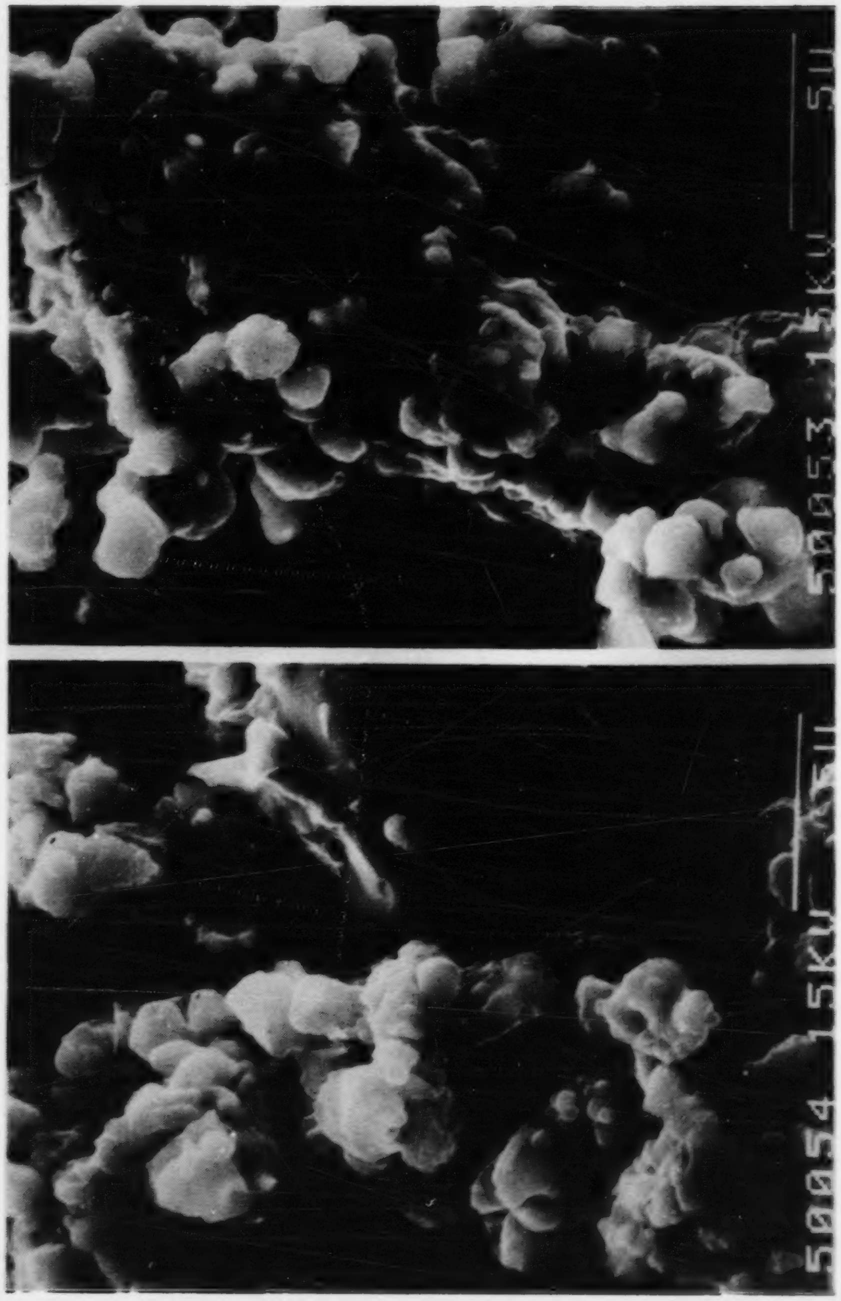
50053 15KV 5U
50054 15KV 5U

Figure 9-14. SEM photographs of sulfated Cr_2O_3 doped pressure hydrate.

COLOR PHOTOS AVAILABLE FOR
INSPECTION ONLY AT EPA/AEERL

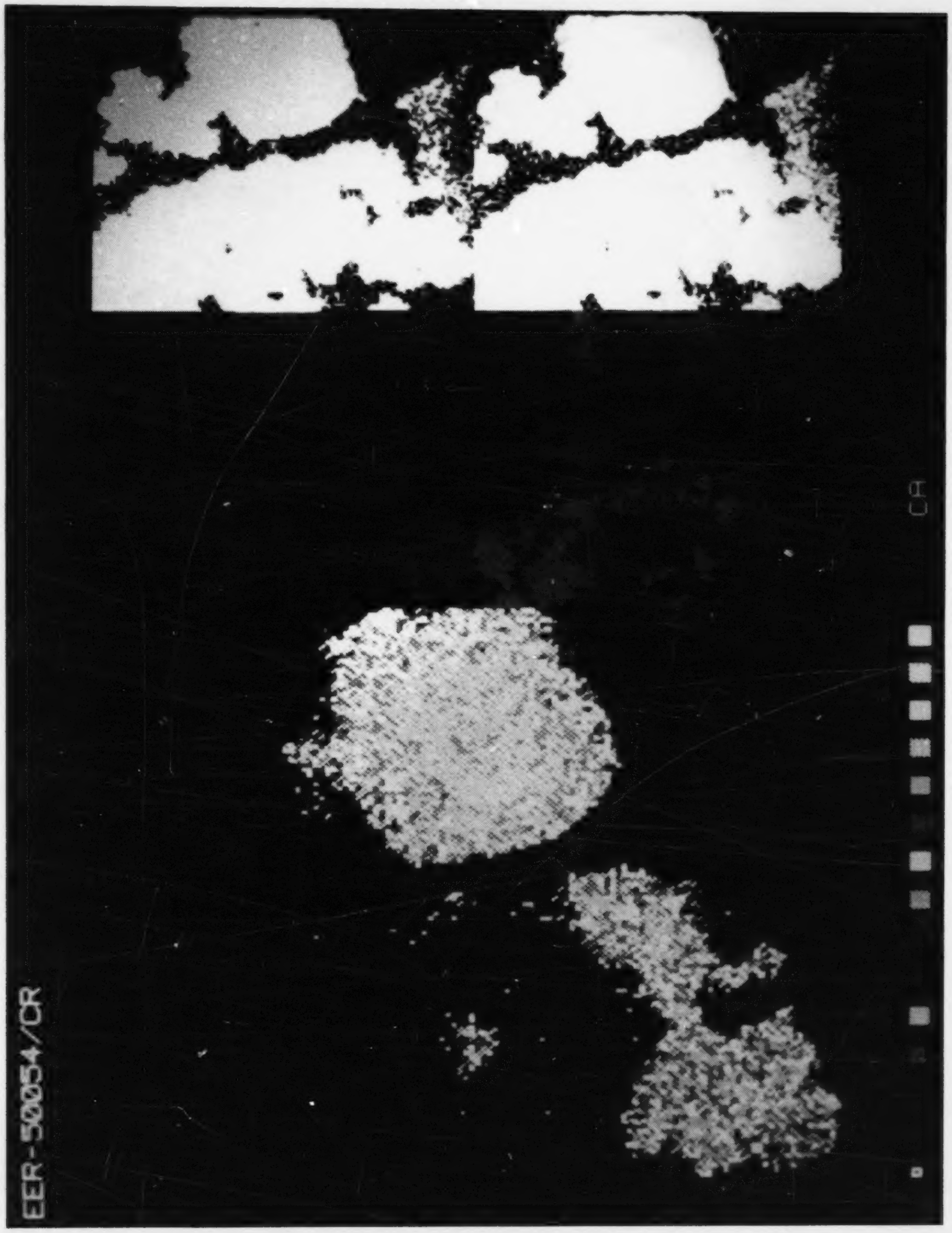

Figure 9-15. EDS analysis of sulfated Cr_2O_3 doped pressure hydrate; sulfur intensity map (Micrograph No. 50054).

In general, the three externally generated dopant/sorbent combinations designed to reduce (or eliminate) the detrimental effect of the mineral ash were not completely successful. Clearly, the sodium promoted calcine while posting a low overall capture (~24 percent, at Ca/S = 2) had an enhancement of 26 percent in the CTT fired with coal. Unfortunately, with coal as the fuel a near complete loss of promotion was seen for the sodium doped pressure hydrates.

PART V. CLOSURE

10.0 CONCLUSIONS

This work examined mineral interactions with calcium-based sorbents to determine promoter effects and possible uses and restrictions of this relatively new technology. Several significant findings were made in this study and are summarized in this section.

10.1 Interaction Mechanisms

To effectively evaluate the possible uses and restrictions of this technology it was important to characterize the coal ash/sorbent/promoter interactions. The interactions investigated include:

- influence of mineral ash on the performance of calcium-based sorbents,
- influence of promoters on performance of calcium-based sorbents, and
- influence of mineral ash on performance of promoters.

The data presented in the previous sections (i.e., Sections 5, 6, 7) indicated that:

Sorbents injected separately from the pulverized coal (either with secondary air or downstream) are not deactivated by mineral matter components. Only if the mineral matter and sorbent are in direct contact prior to injection, can ash components significantly reduce calcium availability, and therefore sulfur capture.

Chromium series transition elements and alkali metals effectively increase the ability of calcium based sorbents to capture sulfur. Both sodium and chromium react chemically with the CaO to produce local physical changes that increase the accessibility of the interior Ca and to decrease the rate of site loss by pore mouth plugging. In addition, these promoters often produce low melting eutectics which probably enhance the transport of the sulfur to unreacted CaO. (The alkali metals can react directly with SO_2 to produce sulfates; the chromium compounds do not.)

The effectiveness of sodium promotion is reduced in coal-fired systems because sodium condensation on the submicron ash aerosol decreases the amount of sodium which actually reaches the calcium sorbent and the benefits to sorbent morphology are decreased correspondingly. In addition, part of the sodium which condenses on the ash reacts to form silicates and is unavailable for direct sulfation. The submicron ash aerosol can also consume chromium and reduce its enhancement effect; however, this impact is smaller because only a small fraction of the chromium is vaporized.

10.2 Process Evaluation

This research also examined processes for addition of the promoter to the calcium sorbent and for subsequent injection into the coal-fired boiler. In particular, these studies examined the influence of promoter type, particle size, injection temperature and sorbent type. Externally generated, promoted/sorbents were also considered.

The parametric results from the ash free, natural gas studies indicated that particle size of the sodium promoter was relatively important in effectively vaporizing and dispersing the promoter on the sorbent (i.e., larger particles more difficult to vaporize). Sodium need not be injected with the calcium to be effective in promoting sulfur capture due to the instability of the compounds at the injection temperatures (i.e., 1700 K, and 1500 K). Calcium sorbents when combined with sodium produced an increase in sulfur capture; capture enhancements ranged from 50 percent for Vicron to 20 percent for Genstar Type S.

Three externally generated dopant/sorbent combinations designed to reduce (or eliminate) the detrimental effect of the mineral ash were not completely successful. Clearly, the sodium promoted calcine while posting a low overall capture (24 percent, at Ca/S = 2) had an enhancement of 26 percent in the CTT fired with coal. Unfortunately, with coal as the fuel a near complete loss of promotion was seen for the sodium doped pressure hydrates.

11.0 REFERENCES

1. Attig, R. C., P. Sedor. "Additive Injection for Sulfur Dioxide Control: A Pilot Plant Study." EPA Report APTD 1176 (NTIS PB226761), March 1970.
2. Witten, C. M., R. G. Hagstrom. "Pilot Plant Moving Grate Furnace Study of Limestone-Dolomite for Control of Sulfur Oxide in Combustion Flue Gas." EPA Report APTD 1264 (NTIS PB184944), May 1969.
3. Ciambeli, P., D. Lucarelli, R. Valentino. Fuel. Vol. 64, June 1985. pp. 816-820.
4. Glasson, D., P. O'Neill. "Porosity of Absorbents for Desulphurization of Industrial Flue Gases." Characterization of Porous Solids, S. Gregg ed., Soc. of Chem. Ind., London, 1979. pp. 51-57.
5. Glasson, D., P. O'Neill. Thermal Analysis. Vol. 1, 1980. pp. 517-522.
6. Slaughter, D. "Formation and Control of Nitrogen and Sulfur Oxides in Suspension Coal Combustion." Ph.D. Dissertation, Chemical Engineering Dept., University of Utah, Salt Lake City, Utah, 1986.
7. Wen, C. Y. and M. Ishida. Env. Sci. Tech., 7, 703-708 (1973).
8. Ishihara, Yoshimi. "Kinetics of the Reaction of Calcined Limestone with Sulfur Dioxide in Combustion Gases." Presented at the Dry Limestone Injection Process Symposium, Gilbertsville, Kentucky, June 22-26, 1970.
9. Coutant, R. W., R. E. Barrett, R. Simon, B. E. Campbell, and E. H. Lougher. "Investigation of the Reactivity of Limestone and Dolomite for Capturing SO_2 from Flue Gas." EPA Report APTD 0621 (NTIS PB196749), November 1970.
10. Borgwardt, R. H. AIChE J, 31, 103, 1985.
11. Borgwardt, R. H. Environ. Sci. Technol., 4, 59, 1970.
12. Newton, G., D. Pershing. "Experimental and Theoretical Study Capture by Sized Precalcines CaO in an Isothermal Reactor." AIChE, Submitted for Publication, Sept. 1986.
13. Overmoe, B., S. Chen, L. Ho, W. Seeker, M. Heap, and D. Pershing. "Boiler Simulator Studies on Sorbent Utilization for SO_2 Control." In: Proceedings: First Joint Symposium on Dry SO_2 and Simultaneous SO_2/NO_x Control Technologies, Volume 1, EPA-600/9-85-020a (NTIS PB85-232353), July 1985. p. 15-1.
14. Borgwardt, R., K. Bruce, and J. Blake. "EPA Experimental Studies of the Mechanisms of Sulfur Capture by Limestone." In: Proceedings: First Joint Symposium on Dry SO_2 and Simultaneous SO_2/NO_x Control Technologies, Volume 1, EPA-600/9-85-020a (NTIS PB85-232353), July 1985. p. 6-1.

15. Case, P., L. Ho, W. Clark, E. Kau, D. Pershing, R. Payne, and M. Heap. "Testing of Wall-Fired Furnaces to Reduce Emissions of NO_x and SO_x: Volume 1." EPA-600/7-85-026a (NTIS PB85-224632), June 1985.

16. Overmoe, B., L. Ho, S. Chen, W. Seeker, D. Pershing, and M. Heap. "Boiler Simulator Studies on Sorbent Utilization for SO_2 Control." EPA-600/7-86-028 (NTIS PB87-101770), Sept. 1986.

17. Green, S., S. Chen, D. Clark, M. Heap, and D. Pershing. "Bench-Scale Process Evaluation of Reburning and Sorbent Injection for In-Furnace NO_x/SO_x Reduction." EPA-600/7-85-012, (NTIS PB85-185890), March 1985.

18. Gordon, S., B. McBride. "Computer Program for Calculation of Complex Chemical Equilibrium Compositions, Rocket Performance, Incident and Reflected Shocks and Chapman-Jouquet Detonations." NASA SP-273, March 1976.

19. Gelbert, F. "MAEROS Users Manual." Sandia National Laboratory Report No. SAND 80-0822, NUREG/CR-1391, 1982.

20. Cole, J., J. Kramlich, G. Samuelsen, W. Seeker, and G. Silcox. "Fundamental Studies of Calcium-Based Sorbents for SO_2 Control from Coal-Fired Boilers." EPA-600/7-87-002, (NTIS PB87-152500), January 1987.

21. Overmoe, B., T. McCarthy, S. Chen, W. Seeker, and D. Pershing. "Reactivity Study of SO_2 Control with Atmospheric and Pressure Hydrated Sorbents." EPA-600/7-86-040 (NTIS PB87-129250), Nov. 1986.

22. Reference Number Not Used.

23. Gjostein, N. A. Short Circuit Diffusion. In: Diffusion. American Society for Metals, Metal Park, OH, 1973. pp. 241.

24. Elliott, M. A. Chemistry of Coal Utilization. 2nd Supp. Vol., Chap. 21, Wiley-Interscience, Copyright 1981.

25. Levi, Robbins, C., McMurdie, H. Phase Diagrams for Ceramists. Vol. 1, Amer. Cer. Soc., 1964. p. 48.

26. Desal, N., R. Yang. Ind. Chem. Des. Dev. Vol. 22, 1983. pp. 119-123.

27. Satterfield, C. N. "Heterogeneous Catalysis in Practice." McGraw Hill, NY, 1980.

PART VI. APPENDICES

APPENDIX A

QUALITY ASSURANCE

A.0 QUALITY ASSURANCE

The collection and analysis of quality data has been the primary objective of this program. In order to ensure that the reported data is accurate, many quality assurance measures have been taken in all phases of the program. Most of the procedures and measurements used for data acquisition have been standardized by EPA or ASTM and those which have not are described in detail in this appendix. (As required by the EPA, a Quality Assurance Plan was submitted and approved prior to the start of this program).

Three facilities at EER were involved in procuring the data presented in this report; the CTT, BSF, and Rotary Kiln and DXRD. All of the quality assurance information presented in this appendix applies to these facilities.

A.1 Gas Species Measurements

Exhaust gas-phase species composition was measured using the BSF and CTT laboratory sampling systems. These systems were constructed in strict conformance with EPA performance specifications and their use helped ensure data quality. The species that were measured included: NO, NO_2, SO_2, CO, O_2, and CO_2, all of which were measured by continuous gas analyzers.

Table A-1 lists the specific instruments and full-scale ranges. The instrument ranges have been selected to exceed the maximum expected concentrations by a small margin.

Figure A-1 shows a schematic diagram of the continuous monitoring system for NO, NO_x, CO, CO_2, and O_2. The system was nearly identical for both the BSF and CTT. All components in contact with the sample were stainless steel or Teflon to ensure sample integrity and corrosion resistance. The gas sample was provided to the instruments by a sample conditioning system consisting of a pump, moisture condenser and particulate filters.

TABLE A-1. BSF AND CTT INSTRUMENTATION

Gas Measured	Type of Instrument	Manufacturer	Model No.	Range	Reference
NO, NO_x	Chemiluminescent	Thermo Electron Corp. (TECO)	10 AR	1000 RPM	Teco Model 10 Operating Manual
CO	Nondispersive Infrared (NDIR)	Anarad, Inc.	{BSF} AR500R {CTT} AR600R	500 ppm 10 percent	Anarad AR 500 Operating Manual Anarad AR 600 Operating Manual
CO_2	Nondispersive Infrared (NDIR)	Anarad, Inc.	{BSF} AR500R {CTT} AR600R	25 percent 40 percent	Anarad AR 500 Operating Manual Anarad AR 600 Operating Manual
O_2	Paramagnetic	Beckman Taylor Servumex	{BSF} 755 {CTT} 0A250	10 percent 100 percent	Beckman 755 Operating Manual Taylor 0A250 Operating Manual
SO_2	UV Absorption	DuPont	400	5000 ppm	DuPont 400 Operating Manual

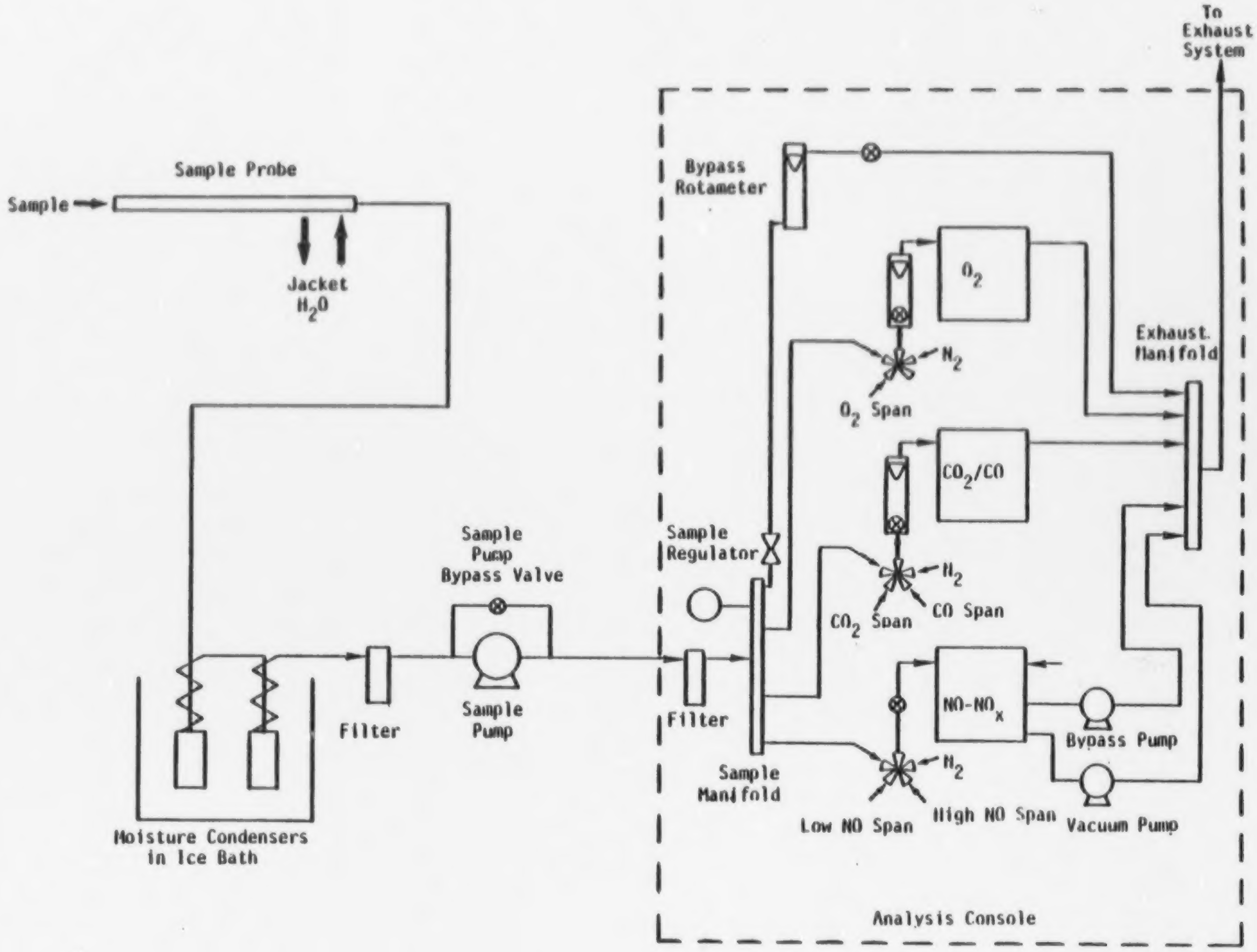
To Exhaust System
Sample Probe
Sample
Jacket H_2O
Bypass Rotameter
O_2
N_2
O_2 Span
Exhaust Manifold
CO_2/CO
Sample Pump Bypass Valve
Sample Regulator
N_2
CO_2 Span
CO Span
NO-NO_x
Filter
Sample Pump
Filter
Bypass Pump
Sample Manifold
N_2
Low NO Span
High NO Span
Vacuum Pump
Moisture Condensers in Ice Bath
Analysis Console

Figure A-1. Continuous monitoring sampling system.

Gas phase measurements were made routinely at Port 10B in the BSF and at the exhaust in the CTT. Phase discrimination probes (see Figure A-2 were used at both locations. The probes supplied two gas streams simultaneously. The main, particle-laden stream, which was used for continuous monitoring of O_2, CO, CO_2, NO_x, and the side, nearly particle-free stream, which was used for SO_2 measurement.

Figure A-3 shows a diagram of the continuous monitoring system for exhaust SO_2 measurements. The SO_2 gas sample in the nearly particulate-free stream was transported in a heated Teflon line maintained above 115°C under vacuum to a heated filter followed by a permeation tube drier. The permeation tube drier selectively removed water vapor from the gas sample. Dry air was used as the dry gas medium in the permeation drier. The sample was then pressurized and delivered to the analyzer. SO_2 concentration was measured using a non-dispersive ultraviolet instrument manufactured by DuPont.

Table A-2 gives the precision, accuracy, and completeness data for both sets of instruments used on the BSF, CTT, and rotary kiln. In every case, the program goals for precision and accuracy were met.

A.2 Solid Species Measurements

A.2.1 Grab Samples

Grab samples are used to obtain materials for specific surface area and particle size analysis. Suitably sized samples are removed at random from bulk containers of the material to be tested. Since the total quantity of each of the bulk materials involved in this study is quite small (a few kg at most) minimal effort, beyond stirring, needs to be taken in order to ensure the representativeness of the sample.

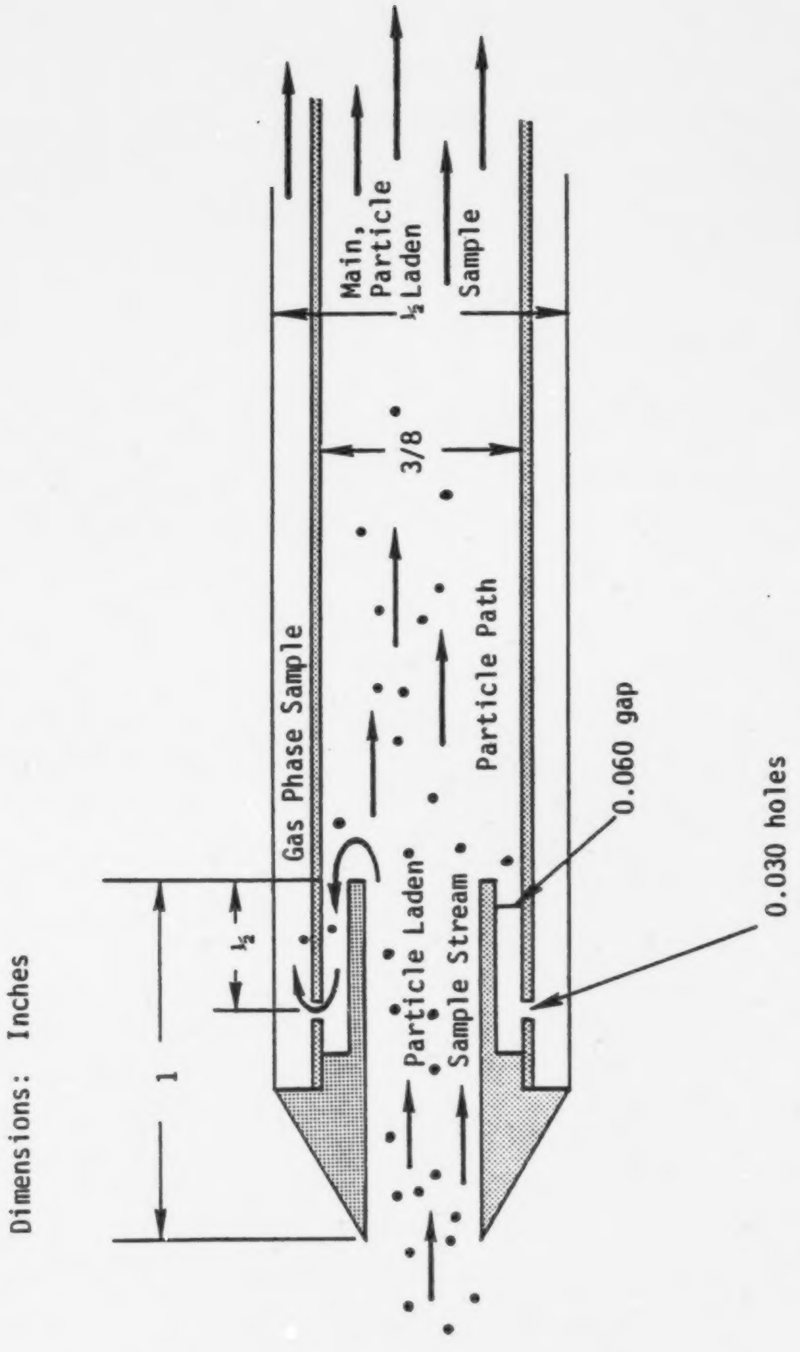
Dimensions: Inches
1
½
Gas Phase Sample
Particle Laden
Sample Stream
Particle Path
3/8
Main, Particle Laden
½
Sample
0.060 gap
0.030 holes

Figure A-2. Phase discrimination probe.

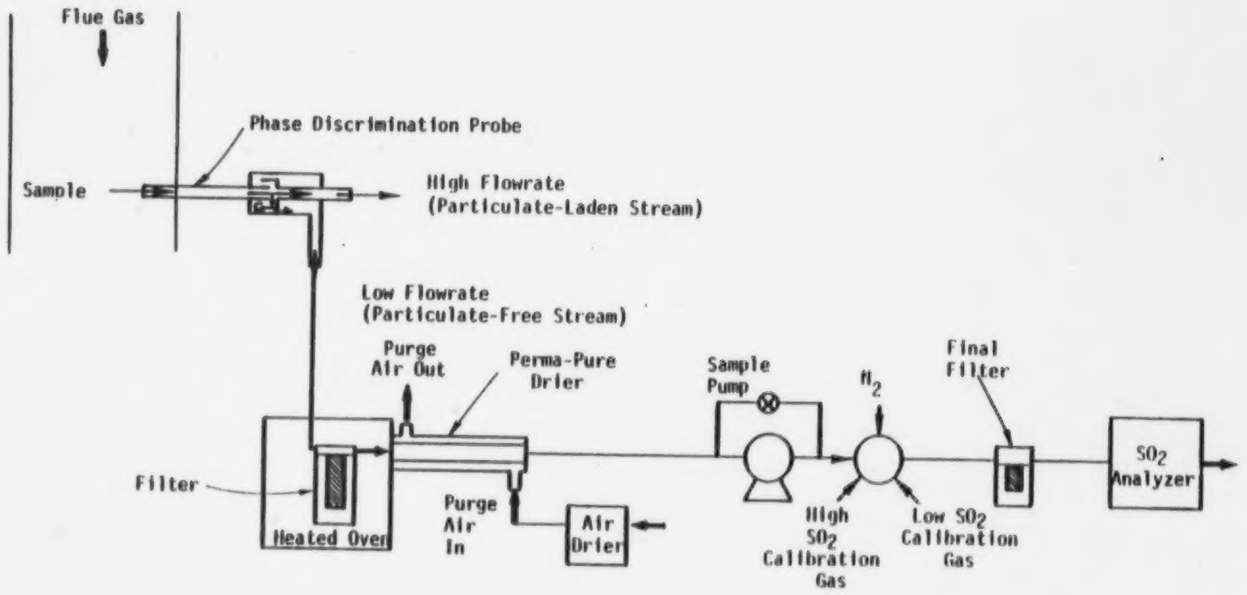
Flue Gas
Sample
Phase Discrimination Probe
High Flowrate
(Particulate-Laden Stream)
Low Flowrate
(Particulate-Free Stream)
Purge Air Out
Perma-Pure Drier
Filter
Heated Oven
Purge Air In
Air Drier
Sample Pump
N_2
High SO_2 Calibration Gas
Low SO_2 Calibration Gas
Final Filter
SO_2 Analyzer

Figure A-3. SO_2 continuous monitoring system.

TABLE A-2. PRECISION, ACCURACY, AND COMPLETENESS DATA FOR GAS SPECIES INSTRUMENTS

Gas Measured	Precision (%)				Accuracy (%)				Completeness (%)			
	Goal	Actual BSF	Actual CTT	Actual Kiln	Goal	Actual BSF	Actual CTT	Actual Kiln	Goal	Actual BSF	Actual CTT	Actual Kiln
NO_x (Chemiluminescent)	2	1.4	0.3	-	20	14.2	12.3	-	90	100	100	-
CO (NDIR)	2	0.4	0.5	-	20	No Std.	No Std.	-	90	100	100	-
CO_2 (NDIR)	2	0.8	0.1	0.8	20	6.7	2.5	6.7	90	100	100	100
O_2 (Paramagnetic)	2	0.5	0.2	0.5	20	11.2	13.1	11.2	90	100	100	100
SO_2 (UV Absorption)	2	0.2	0.3	-	20	8.1	10.2	-	90	100	100	-

A.2.2 Solids Analysis

The composition of solid samples was determined by EER's Analytical Lab and an independent laboratory. Carbon, Hydrogen and Nitrogen were analyzed on a Perkin-Elmer 240B and solid sulfur species were determined from a Leco SC32 Analyzer. Chemical (and elemental) composition was determined by a variety of techniques; X-ray diffraction, X-ray fluorescence, and energy dispersive spectroscopy. Table A-3 gives the precision and accuracy for the solid data obtained in this program. Calcium analysis was done with a Chelometric titration method which is covered under ASTM D 2795.

A.3 Temperature Measurements

High-temperature gas measurements within furnaces are subject to large inaccuracies due to the effects of thermal couple radiation loss. Therefore, in-furnace gas temperatures were measured using a suction pyrometer system as shown in Figure A-4. The suction pyrometer consisted of a high-temperature thermocouple (B type) in a porous ceramic radiation shield. The pyrometer was placed in the gas stream with the opening in the alumina sheath pointing downstream. A high flow rate of furnace gas was withdrawn through the sheath and over the thermocouple to increase convective heat transfer to the thermocouple and reduce radiation loss. As the gas flow rate was increased, the gas temperature increased to a constant value, indicating no additional reduction in radiation loss. Figure A-5 shows the results of the motive side pressure (a measure of suction flow rate) calibration for the CTT. A suction pressure of 40 psig was adopted for all the temperature measurements for the CTT system.

The BSF system used a pressure of 30 psig for all temperature measurements (see Figure A-6).

A.4 Calibration Procedures

Calibration procedures and frequency for each measurement system are listed in Table A-4. As shown in the table, standard calibration procedures

TABLE A-3. SOLID ANALYSES PRECISION AND ACCURACY DATA

Measurement		Precision (%)		Accuracy (%)	
		Actual	Goal	Actual	Goal
Carbon		.24	2	0.8	2
Hydrogen		1.38	5	0.6	5
Nitrogen		2.13	10	1.9	10
Ash		0.33	10	1.42	10
Moisture		2.55	10	8.71	10
Sulfur--Leco SC32		2.36	10	0.55	10
X-Ray Diffraction		3.0	5	10	10
X-Ray Fluorescence	Major:	0.3	5	0.5	5
	Minor:	0.8	5	3.0	5
Energy Dispersive Spectroscopy		3	8	5	5
DXRD		5	8	5	10

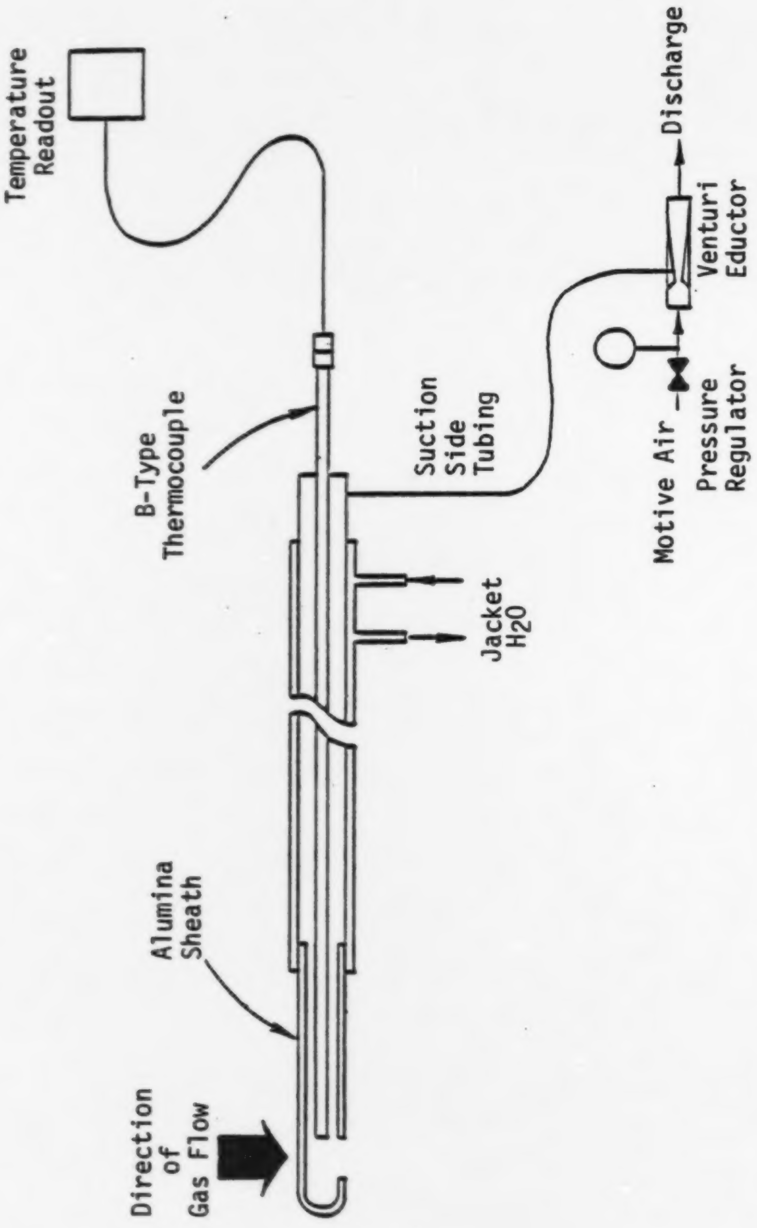
Temperature Readout
Discharge
Venturi Eductor
B-Type Thermocouple
Suction Side Tubing
Motive Air
Pressure Regulator
Jacket H_2O
Alumina Sheath
Direction of Gas Flow

Figure A-4. Gas temperature measurement system.

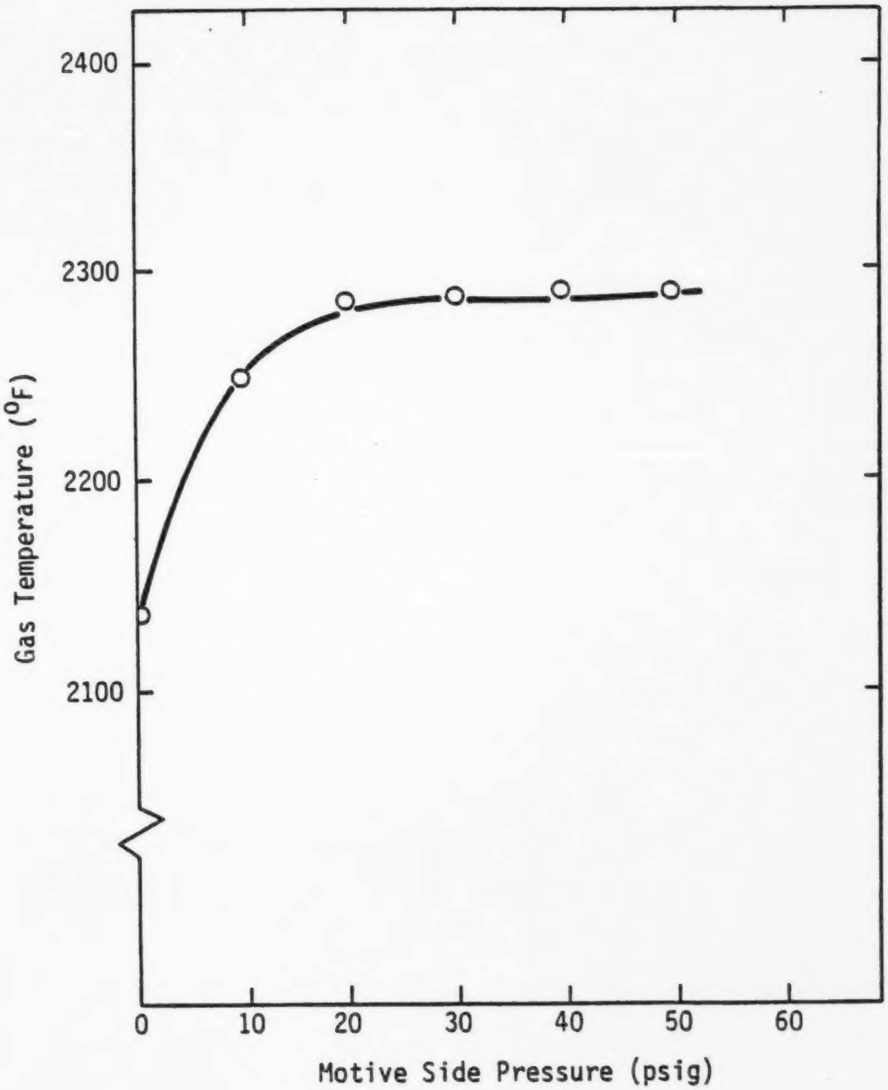

Figure A-5. Suction pyrometer aspirator pressure calibration for CTT.

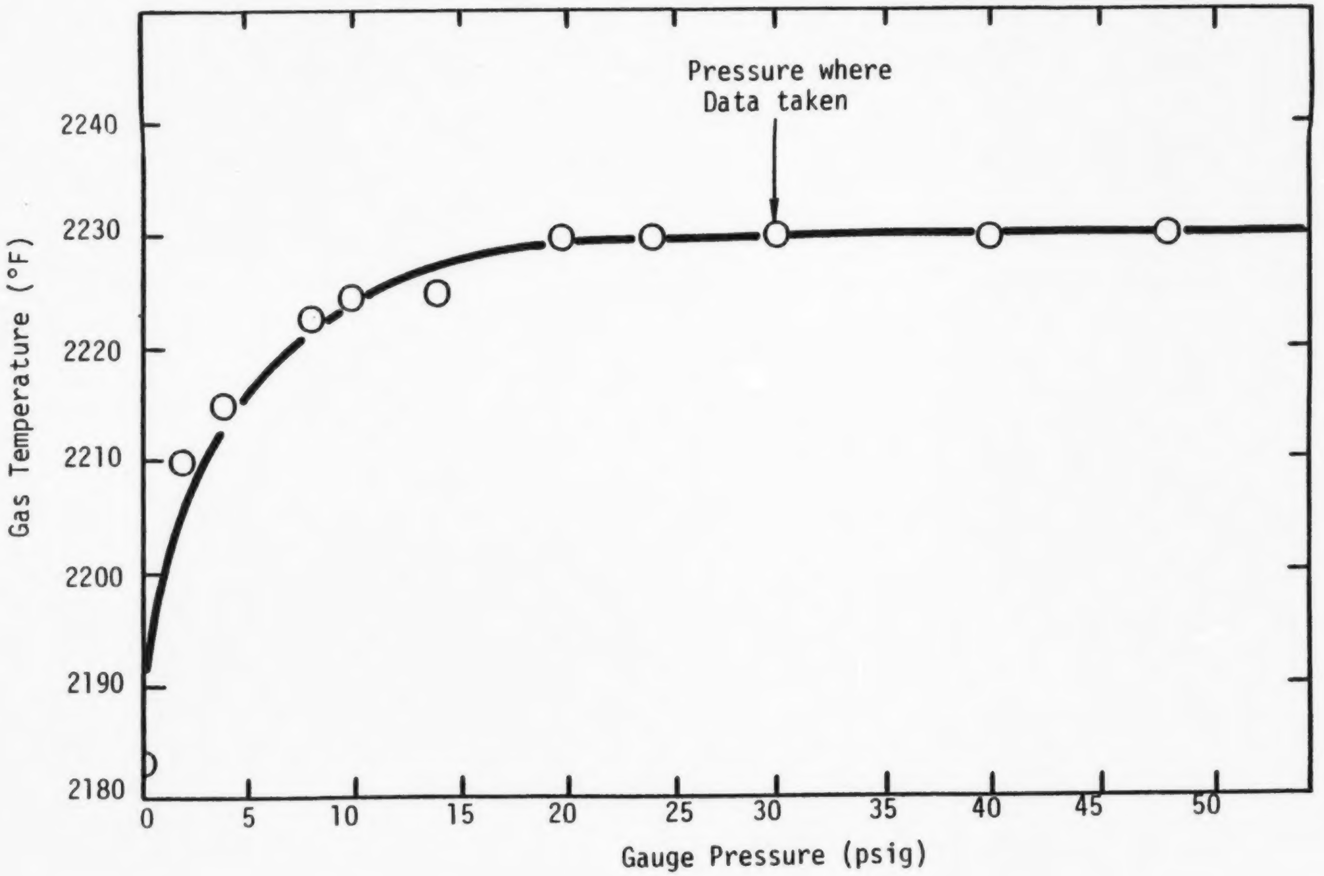

Figure A-6. Suction pyrometer aspirator pressure calibration for BSF.

TABLE A-4. CALIBRATION PROCEDURES

MEASUREMENT PARAMETER	CALIBRATION PROCEDURE	CALIBRATION FREQUENCY	CALIBRATION STANDARD	REFERENCE
Fuel Composition:				
Carbon	Standard Samples	Daily	Known quantity of 100% acetanilide	Perkin Elmer 240 B Operating Manual
Hydrogen				
Nitrogen				
Ash				
Moisture				
Sulfur	Standard Sample	Daily	Certified sulfur standards	Leco SC 32 Operating Manual
Exhaust Gas Composition				
NO, NO_2	Compare to standard compressed gas	Daily	EPA Protocol 1 Gases or custom gas blends. See Section 10.0	EPA EMSL Protocol No. 1, June 1, 1978
O_2				
CO				
CO_2				
SO_2				
Hydrocarbons				
Sorbent Surface Area		Daily	Known quantity of N_2	Quantasorb Surface Area Analyzer Operating Manual
Sorbent Flowrate	Weigh feed over measured time with independent balance		Standard weights	

were used for each system. Each system was calibrated at the frequency shown in the table to ensure the accuracy of the measurement were traceable to the calibration standards.

Each of the continuous monitoring instruments was calibrated with three gases: a zero gas and two span gases. Table A-5 lists the span gases used to calibrate instruments for the CTT sample system.

A.5 Data Reduction

Equations used to calculate results for each of the measurements are discussed below. Many of the results are obtained directly from the measurements and thus do not require calculations.

A.5.1 SO_2 Capture

The gas compositions are measured as chart divisions on a strip chart recorder. The measured divisions are converted to concentration (ppm or percent) based on calibrations with certified gases.

SO_2 capture with sorbent injection is defined as:

$$\text{Percent Capture} = \frac{(SO_2)_1 - (SO_2)_2}{(SO_2)_1} \times 100\%$$

where: $(SO_2)_1$ = SO_2 concentration without sorbent, ppm

$(SO_2)_2$ = SO_2 concentration witn sorbent injection, ppm

A.5.2 Percent Calcination

Percent calcination is the percentage of the calcium in a sample of initially $CaCO_3$ or $Ca(OH)_2$ which has been converted to CaO due to heating.

TABLE A-5. CALIBRATION GASES

Gas	Concentration	Percent of Full-Scale	Balance Gas	Grade
NO	836 ppm	84	Nitrogen	Certified Standard
NO	166 ppm	16	Nitrogen	Certified Standard
SO_2	2915 ppm	73	Nitrogen	Certified Standard
SO_2	437 ppm	11	Nitrogen	Certified Standard
CO	1227 ppm	82	Nitrogen	Certified Standard
CO_2	12.3%	31	Nitrogen	Certified Standard
CO_2	5%	13	Nitrogen	Certified Standard
O_2	10%	10	Nitrogen	Certified Standard
O_2	4%	4	Nitrogen	Certified Standard
CO	10%	100	Nitrogen	Certified Standard
CO	2%	20	Nitrogen	Certified Standard

Percent calcination is calculated directly from results of the 240B (wt% C) and the calcium titration (wt% Ca).

$$\text{Percent Calcination} = \left(1 - \frac{10}{3} \times \frac{\text{wt\% C}}{\text{wt\% Ca}}\right) \times 100\%$$

An alternate check on the percent calcination is obtained by a mass balance involving the results from the 240B (wt% C, wt% H, wt% ash) and the SC32 (wt% S). Tests have shown that during 240B analysis, $CaSO_4$ is retained in the ash, while $Ca(OH)_2$ and $CaCO_3$ are completely devolatilized. Percent calcination is calculated as follows:

$$\text{Percent Calcination} = \left(1 - \frac{14}{3} \left(\frac{\text{wt\% C}}{\text{wt\% Ash} - 2.5 \times \text{wt\% S}}\right)\right) \times 100\%$$

A.5.3 Particle Size Distribution

Particle size distribution is provided directly as a plot of cumulative mass-percent finer versus equivalent spherical diameter. An example particle size distribution plot is shown in Figure A-7.

A.5.4 Specific Surface Area

Specific surface area is measured by a Quantasorb Analyzer by the BET method. This analyzer measures the quantity of nitrogen adsorbed on a sample surface as a function of the relative (to saturation) partial pressure of nitrogen. Two equations are used to determine the specific surface area:

$$\frac{1}{X(Po/P-1)} = \frac{C-1}{X_m C} \frac{P}{P_o} + \frac{1}{X_m C}$$

where:

X = weight of N_2 adsorbed at P/Po

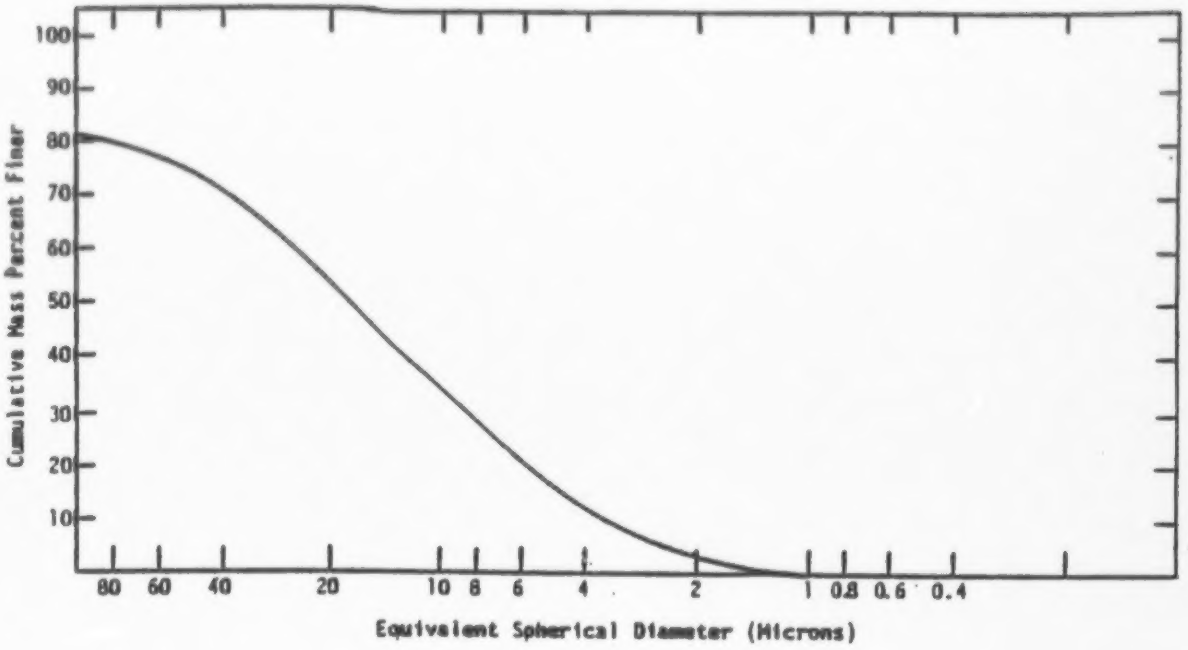

Figure A-7. Example of sorbent particle size distribution.

P = partial pressure of N_2

P_o = saturation pressure of N_2

X_m = weight of N_2 adsorbed for monolayer coverage

C = a constant which is a function of the heat adsorption and the heat of condensation of N_2

By measuring X for two or more values of P/Po the slope, $c-1/x_m c$, and intercept, $1/x_m c$, are obtained. After solving for X_m the specific surface area, S, is obtained from:

$$S = \frac{X_m NA}{M_a M_s}$$

where:

N = Avogradro's number

A = cross-sectional area of an adsorbed N_2 molecule

M_a = mass of N_2 molecule

M_s = mass of sample

A.5.5 Combustion Air Flowrate/Distribution

Combustion air flowrate is read directly from rotameters or is calculated from pressure drop measured across laminar flow elements based on the equation:

$$Q = K \left(\frac{\Delta P}{T}\right)^{1/2}$$

A.5.6 Combustion Air, Furnace Gas, and Exhaust Gas Temperatures

Temperatures are measured by thermocouples and provide results in units of degrees centigrade which can then be converted to other temperature scales, as required.

A.5.7 Residence Time

Residence times are calculated by assuming a one-dimensional flow in the furnace. Based on the measured temperatures, the bulk mean residence time of the reburning zone (τ_2) was calculated by using the following equation:

$$2 = \frac{V}{\dot{V}} \; \frac{T_o}{T_m}$$

where:

V = volume of reburning zone, ft^3

$\dot{V}$ = volumetric flow rate of gas, SCF-S

T_o = 530^oR

T_m = bulk mean gas temperature

= $1/2\ (T_1 + T_2)$

T_1 and T_2 are center line temperatures measured at the exit of the primary and reburning zones, respectively.

APPENDIX B

DEVELOPMENT OF THE DXRD TECHNIQUE

The DXRD development was focused on the need to extract repeatable data in the form of species volume fractions and to determine the minimum time necessary to obtain quality reaction rate data for fast reactions. The former was a software problem while the latter required a full-scale optimization of the pertinent DXRD scan parameters. In addition, obtaining accurate measurements of the solid sample surface temperature was also found to be a problem and a considerable development effort was expended in resolving this problem.

Species Concentration. The quantitative conversion from integrated intensities to concentrations is not trivial. Two basic methods exist for doing this. One method involves the use of an internal standard and reference intensity ratios. This method lends itself well to systems in which only a few phases among many are of interest. The concentration of a phase is calculated from the ratio between its intensity and the intensity of the internal standard. The only requirement is to know the concentration of the internal standard throughout the reaction. The second method avoids the need for an internal standard by employing absorption coefficients. It requires that all significant phases are monitored at least once during reaction. The strength of this method is that it is completely general, requiring no external knowledge of how the concentration of an internal standard will change as the sample reacts. The latter method was the one chosen for this work. It requires the solution of a set of linear equations. For a mixture of n phases, the equation for the j^{th} row will be

$$\sum_{i = 1, i \neq j}^{n} \nu_i \mu_i + \nu_j \mu_j \left(1 - \frac{I_{jp}}{I_j}\right) = 0 \qquad (B.1)$$

where ν_i is the volume fraction of component i and $_i$ is the linear absorption coefficient of component i. The latter may be calculated from data tabulated in literature. I_{jp} is the intensity that phase j would have if the sample were pure phase j.

It is sometimes possible to measure the pure phase intensity directly. Usually, however, it is necessary to determine it from reference intensity ratios. The reference intensity ratio (RIR) used here is defined as the ratio of the integrated intensities of the major peaks of the phase in question and a reference phase (typically corundum) in a 50 weight percent mixture. It is related to pure phase intensity according to Equation (B.2).

$$\frac{I_{\alpha p}}{I_{\beta p}} = \frac{\mu_\beta}{\mu_\alpha} \frac{RIR_\alpha}{RIR_\beta} \tag{B.2}$$

where α and β are particular phases.

Although reference intensity ratio measurements are straightforward, the JCPDS has published values for very few of them, and those values that have been measured are known to be in error by as much as ±20 percent. This large margin for error arises because integrated intensity was approximated by peak height in the JCPDS measurements. Peak heights have been shown to approximate integrated intensity only within 20 percent. All DXRD results have consequently used RIR measurements performed in this lab and based upon integrated intensity. It should be noted that the actual magnitude of the pure phase intensities calculated from Equation 4 will not matter as long as the sum of the calculated volume fractions is set equal to one. Software has been developed for rapid data analysis in the manner just described.

Scan Parameter Optimization. If DXRD is to be used for relatively fast solid state reactions, then it is important to reduce the amount of time necessary to scan a peak and obtain a valid intensity. Optimization with respect to time allows manipulation of the two time-related parameters, which are the number of points in a scanned peak and the count time at each point. These are dependent upon each other. The scan time is equal to the number of points scanned multiplied by the count time at each point, neglecting the time required to slew the goniometer from one point to another. Since we seek to obtain the most accurate and easily integrated peak in a minimum time, we may scan a typical peak over a fixed range, varying the number of points and the count time simultaneously to keep the total scan time constant. In order to evaluate this aspect of DXRD, an arbitrary time of one minute was selected to scan the major peak of calcite from 28 to $30^{o}, 2\theta$. This range scans the major calcite peak in its entirety at any reasonable temperature. Since it takes the same amount of time to scan the width of the peak in any of these one-minute scans, the optimal step size and count time are those that result in the most accurate and easily integrated peak.

The criteria for selecting the optimum scan parameters must reflect two things: peak definition and the statistical deviation of the points in the peak. Peak definition is related to the number of points used to integrate the peak and the positioning of those points. For example, in the simplest case of approximating integrated intensity by peak height, 20 percent error can result (JCPDS, 1978) because the broadness of the peak is not taken into account. On the other extreme, if a large number of points define the shape of the peak, the count time per point will need to be very small to be able to scan the peak in a short enough time to be of use to DXRD. The resulting statistical scatter of the points (due to a low signal-to-nose ratio) can result in integration attempts of low integrity. Calcite was chosen as the species to scan since it and its decomposition reaction to CaO ($CaCO_3$ CaO + CO_2) has been well studied. Visual inspection of the peak between 28^{o} and $30^{o}, 2\theta$ indicated that the signal-to-noise ratio was adequate for count times greater than or equal to 1.5 seconds. For a one-minute scan this corresponds to sampling 29 points actually on the peak at a 0.05^{o} step size. The resulting peak definition is excellent.

The next step in the optimization task was to determine the error involved by deviating from these parameters to shorten the total time spent scanning. To assess this, DXRD was applied to calcite decomposition. Calcite decomposition is known to be first order up to 80 percent conversion, so a rate constant is easily calculated. The scans of the major calcite peak were cycled continuously as the decomposition proceeded at 1023 K. Each cycle consisted of a 17 point scan of 0.05^{o} step sizes and 1.5 second count times. The full set of 17 point samples was taken to be the "best" data set and the first order rate constant was determined by numerically integrating the peak intensities to calculate fraction converted versus time. The rate constant obtained from this value when using truncated data sets was taken as the error. The other rate constants were calculated from the same data, except with points symmetrically truncated from the leading and trailing edges of the peaks inwards. This simulates scanning a narrower portion of the peak. Data were also systematically deleted from the full data set to simulate scans of 0.10° step sizes at several total scan widths. Figure B-1 shows the results of this exercise. As can be seen, either a 0.05° or a 0.10° step size gives comparable results (less than 5 percent error) for scan times greater than 12 seconds. To achieve the smallest error in the shortest scan time, however, a step size of 0.10° can be safely used to measure an entire peak every 7.5 seconds. The reason that the larger step size is preferable for short scan times is due to the fact that it results in a broader coverage of the entire peak. For example, at a scan time of 7.5 seconds, the 0.10° step size only covers 30 percent of the peak width. Thus we have concluded that the minimum number of points that must be sampled is 5, and the 5-point scan must cover at least 60 percent of the peak width. The minimum count time per point is 1.5 seconds. Including overhead time, this corresponds to the acquisition of three data points every 50 seconds.

F B-1

Surface Temperature Measurements. The heating strip/sample holder in the HTK-10 hot stage is a flat strip of platinum, approximately 1 mm thick. Since platinum is an excellent conductor it was initially assumed that the temperature measurement at the bottom of the strip would closely correspond to the temperature of the thin layer of the solid resting on the top of the strip. However, in order to prevent the solid sample from rolling during goniometer movement (causes peak shifts), it was necessary to use a relatively thick sample bed ($\sim$1.6 mm). While the solid-solid friction was sufficient to eliminate solids rolling, calibration experiments with calcite decomposition indicated that the surface temperature was considerably less than the temperature at the bottom of the heating strip ($\sim$ 60 K at 1073 K). As a result it was decided to place a small Pt-Rh thermocouple (5 mil wires) directly into the bed, as close to the top surface as possible.

While this solution was a great improvement, the thermocouple junction was still large enough so that it occupied about 25 percent of the bed depth.

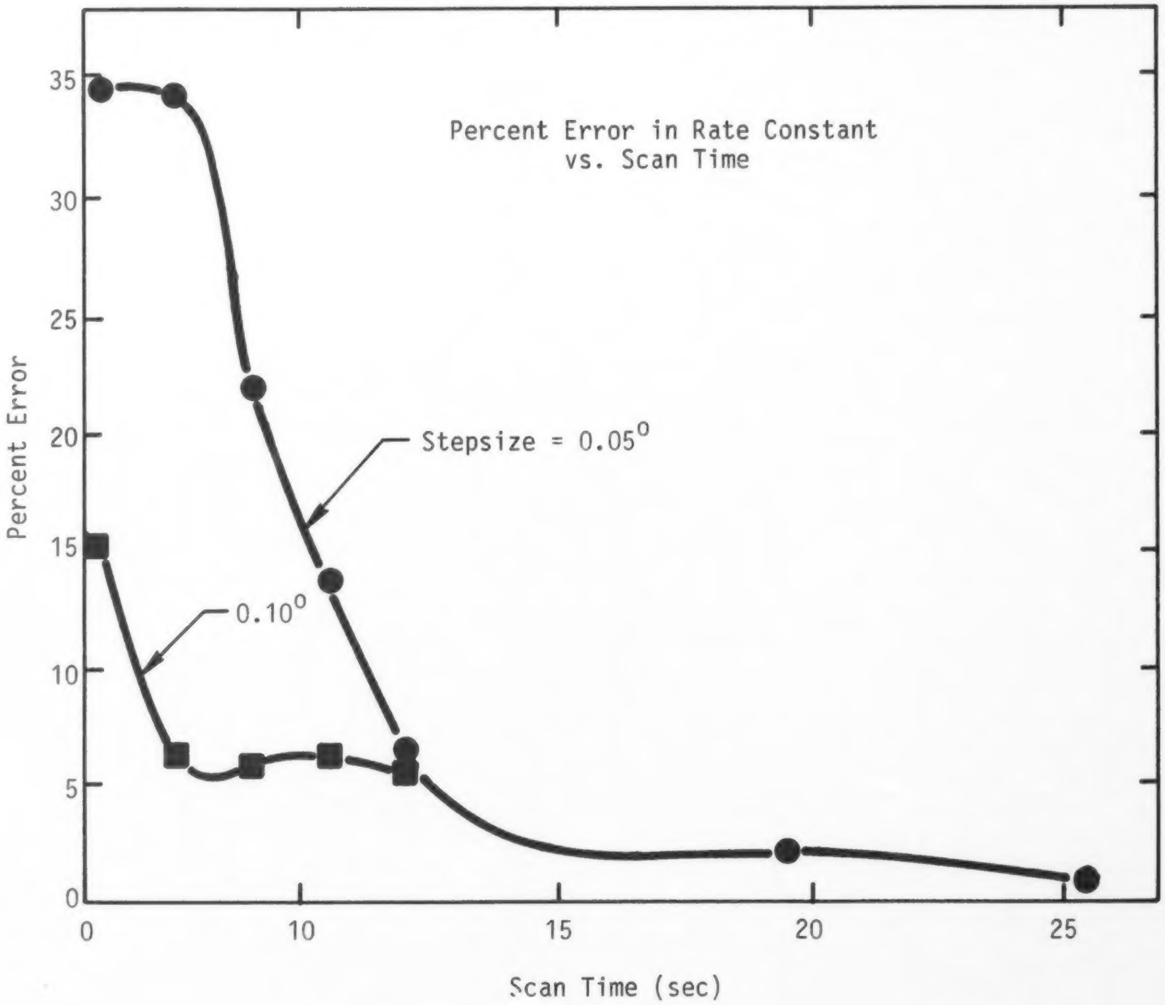

Figure B-1. Scan parameter optimization results.

Consequently, we were only able to measure an average temperature near the surface. Although all of the data collected as part of this investigation utilized this temperature measurement, subsequent experiments were able to correct these measurements for the true surface temperature. This was accomplished by developing a new sample mounting technique so that a very thin solid film (~ 100μ) was placed on the strip and then repeating the original calcite decomposition experiments. By comparing the reaction rates as a function of temperature for both the 1.6 mm thick sample and the 100 μ thick sample, the original temperature could be corrected to reflect the true surface temperature. All of the temperature data presented here have been corrected in this manner.